Stimulus characteristics of a novel air-based multiple stimulus aesthesiometer

by

Melanie Asha Mungalsingh

A thesis
presented to the University of Waterloo
in fulfillment of the
thesis requirement for the degree of
Doctor of Philosophy
in
Vision Science

Waterloo, Ontario, Canada, 2021

EXAMINING COMMITTEE MEMBERSHIPS

The following served on the Examining Committee for this thesis. The decision of the Examining Committee is by majority vote.

External Examiner	Dr. Edward Mallen Professor, School of Optometry and Visual Science University of Bradford
Supervisor(s)	Dr. Paul J. Murphy Professor, School of Optometry and Vision Science University of Waterloo
	Dr. Benjamin Thompson Professor, School of Optometry and Vision Science University of Waterloo
Internal/External Examiner	Dr. Richard Staines Professor, Department of Kinesiology & Health Sciences University of Waterloo
Other Member(s)	Dr. Lyndon Jones Professor, School of Optometry and Vision Science University of Waterloo
	Dr. Sean Peterson Professor, Department of Mechanical & Mechatronics Engineering University of Waterloo

AUTHOR'S DECLARATION

This thesis consists of material all of which I authored or co-authored: see Statement of Contributions included in the thesis. This is a true copy of the thesis, including any required final revisions, as accepted by my examiners. I understand that my thesis may be made electronically available to the public.

STATEMENT OF CONTRIBUTIONS

Melanie Mungalsingh was the sole author for Chapters 1 to 10. These chapters were written under the supervision of Dr. Paul J. Murphy and Dr. Benjamin Thompson, and have not been published or submitted for publication.

The contributions of others to various aspects of this thesis are as follows:

- Xueqing Zhang- Instrument development
- Zhenwen Wang- Hardware design
- Ehsan Zare Bidaki- Software design
- Dr. Paul J. Murphy- Data processing
- Dr. Benjamin Thompson- Data analysis and interpretation
- Dr. Vivian Choh- Image processing
- Dr. Sean Peterson- Image processing and data interpretation
- Dr. Trefford Simpson- Data analysis and interpretation
- Dr. Andrew Silva- Data analysis and interpretation
- Katelyn Tsang- Experimental design and data collection
- Collin McLaren- Experimental design and data collection
- Elisabet Simó Bertran- Experimental design, data collection, and image processing
- Stephanie Wong- Data collection

ABSTRACT

Purpose: To **(1)** develop a novel air-based aesthesiometer capable of producing and applying multiple stimuli separated either by time or space; **(2)** identify the stimulus airflow characteristics and confirm the consistency of the novel aesthesiometer; **(3)** determine if the instrument can be used to investigate spatial and temporal summation in the human cornea.

Methods: **(1)** A novel aesthesiometer (called the Dolphin Aesthesiometer) was designed around a micro-blower (Murata^{TM} Manufacturing Co., Japan) under software management. **(2)** Four studies that tested consistency and characteristics of the airflow (with and without a nozzle) were completed: (i) airflow pattern/trajectory measured using lycopodium powder, (ii) airflow surface dispersion by measuring lycopodium powder displacement; (iii) force of airflow across a range of stimulus strengths measured using a microbalance, (iv) thermal effects on the ocular surface measured using a thermal camera. **(3)** Two studies were performed to explore the effects of time delay and spatial separation on an *in vitro* eye model using thermography.

Results: **(1)** The instrument consists of four micro-blowers, each capable of separate or sequential stimulus delivery. Stimulus delivery under software management provided refined control of airflow rate and duration. **(2)** Stimulus characteristics studies: (i) airflow is coherent within the expected test distance range for the instrument, and the spread rate is constant irrespective of the stimulus strength; (ii) airflow dispersion occurs upon encountering a surface, and dispersion increases with increasing airflow rate; (iii) a consistent and small force (of the order of 10^{-4} N) is applied in relation to airflow; (iv) repeatable thermal effects occur in relation to the airflow, and the mode of stimulation of the Dolphin aesthesiometer is predominantly thermal in nature. Fitting a narrow diameter (1 mm) nozzle to the airflow exit of a micro-blower reduced stimulus airflow dispersion. **(3)** Effects of time delay and spatial separation studies: the Dolphin Aesthesiometer can deliver single stimuli, repeated single stimuli with a variable time-delay, or multiple stimuli either simultaneously or with time delay between them.

Conclusions: These studies confirm the repeatability and consistency of the novel instrument. The device is suitable for measuring corneal sensitivity. The availability of additional air-jets allows the application of multiple stimuli to facilitate corneal summation investigations. With some additional studies and calibration, this instrument will allow *in vivo* studies of neural signal summation in the corneal sensory nerves.

ACKNOWLEDGEMENTS

I would never have made it this far in my academic career or in this PhD program without the kindness and support of many individuals. I would first like to thank my supervisors, Dr. Paul Murphy and Dr. Ben Thompson. Thank you Dr. Murphy for taking a chance on someone with limited research experience. Thank you Dr. Thompson for your continual guidance, encouragement, and mentorship throughout the course of this degree. The skills I have developed, and the knowledge I have gained from both of you will definitely serve me well in the future.

My committee has also been pivotal to the completion of this PhD project. Thank you to committee members Dr. Lyndon Jones and Dr. Sean Peterson. You have both helped me to stay on course by offering your insightful comments and sharing your wisdom. I would especially like to thank Dr. Peterson for his time and patience when discussing the multitude of physics/engineering based questions I often had.

I have also been truly blessed to have the opportunity to learn from mentors outside of my committee. I would like to thank Dr. Trefford Simpson for his boundless support; taking the time to teach me about research, data analysis, academia, and life in general. There are truly no words to sufficiently express my gratitude. Your dedication to your students and invested interest in their success even beyond their program of study is admirable. I would also like to thank Dr. Vivian Choh for her assistance with image processing, holistic caring nature towards students, and for always reminding me to make the most of what graduate studies has to offer. You have both helped me to overcome several challenges, and exemplified the kind of researcher, teacher, and mentor I hope to become one day.

Thank you to the graduate coordinators Miss Emily O'Connor, Miss Holly Forsyth, and Miss Stephanie Forsyth. You all continue to work hard to put together successful conferences, ensure that I met my required milestones, offer advice whenever needed, and assist with any concerns I had.

I would also like to thank the amazing staff at the Witer Learning Resource Center who allowed me to work in the warm library space every day for the first two years of the program.

I was fortunate to be a part of two labs during my time at UW. I would like to thank all my lab mates in the MLEO and Thompson Lab, both past and present. I especially would not have survived this program without my fellow Thompsoners, as they like to call themselves. You all have managed to make those most difficult days that graduate students often face bearable, and I will be forever grateful. A special thank you is owed to Dr. Andrew Silva for always being so willing to help with my research endeavors and encouraging me to have faith in myself. Thank you to Dr. Amy Chow for being my writing companion before and during the pandemic period, reminding me that there is more to life than being a student, and your inspiring pep-talks. You are truly a unique individual, and I feel lucky to have met you during my time here. I would also like to thank my fellow graduate students in vision science for their continual support, kindness, and for sharing their experiences with me. In particular I would like to thank: Dr. Dania Abuliel, Dr. Taylor Brin, Dr. Clement Afari, and Dr. Varadhu Jayakumar.

I would especially like to thank Katelyn Tsang for all her assistance, encouragement, uplifting work ethic, and her glass half full attitude. To Nursama Juman, Brittanee Alexander, Melanie Ramsuchit, Louise Raudzus, Ebele Mogo, Joanne Qiao, Boon Khoo, as well as J. and K. Harricharan thank you for your friendship and for checking in on me. To Dr. John Randall, Dr. Sandra Wang, Miss Jacinta Chin-Aleong, Dr. Sarah Appel, and Miss Lachelle Smith thank you for teaching me what it means to be a thoughtful and caring clinician. To Dr. Dragana Miskovic and Dr. Steven Forsey thank you for showing me how to be a scientist and believing in me.

Lastly, but certainly not least, I would like to thank my family. I would like to thank the Yee Foon, Mungalsingh, Juman, and Chen families; as well as Granny Merle and Ria Mark. Thank you for believing in me, inspiring me, and giving me strength to face life and all its challenges. To my wonderful mother, thank you for your patience, understanding, counsel, and unwavering support throughout my life. Thank you for reminding me to be strong and where I come from. If I become half the person you are I would consider myself to be lucky. To my brother, Michael, thank you for all that you have done for me and for always being there for me, especially during my most stressful times. To my father, thank you for encouraging me to always do my best and showing me the results of hard work.

DEDICATION

This thesis is dedicated to my father, mother, Michael, Trixie and in loving memory of Aunt Jean, Aunt Moye, Uncle Archie, and Uncle Soy.

TABLE OF CONTENTS

LIST OF FIGURES

LIST OF TABLES

LIST OF ABBREVIATIONS

AC: Alternating current

BOPM: Belmonte Ocular Pain Meter gas-jet aesthesiometer

C-BA: Cochet-Bonet Aesthesiometer

CS: Corneal sensitivity

LoA: Limits of agreement

MLEO: Murphy Laboratory for Experimental Optometry

NCCA: Non-Contact Corneal Aesthesiometer

OST: Ocular surface temperature

PDD: Powder displacement diameter

PF: Peak force

SSF: Steady state force

SD: Standard deviation

SDT: Signal detection theory

V_{AC}: Alternating current voltage

V_{rms}: Root mean square voltage

CHAPTER 1: INTRODUCTION

1.1 General introduction

Corneal sensitivity can be defined as the neurological response of the free nerve endings in the epithelium layer of the cornea to stimuli. It is an important parameter to measure because it gives a better understanding of the neural and physiological functioning of the cornea (Nosch, 2015). For instance, it can explain the ocular symptoms associated with dry eyes and end of day irritability due to contact lens wear (Golebiowski et al., 2005; Golebiowski et al., 2011).

Aesthesiometry is a measure of the degree of sensitivity. By stimulating the corneal nerves and noting the psychophysical response of the subject, researchers are able to measure corneal sensitivity. Aesthesiometry has been studied for centuries, and because the human cornea is capable of detecting a variety of external stimuli, different types of aesthesiometers have been developed to investigate, as well as measure, various aspects of corneal sensitivity (Lum, 2014).

The Cochet-Bonnet aesthesiometer uses a nylon filament to supply a mechanical stimulus. The length of the filament is inversely related to the force that is applied to the corneal surface, and the mechanically-sensitive Aδ nerve fibers of the cornea typically respond to such stimulus. Despite being the gold-standard for measuring corneal sensitivity, the device is invasive, and suffers from numerous drawbacks (see Section 2.6.2 in Chapter 2) (Cochet & Bonnet, 1960; Murphy et al., 1996). Consequently, non-contact gas aesthesiometers were developed. These types of aesthesiometers utilize a regulated pulse of pressurized air, which can be heated or mixed with carbon dioxide to provide different types of stimuli. They are non-invasive and several studies have revealed good repeatability with them. However, there are limitations with their designs (Murphy et al., 1996; Stapleton et al., 2004). For example, with the Non-Contact Corneal Aesthesiometer (NCCA) developed by Murphy et al. (1996), there is a delay of the order of 0.2 seconds in reaching the maximum stimulus intensity after initializing a stimulus because of the tube arrangement used to deliver the air to the probe (Murphy et al., 1996). Another challenge associated with gas-jet aesthesiometers is that the exact mode of stimulus is less defined as there is often an overlap of stimuli. For instance, when applying air at room temperature to the cornea, there is both deformation of the ocular surface and localized evaporation from the ocular surface due to the airflow, which elicits a response from the mechanically-sensitive Aδ fibers, as well as the temperature-sensitive C nerve fibers, respectively (Belmonte et al., 1999; Belmonte et al., 2017; Murphy et al., 1999; Nosch et al., 2017). This means that the detection threshold measured (the smallest amount of stimulus needed to produce a sensation) in order to determine corneal sensitivity (the inverse of the threshold) could either be mechanical and/or thermal. In addition, it is difficult to compare threshold measurements between the various non-invasive gas-jet aesthesiometers because they are not standardized in terms of their units of measurement. Having an instrument that measures appropriate detection thresholds, which are associated with the actual mode of stimulation would allow more accurate measures of corneal sensitivity, and could lead to more standardization (Lum, 2014). This thesis describes a novel air-based aesthesiometer, known as the Dolphin aesthesiometer, that is based on the design of the NCCA and was developed to overcome many of the challenges associated with the gas-jet aesthesiometers. In addition, it will examine the stimulus airflow characteristics of the Dolphin aesthesiometer.

Furthermore, from a neuroscience perspective, research has shown that the free nerve endings in the sub-epithelial layer of the cornea exhibit large receptive field overlap, and that more than one type of corneal receptor can be activated by a particular mode of stimulation during aesthesiometry. Summation, which is the adding up of sensory information, occurs in the eye at the retinal level, and also in the skin, another touch-based tissue. However, to date, no aesthesiometry and corneal sensitivity studies have assessed summation, more specifically temporal and spatial summation (the adding up of sensory information over time and space, respectively) in the cornea. This is an important knowledge gap because summation may explain variation in sensitivity measurements, such as the differences in the degree of sensitivity measured in the peripheral and central regions of the cornea (Belmonte et al., 2011; Shaheen et al., 2014). Moreover, the lack of studies regarding summation in the cornea may be due to the fact that current non-contact gas-jet aesthesiometers only provide a single stimulus, and therefore cannot facilitate the investigation of summation in the cornea. This thesis will further investigate whether the Dolphin aesthesiometer, which consists of several micro-blowers and air-jets and can therefore deliver multiple stimuli, may be used to investigate spatial and temporal summation in the cornea through a series of *in vitro* studies.

1.2 Thesis objectives and components

Overall, this thesis has three main goals: (i) to develop a novel air-based aesthesiometer which is capable of producing and applying multiple stimuli separated either by time or space, (ii) examining the characteristics of the airflow stimulus produced by the aesthesiometer, and (iii) determining if the instrument can be used in the future to investigate spatial and temporal summation in the true cornea.

This thesis is composed of six separate, but related experiments, each with its own subsidiary aims. These experiments are organized into chapters in the body of the thesis. These studies were developed to investigate the characteristics of the stimulus and determine if the multiple air-jet feature of the instrument can be used to explore summation using an *in vitro* model eye. Chapter 2 reviews the literature on the anatomy of the cornea; the architecture of its nerves; corneal sensitivity (CS); aesthesiometry; sensory processing at the corneal level, as well as higher-level areas of the central nervous system (CNS) that are involved in the perception of sensation; the neuroscience of detection; and instruments (aesthesiometers) used for measuring corneal sensitivity. Chapters 3 to 8 describe studies geared towards learning more about the characteristics of the stimulus the aesthesiometer produces (Experiments 1-5). Chapter 9 explores the possibility of using the instrument to study summation at the corneal level through a series of *in vitro* experiments (Experiment 6), and Chapter 10 discusses the overall results, as well as future studies that can be performed with the instrument.

CHAPTER 2: LITERATURE REVIEW

2.1 Cornea

The cornea is the transparent, avascular, outer-surface structure of the eye. Light rays entering the eye must first pass through the cornea in order to form an optical image on the retina. On a basic level, its structure could be described as being clear and curved. Often in science, the function of something depends on its structure, and the same can be said of the cornea. The surface within the central radius of the cornea is spherical, however it progressively flattens peripherally to create an overall elliptical shape. This ocular structure provides 70% of the refractive power of the eye. The cornea is composed of five layers. From most anterior to posterior these layers are: the surface epithelium, Bowman's layer, the main body or stroma, Descemet's membrane and the endothelium. Each contributes to the proper functioning of the cornea (Lum, 2019; Riordan-Eva et al., 2011).

The cornea protects the interior structures of the eye. More specifically, the network of fine nerve endings in the epithelium is capable to detecting potentially noxious agents on the surface of the cornea, and consequently stimulate eyelid closure and tear production. Corneal innervation also aids in the maintenance and repair of the corneal epithelium (Lum et al., 2019).

Bowman's layer is a clear, acellular extension of the stroma. The stroma makes up 90% of the cornea. It consists of lamellae of collagen fibrils, which run parallel to the surface of the cornea and are optically clear. This structure helps to keep the cornea transparent by taking in fluid in a controlled manner (Riordan-Eva et al., 2011).

Descemet's membrane adds to the protective nature of the cornea by its strong elastic tissues which makes penetrating the cornea difficult. The endothelium is one cell layer thick and keeps the cornea at a fixed hydration level using sodium pump systems. A constant hydration level helps to maintain corneal transparency. The avascularity, uniform structure, and deturgescence of the cornea contribute to its transparency (Riordan-Eva et al., 2011).

The cornea gets it nutrition from blood vessels of the limbus, and from the aqueous and tears. The superficial cornea gets the majority of its oxygen from the atmosphere. The sensory nerves of the cornea are supplied by the ophthalmic division of the trigeminal nerve (Riordan-Eva et al., 2011).

2.2 Corneal innervation

The cornea is densely populated with sensory nerve fibers. Innervation first arises from the limbal plexus. A series of penetrating nerve bundles enter the stroma and repeatedly bifurcate as they proceed to the epithelial layer. The nerves converge at the sub-epithelial layer (Belmonte et al. 2011; Nosch, 2015; Shaheen et al., 2014). Whilst studies have yet to elucidate the precise relationship between corneal nerve fiber type, receptor type, and receptor field size, ultrastructural studies on the human cornea have strongly suggested that corneal free nerve endings may be specialised both functionally and structurally (Stapleton et al., 2004).

Two main groups have studied corneal nerves and some of these studies looked specifically at the corneas of animals, namely rabbits and/or cats. In terms of their findings, both groups agree that the nerves mediate our sensations. Whilst both groups essentially categorize the various nerve types based on how they respond to various modes of stimuli, the classifications are slightly different.

2.2.1 Corneal nerve characteristics based on fiber composition classification

MacIver and Tanelian categorized the nerves based on their fiber composition. There are two types of nerves in the epithelium, namely Aδ fibers and C fibers. Unmyelinated C fibers travel upward from the epithelial plexus towards the surface, traversing the epithelium. They travel to within 5 μm of the surface (Figure 1). These fibers are large and beaded. They conduct nerve impulses at a low velocity, and have been found to respond to thermal and/or chemical stimuli. Many of these fibers are also polymodal, and are therefore stimulated by near-noxious mechanical energy (Belmonte et al. 1991; Gallar et al. 1993; Nosch, 2015; Tanelian & Beuerman, 1984).

Conversely, the myelinated Aδ fibers are smaller in diameter, are straight, and travel both parallel and deeper below the surface of the cornea (Figure 2.1). They are fast-adapting nerves, which conduct nerve impulses at a fast velocity. They respond to mechanical stimuli, and it is postulated that they may also be polymodal nociceptors (Belmonte et al., 1991; Gallar et al., 1993; McIver and Tanelian, 1993a; McIver and Tanelian, 1993b; Nosch, 2015).

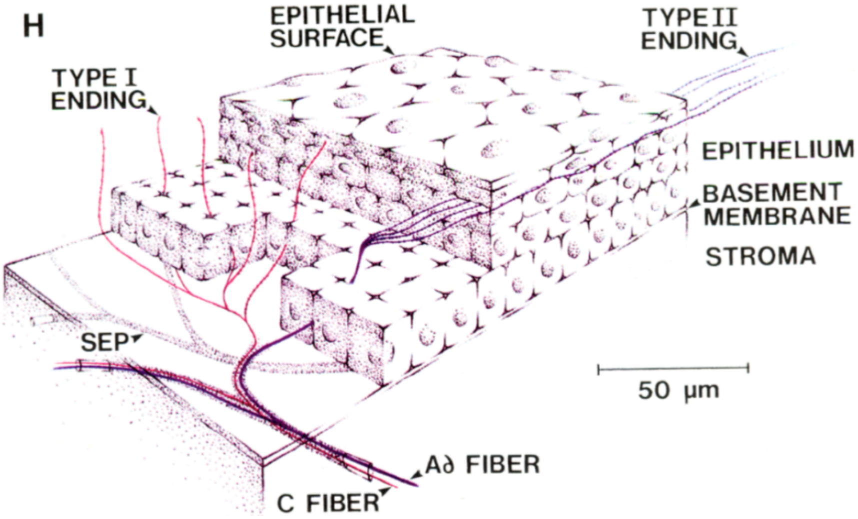

Figure 2.1: The different fiber types of the nerve ending morphology.

Reproduced from Journal of Neuroscience, 69(5), MacIver, M. B., & Tanelian, D. L., Free nerve ending terminal morphology is fiber type specific for A delta and C fibers innervating rabbit corneal epithelium, page 1781, Copyright (1993), with permission from The American Physiological Society (See Letters of Copyright Permission).

2.2.2 Corneal nerve characteristics based on mode of stimulation classification

Until the mid-19th century, corneal sensory receptors were believed to be capable of detecting only pain (nociceptive). Electro-physiological studies on the cornea revealed that sensory nerve terminals convert energy from different types of stimulus modalities into action potentials, which are then propagated along the nerve fiber. The response of the peripheral endings of sensory axons to a variety of stimulus modalities is the second way of distinguishing the functional classes of sensory fibers, which innervate the cornea, and is based on the works of the Belmonte group.

Corneal mechano-receptors are similar to Aδ mechanoreceptors found in the skin. They respond only to mechanical stimulation, which can include stimuli such as sustained or brief indentation of the surface of the cornea (Belmonte et al., 2004; McIver and Tanelian, 1993a; Nosch, 2015). According to studies, the mechano-receptors make up around 20% of the corneal nerve fibers in cats and about 70% in rabbits (Müller et al., 2003; Nosch, 2015; Tanelian & Beuerman, 1984).

Due to the fact that they occur in high density over a small area, the corneal mechano-receptors have been found to exhibit a lower threshold when compared to the mechano-nociceptor fibers of the skin. These receptors signal the onset of a stimulus and readily adapt when the stimulus is sustained. Consequently, they are deemed more suitable for detecting a stimulus rather than encoding its velocity and intensity (Belmonte & Giraldez, 1981; Belmonte et al., 2004; Bessou & Perl, 1969; Giraldez et al., 1979; McIver and Tanelian, 1993b; Nosch, 2015; Tanelian & Beuerman, 1984). This was further confirmed by Acosta and colleagues (2001a) who performed electrophysiological and psychophysical experiments in humans and cats. They found that the mechanosensory units were not responsive to an increase in mechanical stimulation, and postulated that the polymodal units may therefore encode the stimulus intensity instead (Acosta et al., 2001a; Nosch, 2015). The corneal mechano-receptors receptive fields are large, round or oval. MacIver and Tanelian (1993b) found that the receptive fields covered 4-6 mm^2 of the ocular surface in rabbits, whereas Tanelian and Beurman (1984) also measured the receptive field in rabbits, and reported them to be 10-20 mm^2 (Nosch, 2015; Tanelian, 1993b; Tanelian & Beuerman, 1984). Belmonte (1991) measured a vertical axis of 11.5 mm in cats (Belmonte et al., 1991; Nosch, 2015).

Polymodal nociceptors have been found in cats, and are believed to account for 70% of all corneal sensory fibers. These nociceptors are akin to the ones found in our skin. They respond to near-noxious mechanical stimuli, but can also sense chemical stimuli, as well as heat. They are predominantly C fibers, however some polymodal Aδ fibers have also been found. These receptors discharge irregular and continuous nerve impulses, which last for the duration of the stimulus. Their frequency of firing is related to the degree of stimulus intensity. When compared to the threshold of mechano-receptors, their mechanical threshold is lower. With respect to a heat stimulus, they only respond to heat over 39-40˚C (Acosta et al., 2001a; Acosta et al., 2001b; Belmonte & Giraldez, 1981; Müller et al., 2003; Nosch, 2015). With increasing concentrations of carbon dioxide, no difference has been found between the firing frequency of C and Aδ fibers in cat corneas. However, the C fibers showed longer response latencies and slowly reached their peak-firing rate (Belmonte & Giraldez, 1981; Gallar et al., 1993; Nosch, 2015). Along the vertical axis, the receptive field size of C and Aδ fibers in cats was found to be 4.9 and 8.2 mm, respectively (Chen et al., 1995; Nosch, 2015).

Studies have revealed a sub-type of corneal Aδ fibers in cats and rabbits that are not responsive to chemical stimulation, but are instead only sensitive to heat and mechanical stimulation. These fibers have higher mechanical thresholds and can sense an increase in temperature above 43˚C in cats and 39˚C in rabbits. The receptive size has been measured to be 8.5 mm along the vertical axis. The receptive fields are large. Moreover, because of their similar response profile, they can also be polymodal receptors with higher chemical thresholds (Belmonte et al., 1991; McIver and Tanelian, 1993b; Nosch, 2015; Tanelian & Beuerman, 1984).

Studies conducted on rabbits and cats revealed that 10-15% of the corneal nerve fibers are cold sensitive receptors. Whilst some of them may be Aδ fibers, the majority are C fibers. These fibers are tonically active at resting temperature, but their discharge frequency can vary with temperature. When the temperature is reduced to 33˚C the frequency increases, and when there is a rise in temperature the discharge frequency decreases. By blowing cold air onto the cornea, evaporation is produced from the tear film over the ocular surface, and consequently a reduction in corneal temperature is created, which leads to an increase in the firing rate of the cold sensitive fibers (Gallar et al., 1993; Tanelian & Beuerman, 1984; McIver and Tanelian, 1993b; Nosch, 2015). MacIver and Tanelian (1993a) noted a 50% decrease in the firing frequency when the corneal temperatures of rabbits were increased from 35 to 37˚C. These receptors stopped responding when the cornea was cooled down to below 5˚C (McIver and Tanelian, 1993b; Nosch, 2015). When warmed, cold receptors are silent in cats. However, they are activated proportionally to temperature decrease. The minimum amount of temperature change that the cat cornea is able to sense is approximately 0.1˚C or less (Acosta et al., 2001a; Gallar et al., 1993; Nosch, 2015). Gallar et al. (1993) noted variable receptive field sizes in cats (between 2 and 9 mm^2), whilst Tanelian and Beuerman (1984) found a greater overlap of receptive fields in the center of the rabbit cornea (Gallar et al., 1993; Tanelian & Beuerman, 1984; Nosch, 2015).

It is important to note that it has been postulated that silent nociceptors may also exist in the cornea. These fibers are insensitive to all types of stimulus when the tissue is intact. However, they become rapidly excitable to thermal, chemical, and mechanical stimulation when local inflammation develops. The presence of such receptors in the cornea has been studied, and the evidence indirectly suggests their plausible existence (Belmonte et al., 2011; Nosch, 2015).

The density of the epithelial nerves at the center of the cornea is greater than the density at the peripheral regions. The free nerve endings exhibit a density of about 605.8 terminals per square millimeter in the central cornea (Belmonte et al. 2011; Nosch, 2015; Shaheen et al., 2014). Sensory recordings, performed predominantly in cats and rabbits, have verified that nerve receptive field sizes are large and overlap extensively. This rich innervation gives the cornea a highly sensitive detection system (Belmonte et al., 1991; MacIver & Tanelian, 1993b; Nosch, 2015; Tanelian & Beuerman, 1984). However, whilst this results in a large amplification effect to any foreign body stimulus, it also affects the ability to localise stimuli on the cornea, as a single stimulus can stimulate many receptive fields (Boberg-Ans, 1995).

Even though there is a lot of literature on corneal nerves, it is important to note that our knowledge of the functional properties of the different corneal nerve fibers is still limited. A summary of the characteristics of the nerves based on their classification can be found in Table 2.1.

Nerve characteristic	Mechano-receptors	Polymodal receptors	Cold receptors
Population	• About 15-20%	• Approximately 67%	• About 10-15%
Fiber composition	• Myelinated (not fully within the cornea). • Fibers are thin and are Aδ fibers .	• Most are unmyelinated. • A small proportion are myelinated Aδ fibers depending on species. • Predominantly C fibers (some polymodal Aδ fibers have also been found).	• Myelinated (not fully within the cornea). • Fibers are thin. • Majority are C fibers.
Receptive fields	• Round and medium sized. • Cover 10% of the corneal surface.	• Large, round, and oval. • Covers up to 25% or more of the cornea.	• Small round receptive fields → all over the corneal surface (more abundant in peripheral cornea regions) • Cover 10% of the corneal surface.
Stimulus and response	• Responds to mechanical stimuli. • Fires only one or a few nerve impulses in response to brief or sustained mechanical stimulus.	• Responds to thermal (temperatures over 39-40°C, and below 29°C), mechanical, and chemical stimuli. • Responds to stimulus is continuous, irregular, and last as long as the stimulus is maintained.	• Responds to thermal stimuli. • Discharges spontaneously at corneal surface temperature (33°C). • Increases firing rate when temperature is decreased. Can detect temperature drops of 0.1°C or less) • Transiently silenced when warmed.

Table 2.1: Summary of the nerve characteristics of the three main types of corneal nerves based on Belmonte's categorization of corneal innervation (Acosta et al., 2001a; Acosta et al., 2001b Belmonte et al., 1981, 2004, 2011; MacIver & Tanelian, 1993a; MacIver & Tanelian, 1993b; Gallar et al., 1993; Tanelian & Beuerman, 1984; Müller et al., 2003; Nosch, 2015).

2.3 Sensations arising from the cornea

Previous studies have established that when different types of controlled stimuli (acidic, thermal, and mechanical stimulation) are applied to the cornea (using the Belmonte aesthesiometer (see Section 2.6.4), they each evoke sensations of varying quality, thus facilitating the identification of the applied mode of stimulus by the subject. Electrophysiological studies on the cornea of cats have supported this theory, and recorded the impulse activity in nerve fibers of these ocular structures when stimulated. These studies showed that the different types of stimuli aroused variable levels of responses from different types of sensory receptors. This led to the theory that the type of receptors innervating the cornea (polymodal nociceptors, cold receptors, and mechano-nociceptors) determines the nature and quality of the sensation evoked when they are stimulated (Belmonte et al., 2011).

Sensations produced in healthy humans by corneal stimulation with moderately cold stimuli excited only a non-noxious cooling sensation, which eventually became irritating when the temperature applied was further reduced. When mechanical forces, acid, or heat were applied to human corneas, the sensations produced were accompanied by some irritation. In the case of acidic or chemical stimuli, as the pH of the cornea decreased subjects usually reported a stinging or burning pain, which could last even after the stimulus is removed. With thermal stimulation, sensations have been also described as having a cooling effect. This could be attributed to the fact that the polymodal nociceptors were aroused with all the stimuli (Belmonte et al., 1999; Belmonte et al., 2004; Belmonte et al., 2011; Feng & Simpson, 2004; Murphy, 1996).

2.4 Sensory processing

2.4.1 Corneal psychophysical channels and higher-level areas of CNS involved in perception of sensation

The cornea is innervated by the first branch of the trigeminal nerve. Afferent information is delivered from this nerve to the trigeminal spinal nucleus, and the nerve bundles are projected to the somatosensory cortex through the thalamus. Electro-physiological studies on the cornea have revealed that sensory nerve terminals convert energy from different types of stimulus modalities. It is hypothesized that different sub-modalities in the somatosensory system are processed by different psychophysical channels and produce different sensations (Feng & Simpson, 2004).

When a polymodal nociceptor is stimulated by a noxious substance it causes direct depolarization (the resting potential of the neuron is reduced) of the nerve endings being stimulated. Once the neuron reaches its critical threshold it fires and action potential. These action potentials are propagated along the nerve fibers. (Belmonte et al., 1999; Belmonte et al., 2011; Gallar et al.,1993; Golebiowski et al., 2011; MacIver & Tanelian, 1993a; MacIver & Tanelian, 1993b; Moulton et al., 2012; Murphy et al., 1996; Stapleton et al., 2004; Tanelian & Beuerman, 1984).

It has been believed for some time that nociception is the only sensation that can be elicited from the human cornea. However, with the advent of gas-jet aesthesiometers, such as the Belmonte aesthesiometer (see Section 2.6.4), which can produce mechanical, thermal, and chemical stimuli, our knowledge of the sensations arising in the cornea has shifted. Nociceptive sensation is not the only corneal sensation. Studies show that sub-components of the sensory information in the cornea are processed by different psychophysical channels, but they have alluded to the fact that these channels are not completely independent at threshold. Moreover, since most external stimuli do not contain just one sub-modality, it is highly likely the corneal nerves represent sensory information in parallel and simultaneously (e.g. stinging and cold) (Feng & Simpson, 2004).

In terms of how the individual neurons are able to integrate multi-dimensional sensory information, and transmit these different sub-modalities to the brain to produce a variety of sensations, Feng and Simpson (2004) postulated that molecular receptors are expressed on the same neuron and excite it in different ways. For example, the corneal chemical channel-H^+, through the vanilloid receptor (VR)-1 and/or acid-sensitive ion channels (ASICs) that are expressed on Aδ and C fibers sense hydrogen ions and produce the burning or stinging pain often reported. The corneal itching channel (CIC) that processes histamine and other itch stimuli can also sense the ions.

With respect to representation of corneal sensation in the primary cortex, there is currently no data. One study induced pain stimulation in the cornea using a light source. Their results suggested that they might be cortical representation in the primary somatosensory cortex (Moulton et al., 2012).

2.4.2 Neuroscience of detection

Taking vision as an example, visual summation combines the responses of individual photoreceptor cells. This aids in visual detection and, together with physical and chemical changes, it adds to the wide dynamic range of the visual system. At a higher level, it helps to combine visual signals into information that is crucial for decision-making (Holmes et al., 2017). Temporal summation is described as the adding up of sensory information over time, whereas spatial summation is defined as the adding up of sensory information over space (surface area). Both types of summation have been found to occur within the visual system, more specifically in the photopic (cones) and scotopic (rods) systems (Schwartz, 2010).

According to Ricco's Law, by presenting a small spot of light, the threshold number of quanta needed to detect the light can be determined. The law states that the detection threshold monotonically decreases with the stimulus size to a crucial area. Within this area, an equal reciprocal relationship between the size and the luminance of the stimulus necessary for detection exists, whereby the stimulus detection occurs once the product of the area of the stimulus and the luminance is the same or greater than a constant value. For areas greater than the crucial area, contrast sensitivity improves with the square root of the stimulus area (Schwartz, 2010; Khuu & Kalloniatis, 2015).

There are two types of photoreceptors in the retina. Rods are responsible for scotopic vision, that is vision occurring in low light levels, whereas cones, which are responsible for our crisp and clear vision, become active in high levels of light (photopic vision). Due to the connectivity of the rods and cones to post-receptor elements of the retina, the rods communicate with more elements than the cones. The scotopic system (rods) therefore sums up information over space, manifesting greater spatial summation. The system has great sensitivity in that a stimulus is seen (good spatial summation), but there is poor spatial resolution because only one stimulus is seen from multiple separate stimuli. Conversely, the photopic system exhibits less spatial summation, leading to poorer sensitivity, but great spatial resolution. The scotopic system exhibits total spatial summation for stimuli, which fall within a critical diameter. The difference in spatial summation seen between photopic and scotopic systems is manifested as the difference in the critical diameters for these two systems. The critical diameter of the photopic system is smaller than the scotopic system. Consequently, the photopic system exhibits a reduced capacity for spatial summation (Schwartz, 2010). The exact neural mechanism responsible for spatial summation remains unclear at present (Khuu & Kalloniatis, 2015).

The integration window, or the length of time over which incoming visual signals are summed, is one important characteristic of temporal summation. It is typically taken to be the range of stimulus durations at which the threshold intensity is inversely proportional to the duration, that is, where Bloch's Law holds (Holmes et al., 2017). Bloch's Law is the temporal equivalent of Ricco's Law. Within the critical duration/period there is total temporal summation. The scotopic system sums up information over time to a greater extent than the photopic system. It therefore exhibits greater temporal summation. However, the photopic system is better able to distinguish two flashes of light separated by a brief interval in time, thereby having superior temporal resolution. The scotopic system's high degree of temporal summation limits its ability to resolve distinct temporal events, but is consistent with its greater absolute sensitivity. Once the threshold number of quanta is delivered within the critical period, it does not matter how they are delivered (as one or more flashes). When several flashes are presented within this critical period they are not resolved, and only one flash is seen (Schwartz, 2010). Holmes et al., (2017) found that temporal summation stays efficient over the integration window, but noted that there is variation between individuals.

As previously mentioned, the free nerve endings in the sub-epithelial layer of the cornea exhibit large receptive field overlap (Belmonte et al., 2011, Shaheen et al., 2014). Moreover, studies show that more than one type of corneal receptor can be activated by a particular mode of stimulation during aesthesiometry (the study of sensitivity) (Murphy, 1996; Murphy et al., 1999a). However, there are currently no corneal sensitivity and aesthesiometry studies that have assessed temporal and spatial summation in the cornea. In addition, it is possible that the concept of summation can explain sensitivity measurements, such as differences in degree of sensitivity measured in the peripheral and central regions of the cornea (the central cornea has been shown to be more sensitive than the periphery) (Millodot, 1984).

2.5 Corneal sensitivity

2.5.1 Definition

Corneal nerves are essential to the health of the eye. They are involved in epithelial wound-healing and repair, as well as epithelial cell growth and proliferation of epithelial cells in the cornea. According to Nosch (2015), corneal sensitivity can be described as the "neurological response from the free nerve endings within the epithelium" (p.24). The corneal nerves exhibit sensitivity to a wide variety of stimuli, including chemical, mechanical or thermal stimulation. The nerves therefore play a vital part in ensuring the protection of the cornea (Accornero et al., 1980; Nosch, 2015). It is important to measure corneal sensitivity because it gives clinicians a better understanding of the effects of refractive surgery, contact lens wear, ocular surface and systemic diseases, as well as the application of therapeutic interventions on both the neural functioning and physiology of the cornea and conjunctiva (Golebiowski et al., 2011).

2.5.2 Methods for determining corneal sensitivity

Corneal sensitivity is often indirectly measured by assessing the threshold, which is defined as "the minimum value of a stimulus, which is required to elicit a perceptual response or an alerted perceptual response" (Corliss & Norton, 2002, p. 34). Corneal sensitivity is considered to be the inverse of these thresholds. However, the inverse of the threshold is only used as a concept to determine if an individual exhibits low or high sensitivity. High threshold values indicate low corneal sensitivity, whereas low thresholds indicate high sensitivity (Millodot, 1984; Murphy et al., 1996; Murphy et al., 1998). The distinction between sensitivity and sensation is also of crucial importance. Sensitivity is an actual measure of a neurological response after the cornea is stimulated, whilst corneal sensation refers to the summary of all the perceived mental responses following arousal (E. Lum, personal communication, June 29, 2017).

Murphy defined psychophysics as "the study of the relationship between the physical nature of a stimulus to a component of the body's sensory system, and the subject's response to that stimulus" (Murphy, 1996, p.112, 114). A threshold can be classified as being either an absolute or a difference threshold. An absolute, or detection threshold as it is sometimes called, is considered to be the smallest amount of stimulus energy that produces a certain level of performance or sensation in a detection task. The difference threshold is the smallest amount of stimulus energy needed to attain a particular level of performance, or a distinguishable change in sensation in a discrimination task (Gescheider, 1997). Sensitivity is often indirectly measured by assessing threshold. Sensitivity is the inverse of threshold.

Several psychophysical methods have been developed to measure threshold, each with its own advantages and drawbacks.

2.5.2.1 Method of limits

The method of limits is a classical psychophysical method that is frequently used to ascertain an individual's sensory threshold. With this method, an individual/observer is presented with stimulus values in a decreasing or increasing sequence. Essentially, a set of stimulus values, which includes the expected threshold, is used. With the ascending series, the stimulus intensity is increased on successive trials until the stimulus is detected in the case of measuring absolute thresholds, or until a stimulus difference is no longer noticed, in the case of measuring difference thresholds. Conversely, in a descending series, the stimulus intensity is diminished on successive trials until the stimulus is no longer detected, or a stimulus difference is no longer noticeable. Each transition point is the point on the physical dimension that is midway between the stimulus for the last “Yes” and the first “No” response or vice versa, and is considered to be an estimation of the threshold. Typically, the threshold is calculated as the average of all the transition points (Gescheider, 1997).

2.5.2.2 Method of constant stimuli

Another commonly-used technique is the method of constant stimuli. With this method, a range of stimuli, which consists of an intense stimulus above the threshold, the least stimulus below threshold, and stimuli between these two extremes are selected. Each stimulus is randomly presented a fixed number of times. The threshold is determined by plotting a graph of percentage detected, against the stimulus intensity, and extrapolating to determine at which threshold 50% of the sensation is detected (Gescheider, 1997).

2.5.2.3 Drawbacks of classical psychophysical methods

Whilst these methods are efficient, the introduction of constant errors, and biases in the observer’s response can affect the measure of threshold obtained. Response bias is the tendency of the observer to favor one response over another, and is often influenced by factors other than the stimulus intensity. A constant error is a systematic error in judgment. Errors of habituation (the tendency for the participant to develop a habit of repeating the same response), and expectation (the tendency for the subject to respond before it is appropriate to do so), are two such examples of constant errors, which can have an impact on the detection threshold measured. Providing preliminary training, which includes catch-trials (trials that consist of no stimulus), and careful instructions to the participant, as well as varying the stimulus values at the starting point of successive trials, is believed to control these types of errors (Corliss & Norton, 2002; Gescheider, 1997). In addition, both descending and ascending series of stimulus intensities is also said to counter-balance these errors. One of the major criticisms of classical psychophysical methods, and the use of preliminary training, is that they do not allow the separation of the response bias from the participant's threshold, and hence sensitivity, despite efforts to reduce these biases (Gescheider, 1997). In addition to the lack of control over the observer's decision/response criteria, and the inability to measure this criterion independent of the threshold, a large amount of data is often wasted in classical psychophysical methods because the stimulus presented is far from the threshold, where little information is gained (Swets, 1961; Treutwein, 1995).

2.5.2.4 Signal detection theory (SDT)

The psychophysical signal detection theory (SDT) was developed to allow pure measures of sensitivity to be obtained by essentially isolating the effects of the observer's decision criteria. Moreover, the data collected from such experiments have led researchers to question the existence of sensory thresholds, and to postulate that the threshold may be due to observer's criterion being restricted to two response categories (yes or no) (Swets, 1961). Signal detection experiments differ from classical psychophysical experiments in two ways: with detection experiments, only one stimulus intensity is presented, and on some trials no stimulus or signal is presented (Goldstein, 1989). The SDT assumes a single supra-threshold state exists irrespective of the presence or absence of a stimulus (signal). When no signal is present, the value of the supra-threshold is described as noise distribution, and when a signal is present, it is described as the signal-plus-noise distribution. The observer has to decide if the supra-threshold observation is due to the noise or the signal. This is achieved by setting a decision criterion below which no signal is reported, and above which a signal is reported (Gescheider, 1997).

2.5.2.5 Methods used in corneal sensitivity literature

The instrument and psychophysical methods used can affect the measures of corneal sensitivity. Other factors which can influence the results include: the number of stimulus presentations, the time between stimuli, the time taken to perform the measurements, as well as the order of stimuli presentations. In terms of the psychophysical techniques used to measure ocular surface sensitivity and the repeatability of these techniques, little has been published (Murphy et al., 1996; Murphy et al., 1998; Stapleton et al., 2004; Vega et al., 1999). Typically, the method of ascending limits is used to measure threshold, as it is more efficient. However, it is important to note that threshold measurements are therefore larger than what they may be in actuality. In addition, very few studies have used SDT (Beuerman & Rozsa, 1985), and only one study has measured the difference threshold (Rao & Simpson, 2014). Other psychophysical methods used in sensitivity studies include method of levels (similar to staircase and tracking methods) (Acosta et al., 2006; Belmonte et al., 1999), and method of minimum stimulus (Acosta et al., 2001b; Acosta et al., 2005). With the latter, the intensity and perceived magnitude of the sensations are scored using a visual analog scale (VAS), and the thresholds are usually expressed as the stimulus intensity that evoked a VAS score > 0.5. However, all the papers that used this method fail to explain the choice of the VAS score that constitutes the threshold. Care must therefore be taken when selecting the most appropriate psychophysical method for corneal sensitivity studies.

2.6 Instruments for measuring corneal sensitivity

2.6.1 Aesthesiometry

Aesthesiometry is the measure of the degree of sensitivity. It involves stimulating the corneal nerves, and noting the psychophysical response of the subject. Different types of aesthesiometers have been developed to investigate the various aspects of corneal sensitivity (Lum, 2014).

The first technique, which focused on determining the effects of a mechanical stimulus on corneal sensitivity, used a wisp of cotton to gently touch the ocular surface. The examiner either viewed an evoked blink reflex (objective evaluation) or asked the participant questions regarding the sensation they felt (subjective evaluation) (Belmonte et al., 2011).

In 1894, von Frey used a different technique to measure similar effects by applying horse-hairs attached at right angles to a glass rod. With this system, the horse-hair would bend when it was perpendicularly applied to the corneal surface. Consequently, due to the elastic characteristics of the hair, a counter-pressure was produced on the corneal surface. The force exerted was determined separately by pressing the hair against a scale. By altering the length and diameter of the hair, different pressures could be applied to the cornea. However, the results of this instrument were not reproducible because the elasticity of the hair depended on several factors, such as the type and age of the hair, as well as its moisture content. Later, more quantitative techniques were employed using modified von Frey filaments to investigate cutaneous sensitivity to mechanical stimulation. The filaments were nylon threads of various lengths, fixed in diameter. When the tip of the filament was pressed against the skin it began to bend, and the force per surface unit that it exerted was both proportional to its length and more constant (Belmonte et al., 2011; Murphy, 1996; Nosch, 2015). Other studies performed during the 19th and 20th century used a wide variety of apparatus, which ranged from thin glass tubes containing cold and warm water, surgical probes made of metal that were immersed in cold and hot water, metal knobs at different temperatures, and even cocaine (Murphy, 1996; Nosch, 2015).

2.6.2 Cochet-Bonnet Aesthesiometer

The Cochet-Bonnet aesthesiometer (Figure 2.2) was developed in 1960 using a similar principle to von Frey. The instrument is used clinically to assess corneal mechanical thresholds, and hence corneal sensitivity to a touch stimulus. It consists of a small diameter nylon thread/filament, which fits into a thread holder. When taking measurements with this device, the thread is pressed gently against the cornea, and the operator can view the thread, using a slit-lamp, to see when it just bends. The opposing elastic force within the thread creates the force that is applied to the cornea. Increasing or decreasing the length of the thread can change the force applied to the cornea, thus varying the intensity of the stimulus presented. The pressure exerted on the cornea is inversely proportional to the length of the filament, so that as the length of the filament is increased, the pressure or stimulus intensity decreases, and vice-versa. It therefore follows that the lower the threshold, the greater the corneal sensitivity, and the longer the filament will be. When determining the threshold, the longest filament is first used, and the length is then decreased until a threshold response is given (Belmonte et al., 2011; Douthwaite & Kaye, 1980; Murphy et al., 1996; Nosch, 2015). Each filament causes a certain amount of corneal deformation. This deformation is a result of the mechanical action of the thread, which leads to a touch sensation. The filament is 6 cm in length, and comes in two diameters: 0.08 and 0.12 mm (Belmonte et al., 2011; Murphy et al., 1996; Nosch, 2015). These produce pressures that range from 2-90 mg/0.05 mm^2 and 11-200 mg/0.05 mm^2, respectively (Douthwaite & Kaye, 1980).

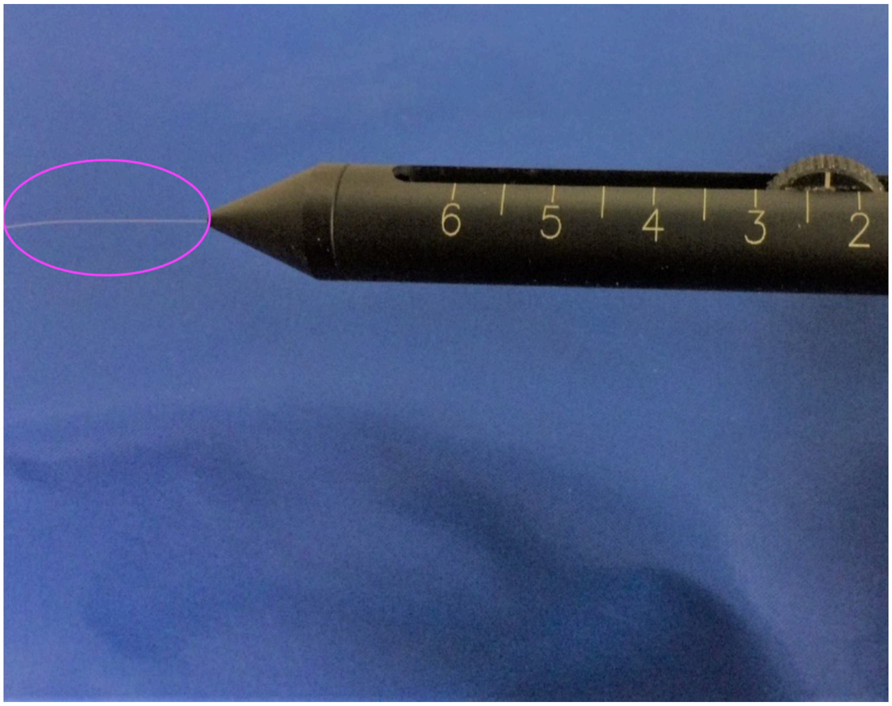

Figure 2.2: Photograph of the Cochet-Bonnet Aesthesiometer (C-BA).

The filament or thread is in the pink circle.

It should be noted that whilst the thinner filament can offer a lower stimulus intensity, which may be advantageous when measuring sensitivity in individuals with thresholds lower than the minimum stimulus intensity offered by the thicker filament, it is no longer manufactured and is therefore used infrequently (Murphy, 1996; Murphy et al., 1998; Stapleton et al., 2004). A conversion table is typically provided with the instrument to convert the length of the filament into a measure of pressure, thus allowing the corneal touch threshold to be stated in terms of pressure. Corneal sensitivity is considered to be the inverse of this measurement (Douthwaite & Kaye, 1980).

The Cochet-Bonnet is portable, easy to use, maintain, and is commercially available. Despite being the gold-standard technique, the method is invasive, can cause trauma to the corneal epithelium, and, consequently, can affect the threshold measured (Belmonte et al., 2011; Murphy et al., 1996;

Murphy et al, 1998; Stapleton et al., 2004). Furthermore, the pressure needed to cause a sensation is more than that required to produce punctate staining (Bonnet & Millodot, 1966; Millodot & O'Leary, 1981). Other drawbacks include: a limited range of stimulus pressure intensities, with stimuli typically presented at supra-threshold levels (Golebiowski et al., 2011; Murphy et al., 1996; Stapleton et al., 2004); difficulty when trying to accurately position the filament at the same point on the cornea for repeat readings (Murphy et al., 1996); errors in measurements because of humidity (Lum & Murphy, 2018), and/or previous usage of the thread, which can influence its shape; reduced precision of the estimated force applied, produced by a short time delay, because it is difficult to notice when the filament bends, and hence when the force applied (Murphy et al., 1996). The shape of the filament tip and its edges can also affect the results obtained. It is important to note that the handle of the instrument has to be held slightly upwards to overcome the fact that the thread naturally bends under its own weight (Murphy et al., 1996). In addition, according to the manufacturers, the force for each filament length is based on a 5° change of the tip angle as a result of its bending when a force is applied to the cornea. However, as previously mentioned, it is difficult for the examiner to measure the angle of the tip. If the angle of bending is greater than it is supposed to be, the pressure applied will be greater, than desired, and conversely, if the angle is smaller than expected, the pressure will be less (Douthwaite & Kaye, 1980; Murphy et al., 1996). Therefore, an exact measure of the force applied cannot be made (Murphy et al., 1996). Furthermore, patient apprehension when seeing the thread can lead to a reduction in threshold or increased sensitivity (Millodot, 1984; Murphy et al., 1996; Murphy et al., 1998; Stapleton et al., 2004). Bonnet and Millodot verified this in 1966 when they performed corneal aesthesiometry in the dark (Bonnet & Millodot, 1966).

Furthermore, the repeatability of the Cochet-Bonnet when measuring corneal sensitivity in human subjects has not been previously reported. However, several studies published on its calibration using the 0.12 mm nylon filament have confirmed the variability of the device. More specifically, these studies have found that there are differences between the nominal values quoted in the manufacturer's calibration table and the actual measured values of the force exerted by the filament (Lawrenson & Ruskell, 1993; Lowther & Hill, 1968; Murphy, 1996; Norn, 1973; Golebiowski et al., 2011). The invasive nature of the device also limits its use because it cannot be used on individuals whose cornea has been compromised. Therefore, the development of non-invasive techniques is essential (Belmonte et al., 2011; Murphy et al., 1996; Murphy et al., 1998; Stapleton et al., 2004).

2.6.3 Non-Contact Corneal Aesthesiometer (NCCA)

The designers of the NCCA (Figure 2.3) used an air pump to deliver atmospheric air to an air reservoir, which acts to dampen the pressure pulses created in the airflow by the pump. Another benefit of the reservoir is that it ensures a steady supply of air, which is also slightly pressurized. An electronic pressure sensor allows the operator to monitor the pressure of the air. The sensor digitally displays pressure readings in millibars (mbars) above atmospheric pressure. A manual control valve is used to regulate the air outflow, and therefore the pressure of the reserve. Two switch-valves (two-way), which are electronically controlled, direct the flow of air either to the stimulus jet (when a stimulus is being applied), or an exhaust jet. The air-jet also has a central bore of diameter 0.5 mm, which facilitates the delivery of the air stimulus. The switch valves can be electronically manipulated to vary the duration of the stimulus (0.5, 0.9, or 1.5 seconds). The different components of the instrument are connected to one another using tubing made of nylon. This tubing is 4 mm in diameter, and has a central bore of 2.5 mm. The valves, pressure sensor and display, as well as the reservoir and connecting tubes, are all contained in a sealed polycarbonate box (Murphy et al., 1996; Murphy et al., 1999b).

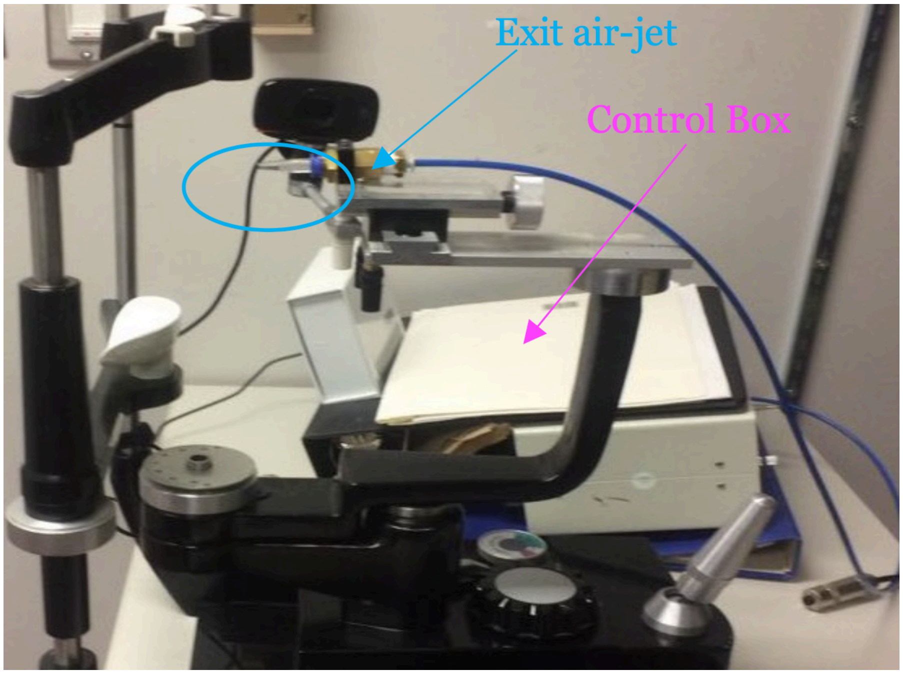

Figure 2.3: Photograph of the Non-Contact Corneal Aesthesiometer (NCCA).

The NCCA uses a controlled pulse of air at room temperature to stimulate the thermally-sensitive corneal nerve supply. Studies have shown that a stimulus can be delivered consistently and in a repeatable manner, and have determined the most suitable air-jet diameter, working distance, and stimulus duration for measuring corneal sensitivity. Calibration of the instrument is completed prior to each measurement session (Lum, 2015; Murphy et al., 1996; Murphy et al., 1998). The air-jet should be aligned with the central cornea and positioned at a working distance of 1 cm. Two other working distances were trialed before determining that this was the optimum. The working distance of 0.5 cm was ruled out, as it was considered to be too close for safe use of the probe. The distance of 1.5 cm was rejected, as the ocular surface would be close to the area where the airflow would degenerate into turbulence (Murphy et al., 1996; Nosch, 2015). Alignment is achieved by using a customised slit-lamp attachment. For optimal results, the 0.5 mm air-jet should be used with stimulus duration of 0.9 seconds. This stimulus duration was selected because 1.5 seconds duration might result in excessive drying of the corneal surface with repeated stimulus delivery, and 0.5 seconds was believed to be too fast for subjects who were not very vigilant. The 0.5 mm air-jet was selected because it allowed the stimulus pressure to be easily set, whilst also limiting the airflow dispersion (Murphy et al., 1998). The nerves are stimulated by aiming an air-pulse towards the anterior surface of the cornea, set at a predetermined pressure in millibars. Subjects usually find it difficult to describe the stimulus, especially when it is close to the threshold, but when a sensation is felt; it is typically described as a cold sensation or a light breeze on the eye (Murphy et al., 1996; Murphy et al., 1998; Murphy et al., 1999b).

Using Schlieren interferometry, it was shown that the pulse from the NCCA air-jet remained narrowly confined within the air-jet working distance, and thermal imaging demonstrated that the air-pulse only stimulated the area of the cornea that it was in direct contact with. The overall surface area of the cornea is approximately 95 mm^2. The NCCA stimulates an area of 0.8 mm^2 of the corneal epithelium, whereas the Cochet-Bonnet aesthesiometer only stimulates an area of 0.011 mm^2. Studies have shown that the NCCA can be used to determine corneal sensitivity in an accurate and repeatable manner (Murphy et al., 1996; Murphy et al., 1998).

It is important to note that the device does not measure corneal touch threshold, as with the Cochet-Bonnet aesthesiometer, but rather the corneal nerves' threshold in response to a stimulus composed of tear evaporation and disruption. This was confirmed by fact that there was no correlation between the corneal threshold of the Cochet-Bonnet and NCCA. It is believed that the air-pulse causes a localised thinning of the tear film by either evaporation or convection, and then there is a cooling effect from evaporation, which stimulates the nerve endings through conduction. Therefore, the corneal nerves in the epithelium are stimulated by surface temperature changes produced by the air-jet pulse stimulus (Murphy et al., 1996; Murphy et al., 1998; Murphy et al., 1999b).

In order to truly determine if the airflow delivered from the NCCA caused a change in temperature of the corneal surface, Murphy et al. (1999b) used a thermal camera to measure the temperature change that was induced on the cornea as the stimulus pressure was applied and increased. The results of the study showed that as the airflow rate increased, the corneal temperature diminished. This was attributed to the evaporation of the tear film as the stimulus was applied. In terms of the exact mechanism involved, as the air strikes the surface of the cornea, there is an increased rate of evaporation from the tear film. This is caused by the change in the humidity equilibrium of the air above the cornea, together with the removal of evaporated water molecules in that region. As energy is removed from the tear film in the area being stimulated, via evaporation, the region is cooled, and the thermal camera notes a temperature drop**.** The temperature change is transmitted to the cornea via conduction, and consequently, the nerve endings located in the corneal epithelium detect the temperature change, and respond accordingly. The authors could not confirm if there was mechanical deformation as a result of the stimulus. However, they concluded that if any surface deformation did in fact occur, it must be very small, compared to the evident temperature change component of the stimulus emitted by the air-jet, and therefore play only a minor role (Murphy et al., 1999b).

Murphy et al. (1996) deduced that the stimulus could be localised to small regions of the cornea, and determined that the area of the cornea covered by the air-jet that undergoes a cooling effect is approximately 3 mm in diameter (Murphy, 1996). The instrument can detect very small changes in corneal sensitivity over a narrow range of intensities. It is also less susceptible to patient apprehension or influences from the environment, compared to the Cochet-Bonnet aesthesiometer (Murphy et al., 1996; Murphy et al., 1998; Murphy et al., 1999a). Whilst this instrument is not produced for commercial use, this non-invasive device has been safely used in a number of studies over the past 25 years (Murphy et al., 1996; Murphy et al., 1998; Murphy et al., 1999a; Murphy et al., 2001; Murphy et al., 2004; Pritchard et al., 2012).

2.6.4 Belmonte Gas Aesthesiometer

Another instrument in this category of aesthesiometers is the Belmonte gas aesthesiometer, which is unique in that it allows the operator to assess corneal sensitivity with a variety of stimuli, including mechanical, chemical, and thermal. The instrument is composed of two gas cylinders: one with 98.5% carbon dioxide, and the other with medical grade compressed air. The cylinders are connected to an electronically-controlled, directionally-proportional, control-valve by two pressure regulators, as well as two uni-directional regulators. This allows the adjustment of the flow of gas, and therefore facilitates the production of mixtures with a controlled amount of air and carbon dioxide. A flow-meter is used to adjust the final flow of the gas mixture. The gas mixture is delivered to a probe that is 0.5 mm in internal diameter, and mounted in a non-contact tonometer housing system. The probe has a temperature-controlling device, which is made up of a thermocouple, a Peltier cell, and a servo-regulator. The temperature-controlling device can warm the gas that flows through the probe, and the three-way solenoid valve directs the output of the gas. The temperature of the stimulus on the eye can vary between 20°C (room temperature) and 34°C. Stapleton et al. (2004) found that there was no significant temperature variability, as well as no temperature reduction or increased variation, as the flow rates were increased for pulse durations of 1 and 2 seconds (Stapleton et al., 2004). The gas is transiently directed towards the tip of the probe using a pulse generator, which changes the direction of the flow in the electronic valve during stimulus delivery. This essentially produces a pulse of gas in the tip of the probe with a specific carbon dioxide concentration, temperature, flow-rate, and duration. The stimulus duration can range from 1 to 3 seconds, and has a precision of 0.1 second (Stapleton et al., 2004). Typically, the distance between the probe tip and the cornea is 5 mm. The stimulus air-jet is mounted on to a slit-lamp holder and this allows the operator to position the probe at the apex of the cornea. Threshold measurements are made in terms of flow of gas in millimeters per minute (Nosch, 2015; Nosch et al., 2017).

With respect to the various types of stimuli generated by the instrument, it is important to note that the pressure applied can be above or below the mechanical threshold. To deliver a chemical stimulus, the air can be mixed with different concentrations of carbon dioxide. When this combines with water on the ocular surface, carbonic acid is formed, and this lowers the local pH, thus resulting in chemical stimulation. The degree of decrease in pH is proportional to the concentration of carbon dioxide used. In order to apply a thermal stimulus, the temperature of the air-jet is adjusted allowing either hot or cold thermal stimulation to be applied (Belmonte et al., 1999; Belmonte et al., 2011). According to Stapleton et al. (2004), stimulus temperatures were selected to provide a mechanical stimulus with maximum cooling effect (20°C), and a mechanical stimulus without a thermally cooling effect (34°C). If the instrument is used without an additional cooling device, the air-pulses cannot be delivered at temperatures lower than 20°C (Stapleton et al., 2004).

It is believed that the mode of stimulation of the Belmonte gas aesthesiometer is predominantly the mechanical pressure of the air-jet on the cornea pressure receptors. However, it is quite possible that ocular surface temperature change may be an additional stimulation factor at the outer edge of the aesthesiometer stimulus, thereby enlisting the temperature sensitive cold nociceptors on the cornea, as well as conjunctival thermosensitive neurons. Whilst the central core of the air-jet of the aesthesiometer is at the corneal temperature, the cooler outer layers of the airflow could stimulate cold sensitive receptors at the peripheral region of the cornea (Nosch, 2017; Golebiowski et al., 2011).

Several studies have used the Belmonte aesthesiometer to detect the presence of different types of corneal neurones, as well as determine their various attributes. The first study to discover cold sensitive, mechano-sensory, and polymodal nerve fibers in cats used both electrophysiological methods and the Belmonte aesthesiometer (Acosta et al., 2001a). Given that the aforementioned neuron types are assumed to be in humans, several subsequent studies have utilized the instrument to investigate the characteristics of these neurones in humans (Acosta et al., 2001b; Acosta et al., 2005; Acosta et al., 2006; Téson et al., 2012).

2.6.5 CRCERT-Belmonte Aesthesiometer

The CRCERT-Belmonte aesthesiometer (Figure 2.4) is a modified version of the Belmonte aesthesiometer (Stapleton et al., 2004). The design is based on a modified American Optical non-contact tonometer. It is capable of administering the same types and range of gas-jet stimuli as the Belmonte aesthesiometer, but is more precise (Lum, 2014).

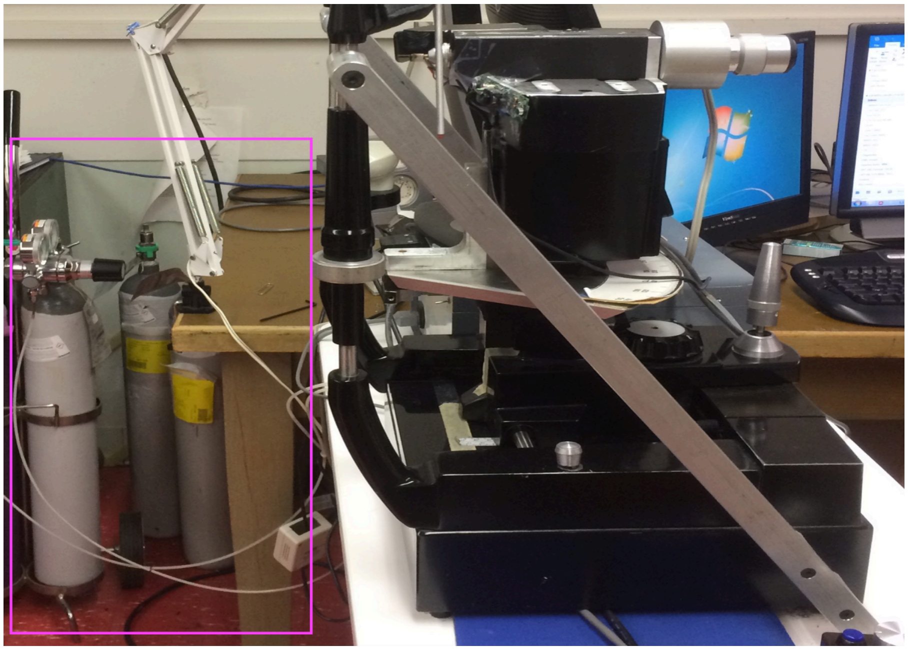

Figure 2.4: Photograph of the Waterloo modified CRCERT Belmonte gas aesthesiometer.

(Photo courtesy of Simpson Lab, University of Waterloo School of Optometry and Vision Science). The two cylinders in the pink square represent the cylinders of medical air and carbon dioxide, respectively, that are used to produce various types of stimuli.

Two laser pointers allow the accurate working distance to be located, thus ensuring the precise positioning of the stimulus on the central cornea. Furthermore, to facilitate any desired change in the stimulus location, moveable fixation lights mounted on the instrument housing can be used. With this CRCERT Belmonte aesthesiometer, the carbon dioxide flow control-meter was converted and recalibrated for air. Consequently, maximum flow increased from 200 to 400 ml/min. (Nosch, 2015; Stapleton et al., 2004).

This instrument is different from other non-contact aesthesiometers in a number of ways. Firstly, the temperature controller and an electronic flow-meter regulates the composition of the air exiting the nozzle, as well as the velocity and temperature of the gas-jet in order to precisely apply the stimulus. A heating coil, which can be found at the tip of the probe, facilitates the delivery of a stimulus at corneal temperature, thus reducing the unwanted stimulation of the temperature sensitive receptors. In addition, a narrower probe diameter and a shorter working distance serve to confine the size of the imprint of the stimulus on the cornea (Golebiowski et al., 2005).

Golebiowski et al. (2011) found that in addition to facilitating the exploration of the response of the three types of neuro-receptors on the ocular surface, the device offered exquisite stimulus reproducibility, as well as better control over stimulus characteristics (Golebiowski et al., 2011). Stapleton et al. (2004) also noted good repeatability with the instrument when measuring central corneal sensitivity (Stapleton et al., 2004). The CRCERT Belmonte aesthesiometer has been used to investigate conjunctival sensitivity in cases of discontinued contact lens wear due to discomfort (Stapleton et al., 2015). It has also been used to determine the effects of soft contact lens wear on corneal sensitivity (Golebiowski et al., 2012).

2.6.6 Belmonte Ocular Pain Meter Gas-Jet Aesthesiometer (BOPM)

One other gas-jet aesthesiometer is the Belmonte Ocular Pain Meter (BOPM). This instrument was a commercially available non-contact aesthestiometer (Deriva Global S.L., Spain), and was based on the design of the Belmonte aesthesiometer. The instrument is no longer available. It used a pulse of pressurised air that was directed through an air-jet located close to the eye to stimulate the cornea. As with the Belmonte aesthesiometer, the stimulus could be altered to generate different stimuli. To stimulate the ocular surface using a cooling stimulus (which was lower than the ocular surface temperature (34°C)), the instrument used a pulse of pressurised air. In order to deliver a warming stimulus, the air could be heated, and to administer a chemical stimulus, it could be mixed with carbon dioxide. It is believed that a mechanical stimulus could be delivered by using air at the ocular surface temperature. However, Nosch et al. (2017) found that the instrument could not generate a true mechanical stimulus, and that there was also a thermal component when the mechanical setting of the device was used. They suggested that the device should incorporate a way of synchronizing stimulus temperature changes with airflow rate in order to produce a purely mechanical stimulus. Although it was the first commercially available non-contact aesthesiometer, it is no longer available (Nosch et al., 2017).

2.6.7 Rebound Technology Based Esthesiometry (RTE)

This is a relatively new instrument. It employs a lightweight probe, which is controlled by a magnetic field. Touch thresholds are measured by determining the minimum perceivable kinetic energy of the probe (in microjoules) when it touches the center of the corneal for 2 milliseconds. The stimulus is delivered in linear increments in steps of 10, and a threshold algorithm is used to increase the stimulus intensity gradually. Sham stimuli are used after each positive response in order to detect false positive results. The algorithm also determines the final threshold using a bracketing method. Subjects are given a trigger button to report their response. The touch threshold is considered to be the lowest intensity of the probe that subjects successfully responded to twice. A comparison with the Cochet-Bonnet aesthesiometer revealed a strong significant association between both types of measurements (r = -0.7), with an 83% agreement between the two instruments in eyes tested (Mihelcic et al., 2021).

2.7 The need for a new instrument

Despite the good repeatability and greater control of the stimulus, when compared to the Cochet-Bonnet aesthesiometer, there are limitations with gas-jet aesthesiometers design (Murphy et al. 1996; Stapleton et al., 2004). The primary limitation is the difficulty that arises when trying to only deliver a mechanical stimulus or a chemical stimulus, since it is impossible to avoid the cooling effect created by the stimulus (Belmonte et al., 1999; Belmonte at al., 2017; Murphy et al., 1999b; Nosch et al., 2017). As a result, a comparison of these aesthesiometers shows that they do not use similar modes of stimulation, nor do they use the same test/working distance or stimulus duration. Consequently, it is difficult to compare measurements between the instruments (Lum, 2014).

The literature also demonstrated a gap between what we know about the various corneal nerves and how they collectively respond to stimuli, as well as the representation of sensation at the corneal level in the somatosensory cortex.

In an effort to bridge this gap, this thesis describes the development of a novel air-based aesthesiometer that is capable of delivering multiple stimuli separated by a time delay or a spatial separation. In addition, its unique multiple exit air-jet feature should prove to be useful for exploring summation in the future.

The overall aims of this thesis are:

(i) To develop an aesthesiometer capable of delivering air-based stimuli that produce a cooling stimulus to the corneal nerves;

(ii) To investigate and describe the mode of stimulation produced by the new aesthesiometer;

(iii) To investigate that the new aesthesiometer is capable of delivering multiple stimuli of the same or different intensity simultaneously to the ocular surface;

(iv) To investigate that the new aesthesiometer is capable of delivering repeat stimuli of the same or differing intensities in a controlled time separated sequence to the ocular surface.

CHAPTER 3: PROTOTYPE SYSTEM DESIGNS

3.1 Micro-blowers

The Dolphin aesthesiometer is a novel instrument developed to overcome limitations of its predecessors, and consequently, allow neurophysiological concepts (spatial and temporal summation) to be studied at the corneal level. It is based on the design of the non-contact corneal aesthesiometer (NCCA) developed by Murphy et al. (1996). In the new design, the micro-valve that controls the airflow in the NCCA has been replaced with a micro-blower (Murata^{TM} Manufacturing Co., Kyoto, Japan), which offers fine control over the velocity of the airflow exiting the stimulus air-jet (Chovet et al., 2016). Moreover, additional micro-blowers that can separately deliver airflow streams are included, which would allow multiple stimuli to be presented simultaneously or in sequence.

The Murata^{TM} micro-blower is commercially available and is able to produce a steady or pulsed airflow (Figure 3.1). It is robust, small, cost-effective, and consumes little energy, due to the efficiency of its piezoelectric ceramic drive system. Moreover, because it can change the characteristics of flow, it can be used as a flow control device.

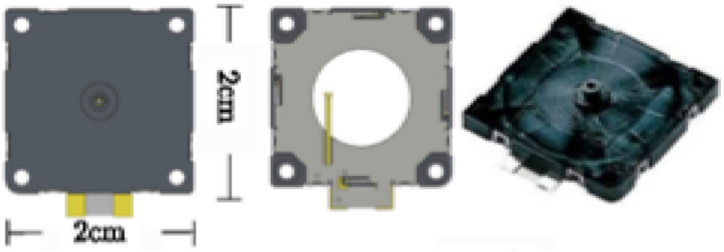

Figure 3.1: The basic characteristics of the micro-blower.

Reproduced from Sensors and Actuators, A 249, C. Chovet, M. Lippert, L. Keirsbulck, and J.-M. Foucaut, Dynamic characterization of piezoelectric micro-blowers for separation flow control, page 123, Copyright (2016), with permission for Elsevier (See Letters of Copyright Permission).

The device is designed to function as an air pump by using ultrasonic vibration of ceramics, which creates high pressure discharges of air from the compact and thin body. The device consists of a double cavity and a metal diaphragm. The diaphragm flexes in response to the piezoelectric drive system (that vibrates at up to 26 kHz), which draws air into a central cavity, and then expels the air out from a central, annular nozzle (diameter: 0.86 mm). The micro-blower is driven by a manufacturer-designed driver circuit (Figure 3.2), which outputs an amplitude-modulated square wave with an amplitude that is proportional to the input voltage of the circuit. It is important to note that this linear velocity relationship is atypical for other micro-blowers composed of piezoelectric elements, but is nevertheless an invaluable characteristic, which can be exploited for feedback control (Chovet et al., 2016).

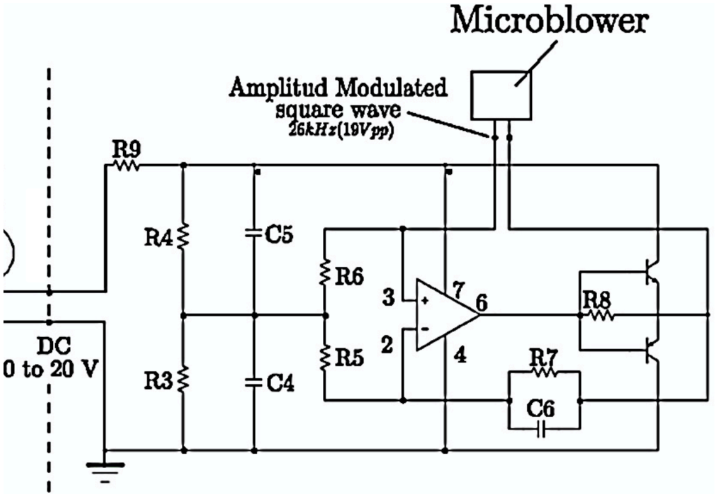

Figure 3.2: Micro-blower driver circuit.

Reproduced from Sensors and Actuators, A 249, C. Chovet, M. Lippert, L. Keirsbulck, and J.-M. Foucaut, Dynamic characterization of piezoelectric micro-blowers for separation flow control, page 123, Copyright (2016), with permission from Elsevier (See Letters of Copyright Permission).

Under driver circuit control, the micro-blower can generate a continuous air flow, and operates on a phase-by-phase principle. In the first phase the ceramic is in a neutral position. This is the situation before the micro-blower is switched on. Once the micro-blower is activated, it enters a second phase in which the ceramic diaphragm flexes in an outward direction to draw air from outside the micro-blower through inlet apertures into the central cavity. In the third and fourth phases, the current to the ceramic is switched to make it flex in an inward direction and the air within the central cavity is expelled through a small exit nozzle, which facilitates a strong output velocity. At the end of Phase 4, the current is once again switched, and the ceramic is flexed to move in an outward direction to begin the process of drawing air back into the central cavity to recharge the micro-blower. Phases 2-4 then continue in sequence to produce a steady airflow from the micro-blower (Chovet et al., 2016) (Figure 3.3).

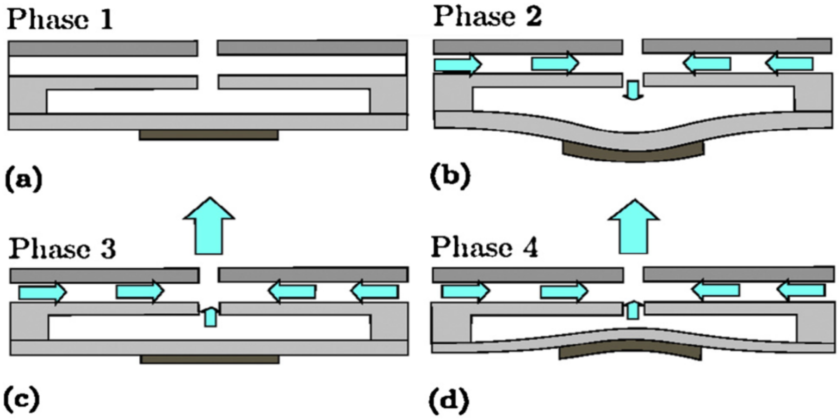

Figure 3.3: The different phases of pulse jet generation of the micro-blower.

Reproduced from Sensors and Actuators, A 249, C. Chovet, M. Lippert, L. Keirsbulck, and J.-M. Foucaut, Dynamic characterization of piezoelectric micro-blowers for separation flow control, page 123, Copyright (2016), with permission from Elsevier (See Letters of Copyright Permission).

Studies by Chovet et al. (2016) to assess the continuous and pulse mode of the micro-blower found that both the pulsed and continuous maximum airflow exit velocities were linearly dependent on the input voltage. They also found that the device exhibited a non-linear relationship between the exit velocity and voltage when the input voltages were less than 8V (Figure 3.4). Furthermore, the response of the device was influenced by the pulsed frequency, and flow visualisations displayed strong efficiency when active control was used. Overall, they concluded that the device was advantageous for flow control because it was flexible. More specifically, the flow control allows different forms of signals to be generated (Chovet et al., 2016).

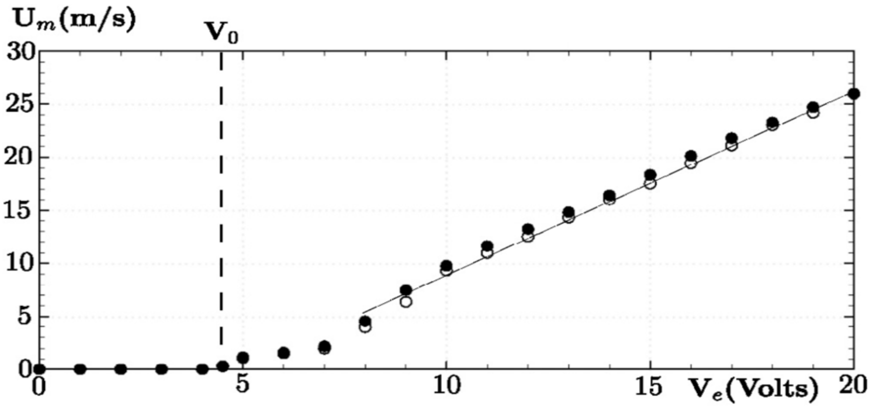

Figure 3.4: The maximum velocity against the supply voltage for a continuous and pulsed jet (black and open symbols, respectively).

V_0 represents the minimum voltage supply needed for the micro-blower to produce an airflow. Reproduced from Sensors and Actuators, A 249, C. Chovet, M. Lippert, L. Keirsbulck, and J.-M. Foucaut, Dynamic characterization of piezoelectric micro-blowers for separation flow control, page 125, Copyright (2016), with permission from (See Letters of Copyright Permission).

3.2 Dolphin Aesthesiometer

For the Dolphin Aesthesiometer, four separate micro-blowers were incorporated into the design. Each micro-blower was labelled as yellow, purple, blue, and green for identification purposes. A control box incorporating the driver circuit and USB computer connection for data and power was manufactured by Mr. Zhenwen Wang from the Physics Technical Services Workshop in the University of Waterloo. The driver circuit was managed through a customised software developed by Mr. Ehsan Zare Bidaki of the Murphy Laboratory for Experimental Optometry (MLEO) using the C# programming language. Using the software, the voltage delivered to each micro-blower was regulated to enable control of the air outflow rate (intensity), stimulus duration (seconds), and inter-stimulus delay (seconds) (Figure 3.5). This allows the user to manipulate the number of air puffs and micro-blowers used so that a variety of stimulus combinations can be employed. For example, the device can deliver a single puff of air with one blower or with two blowers, as well as multiple air puffs with one or multiple blowers. In cases where multiple puffs are generated, the software allows the user to set a time delay between air puffs.

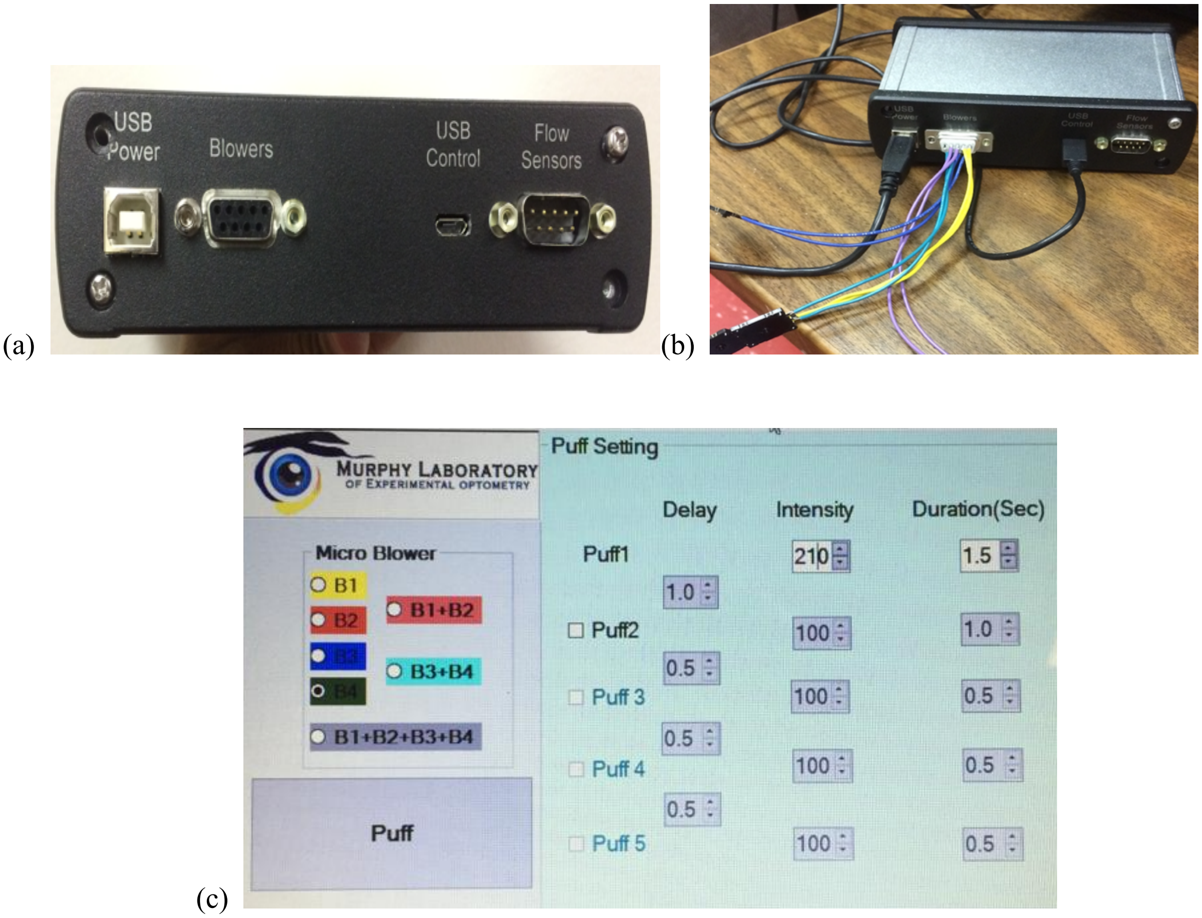

Puff Setting

	Delay	Intensity	Duration(Sec)
Puff1		210	1.5
	1.0		
☐ Puff2		100	1.0
	0.5		
☐ Puff 3		100	0.5
	0.5		
☐ Puff 4		100	0.5
	0.5		
☐ Puff 5		100	0.5

Figure 3.5: MLEO Dolphin control system showing (a) back of control box; (b) control box with connections for power (USB), data (USB), and micro-blower control cables; and (c) software management screen.

Stimulus strength is controlled by the voltage output of the device. The voltage output acts as a surrogate for airflow rate, which is linked to the strength of the stimulus. For the purpose of this thesis it is important to note that the term stimulus strength refers to the stimulus produced and exiting the instrument, whereas stimulus intensity is a quantitative description of the stimulus as it is perceived by a human subject. Furthermore, in terms of units of measurement, the stimulus strength is expressed in this thesis as units since the device has not been calibrated in its mode of stimulation. It is hypothesised that the stimulus intensity is characterised either by the force applied to the corneal surface or to the temperature change (cooling) produced by evaporation driven changes in the tear film, or to some combination of these two factors.

With respect to measuring corneal sensitivity on subjects, the proposed methodology would be to present an individual air-pulse or a combination of air-pulses from the micro-blowers, through a stimulus air-jet directed at the cornea, and to ask the subject to respond as to whether they felt the stimulus. An appropriate psychophysical methodology would be used to locate the detection or differential threshold (García-Pérez et al., 2001; Golebiowski et al., 2005).

CHAPTER 4: PROTOTYPE TESTING, SOFTWARE

4.1 Introduction

To determine the reliability of the prototype instrument, a series of studies was developed to test the consistency of the instrument's control software. This was achieved by using a digital multimeter and an oscilloscope to measure the effect of the control software on the stimulus strength (voltage), stimulus duration, stimulus delay, and to demonstrate repeat presentations of stimuli.

Determining the relationship between the software stimulus strength and the output voltage of the device will help in understanding not only how the device works, but also how the management software functions. The repeatability of the stimulus strength generated by the software is critical to the success of the instrument, as it will affect the repeatability of the air-pulse stimulus interaction with the corneal surface. Ultimately, this will affect the accuracy of ocular surface sensitivity being measured. Measuring the effective duration of different stimulus duration settings using the output voltage will verify the accuracy of the duration settings of the management software, as well as the stimulus delay settings. Determining the consistency of the air puffs facilitates a better understanding of the internal mechanics of the instrument (Nosch, 2015).

4.2 Test Instruments

4.2.1 Digital Multimeter

As previously mentioned, the driving voltage of the micro-blower has a square waveform, and a digital multimeter can be used to interpret the waveform. A multimeter is an instrument that can act both as an ammeter (measures electric current), and a voltmeter (measures the electric potential difference between two points in a circuit). This instrument is typically used to measure functions such as current, voltage, and resistance (Illinois Institute of Technology, 2019). In order to interpret the square waveform, the multimeter produces a digital value known as the root mean squared voltage (V_{rms}), which is a method of defining the AC (alternating current) waveform (that typically fluctuates between positive and negative voltage cycles) as if it was DC (direct current) (a constant one-way voltage free from any cycles). Therefore, the root mean squared voltage provides a simple and numerical way of expressing the square waveform (C. McLaren, personal communication, February 18, 2020; Z. Wang, personal communication, February 19, 2020). For the purpose of this experiment, the EX520 digital multimeter (Extech Instruments, Boston, Massachusetts, USA), with 0.09% accuracy, was used to measure voltage (FLIR Systems, 2019). The multimeter was set to V_{AC} since the driver circuit provided AC output to the micro-blower (C. McLaren, personal communication, February 18, 2020; Z. Wang, personal communication, February 19, 2020).

4.2.2 Digital Oscilloscope

Voltage can also be measured using an oscilloscope. The instrument monitors changes in voltage as a function of time, as well as displays voltage signals as stationary waveforms on its screen. The first oscilloscopes consisted of analog circuitry and cathode-ray tube displays. Digital oscilloscopes consist of LCD displays, but their controls are based on the controls of analog oscilloscopes. An electron gun generates a beam of electrons that are focused on a fluorescent screen. This beam travels through two sets of deflection plates, and one set deflects the beam in the y-direction (y-deflection plates), and the other set deflects the beam in the x-direction (x-deflection plates). When a voltage is applied, a potential difference is produced between the y-direction plates that causes the beam of electrodes to be deflected towards one of the plates, with the amount of deflection proportional to the input voltage. This deflection is made visible on the fluorescent screen as movement either upwards or downwards. If another voltage is generated and applied to the x-deflection plates to represent time, the vertical deflection in the electron beams can be made to deflect across the screen, thus allowing changes in time of the incoming voltage signal to be displayed on the screen. The voltage for horizontal deflection can be produced internally on the oscilloscope by the operator.

The screen of the oscilloscope is divided into several squares by an overlying grid that appears when the instrument is switched on. The horizontal axis on the grid typically represents time, whereas the vertical axis represents the voltage of the incoming signal. Incoming voltage signals can enter the instrument through its input channels, and most oscilloscopes have two channels. Each channel has a knob under the vertical heading on the screen that can be used to control the volts per division (volts/div) of the signal display. Each channel also has a menu that can be used to turn the waveform display option on and off, and the position knob is used to move the voltage signal display up or down on the screen. The scale knob under the horizontal heading on the screen is used to control the seconds per division (sec/div), and hence control the period of time over which the signal is displayed (Illinois Institute of Technology, 2019).

For this experiment, the GDS-840 digital oscilloscope (GW-Instek, Taipei, Taiwan) was used to measure both voltage and time. Voltage was reported as V_{AC}. The accuracy of the vertical system (voltage measurement) was reported as ± (3% x absolute value of the readout + 0.05 div x Volts/div + 0.8 mV), and the horizontal system (time measurement) as 0.01% (Good Will Instrument CO. Ltd., 2004).

The maximum voltage and the time taken for one puff of air to be elicited was measured by manually manipulating the cursor button and the variable knob of the oscilloscope in order to align two sets of adjustable marking lines. The vertical V_1 and V_2 lines (yellow lines) were aligned to the peaks of the waveform to determine the voltage, and the horizontal T_1 and T_2 lines (blue lines) were aligned between a complete cycle of the waveform to measure the time, respectively (Figure 4.1). Once these markers were lined up, the numerical values of the puff duration and voltage were directly obtained from the right hand column of the screen (blue box for time, and yellow box for voltage) (Figure 4.1).

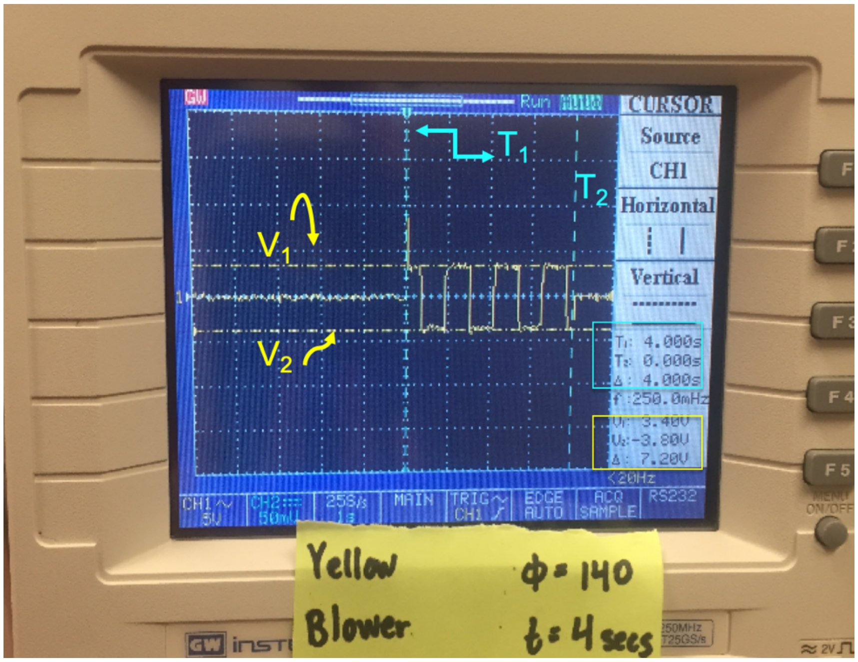

Figure 4.1: Wave profile generated by the oscilloscope with the vertical (T1 and T2) and horizontal lines (V1 and V2) labelled to show how duration and output voltage are measured, respectively.

The average duration and output voltage are given by the delta measurements found for the T_1, T_2, V_1 and V_2 measures on the right-hand side (blue and yellow boxes, respectively).

4.3 Experiment 1: Single micro-blower with varying stimulus strength and duration

4.3.1 Purpose and hypotheses

4.3.1.1 Purpose

To determine how the output voltage supplied to a single micro-blower varies in relation to the management software stimulus strength setting.

4.3.1.2 Hypotheses

1. The output voltage will increase as the stimulus strength setting increases.
2. The stimulus setting/output voltage relationship will not be affected by the stimulus duration.

4.3.2 Digital Multimeter Procedure

Each of the two test-leads of the digital multimeter were connected via crocodile clips to one of the two connecting wires that joins the yellow micro-blower to the MLEO Dolphin control unit. The dial on the multimeter was set to V_{AC}.

Part A: Multimeter and stimulus strength

1. The Dolphin management software was set to supply the yellow micro-blower with a continuous airflow at a stimulus strength of 250 units, at room temperature, and for a duration of 25 seconds.
2. The maximum voltage delivered to the micro-blower by the management software was measured by the multimeter and recorded in a pre-designed test matrix using Microsoft Excel. The process was repeated three times, and the results were averaged for further analysis.
3. The software stimulus strength was then changed to 210, 140, and 70 units, and steps 1-2 were repeated.

Part B: Multimeter and stimulus duration

4. The stimulus duration was changed to 10 seconds and 5 seconds, and steps 1-3 were repeated.

A summary of the constant and changing variables involving the use of the multimeter can be found in Table 4.1.

Experiment	**Aim**	**Variable(s) changed**	**Constant Variable(s)**	**Instrument(s) used to measure voltage**
1	To determine how the output voltage supplied to a single micro-blower varies with management software stimulus strength setting.	Stimulus strength: 70, 140, 210, and 250 units. Duration: 5, 10 and 25 seconds.	Micro-blower: Yellow.	Digital multimeter and oscilloscope.
2	To determine how the output voltage supplied by the management software varies when the maximum stimulus strength setting is selected for different stimulus durations, for four micro-blowers.	Duration: 5, 10, and 25 seconds. Micro-blowers: Yellow, Purple, Blue, and Green.	Stimulus strength: 250 units.	Digital multimeter and oscilloscope.
3	To determine how the output voltage of the Dolphin aesthesiometer varies with the repeated presentation of air-pulses puffs.	Stimulus strength: 140 and 210 units.	Duration: 1 seconds. Delay: 1 second. Micro-blower: Yellow.	Digital multimeter only.

Table 4.1: Summary of changed and constant variables in each experiment and the instruments used to measure voltage.

4.3.3 Oscilloscope Procedure

One each of the two test-leads of the digital oscilloscope were connected via crocodile clips to one of the two connecting wires that join the Murata^{TM} micro-blower to the MLEO Dolphin control unit, in a similar manner to that used for the multimeter studies.

Part C: Oscilloscope and stimulus strength and duration

1. Channel 1 was selected on the oscilloscope control settings, and the auto-set button was pressed to stabilise the detected voltage on the display screen. The voltage division dial was set to 5 V, and the time division dial was set to 1 second. As a result, each horizontal box on the profile generated by the digital oscilloscope represented 1 second, and each vertical box represented 5 V.
2. Step 1 was repeated, with the duration set at 4 seconds.
3. The maximum voltage delivered to the micro-blower by the management software was measured by adjusting the variable knob of the oscilloscope to align the movable vertical V_1 and V_2 lines to the peaks of the waveform to determine the voltage.
4. The duration for each air-pulse was measured by manipulating the movable horizontal T_1 and T_2 lines between a complete cycle of the waveform to measure the time (Figure 4.1).
5. With the stimulus duration unaltered, the stimulus strength was then changed to 210, 140, and 70 units, and steps 7-8 repeated. The results were recorded in a pre-designed test matrix using Microsoft Excel. Photographs of the profiles generated on the screen of oscilloscope for each measurement were also taken.
6. The stimulus duration was then changed to 2 seconds, steps 7-9 repeated.

A summary of the constant and changing variables involving the use of the oscilloscope can be found in Table 4.1.

In order to reduce systematic errors (errors that are repeatable from measurement to measurement), all of the connections between the different components were disconnected and reconnected at random intervals throughout the experiment. Such errors would include poor or incorrect connection of the instrument to the voltmeter, as well as the possible induction of electrical noise into the system via the wires, which may act as antennas.

4.3.4 Analyses

Data were tested for normality using the Shapiro-Wilk assumption test. Normally distributed data were analyzed using repeated measures ANOVA (rm-ANOVA). Holm tests were used for post-hoc analysis. JASP version 0.13.1 (University of Amsterdam, Netherlands) was used for data analysis procedures. A probability value of 0.05 or less was considered to be statistically significant.

4.3.5 Results

Part A: Multimeter and stimulus strength

Micro-blower type	Stimulus strength (units)	Duration (seconds)	Number of puffs	Average Voltage V_{rms} (V)	Standard Deviation
Yellow	70	5	1	0.73	0.0010
Yellow	140	5	1	1.48	0.0015
Yellow	210	5	1	2.22	0.0026
Yellow	250	5	1	2.50	0.0016
Yellow	70	10	1	0.74	0.0012
Yellow	140	10	1	1.48	0.0057
Yellow	210	10	1	2.22	0.0023
Yellow	250	10	1	2.50	0.0013
Yellow	70	25	1	0.74	0.0004
Yellow	140	25	1	1.48	0.0005
Yellow	210	25	1	2.22	0.0008
Yellow	250	25	1	2.50	0.0009

Table 4.2: Mean multimeter output voltage measurements for the different combinations of stimulus strength and duration settings on the MLEO Dolphin management software.

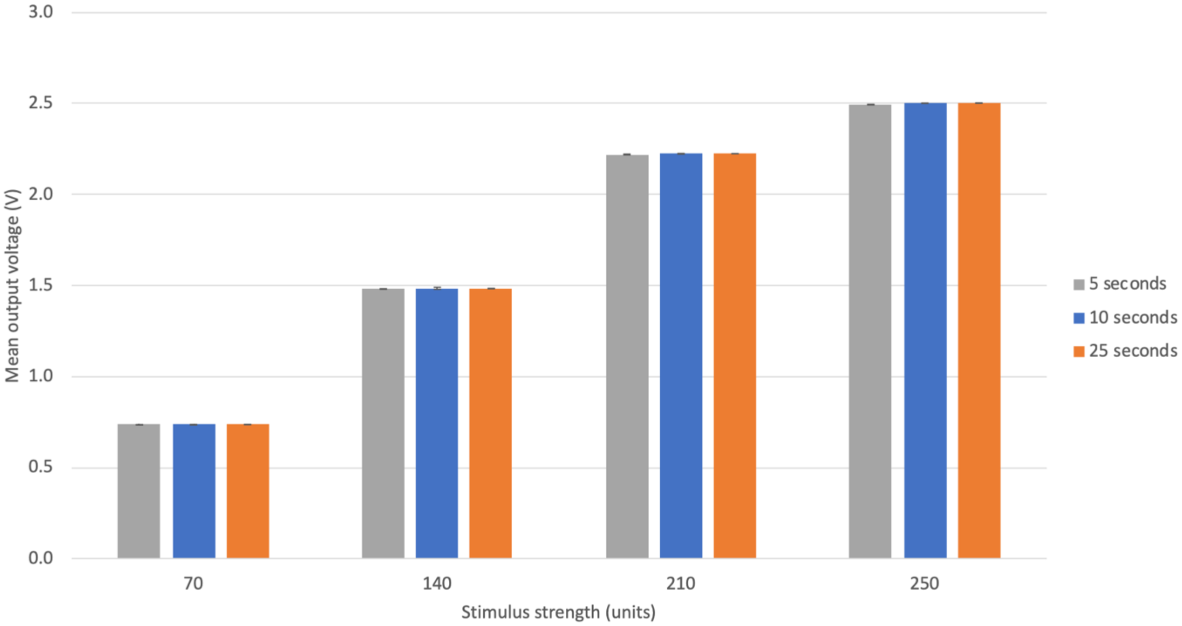

Figure 4.2: Bar chart of the mean multimeter output voltages for the different combinations of stimulus strength and duration settings on the MLEO Dolphin management software. Error bars denote ± 1 standard deviation.

The mean output voltage supplied by the management software was consistent for each stimulus strength. There was a significant effect of stimulus strength on mean output voltage (rm-ANOVA based on Huynh-Feldt correction, $F(3, 8) = 2.273 \times 10^5$, $p < 0.001$, $\omega^2 = 1$). Post-hoc testing revealed the output voltage increased significantly as stimulus strength increased (Table 4.3).

Stimulus strengths compared	Voltage at 140 units – Voltage at 210 units*	Voltage at 140 units – Voltage at 250 units**	Voltage at 140 units – Voltage at 70 units*	Voltage at 210 units – Voltage at 250 units*	Voltage at 210 units – Voltage at 70 units*	Voltage at 250 units – Voltage at 70 units*
Mean difference in output voltage (V)	-0.740	-1.018	0.748	-0.278	1.488	1.765
p-value	$p < 0.001$	$p < 0.001$	$p < 0.001$	$p < 0.001$	$p < 0.001$	$p < 0.001$

Table 4.3: Post-hoc comparisons (using Holm correction) of mean output voltage for different stimulus strength settings (significant results in blue*).

Part B: Multimeter and stimulus duration

There was no significant effect of duration on mean output voltage (rm-ANOVA based on Huynh-Feldt correction, $F(2, 9) = 3.708 \times 10^{-5}$, $p = 1.000$, $\omega^2 = 0$).

Part C: Oscilloscope and stimulus strength and duration

Micro-blower type	**Stimulus strength (units)**	**Duration (seconds)**	**Number of puffs**	**Delta T (s)**	**Delta V (V)**
Yellow	70	2	1	2	3.8
Yellow	140	2	1	2	7.0
Yellow	210	2	1	2	10.0
Yellow	250	2	1	2	10.8
Yellow	70	4	1	4	3.8
Yellow	140	4	1	4	7.2
Yellow	210	4	1	4	10.4
Yellow	250	4	1	4	11.0

Table 4.4: Mean oscilloscope output voltage measurements for different combinations of stimulus strength and duration settings on the MLEO Dolphin management software.

The supplied voltage by the management software, for the various combinations of stimulus strength and duration (Table 4.4), showed that as the stimulus strength setting increased, the output voltage also increased irrespective of the duration of the puff. The values in columns 3 and 5, which represent the duration setting on the MLEO Dolphin management software, and the time taken for one puff of air as registered by the oscilloscope respectively, were similar. This means that the duration setting of the MLEO Dolphin management software was accurate, and stimuli could be delivered for the desired time period.

4.4 Experiment 2: Multiple micro-blowers with maximum stimulus strength and varying duration

4.4.1 Purpose and hypotheses

4.4.1.1 Purpose

To determine how the output voltage supplied by the management software varies when the maximum stimulus strength setting is selected for different stimulus durations, for four micro-blowers.

4.4.1.2 Hypothesis

1. Consistent measures of voltage will be obtained for each micro-blower at each stimulus strength and duration setting.

4.4.2 Procedure

As for Experiment 1, the output voltage supplied by the aesthesiometer management software was measured using both a digital multimeter and an oscilloscope. The multimeter and oscilloscope were connected to each micro-blower using the procedure described in Sections 4.3.2 and 4.3.3. Once again, to reduce systematic errors, the connections between the apparatus were disconnected and reconnected at random intervals throughout the experiment. A summary of the constant and changing variables involving the use of the multimeter and oscilloscope can be found in Table 4.1.

<u>Part A: Multimeter</u>

1. The Dolphin management software was set to supply the yellow micro-blower with a continuous airflow at a stimulus strength of 250 units, at room temperature, and for a duration of 25 seconds.
2. The maximum voltage delivered to the micro-blower by the management software was measured by the multimeter and recorded in a pre-designed test matrix using Microsoft Excel. The process was repeated three times, and the results were averaged for further analysis.
3. The stimulus duration was then changed to 10 seconds and 5 seconds, and steps 1 and 2 were repeated.
4. Steps 1-3 were then repeated using the purple, blue, and green micro-blowers.

<u>Part B: Oscilloscope</u>

5. Channel 1 was selected on the oscilloscope control settings, and the auto-set button was pressed to stabilise the detected voltage on the display screen. The voltage division dial was set to 5 V, and the time division dial was set to 1 second. As a result, each horizontal box on the profile generated by the digital oscilloscope represented 1 second, and each vertical box represented 5 V.
6. Step 1 was repeated, with the duration set at 4 seconds.

7. The maximum voltage delivered to the micro-blower by the management software was measured by adjusting the variable knob of the oscilloscope to align the movable vertical V_1 and V_2 lines to the peaks of the waveform to determine the voltage.
8. The duration for each air-pulse was measured by manipulating the movable horizontal T_1 and T_2 lines between a complete cycle of the waveform to measure the time (Figure 4.1).
9. With the stimulus strength unaltered, the duration was then changed to 2 seconds and steps 7-8 repeated. The results were recorded in a pre-designed test matrix using Microsoft Excel. Photographs of the profiles generated on the screen of oscilloscope for each measurement were also taken.

4.4.3 Analyses

Data were tested for normality using the Shapiro-Wilk assumption test. Normally distributed data were analyzed using repeated measures ANOVA (rm-ANOVA). Holm tests were used for post-hoc analysis. JASP version 0.13.1 (University of Amsterdam, Netherlands) was used for data analysis procedures. A probability value of 0.05 or less was considered to be statistically significant.

4.4.4 Results

Part A: Multimeter

Micro-blower type	Stimulus strength (units)	Duration (seconds)	Number of puffs	Trial 1 V_{rms} (V)	Trial 2 V_{rms} (V)	Trial 3 V_{rms} (V)	Trial 4 V_{rms} (V)	Trial 5 V_{rms} (V)	Trial 6 V_{rms} (V)	Average Voltage V_{rms} (V)	Standard Deviation
Yellow	250	5	1	2.50	2.49	2.49	2.50	2.50	2.50	2.50	0.0016
Yellow	250	10	1	2.50	2.50	2.50	2.51	2.50	2.50	2.50	0.0013
Yellow	250	25	1	2.51	2.51	2.50	2.50	2.50	2.50	2.50	0.0009
Purple	250	5	1	2.45	2.46	2.45	2.46	2.46	2.46	2.46	0.0016
Purple	250	10	1	2.46	2.46	2.46	2.47	2.47	2.47	2.46	0.0031
Purple	250	25	1	2.46	2.46	2.46	2.47	2.47	2.47	2.47	0.0038
Blue	250	5	1	2.44	2.44	2.44	2.44	2.44	2.44	2.44	0.0021
Blue	250	10	1	2.46	2.45	2.45	2.45	2.45	2.45	2.45	0.0035
Blue	250	25	1	2.46	2.45	2.46	2.45	2.46	2.45	2.46	0.0042
Green	250	5	1	2.43	2.43	2.43	2.43	2.43	2.43	2.43	0.0018
Green	250	10	1	2.44	2.44	2.44	2.44	2.44	2.44	2.44	0.0027
Green	250	25	1	2.45	2.45	2.45	2.44	2.44	2.45	2.45	0.0013

Table 4.5: Mean multimeter voltage measurements for the different micro-blowers and stimulus duration settings on the MLEO Dolphin management software.

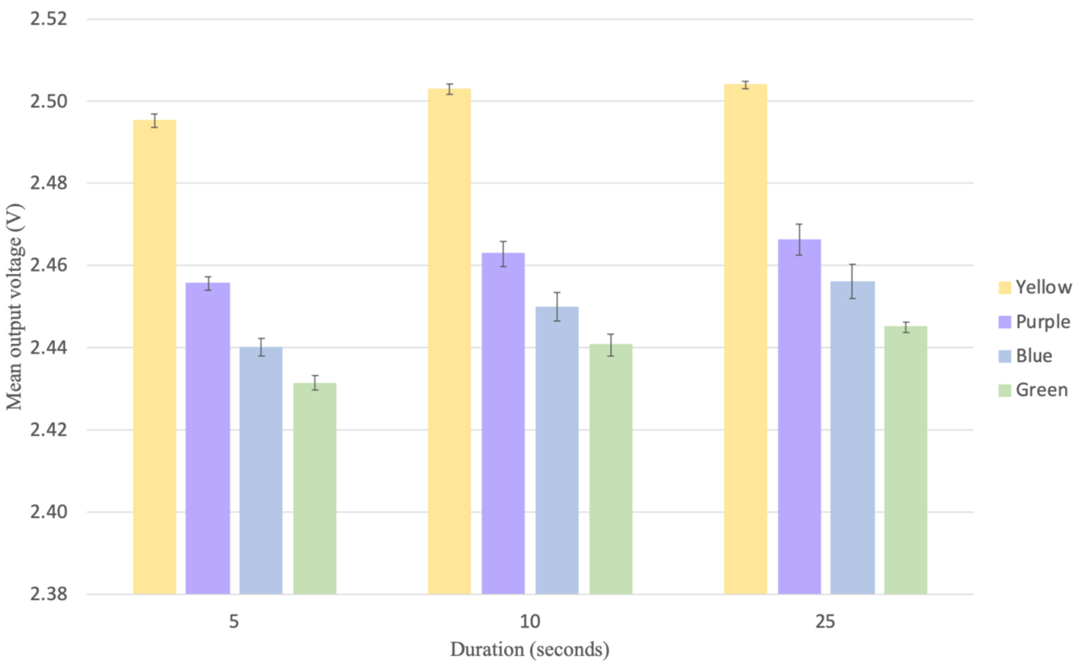

Figure 4.3: Bar chart of the mean multimeter voltages for the different micro-blowers and stimulus duration settings on the MLEO Dolphin management software. Error bars denote ± 1 standard deviation.

At the maximum stimulus strength setting (250 units), each micro-blower produced relatively consistent output voltages at the three levels of duration. There was no significant effect of duration on mean output voltage (rm-ANOVA based on Huynh-Feldt correction, F (2, 9) = 0.212, p= 0.813, ω^2= 0). However, there was a significant effect of the micro-blower type on the mean output voltage (rm-ANOVA based on Huynh-Feldt correction, F (3, 8) = 53.533, p < 0.001, ω^2= 0.929). Post-hoc testing revealed the output voltage was highest for the yellow micro-blower at all levels of duration (Table 4.6).

Micro-blowers compared	Voltage of Blue – Voltage of Yellow*	Voltage of Green – Voltage of Yellow*	Voltage of Purple – Voltage of Yellow*
Mean difference in output voltage (V)	-0.052	-0.062	-0.039
p-value	$p < 0.001$	$p < 0.001$	$p < 0.001$

Table 4.6: Post-hoc comparisons (using Holm correction) of the effects of micro-blower type on the output voltage (significant results in blue*).

Part B: Oscilloscope

Micro-blower type	**Stimulus strength (units)**	**Duration (seconds)**	**Number of puffs**	**Delta T (s)**	**Delta V (V)**
Yellow	250	2.0	1	2.0	10.8
Purple	250	2.0	1	2.0	11.0
Green	250	2.0	1	2.0	11.2
Yellow	250	4.0	1	4.0	11.0
Purple	250	4.0	1	4.0	11.0
Green	250	4.0	1	3.9	11.2

Table 4.7: Mean oscilloscope output voltage measurements for the different micro-blowers and stimulus duration settings on the MLEO Dolphin management software.

The output voltage measurements using the digital oscilloscope for the various combinations of micro-blower and duration setting (Table 4.7) showed that duration had no effect on the output voltage. As indicated in Experiment 1, the values in columns 3 and 5 confirmed the accuracy of the time setting on the MLEO Dolphin management software. The table also showed that there was slight variation in the output voltage of the different micro-blowers.

4.5 Experiment 3: Single micro-blower with multiple stimulus pulses of varying stimulus strengths

4.5.1 Purpose and hypotheses

4.5.1.1 Purpose

To determine how the output voltage of the Dolphin aesthesiometer varies with the repeated presentation of air-pulses puffs using a digital multimeter.

4.5.1.2 Hypothesis

1. Multiple puffs of the same stimulus strength will produce repeatable output voltage measures.

4.5.2 Procedure

The output voltage supplied by the aesthesiometer management software was measured using a digital multimeter. The multimeter was connected to the multi-blower using the procedure described in Section 4.3.2. Once again, to reduce systematic errors, the connections between the apparatus were disconnected and reconnected at random intervals throughout the experiment. A summary of the constant and changing variables for experiments using the multimeter can be found in Table 4.1.

<u>Part A</u>

1. The Dolphin management software was set to supply the yellow micro-blower with two consecutive air-pulses of stimulus strength 140 units and duration 1 second, with an inter-pulse delay of 1 second.
2. The maximum voltage delivered to the micro-blower by the management software was measured by the multimeter and recorded in a pre-designed test matrix using Microsoft

Excel. The process was repeated three times, and the results were averaged for further analysis.

Part B

3. The software stimulus strength was then changed to deliver two consecutive air-pulses of 1 second duration, with a first pulse of 140 units and a second pulse of 210 units, and step 2 was repeated.

4.5.3 Results

Micro-blower type	**Stimulus strength (units)**	**Duration (seconds)**	**Delay (seconds)**	**Puff Number**	**Average Voltage V_{rms} (V)**	**Standard Deviation**
Yellow	140	1	1	1	1.63	0.06
Yellow	140	1	1	2	1.63	0.06

Micro-blower type	**Stimulus strength (units)**	**Duration (seconds)**	**Delay (seconds)**	**Puff Number**	**Average Voltage V_{rms} (V)**	**Standard Deviation**
Yellow	140	1	1	1	1.81	0.11
Yellow	210	1	1	2	2.26	0.05

Table 4.8: Mean multimeter output voltage measurements for different multiple puff settings on the MLEO Dolphin management software for Parts A and B.

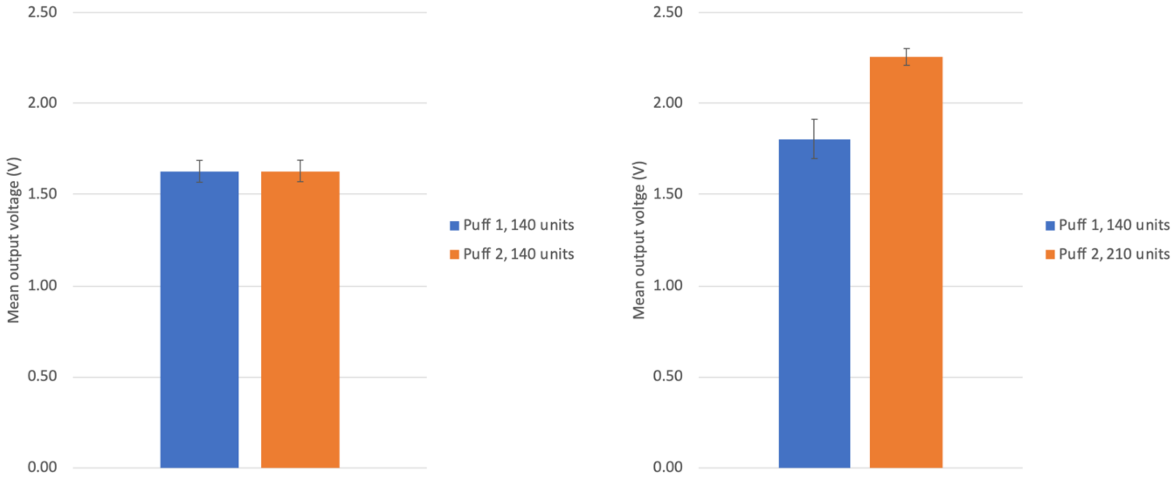

Figure 4.4: Bar charts of the mean multimeter voltages for the different multiple puff settings on the MLEO Dolphin control software (puff duration: 1 second, puff delay: 1 second); (a) Part A, (b) Part B. Error bars denote ± 1 standard deviation.

Table 4.8 showed that the output voltages produced when multiple puffs of the same stimulus strength were generated consecutively were consistent. The mean output voltage was 1.63 V AC for each of the two puffs (Figure 4.4 (a)). When two consecutive puffs of different strengths were generated, the output voltage increased in going from a strength of 140 to 210 units (Figure 4.4 (b)).

4.6 Discussion

These experiments were designed to answer several questions regarding the integrity of the MLEO software used to control the Dolphin aesthesiometer.

The first question was to determine the reliability of the duration setting of the management software. The oscilloscope results of Experiments 1 and 2 confirmed that the duration setting on the software was accurate, thus confirming the reliability of this setting on the MLEO control software. In addition, both experiments also graphically and statistically verified that the duration of the air-puff generated by the novel aesthesiometer had no effect on the output voltage.

The second question was to investigate the effect and reliability of the software stimulus strength setting on the output voltage. Experiments 1 and 2 graphically and statistically confirmed that as the stimulus strength setting increased, so too did the output voltage. This is expected since a larger potential difference would be required to produce a stronger stimulus. Furthermore, the output voltage produced at each stimulus strength level was consistent at each of the stimulus durations used, with very little variability noted in the voltages measured. This finding was evident by the small error bars and standard deviations in Figure 4.2 and Table 4.2.

The third question was to assess the consistency of the management software with respect to the different micro-blowers. Experiment 2 showed graphically and statistically that the output voltages differed between the four micro-blowers. For instance, in Figure 4.3, the mean output voltage between the green and blue, and the blue and purple micro-blowers differed by 0.01 V, between the purple and yellow micro-blowers by 0.04 V, and between the green and yellow micro-blowers by 0.06 V (at each stimulus duration level). These variations are small and are not considered likely to be clinically significant, but should be factored into the calibration of the instrument for its use in measuring corneal sensitivity on human subjects. Calibration will be further discussed in Chapter 10 (overview and future works).

Given that this is the first aesthesiometer with the potential to generate multiple puffs from multiple micro-blowers, it was also crucial that the software management settings for consecutive multiple puffs were also tested. When multiple puffs of the same stimulus strength were generated consecutively, the output voltages were fairly consistent and repeatable, as shown by the small error bars in Figure 4.4(a). Unexpectedly, the output voltages measured from multiple puffs of the 140 unit stimulus strength differed between Experiment 3 Part A and Part B by 0.18 V AC. This may be due to the small sample size since three voltage measurements were taken for each puff, shown by the larger variation in measurements for Experiment 3 Part A. Nevertheless, the results of the multiple puffs of different strengths still show that as the strength is increased, the voltage also increases.

4.7 Conclusion

The results of the experiment validate the software control system of the Dolphin aesthesiometer. Consequently, further studies geared towards determining the characteristics of the airflow as it leaves the instrument, encounters a surface, as well as the various components of the stimulus can be performed.

CHAPTER 5: STIMULUS CHARACTERISTICS, AIRFLOW DISPERSION IN AIR

5.1 Purpose and hypotheses

5.1.1 Purpose

To determine if (i) the airflow dispersion produced by the Dolphin aesthesiometer in air is coherent, and (ii) if the spread rate of the airflow changes with various stimulus strengths and nozzle conditions.

5.1.2 Hypotheses

1. The airflow will be coherent and that coherency would be maintained for further distances with a nozzle attachment.
2. The spread rate will be constant irrespective of the stimulus strength.
3. The coherence zone will exceed that required for the expected instrument test distance.

5.2 Background

5.2.1 Round air-jets

As air leaves the jet it diverges, and it continues to do so as it moves further away. Looking within the cross-section of the airflow, there is a region where spreading of the airflow occurs slowly and a region where it broadens. This gives rise to the Gaussian velocity profile seen in Figure 5.1, whereby the area under the curve is momentum (the product of a body's mass and velocity), and is constant as given by the law of conservation of fluid momentum (the momentum of a system stays constant once the net force acting on it is zero) (Çengel & Cimbala, 2006; Lum, 2014). The airflow eventually reaches a point where it loses its coherence, and there is a transition from laminar to turbulent flow. Several factors contribute to this change, namely gravity acting on the air particles pulling them down, and drag on the stimulus particles as they encounter static air in the environment (the drag has more of an effect at the edges of the airflow than at the center) (S. Peterson, personal communication, June 18th, 2021; White, 2006). For round jets, the spread rate, which is essentially the angle of the spread (Figure 5.2 (c)), is independent of the stimulus strength. Therefore the spread rate and divergence is constant (White, 2006).

In addition, since force is the rate of change of momentum, it follows that if the speed of the jet center changes the momentum will no longer be constant, and the force too will change. Therefore when directed towards a large surface area, given the width of the exit air-jet, the area under both Gaussian curves in Figure 5.1 should be the same, and the force will be constant at any distance away from the exit air-jet. However, when directed towards a smaller target, such as the eye, the area under the second curve in Figure 5.1, that is, the curve furthest from the exit air-jet, will be smaller than that of the first curve, and hence the force would be expected to decrease as one gets furthest from the exit air-jet (Cao et al., 2017; S. Peterson, personal communication, October 30, 2020; White 2006).

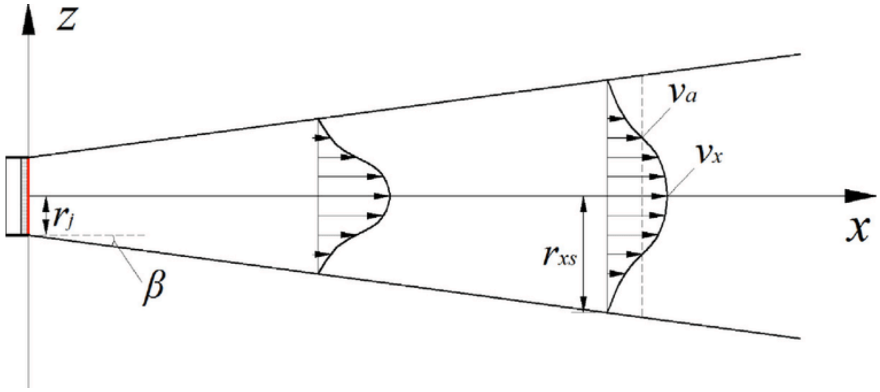

Figure 5.1: Velocity profile of a jet.

Reproduced from Energy and Buildings, 142, Z. Cao, Y. Wang, M. Duan, and H. Zhu, Study of the vortex principle for improving the efficiency of an exhaust ventilation system, page 41, Copyright (2017), with permission from Elsevier (See Letters of Copyright Permission).

5.2.2 Airflow visualization studies

Chapter 4 validated the software control system of the Dolphin aesthesiometer. However, little is known about the airflow stimulus when it leaves the exit air-jet of the instrument. It is therefore important to learn more about the characteristics of the airflow, especially since the device was designed to deliver a precise airflow to stimulate the desired region of the cornea.

In order to visualize the airflow of previous aesthesiometers, a variety of methods have been used. One such technique is Schlieren Interferometry, which was used by Murphy (1996) when working with the Non-Contact Corneal Aesthesiometer (NCCA). This technique relies on the effects from the refractive index changes on the transmission of light produced by the airflow. With this method, the airflow from the NCCA exit air-jet was placed in the optical plane of a white light interferometer, and gas from an aerosol dust remover was passed through it in order to photograph the airflow profile. The air leaving the NCCA exhibited a controlled pattern that was laminar, until coherence was lost at about 1.5 cm from the exit air-jet. The study also found that the central region of the airflow was more coherent (Murphy, 1996). Boberg-Ans (1952) found similar results (Boberg-Ans, 1952). Lum (2014) placed talcum powder inside the nozzle of the Belmonte Ocular Pain Meter (BOPM), and once it was released, the flow of the powder was digitally photographed. He found that the powder dispersed in a Gaussian distribution pattern (Lum, 2014).

To visualize the stimulus when it leaves the Dolphin aesthesiometer, an experiment was designed that used the diaphragm air-intake system of the micro-blower to also draw in lycopodium powder. This yellow powder was selected because of its low density. Once the powder was in the micro-blower it would be pushed out through the exit air-jet, and the airflow profile could then be photographed for various stimulus strengths.

This experiment provides a means of visualizing what happens to the airflow when it leaves the instrument. It will also aid in determining the coherence and spread rate (angle of spread) characteristics of the airflow.

5.3 Methods

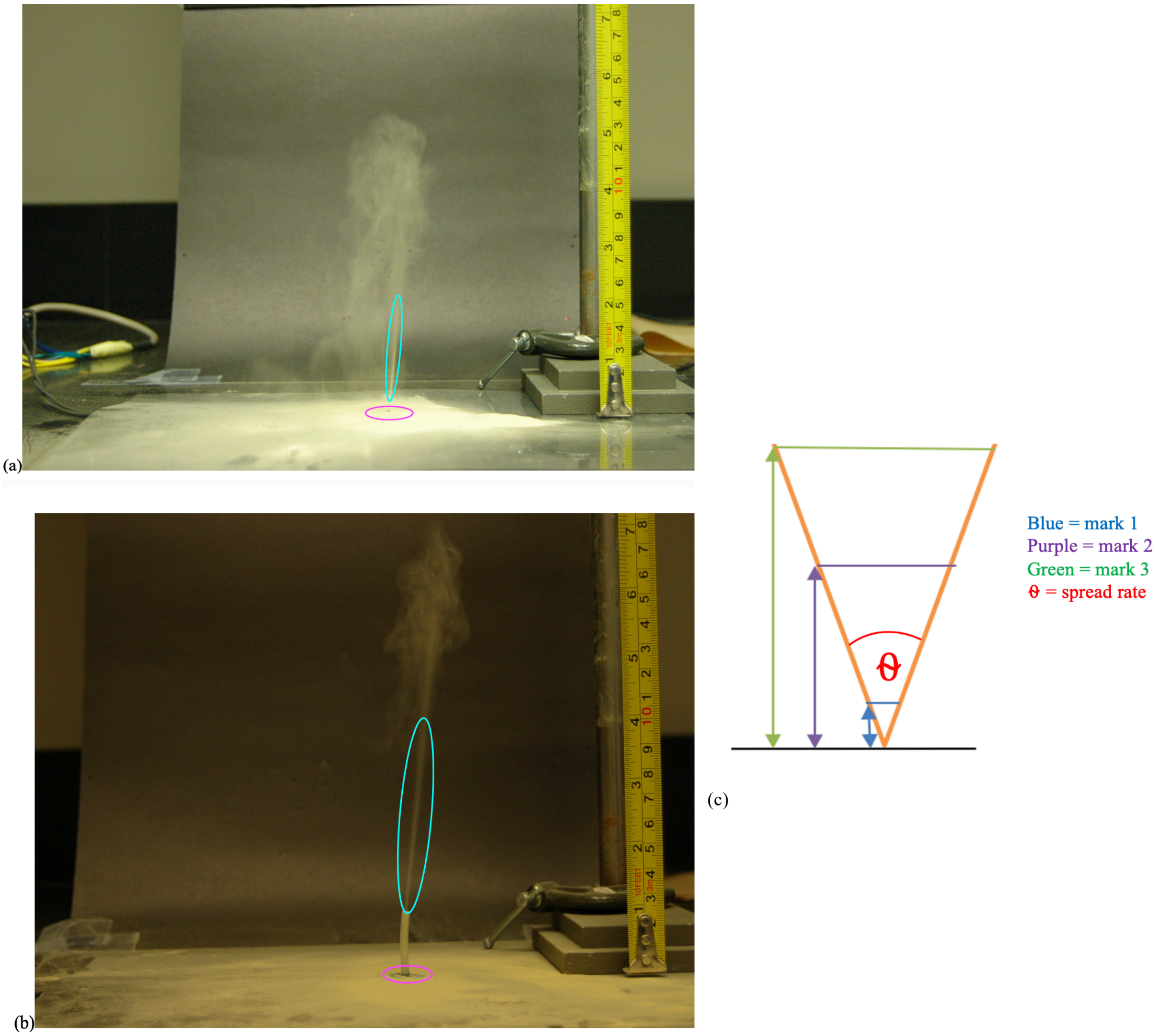

Figure 5.2: Equipment set-up for Experiments 1 and 2: (a) Micro-blower placed on top of lycopodium powder and covered by a clear plastic sheet that only allows the exit air-jet to be exposed; (b) Micro-blower with 1-inch long Tygon nozzle attached to the exit air-jet (micro-blower in pink circle, and region of interest where airflow is coherent is in blue circle); (c) Illustration depicting where measurements were taken.

5.4 Experiment 1: Airflow dispersion in air for a single micro-blower

5.4.1 Purpose

To determine if the airflow produced by a single micro-blower at various stimulus strengths is coherent with and without a nozzle, and if the spread rate changes under these conditions.

5.4.2 Procedure

Lycopodium powder (3.5 grams) (Aldrich Chemical Co LLC, Milwaukee, USA) was placed onto a flat black counter top. The micro-blower was placed on top of the powder in such a way that the majority of the powder made contact with its base. A clear, rigid, plastic overlay with a 1 mm wide hole at the center was placed directly over the micro-blower, so that the exit air-jet was the only part of the system that was exposed. This overlay acted to retard dispersion of the lycopodium powder caused by the pumping action of the micro-blower. A retort stand was used to hold a measuring tape along the plane of the micro-blower, and a matte black piece of cardboard served a backdrop for the experimental set-up (Figure 5.2 (a) and (b)). The micro-blower was connected to the MLEO Dolphin control unit.

In order to reduce systematic errors, that is errors that are repeatable from measurement to measurement, the connections between all the apparatus were disconnected and reconnected at random intervals throughout the experiment.

The airflow dispersion in air produced by the airflow exiting the micro-blower was photographed using a Nikon D5300 DSLR camera, and between trials the retort stand with the measuring tape was checked to ensure that the system was along the plane of the micro-blower. All results were recorded in a pre-designed Microsoft Excel test matrix.

Image J 1.52k (National Institutes of Health, USA, Java 1.8.0_172 (64-bit)) was used to determine the furthest distance from the micro-blower at which the airflow was coherent (mark 3), and the corresponding width of the coherent airflow at that distance (Figure 5.2 (c)). The length of the airflow was then divided into three equal parts starting from mark 3, and the distances from the micro-blower and corresponding width of airflow were also determined using Image J. In total there were three widths and three distances (marks 1, 2, and 3) for each trial (Figure 5.2 (c)). These measurements were then used to calculate the angles of spread (spread rate), using basic trigonometry principles. This study was completed with the assistance of Katelyn Tsang, from the School of Optometry and Vision Science, University of Waterloo, who photographed the airflow dispersion in air, and helped to validate Image J, as well as Elisabet Simó Bertran, from the Faculty of Optometry, Universitat Politècnica de Catalunya, BarcelonaTech, who helped with the image processing.

Part A: Micro-blower without plastic nozzle

1. The MLEO Dolphin management software was set to deliver a continuous airflow with stimulus strength of 250 units for a duration of 10 seconds.
2. The airflow pattern was photographed using a Nikon D5300 DSLR camera, and the process was repeated four more times, with the powder replenished between trials.
3. The stimulus strength was then changed to 210 and 140 units and steps 1-2 were repeated. The stimulus strengths were randomized in terms of the order of their delivery.

Part B: Micro-blower with plastic nozzle

4. The entire experiment was repeated using a 1-inch long Tygon plastic nozzle attached to the exit air-jet of the micro-blower. In terms of measurements however, the distances were measured relative to the end of the nozzle furthest from the micro-blower. In addition, the Tygon nozzle had to be emptied between trials.

5.4.3 Analyses

Data were tested for normality using the Shapiro-Wilk assumption test. Data were analyzed using parametric or non-parametric tests depending on normality and adherence with repeated measures ANOVA (rm-ANOVA) assumptions. Normally distributed data were analyzed using repeated measures ANOVA (rm-ANOVA) followed by Tukey HSD tests for post-hoc analysis, whereas data that violate the assumptions were tested using Durbin test and Conover's post-hoc analysis. JASP version 0.13.1 (University of Amsterdam, Netherlands) was used for data analysis procedures. A probability value of 0.05 or less was considered to be statistically significant.

5.4.4 Results

Stimulus strength (units)	Duration (seconds)	Nozzle	Mean width of mark 1 (cm)	SD	Mean width of mark 2 (cm)	SD	Mean width of mark 3 (cm)	SD	Mean distance from the micro- blower to mark 1 (cm)	SD	Mean distance from the micro- blower to mark 2 (cm)	SD	Mean distance from the micro- blower to mark 3 (cm)	SD	Mean spread rate for mark 1 (°)	SD	Mean spread rate for mark 2 (°)	SD	Mean spread rate for mark 3 (°)	SD
140	10	0	0.20	0.04	0.26	0.05	0.31	0.06	1.21	0.48	3.31	1.00	4.85	1.41	10.41	3.04	4.63	1.10	3.87	1.08
210	10	0	0.21	0.05	0.29	0.09	0.36	0.11	1.51	0.45	3.29	0.61	4.49	0.93	8.43	2.19	5.07	0.96	4.61	0.66
250	10	0	0.23	0.04	0.28	0.05	0.37	0.06	1.07	0.16	2.77	0.35	4.07	0.58	12.53	3.10	5.69	0.50	5.21	0.30
140	10	1	0.18	0.02	0.28	0.05	0.38	0.08	1.01	0.43	2.71	0.40	4.11	0.87	13.75	11.57	5.96	1.33	5.62	2.04
210	10	1	0.27	0.07	0.35	0.04	0.60	0.09	2.55	0.51	5.70	1.04	8.53	1.87	6.24	2.34	3.61	1.07	4.14	0.73
250	10	1	0.21	0.03	0.35	0.10	0.58	0.25	1.24	0.56	5.42	3.66	8.92	6.72	12.17	6.43	5.19	2.89	4.78	1.89

Table 5.1: Mean widths and distances from the micro-blower and spread rates for marks 1, 2, and 3 for the different stimulus strengths. Nozzle is coded as 0 = no nozzle attached and 1 = nozzle attached to the exit air-jet.

Examination of the photographs in Image J 1.52k such as those in Figure 5.2 (a) and (b) showed that the airflow diverges as it leaves the jet and maintains coherence (region of interest in the blue circles of the figure), until it eventually breaks down.

Since one particular area of interest in this experiment was to not only determine if the airflow was coherent, but also to find the distance of the furthest point of coherence from the micro-blower, the measurements taken at mark 3 were studied closely.

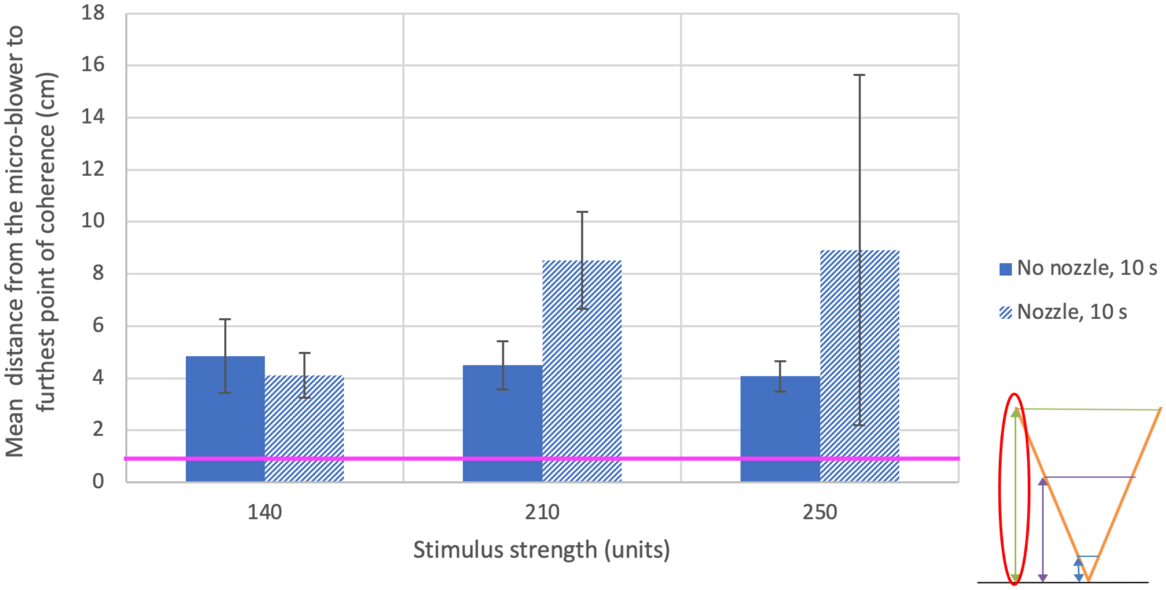

Figure 5.3: Mean distance from the micro-blower to the furthest point of coherence (mark 3) versus stimulus strength (see red circle in bottom right illustration). Error bars denote ± 1 standard deviation.

When no nozzle was attached, the distance was measured from the exit air-jet of the micro-blower, whereas when a nozzle was attached, the distance was measured from the end of the nozzle. The pink horizontal line represents a distance of 1 cm.

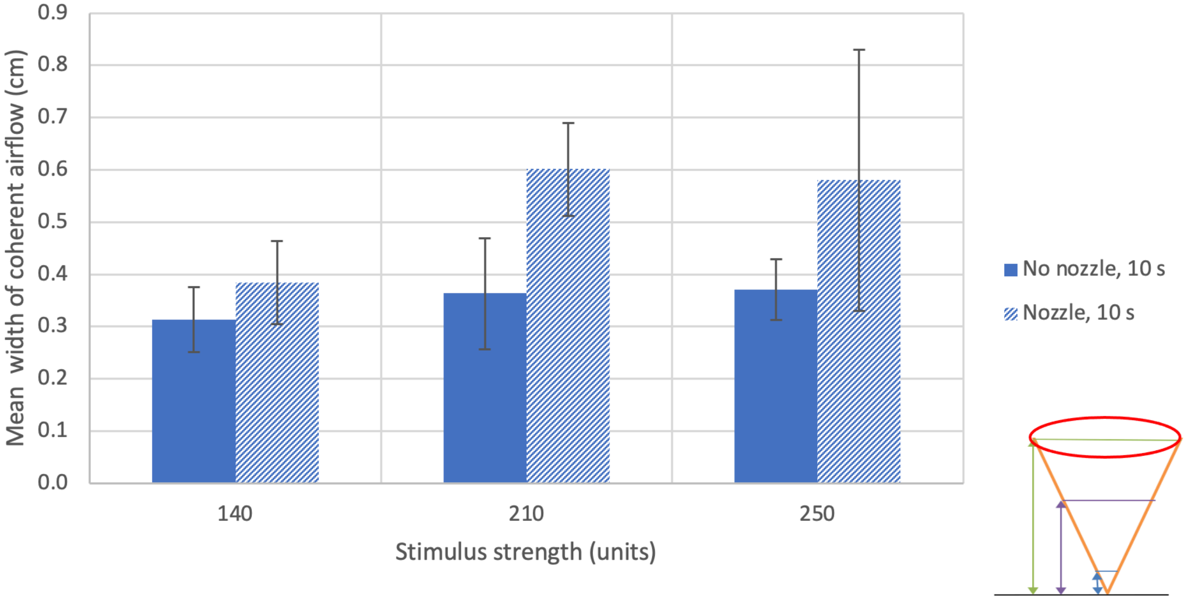

Figure 5.4: Mean width of coherent airflow (at mark 3) versus stimulus strength (see red circle in bottom right illustration). Error bars denote ± 1 standard deviation.

Figures 5.3 and 5.4 show that as the stimulus strength increased, the distance at which coherence was maintained, as well as the corresponding airflow width, was not affected when no nozzle was attached to the instrument. However, coherence was maintained for longer distances when a nozzle was attached to the exit air-jet, and the widths were larger. Figure 5.3 also shows that airflow was coherent for the typical aesthesiometry test distance of 1 cm.

Trial	Stimulus strength (units)	Duration (seconds)	Nozzle	Spread rate for mark 1 (°)	Spread rate for mark 2 (°)	Spread rate for mark 3 (°)
1	140	10	0	9.13	3.45	3.59
2	140	10	0	13.80	5.27	3.86
3	140	10	0	6.77	3.42	2.54
4	140	10	0	13.36	5.73	3.80
5	140	10	0	9.00	5.27	5.54
1	210	10	0	12.06	5.05	4.55
2	210	10	0	7.27	3.89	3.59
3	210	10	0	6.26	4.55	4.49
4	210	10	0	8.26	5.46	5.18
5	210	10	0	8.33	6.43	5.22
1	250	10	0	11.94	5.83	5.36
2	250	10	0	17.81	6.26	5.07
3	250	10	0	9.70	4.88	4.85
4	250	10	0	11.18	5.77	5.64
5	250	10	0	12.00	5.72	5.12
1	140	10	1	8.48	6.72	6.39
2	140	10	1	8.90	5.02	4.10
3	140	10	1	8.50	5.76	5.00
4	140	10	1	8.43	4.48	3.82
5	140	10	1	34.44	7.81	8.80
1	210	10	1	7.36	3.52	3.82
2	210	10	1	4.23	2.59	3.15
3	210	10	1	5.24	3.16	4.05
4	210	10	1	9.80	5.42	4.65
5	210	10	1	4.54	3.37	5.04
1	250	10	1	14.26	6.31	7.15
2	250	10	1	7.67	5.91	5.36
3	250	10	1	22.58	9.07	5.70
4	250	10	1	7.61	1.92	2.63
5	250	10	1	8.75	2.75	3.06

Table 5.2: Spread rates for marks 1, 2, and 3 for the different stimulus strengths. Nozzle is coded as: 0 = no nozzle attached and 1 = nozzle attached to the exit air-jet.

Table 5.2 shows that the spread rate for marks 2 and 3 were the same. These results were therefore combined to increase the sample size when looking at the spread rate at various stimulus strengths. It is important to note that the spread rates for mark 1 were quite large. This is because there was more uncertainty when making measurements so close to the exit air-jet or nozzle. These spread rates were therefore not used for the analysis.

Stimulus strength (units)	Duration (seconds)	Nozzle	Mean spread rate (marks 2 and 3 combined) (º)	Standard deviation
140	10	0	4.25	1.10
210	10	0	4.84	0.82
250	10	0	5.45	0.47
140	10	1	5.79	1.63
210	10	1	3.88	0.91
250	10	1	4.98	2.31

Table 5.3: Mean spread rates when marks 2 and 3 are combined for the different stimulus strengths. Nozzle is coded as: 0 = no nozzle attached and 1 = nozzle attached to the exit air-jet.

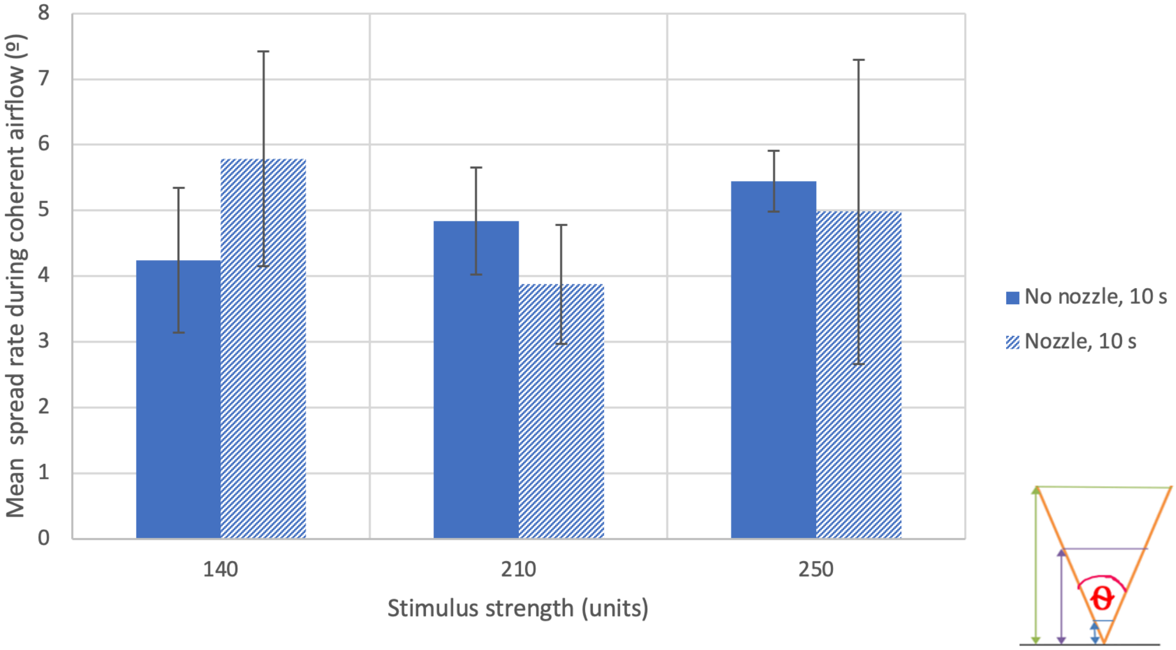

Figure 5.5: Mean spread rate during coherent airflow versus stimulus strength (see spread rate or angle of spread labelled in red in the bottom right illustration). Error bars denote ± 1 standard deviation.

The mean spread rate during coherent airflow varied between 4 and 6º with and without the nozzle. Non-parametric statistics were adopted since homogeneity could not be verified and outliers were present in the data set. There was a significant main effect of stimulus strength on the spread rate (Non-parametric rm-ANOVA, Durbin test, χ^2 (2) = 7.611, p = 0.022, Kendall's W = -23.681). However, pairwise comparisons showed that there was no significant difference in the spread rate for the three levels of stimulus strength (Conover's post-hoc pairwise comparisons), all $p > 0.05$).

5.5 Experiment 2: Airflow dispersion in air for multiple micro-blowers

5.5.1 Purpose

To determine if the spread rate of the airflow varied with repeated presentation of air-pulse puffs.

5.5.2 Procedure

Part A: Micro-blower without plastic nozzle

1. Using the same set-up of the equipment described in Section 5.4.2, the MLEO Dolphin management software was set to deliver consecutive air-pulses of stimulus strength 140 units, and a duration of 10 seconds each, with an inter-pulse delay of 10 seconds.
2. The airflow pattern was photographed using a Nikon D5300 DSLR camera, and the process was repeated four more times, with the powder replenished between trials.
3. The stimulus strengths were then changed so that two consecutive air-pulses of varying strengths would be generated. The strength of the first air-pulse was 140 units, and the second was 210 units. The duration of each pulse and the inter-pulse delay were both 10 seconds, and step 2 was repeated.

Part B: Micro-blower with plastic nozzle

4. The entire experiment was repeated using a 1-inch long Tygon plastic nozzle attached to the exit air-jet of the micro-blower. Distances were measured relative to the end of the nozzle furthest from the micro-blower, and the nozzle was emptied between trials.

5.5.3 Analyses

The means of the spread rate were plotted against the differences between the spread rate for two puffs. The upper and lower 95% limits of agreement (LoA) were calculated as LoA: mean + 2.78SD (upper limit), mean – 2.78SD (lower limit) (when considering the critical values of the student's *t* distribution for 4 degrees of freedom and 2-tailed cases) (Kalra, 2017).

5.5.4 Results

Stimulus strength and puff	**Nozzle**	**Mean spread rate for mark 2 (°)**	**Standard deviation**	**Mean spread rate for mark 3 (°)**	**Standard deviation**
140 puff 1	0	5.33	0.54	5.33	0.92
140 puff 2	0	7.41	1.64	7.92	1.54
140 puff 1	1	4.70	0.87	4.43	1.74
140 puff 2	1	4.27	1.05	4.76	1.50
140 puff 1	0	5.65	0.93	5.60	1.49
210 puff 2	0	5.55	0.74	5.41	1.18
140 puff 1	1	5.43	1.48	5.77	2.24
210 puff 2	1	2.71	0.73	3.55	0.97

Table 5.4: Mean spread rates for marks 2, 3 for the different stimulus strengths and puffs when multiple puffs were generated by the Dolphin aesthesiometer. Nozzle is coded as: 0 = no nozzle attached and 1 = nozzle attached to the exit air-jet.

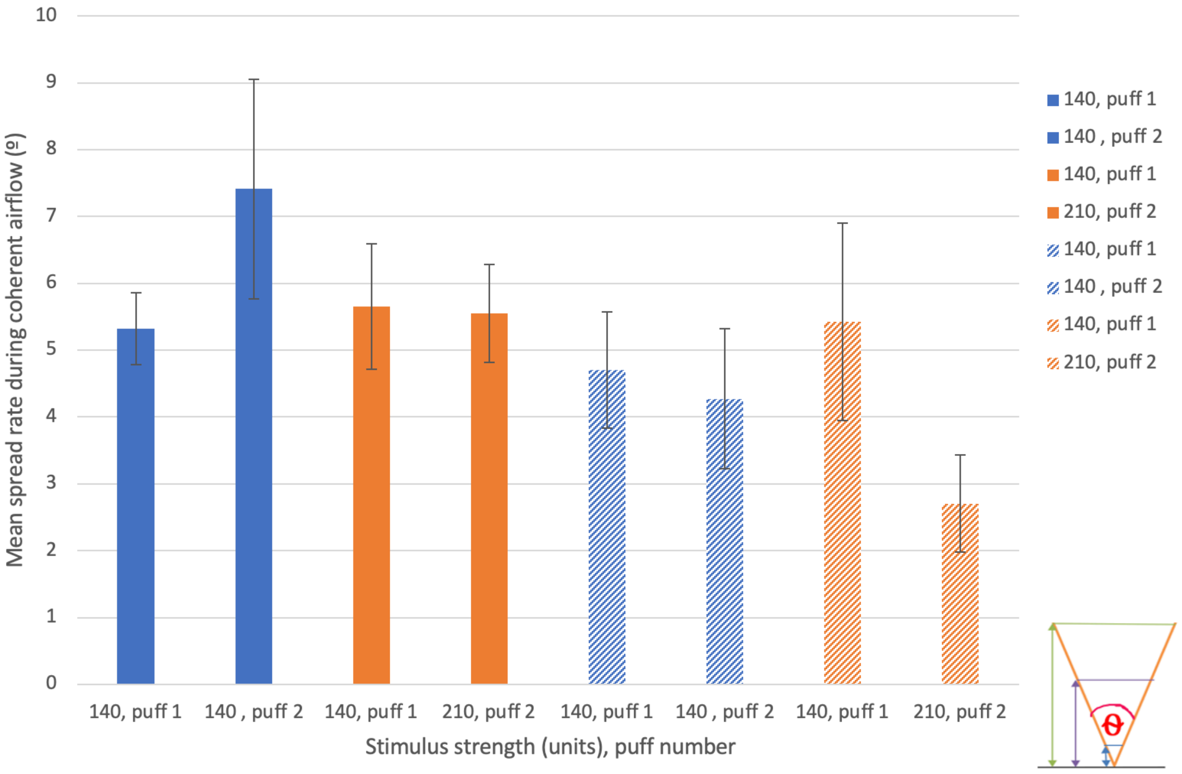

Figure 5.6: Mean spread rate during coherent airflow (mark 3) versus stimulus strength for multiple puffs. Error bars denote ± 1 standard deviation.

The solid bars represent cases where no nozzle was attached whereas the striped bars represent nozzle cases (see spread rate or angle of spread labelled in red in the bottom right illustration).

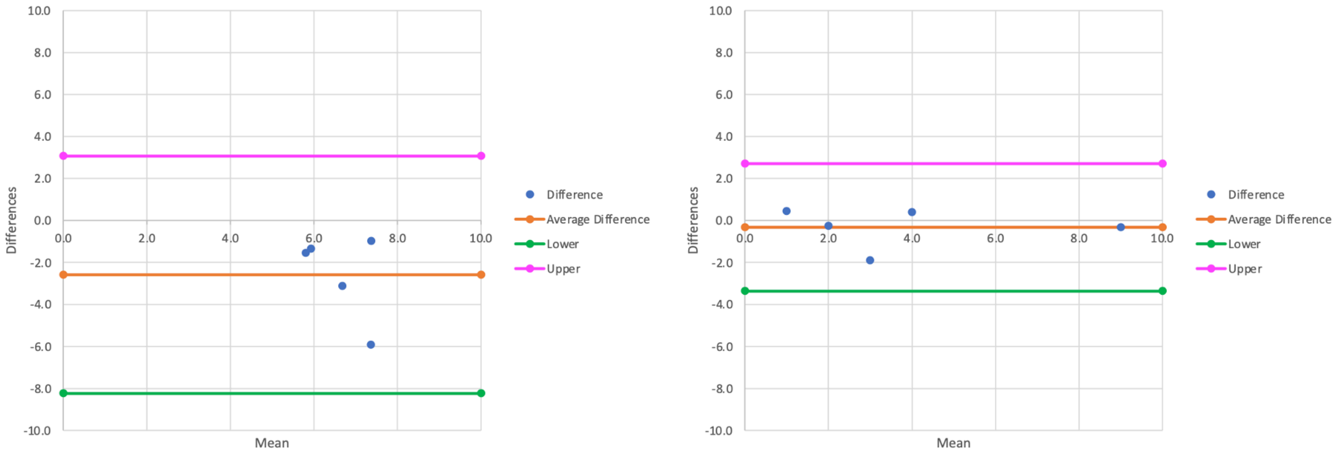

Multiple puffs
140, 140 units (Puff 1, Puff 2)
No nozzle

Multiple puffs
140, 140 units (Puff 1, Puff 2)
Nozzle

(a) (b)

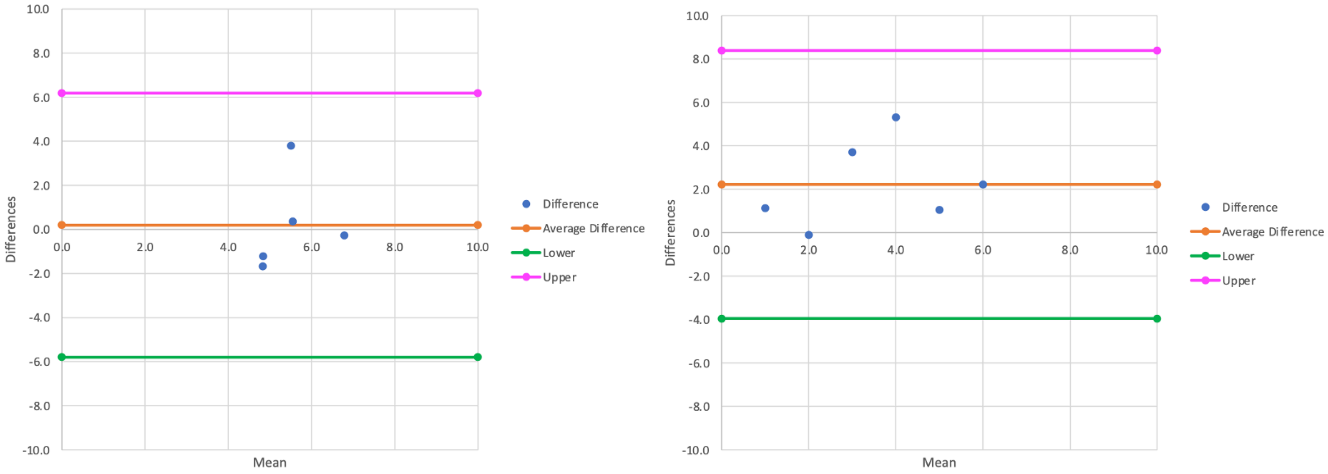

Multiple puffs
140, 210 units (Puff 1, Puff 2)
No nozzle

Multiple puffs
140, 210 units (Puff 1, Puff 2)
Nozzle

(c) (d)

Figure 5.7: Bland-Altman plots for spread rate for puffs 1 and 2 when multiple puffs were generated. (a) & (b) when puffs 1 and 2 are both 140 units, (c) & (d) when puff 1 is 140 units and puff 2 is 210 units (plots on the left are for cases where no nozzle was used, and plots on the right are for nozzle cases).

Figure 5.6 shows that the spread rate was relatively constant with a few exceptions. Figures 5.7 (b) and (c) show that the differences between the two puffs were small, and on average the points were close to zero, so on average there was good repeatability. Figures 5.7 (a) and (d) show that the spread rates of puff 2 were greater than puff 1, the spread rates of puff 1 were greater than puff 2 respectively, and on average the points were farther from zero suggesting poorer repeatability. However, these results may be due to the mean being dragged in one direction by the higher than usual values, which would result in larger standard deviations. Since the sample size was small, it is not possible to trim the data. Instead the best way to elucidate the true nature of the repeatability between the puffs would be to perform more trials, and hence increase the sample size.

5.6 Discussion

Photographs, such as those in Figures 5.2 (a) and (b), show that as the airflow leaves the instrument it maintains coherence before eventually breaking down. This is in keeping with typical jet behaviour and previous aesthesiometry studies (Borberg-Ans, 1952; Murphy 1996; Lum, 2014).

Figure 5.3 showed that when no nozzle was attached to the instrument, and as the stimulus strength and hence airflow rate increased, the distance at which coherence was maintained was not affected. Furthermore, the distances were fairly consistent, as given by the small error bars. When a nozzle was attached to the exit air-jet, coherence was maintained for longer distances.

Two factors must be considered when a nozzle is applied. Firstly, the nozzle narrows the area in which the air can flow, and, as a result, the flow rate and force of the air leaving the device is reduced. Secondly, the nozzle changes the behavior of the flow characteristics within the micro-blower. It is difficult to know exactly what those changes are, and in fact, this is beyond the scope of this thesis. However, what is certain is that with the nozzle, the airflow is more unidirectional, and hence coherence is maintained for further distances. When no nozzle was used, airflow was coherent for distances as far as 5 cm from the exit air-jet, whereas when a nozzle was attached, coherence was maintained for distances up to 9 cm away from the end of the nozzle. These distances are further than the 1.5 cm distance reported by Murphy (1996). Moreover, given that the typical test/working distance for most aesthesiometry studies is 1 cm, the horizontal line drawn in Figure 5.3 confirms that the airflow is coherent at 1 cm whether or not a nozzle is attached to the instrument.

What is interesting about Figure 5.3 is that the distance of coherent flow was unaffected when no nozzle was attached to the device, but with the nozzle, the distance increased as the stimulus strength increased from 140 to 210 units, and then plateaued as the strength increased from 210 to 250 units. These trends suggest that saturation was occurring in non-nozzle cases (since the distance was unaffected), and there were both instances of no saturation and saturation (plateauing) occurring in the nozzle cases. Saturation is likely due to the limited capacity of the micro-blower to effectively change its stimulus strength, and hence the jet output, thus causing the distance of coherent flow to converge to a certain value.

The same trends are seen in Figure 5.4 when studying the width of coherent flow. In Figures 5.3 and 5.4 it appears as though saturation occurred sooner, that is, at lower stimulus strengths for the non-nozzle cases compared to the nozzle cases. However, this is not really the case since, as previously mentioned, in addition to making the flow more unidirectional, the nozzle decreased the flow rate. Therefore, the results of distance and width for cases when the strength is 140 units and no nozzle was attached should be similar to that of cases where the strength is 210 units and a nozzle was attached. This explanation is supported by the results of the next experiment in Chapter 6, where the dispersion of the airflow when it comes into contact with a surface is studied, and will be further discussed in section 6.6 of Chapter 6.

Table 5.3 and Figure 5.5 show that spread rate varied between 4° and 6º for non-nozzle and nozzle cases. Whilst there are small deviations, the spread rate was relatively constant irrespective of the stimulus strength. This is supported by statistics and in keeping with the published literature on round air-jets (Pope, 2012).

The variability noted for the nozzle and non-nozzle cases in Figures 5.3 to 5.5 may be due to the fact that, even though a fixed mass of powder was used and the powder was replenished between trials, it was difficult to ensure the same amount of powder was in contact with the base of the micro-blower, and the same amount of powder was absorbed by the instrument. In addition, for the nozzle case, the flexible nature of the Tygon material may have caused it to move during the process of taking up and expelling the powder.

The results of experiment 2 confirm that the spread rate is constant irrespective of the stimulus strength with the exceptions of puff 2 when the stimulus strengths are both 140 units and no nozzle is used, and puff 2 when the strengths of the consecutive puffs are 140 and 210 units and a nozzle is applied. The discrepancy with the first exception can be explained by the larger than usual spread rate noted for one of the five trials, whilst the second exception may be attributed to the flexibility of the nozzle material. Despite this, the results of the Bland-Altman plots support the agreement between the spread rate of the puffs.

The consistency in the spread rate further confirms the fact that the airflow was coherent. From an aesthesiometry perspective, being able to maintain coherence at distances beyond 1 cm is ideal since larger test distances may help to promote participant compliance, and ease anxiety that is often associated with having stimuli or objects directed close to the surface of the eye. Furthermore, the consistent spread rate could also mean that the once the device is positioned towards the cornea, there is a higher chance that the same region of the cornea will be stimulated with repeated trials. However, this depends on certain factors being controlled. For instance, one would have to be sure that the patient does not move their eyes and the length of the stimulus is not too long that there is involuntary movement. Other factors would include the room conditions, since having an air condition vent in the direction of the instrument could cause drying of the tear film and hence blinking.

5.7 Conclusion

The results of the experiment confirm that when the airflow leaves the instrument it is coherent. Coherence is maintained for the desired test distance of 1 cm, and for further distances when a nozzle is attached to the instrument. The spread rate of the instrument is not dependent on stimulus strength. Studies focused on what happens to the airflow when it encounters a boundary or surface can be performed.

CHAPTER 6: STIMULUS CHARACTERISTICS, AIRFLOW DISPERSION ON A SURFACE

6.1 Purpose and hypotheses

6.1.1 Purpose

To determine if there is a change in dispersion of the airflow produced by the Dolphin aesthesiometer on a flat surface at various stimulus strengths, durations of air puff, and test/working distances, and for different micro-blowers.

6.1.2 Hypotheses

1. The powder displacement diameter (PDD) will increase as stimulus strength increases.
2. The powder displacement diameter (PDD) will decrease as the test distance increases.
3. The powder displacement diameter (PDD) will not be affected by stimulus duration.
4. All micro-blowers will produce similar PDDs for the same stimulus strength.
5. The powder displacement diameter (PDD) will decrease when a nozzle was applied to the instrument.

6.2 Background

Previous chapters have described how the instrument is able to deliver a narrow coherent airflow, and therefore ensure that it is focused on and stimulates the cornea rather than spreading to the lashes or the conjunctiva. Chapter 5 showed how the airflow behaved when it exited the aesthesiometer. More specifically, it confirmed that airflow dispersion was coherent up to distances as far as 5 cm without a nozzle, and 9 cm when a nozzle was attached to the exit air-jet. It also showed that the spread rate (angle of spread) is independent of the stimulus strength. However, it is important to understand what happens to the airflow when it encounters a surface or a boundary, and how far it spreads out as a result. This is especially important since the stimulus airflow will ultimately be directed towards the cornea, and with the extensive corneal receptive field overlap, we want to be sure that the finalized stimulus airflow only interacts with the receptive fields of the cornea.

To visualize what happens when the stimulus comes into contact with a surface, the experiment first performed by Boberg-Ans in 1952, and later by Murphy in 1996 was repeated. Both previous experiments used lycopodium powder, which is a fine yellow powder of low density. Varying the stimulus pressure and test/working distance, a stimulus was released and directed towards a thin layer of the powder. The stimulus displaced the powder, thereby creating a crater, and the diameter of each crater was measured. This allowed a determination of whether the amount of powder displaced (due to the dispersion of the airflow stimulus) changed as the pressure and working distance were varied (Boberg-Ans, 1952; Murphy, 1996). Murphy (1996) found that as the stimulus pressure increased, the amount of powder displaced also increased. In addition, the duration of the stimulus and the test/working distance (distance between the exit air-jet of the aesthesiometer and the surface of the powder) had no effect on the diameter of the craters produced (Murphy, 1996).

In addition to altering the stimulus strength and test/working distance, the stimulus duration will also be varied. The test/working distances and stimulus durations selected were in accordance with aesthesiometry/corneal sensitivity literature (Lum, 2014; Murphy, 1996; Murphy et al., 1996). The test/working distances were selected to examine the effect of working distance, and the durations were chosen to examine the effect of airflow volume (Lum, 2014; Murphy, 1996; Murphy et al., 1996).

This experiment will aid in determining the consistency of the hardware, and hence the stimulus. It will also provide a means of visualizing what happens to the airflow produced by the instrument when it comes into contact with a surface.

6.3 Methods

A 28 x 14.7 cm rectangular frame was made from a rectangular sheet of paper (35.5 x 21.5 cm). This frame was then placed onto a larger piece of black card (Figure 6.1). Lycopodium powder (4.6 grams) (Aldrich Chemical Co LLC, Milwaukee, USA) was evenly and thinly spread within the area of the frame using the flat end of a spatula. The frame was used to confine the powder. A 3 cm wide centimeter ruler was placed along one length of the rectangular frame to facilitate scale measurements, and evenly spaced markings were made along the opposite length of the border to allow equal spacings between each stimulus release. A retort stand was used to firmly hold a selfie stick, which was modified to house the micro-blower. This system allowed the air-jet of the micro-blower to be positioned with the exit air-jet perpendicular to the powder. It also allowed the distance of the air-jet from the powder surface to be altered as needed. The micro-blower was connected to the MLEO Dolphin control unit.

In order to reduce systematic errors (errors that are repeatable from measurement to measurement), the connections between all the apparatus were disconnected and reconnected at random intervals throughout the experiment.

The lycopodium displacement patterns were photographed using a Nikon D50 DSLR camera. For an accurate recording of the dimensions of each dispersion crater, the camera alignment should be directly above the test surface in a consistent manner and not skewed. However, this was not possible within the experimental set-up. To remedy this error, Image J 1.52k (National Institutes of Health, USA, Java 1.8.0_172 (64-bit)) was used to un-skew the images, using the following method.

The pixel coordinates of the corners of the rectangular frame, as well as four points on each crater (the most northern, southern, western, and eastern positions of each crater) were identified and marked. Affine transformation was then applied to determine the diameter of the craters. Affine transformation is a type of geometric transformation that maintains both the collinearity and the ratios of distances between points on a line. There are three main types of affine transformation, namely rotation (turning a figure about a point), translating (moving the figure), as well as scaling (which involves decreasing or increasing the size of the figure) (Brilliant. Org, 2021; Weisstein, 2021). Affine transformation was performed instead of repeating the experiment to try to get un-skewed pictures because the main researcher would become very ill when exposed to lycopodium powder.

This study was completed with the assistance of Katelyn Tsang, from the School of Optometry and Vision Science, University of Waterloo, who photographed the airflow dispersion on a surface, and helped to validate Image J; Dr. Vivian Choh, University of Waterloo, School of Optometry and Vision Science and Dr. Sean Peterson, University of Waterloo, Fluid Flow Physics Group, who assisted with the process of affine transformation; as well as Elisabet Simó Bertran, from the Faculty of Optometry, Universitat Politècnica de Catalunya, BarcelonaTech, who helped with the image processing. Figure 6.2 (a) & (b) shows an example of a skewed and un-skewed photograph of the craters.

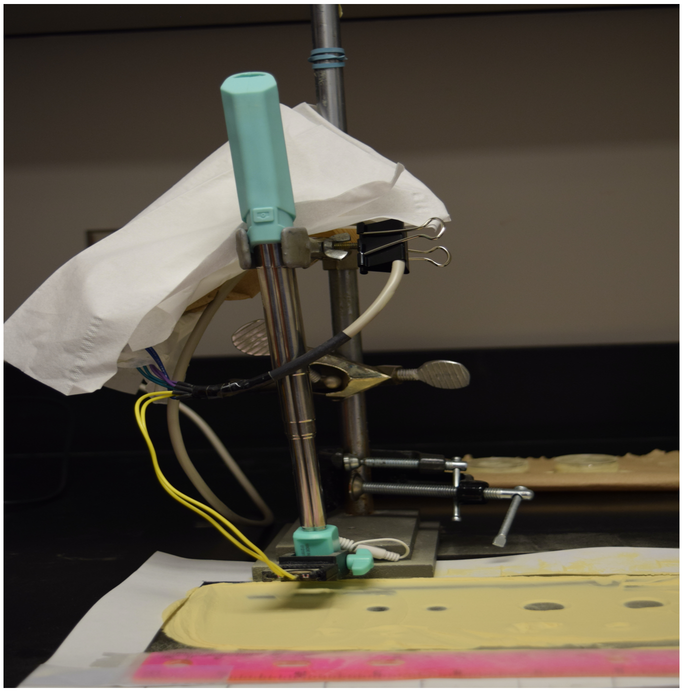

Figure 6.1: Equipment set-up for Experiments 1 and 2.

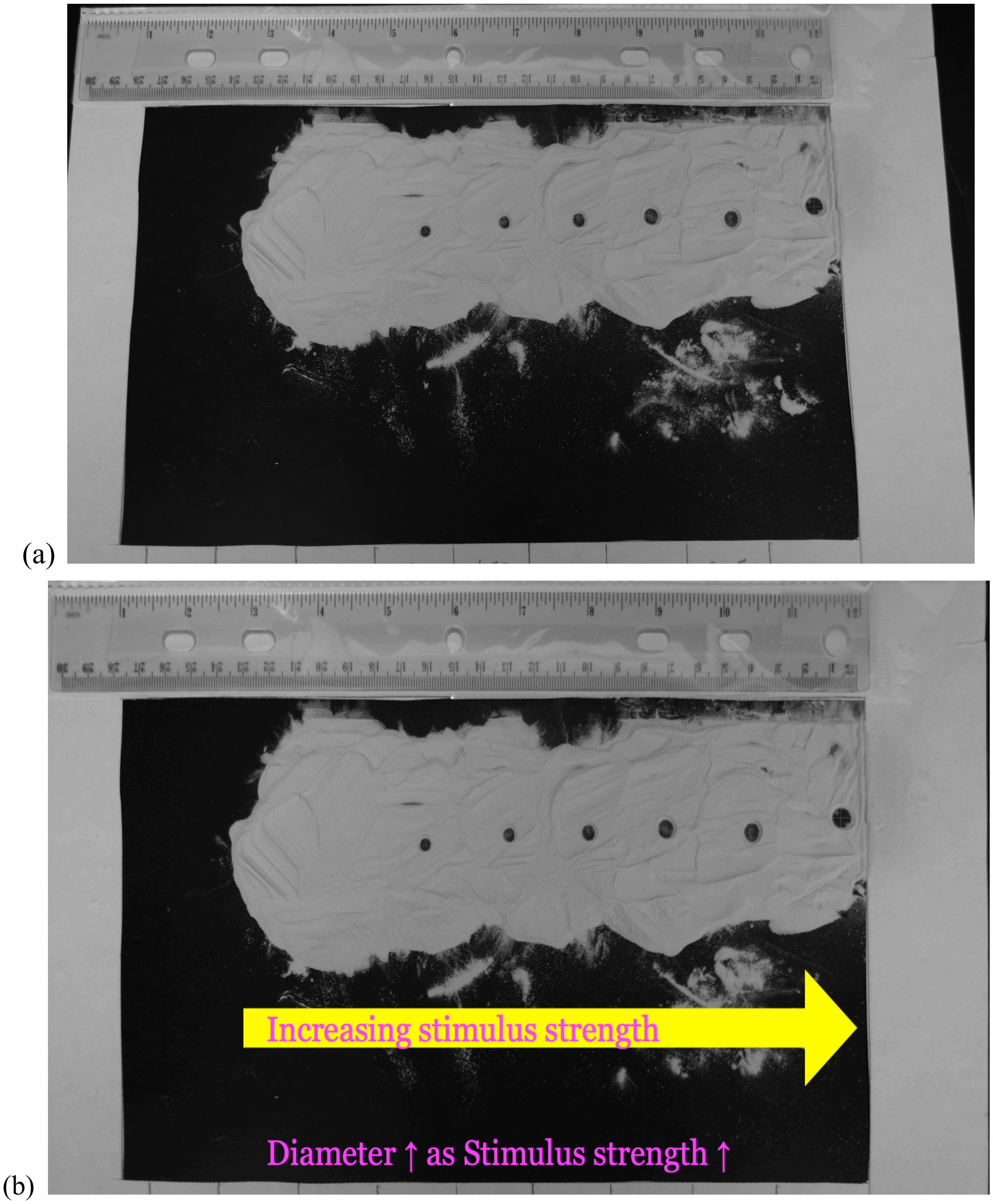

Figure 6.2: Aerial views of the craters produced for a test/working distance and stimulus duration combination, with (a) being the skewed photograph, and (b) being the un-skewed photograph produced by affine transformation.

Moving from left to right in both pictures, it is evident that as the stimulus strength increased, the size of the resulting crater increased as more powder was displaced by the airflow stimulus.

All of the dispersion crater diameters were recorded in a pre-designed Microsoft Excel test matrix, and the four resulting diameters (2 vertical and 2 horizontal) for each stimulus strength were averaged and tabulated.

6.4 Experiment 1: Airflow dispersion for a single micro-blower

6.4.1 Purpose

To determine the airflow dispersion on a flat surface produced by a single micro-blower at various stimulus strengths, durations of air puff, and test/working distances.

6.4.2 Procedure

Part A: Micro-blower without plastic nozzle

1. The air-jet of the yellow labelled micro-blower was positioned 3 cm from the surface of the powder. The MLEO Dolphin management software was set to deliver an air-puff of stimulus strength 250 units for a duration of 1.5 seconds. On release of the air-puff, the lycopodium powder was displaced and a crater formed.
2. The procedure was repeated so that each stimulus strength, test/working distance and stimulus duration combination, there were two trials. After each stimulus release, the exit air-jet was realigned with a new testing location on the powder surface.
3. The stimulus strength was then changed to 210, 140, and 70 units and steps 1-2 repeated. The stimulus strengths were randomised in terms of the order of their delivery.
4. The lycopodium displacement patterns were photographed. Each photograph recorded the results for a particular test/working distance and stimulus duration, and consisted of eight craters, since two trials were performed for each stimulus strength.

5. The process was repeated for test/working distances 1.5, 1.0, and 0.5 cm, with the powder replenished between changes in the test/working distance and stimulus duration combinations.
6. Steps 5-9 were then repeated using stimulus durations of 0.9 and 0.5 seconds.

Part B: Micro-blower with plastic nozzle

7. The entire experiment was repeated using a 1-inch long Tygon plastic nozzle attached to the exit air-jet of the micro-blower. The same test/working distances were used as in Part A, but were measured from the end of the nozzle to the surface of the powder.

6.4.3 Analyses

Data were tested for normality using the Shapiro-Wilk assumption test. A correlation analysis was performed on the normally distributed data, and subsequent linear regressions were executed. JASP version 0.13.1 (University of Amsterdam, Netherlands) was used for data analysis procedures. A probability value of 0.05 or less was considered to be statistically significant.

6.4.4 Results

It is important to note that there were some stimulus strength, stimulus duration, and test/working distance combinations in which no powder displacement was observed. This was either due to the working distance being too long for the stimulus strength used, to a weak stimulus strength, a short stimulus duration, the presence of the nozzle (which reduced airflow), or to some combination of these. As a result of this, only three stimulus strengths (140, 210, and 250 units), two working distances (1.0 and 1.5 cm), and two stimulus durations (0.9 and 1.5 seconds) were used for the analysis in Experiment 1.

Stimulus strength (units)	**Duration (seconds)**	**Distance from exit air-jet or nozzle to powder surface (cm)**	**Nozzle**	**Mean powder displacement diameter (PDD) (cm)**	**Standard deviation**
140	0.9	1.5	0	0.83	0.05
210	0.9	1.5	0	1.48	0.08
250	0.9	1.5	0	1.48	0.05
140	1.5	1.5	0	0.89	0.03
210	1.5	1.5	0	1.55	0.04
250	1.5	1.5	0	1.51	0.03
140	0.9	1.0	0	0.94	0.10
210	0.9	1.0	0	1.61	0.03
250	0.9	1.0	0	1.77	0.12
140	1.5	1.0	0	1.10	0.26
210	1.5	1.0	0	1.57	0.15
250	1.5	1.0	0	1.72	0.07
140	0.9	1.5	1	0.84	0.07
210	0.9	1.5	1	1.11	0.03
250	0.9	1.5	1	1.12	0.03
140	1.5	1.5	1	0.91	0.05
210	1.5	1.5	1	1.07	0.02
250	1.5	1.5	1	1.11	0.05
140	0.9	1.0	1	0.89	0.03
210	0.9	1.0	1	0.93	0.15
250	0.9	1.0	1	1.04	0.06
140	1.5	1.0	1	0.89	0.01
210	1.5	1.0	1	1.19	0.07
250	1.5	1.0	1	1.26	0.07

Table 6.1: Mean powder displacement diameter (PDD) for the different combinations of stimulus strength, duration, and test-working distances for Part A and B. Nozzle is coded as: 0 = no nozzle attached and 1 = nozzle attached to the exit air-jet.

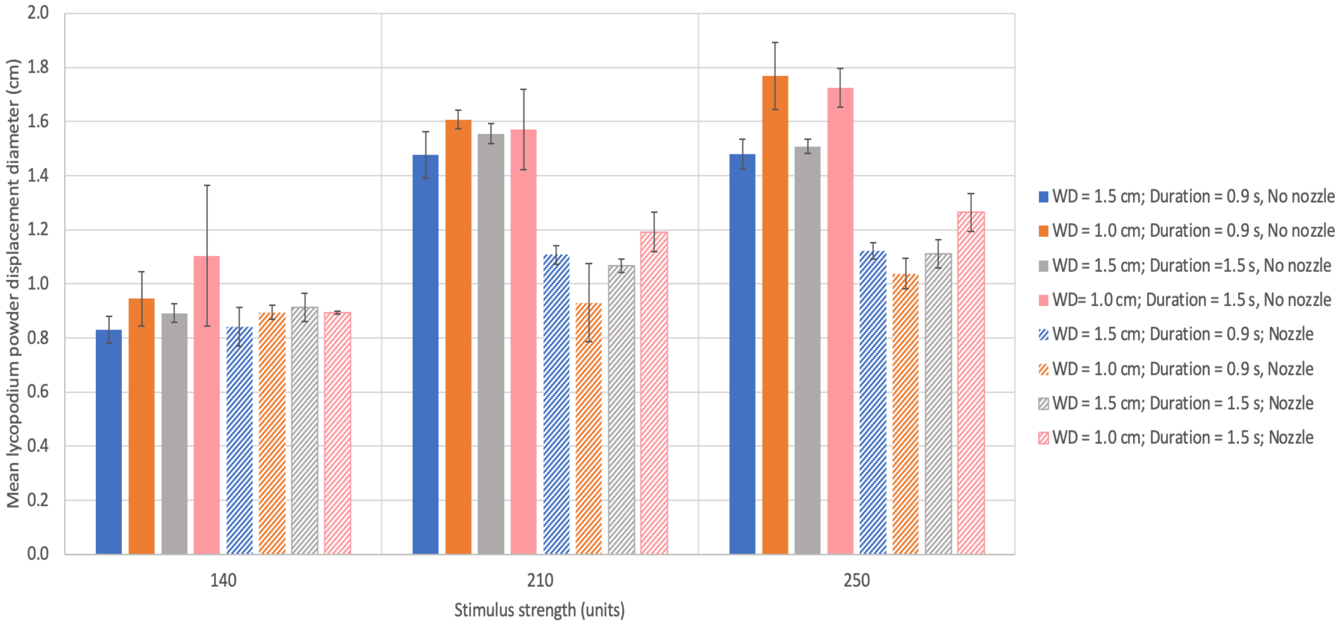

Figure 6.3: Mean powder displacement diameter (PDD) (cm) versus stimulus strengths (units) for various test/working distances (WD) and durations when no Tygon nozzle was attached to the exit air-jet of the Dolphin aesthesiometer (solid colours), and when a Tygon nozzle was attached (patterned). Error bars denote ± 1 standard deviation.

With respect to the nozzle cases, it should be noted that when the duration of the stimulus was 1.5 seconds, for the stimulus strength 250 units and test/working distance 1.5 cm combination, as well as the stimulus strength 210 units and test/working distance 1.0 cm combination, the mean PDD was calculated using three diameters rather than four due to the presence of an outlier.

Table 6.1 and Figure 6.3 show that as the stimulus strength increased, the PDD also increased. The figure also shows that duration had no effect on PDD since, for any given distance, the PDD when the duration is 0.9 and 1.5 seconds are equivalent. In addition, the closer the exit air-jet was to the surface of the lycopodium powder, the more dispersion occurred, and the PDD decreased when the nozzle was attached to the exit air-jet of the micro-blower.

Variables	Pearson Correlation r	p-values
Stimulus strength and powder displacement diameter (PDD)*	0.656	< 0.001
Test/working distance and powder displacement diameter (PDD)	-0.138	0.184
Duration and powder displacement diameter (PDD)	0.107	0.306
Nozzle and powder displacement diameter (PDD)*	-0.558	< 0.001

Table 6.2: Results of correlation analysis performed using JASP version 0.13.1 (significant results in blue*).

A Pearson correlation on the data showed a significant moderate positive association between stimulus strength and powder displacement diameter (PDD) ($R^2 = 0.43$, $p < 0.001$). The statistical analysis also showed a significant moderate negative association between nozzle and powder displacement diameter (PDD) ($R^2 = 0.311$, $p < 0.001$).

Multiple linear regression (using the entry method) showed that stimulus strength and the presence or absence of a nozzle could significantly predict the powder displacement diameter (PDD), $F(4, 89) = 70.072$, $p < 0.001$ using the regression equation:

Powder displacement diameter (PDD) = + 0.567 + 0.004 (strength) - 0.164 (distance) - 0.339 (nozzle) + 0.108 (duration), where nozzle is coded as 0 = no nozzle attached and 1 = a nozzle attached to the exit air-jet.

6.5 Experiment 2: Airflow dispersion for multiple micro-blowers

6.5.1 Purpose

To determine if there is a change in dispersion of the airflow produced by the Dolphin aesthesiometer when only stimulus strength is varied for each labelled micro-blower. This aids in determining the consistency between the three micro-blowers.

6.5.2 Procedure

Part A: Micro-blower without plastic nozzle

1. Using the same set-up of the equipment described in Section 5.3, the purple micro-blower was placed into the modified selfie stick holder and positioned 1 cm away from the powder surface. A stimulus duration of 0.9 seconds and stimulus strength of 250 units was set using the MLEO Dolphin management software. Once a crater was formed, the procedure was repeated so that for each stimulus strength there were two trials. After each stimulus release, the exit air-jet was realigned with a new testing location on the powder surface.
2. The stimulus strength was then changed to 210, 140, and 70 units, using the same 1 cm test/working distance and 0.9 seconds stimulus duration. The stimulus strengths were randomised in terms of the order of their delivery. The lycopodium displacement patterns were then photographed using a Nikon D50 DSLR camera.
3. The green labelled micro-blower was then placed into the holder and steps 1 to 2 was repeated.

Part B: Micro-blower with plastic nozzle

4. The entire experiment was repeated using a 1-inch long Tygon plastic nozzle attached to the exit air-jet of the purple and green micro-blowers. The 1 cm test/working distance was the same as that used in Part A, which was measured from the end of the nozzle to the surface of the powder.

6.5.3 Analyses

Data were tested for normality using the Shapiro-Wilk assumption test. A correlation analysis was performed on the normally distributed data, and subsequent linear regressions were executed. JASP version 0.13.1 (University of Amsterdam, Netherlands) was used for data analysis procedures. A probability value of 0.05 or less was considered to be statistically significant.

6.5.4 Results

As previously mentioned, there were some stimulus strengths in which no powder displacement was observed since the strength was too weak. Consequently, for Experiment 2, measurements for the stimulus strength of 70 units were omitted because it was difficult to observe any displacement.

Stimulus strength (units)	Distance from exit air-jet or nozzle to powder surface (cm)	Duration (seconds)	Nozzle	Micro-blower	Mean powder displacement diameter (PDD) (cm)	Standard deviation
140	1.0	0.9	0	1	1.62	0.01
210	1.0	0.9	0	1	2.11	0.03
250	1.0	0.9	0	1	2.25	0.02
140	1.0	0.9	0	0	1.42	0.03
210	1.0	0.9	0	0	1.95	0.03
250	1.0	0.9	0	0	2.04	0.03
140	1.0	0.9	0	-1	1.32	0.04
210	1.0	0.9	0	-1	1.76	0.08
250	1.0	0.9	0	-1	2.00	0.04
140	1.0	0.9	1	1	0.89	0.03
210	1.0	0.9	1	1	0.93	0.15
250	1.0	0.9	1	1	1.04	0.06
140	1.0	0.9	1	0	0.84	0.04
210	1.0	0.9	1	0	1.21	0.01
250	1.0	0.9	1	0	1.29	0.01
140	1.0	0.9	1	-1	0.65	0.05
210	1.0	0.9	1	-1	0.74	0.03
250	1.0	0.9	1	-1	1.07	0.10

Table 6.3: Mean diameter for the different stimulus strengths and micro-blowers for Part A and B. It should be noted that nozzle is coded as: 0 = no nozzle attached and 1 = nozzle attached to the exit air-jet; and the micro-blowers are coded as: 0 = yellow, 1 = purple, and -1 = green.

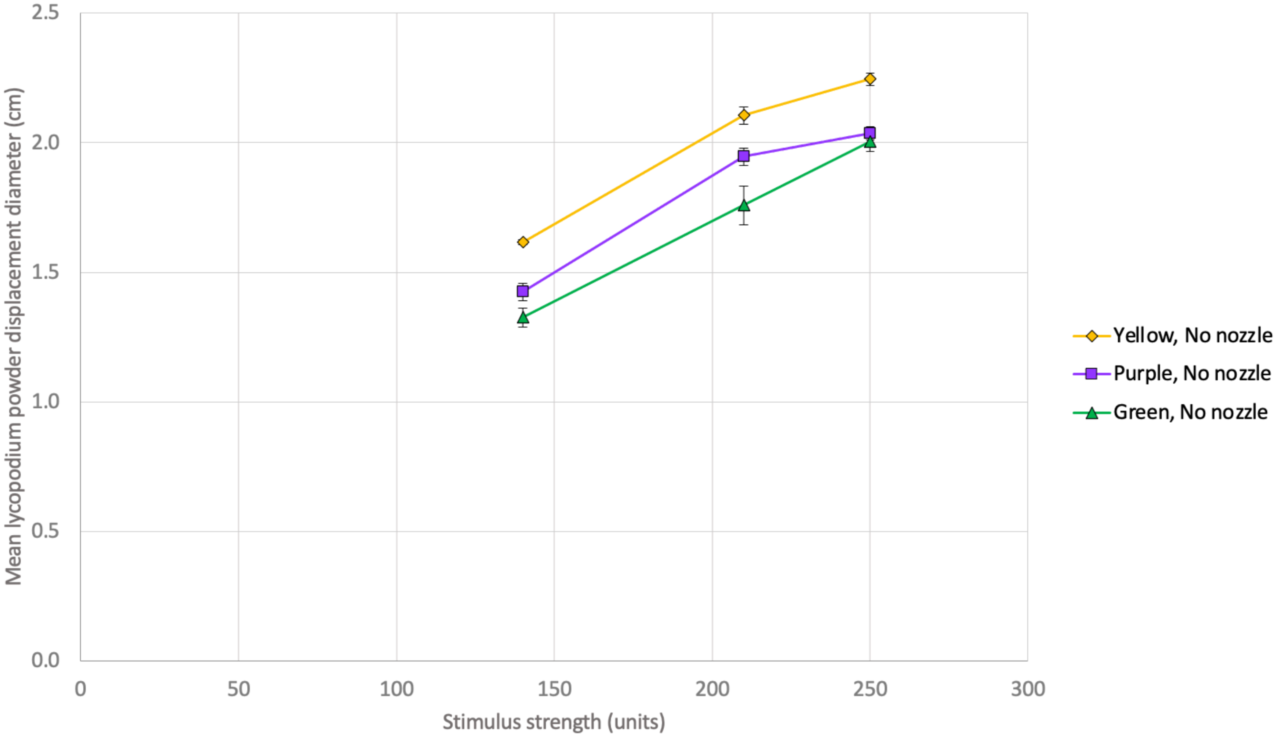

Figure 6.4: Mean powder displacement diameter (PDD) (cm) versus stimulus strengths (units) for the three micro-blowers (working distance: 1 cm and duration: 0.9 seconds) when no Tygon nozzle was attached to the exit air-jet of the Dolphin aesthesiometer. Error bars denote ± 1 standard deviation.

It is important to note that when the stimulus strength was 250 units for both the yellow and green blowers, the mean PDD was calculated using three diameters rather than four due to the presence of an outlier.

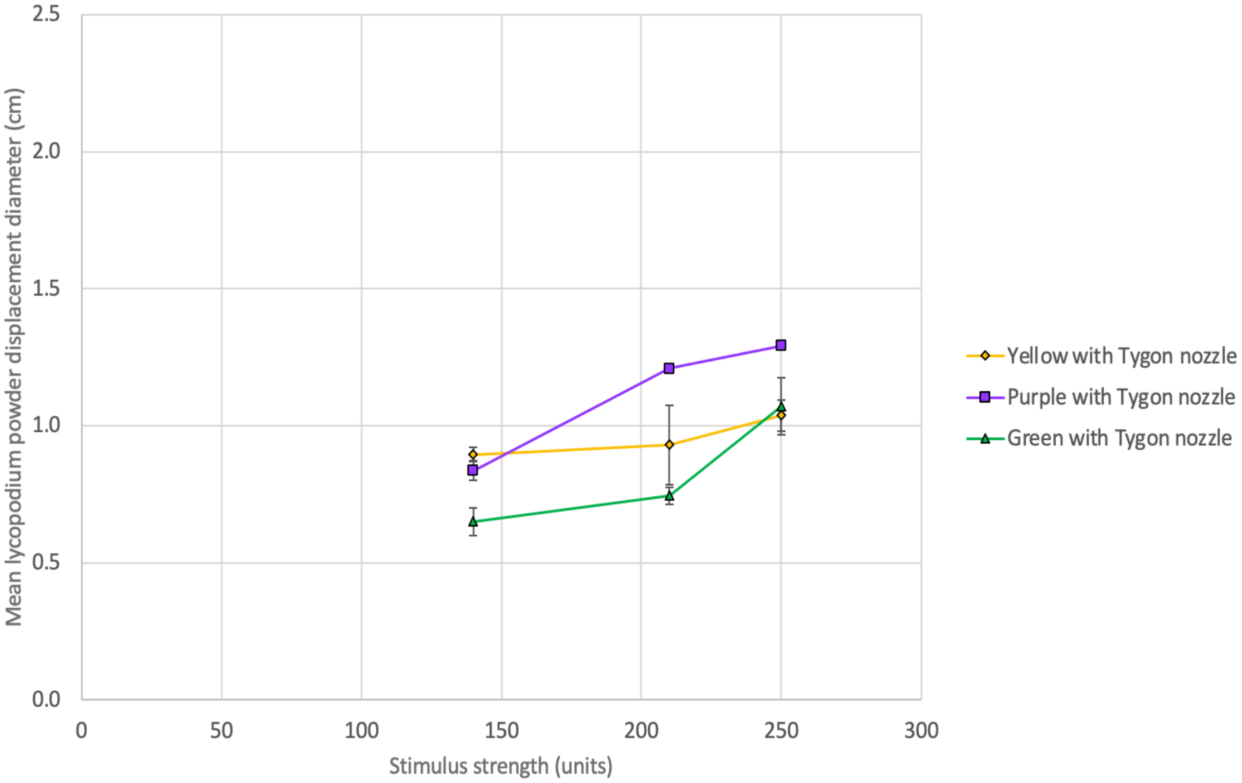

Figure 6.5: Mean powder displacement diameter (PDD) (cm) versus stimulus strengths (units) for the three micro-blowers (working distance: 1 cm and duration: 0.9 seconds) when a Tygon nozzle was attached to the exit air-jet of the Dolphin aesthesiometer. Error bars denote ± 1 standard deviation.

Table 6.3, and Figures 6.4 and 6.5, show that as the stimulus strength increased the powder displacement diameter (PDD) increased for all micro-blower types. The PPDs were reduced (approximately halved) when a nozzle was attached to the exit air-jet to the Dolphin aesthesiometer.

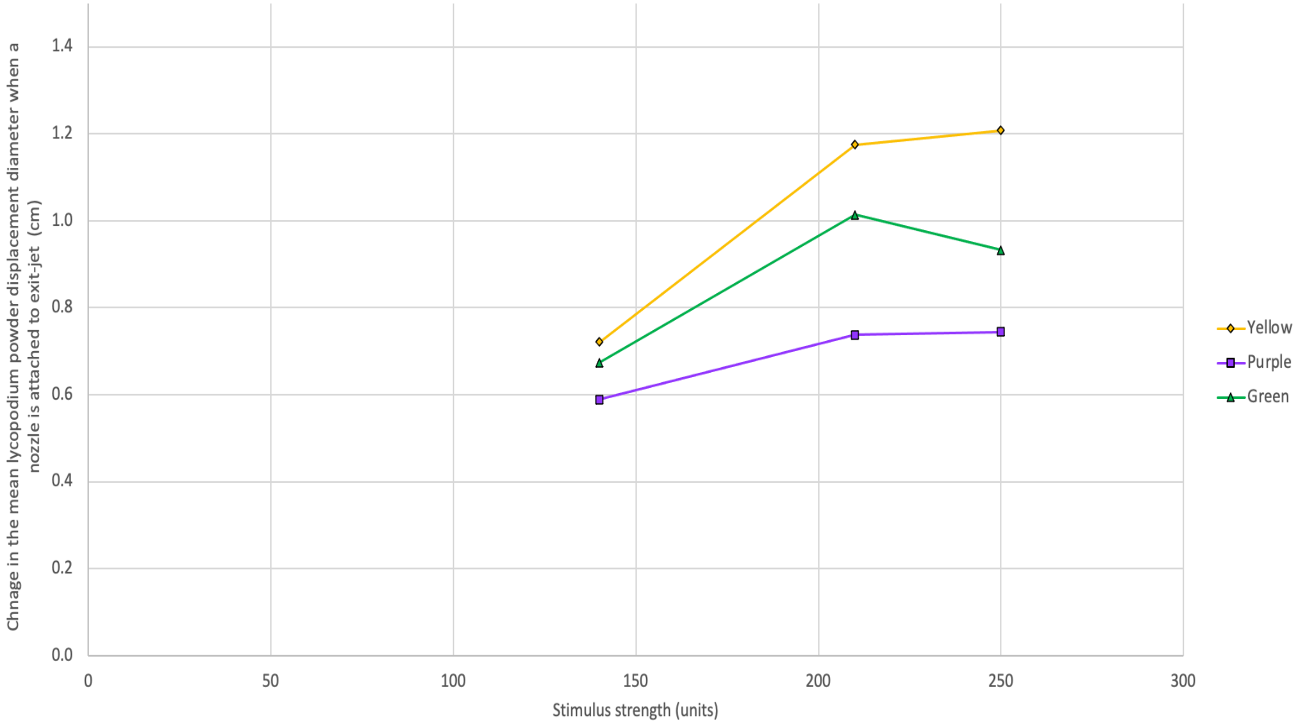

Figure 6.6: Change in mean powder displacement diameter (PDD) (cm) versus stimulus strengths (units) for the three micro-blowers (test/working distance: 1 cm and duration: 0.9 seconds) when a Tygon nozzle was attached to the exit air-jet of the Dolphin aesthesiometer.

It is important to note that when no nozzle was attached, and the stimulus strength was 250 units for both the yellow and green blowers, the mean PDD was calculated using three diameters rather than four due to the presence of an outlier.

Figure 6.6 shows that when a nozzle was attached to the exit air-jet of the aesthesiometer and as the stimulus strength increased, the change in PDD was highest for the yellow micro-blower and lowest for the purple micro-blower.

Variables	**Pearson Correlation r**	**p-values**
Stimulus strength and powder displacement diameter (PDD)*	0.376	0.001
Nozzle and powder displacement diameter (PDD)*	-0.857	< 0.001
Micro-blower type and powder displacement diameter (PDD)	0.173	0.152

Table 6.4: Results of correlation analysis performed using JASP version 0.13.1 (significant results in blue*).

A Pearson correlation on the data showed a significant positive association between stimulus strength and powder displacement diameter (PDD) ($R^2 = 0.14$, $p = 0.001$). The statistical analysis also showed a significant negative association between nozzle and powder displacement diameter (PDD) ($R^2 = 0.73$, $p < 0.001$).

Multiple linear regression (using the entry method) showed that stimulus strength, micro-blower type, and the presence or absence of a nozzle could significantly predict the powder displacement diameter (PDD), F (3, 66) = 277.999, $p < 0.001$ using the regression equation:

Powder displacement diameter (PDD) = + 0.941 + 0.004 (strength) - 0.862 (nozzle) + 0.106 (micro-blower type) where nozzle was coded as 0 = no nozzle attached and 1 = a nozzle attached to the exit air-jet; and the micro-blowers were coded as 0 = yellow, 1 = purple, and -1 = green.

6.6 Discussion

This study showed that when the airflow stimulus came into contact with a surface it disperses. The PDD increased as the stimulus strength increased, because higher airflow rates are able to penetrate more powder and hence displace more of it. Stimulus duration did not however have an effect on PDD as seen in Table 6.1 and Figure 6.3, and this trend was further supported by the results of the statistical analyses. The correlation analysis for Experiment 1 (where the PDD produced by the device was measured at various stimulus strengths, stimulus durations, and test distances), showed that PDD was associated with stimulus strength, and the presence or absence of the plastic nozzle. In fact, the stimulus strength had the greatest influence, as given by Pearson correlation r. This indicated that when the airflow was extended by increasing the duration of the stimulus, no additional dispersion occurred. As a result, the crater was formed by the initial impact of the air puff on the surface of the powder. These findings are in keeping with similar experiments performed using the Non-Contact Corneal Aesthesiometer (NCCA) (Murphy, 1996).

In Experiment 2, where the change in PDD was measured for three different micro-blowers with varying stimulus strength, it was revealed that the presence or absence of the plastic nozzle had the greatest influence, based on the Pearson correlation r, and the coefficients of the regression equation. The previous chapter (airflow dispersion in air study) showed that when the plastic nozzle was attached to the exit air-jet of the micro-blower it altered the rate of airflow. More specifically, it narrowed the area in which the air could flow, and consequently decreased the flow rate. The nozzle also affected the in-air dispersion of the airflow, namely the coherence of the airflow. However, in the case of this experiment, the altered rate of airflow had the greatest effect on the displacement of the powder, and resulted in less powder being displaced. It is therefore important to indicate if a nozzle is used with the instrument, especially when reporting threshold measurements.

Furthermore, the diameter of the cornea is considered to be the limbus-to-limbus distance. The normative corneal diameter of the adult human is 11 mm (horizontally) and 12 mm (vertically) (Mashige, 2013). From an aesthesiometry perspective, given that the diameters measured with the Dolphin aesthesiometer are only less than the normative corneal diameter when the stimulus strength was <140 units for non-nozzle cases, and <250 units once a nozzle was attached (Table 6.1), then in order to ensure that only corneal nerves are stimulated, and not the eyelid margin or conjunctiva, it is best to have a nozzle attached to the exit air-jet of the aesthesiometer.

Theoretically, the test/working distance should not affect the dispersion of the powder, since the ratio of the width of the jet to the surface of the powder, the rate of change of momentum, and hence the force applied should be constant regardless of the test/working distance (See Figure 5.1 in Chapter 5). However, Figure 6.3 showed that the closer the exit air-jet was to the surface of the lycopodium powder the more dispersion occurred. Despite noting this systematic change, the relationship between the test/working distance and the amount of dispersion was not statistically significant. The systematic change in dispersion as test/working distance varies could be a consequence of the experimental set-up, which will be further discussed below. However, it is important to note that, from an aesthesiometry perspective, whereby the surface of the powder is replaced with an eye or a model eye, the force would be expected to decrease as the test/working distance increases, thus resulting in less dispersion. This would be due to the decay of the center speed of the jet at further distances and hence the reduction of force, which is dependent on the speed (S. Peterson, personal communication, March 3, 2021; White, 2006).

The regression analyses also showed that PDD could be predicted by stimulus strength, the presence or absence of the plastic nozzle, and by the micro-blower used.The PDDs produced for each experiment were consistent with little variability, as reported by the small error bars. However, it is important to address the larger than usual error bars that arose for some test combinations. These errors may be due to a lack of powder thickness standardization and/or movement of the nozzle. Despite efforts to control the amount of powder used (by using the same mass of powder for each test), as well as the thickness of the layer of the powder after each test, there was no real quantitative standardization of the thickness of the powder. It is therefore possible that, in some cases, more powder may have had to be dispersed before an effect was observed (Murphy, 1996). In addition, whilst the nozzle attachment was checked between tests, it is possible that it may have moved given the flexibility of the material it is made of, which would mean a loss in exit air-jet velocity, momentum, and hence the force applied to the surface of the powder. However, even though the error bars are larger than the others, they are still considered to be small.

Figures 6.4 and 6.5 show that at each stimulus strength, the PDDs produced by the micro-blowers differ by approximately 1 cm or less from one another. This suggests that the micro-blowers are producing similar stimuli, and therefore the variability is small compared to the local variation seen in the measures of corneal thresholds in human subjects.

When no nozzle was attached to the instrument, the yellow micro-blower produced larger displacement diameters, whereas the green micro-blower produced slightly smaller ones. Conversely, with the nozzle attached to the exit air-jet, the purple micro-blower produced larger displacement diameters and the green micro-blower produced slightly smaller ones. These differences are noticeable in Figure 6.6, where the change in PDD when a nozzle was attached to the exit air-jet was plotted against stimulus strength for the three micro-blowers. It is difficult to explain this trend. It could be a consequence of the experimental set-up, namely the aforementioned effects of the nozzle movement. However, it is more likely due to the fact that the output voltage of the yellow micro-blower is higher, and it therefore receives more power from the power source as revealed in the software studies in Chapter 4. Whilst such variations in PDDs and output voltages between the micro-blowers are quite small, they may still need to be considered when calibrating the instrument, and this will be further discussed in Chapter 10 (overview and future works).

Murphy (1996) conducted a similar study using lycopodium powder to examine the effect of stimulus pressure produced by the NCCA on the dispersion of air when it comes into contact with a surface. Several air-jet diameters, test/working distances, and stimulus durations were used. Murphy (1996) used nozzle attachments of 1.0 and 1.5 mm, and found that the mean PDDs were between 0.28 and 0.56 cm; and 0.23 to 0.54 cm respectively when the test/working distance was 1 cm and the stimulus duration lasted 0.9 seconds (Murphy, 1996). The diameter of the exit air-jet of the micro-blower is 0.86 mm, and the diameter of the Tygon tubing is 1.59 mm. When a test/working distance of 1 cm and stimulus duration of 0.9 seconds was used, the mean PDDs produced by the Dolphin aesthesiometer ranged from 0.95 to 2.11 cm when the no nozzle was attached, and ranged from 0.65 to 1.39 cm when the Tygon nozzle was attached to the instrument. Whilst the nozzle diameters used for the NCCA and the Dolphin aesthesiometer are different, therefore making it difficult to reliably compare findings, it is evident that the Dolphin aesthesiometer produces more dispersion.

Lastly, in Chapter 5 where the airflow dispersion in air was studied, saturation appeared to occur at lower stimulus strengths for non-nozzle cases compared to nozzle cases (Figures 5.3 and 5.4). It was suggested in Chapter 5 that since the nozzle decreases the flow rate, the distances and widths for cases when the strength was 140 units and no nozzle was attached should actually be similar to that of cases where the strength was 210 units and a nozzle was attached. This explanation is strongly supported by the results of the mean powder displacement diameters (PDDs) measured in this experiment, and Table 6.5 below provides a summary of the comparisons of such cases.

Stimulus strength (units)	Duration (seconds)	Distance from exit air-jet or nozzle to powder surface (cm)	Nozzle	Mean powder displacement diameter (cm)	Standard deviation
140	0.9	1.5	0	0.83	0.05
140	1.5	1.5	0	0.89	0.03
140	0.9	1.0	0	0.94	0.10
210	0.9	1.5	1	1.11	0.03
210	1.5	1.5	1	1.07	0.02
210	0.9	1.0	1	0.93	0.15

Table 6.5: Mean powder displacement diameter for various stimulus strengths, test/working distances, and durations taken from Chapter 6.

Table 6.5 shows that when the strength of the stimulus was 140 units and no nozzle was attached, the powder displacement diameter (PDD) was 0.94 cm, and when the strength was 210 units with a nozzle applied, the PDD was 0.93. Therefore, both nozzle and non-nozzle cases were saturated for all stimulus strengths in Chapter 5.

6.7 Conclusion

The results of the experiment confirm that when the airflow comes into contact with a surface it disperses. However dispersion is reduced when a nozzle was applied to the instrument, and the nozzle will be necessary to ensure that only the corneal nerves are stimulated in future *in vivo* aesthesiometry studies. This experiment also showed that the micro-blowers produced similar stimuli. Further studies aimed at learning more about the mode of the stimulus can be performed.

CHAPTER 7: STIMULUS CHARACTERISTICS, FORCE

7.1 Purpose and hypotheses

7.1.1 Purpose

To measure the force exerted by the air stimulus of the Dolphin aesthesiometer at various stimulus strengths, durations of air puff, and test/working distances using a digital microbalance. This will aid in determining the consistency of the hardware, and hence the stimulus, as well as help to characterise the mode of stimulus.

7.1.2 Hypotheses

1. The steady state force (SSF) (average force) and the peak force (PF) (maximum force) will increase as the stimulus strength increases and decrease when a nozzle is attached, but will not be influenced by either the duration or test distance.
2. Forces measured will be consistent and repeatable.

7.2 Background

Chapters 4 to 6 confirmed that the software control system of the Dolphin aesthesiometer was accurate, the airflow was coherent with a constant spread rate, and when it came into contact with a surface it dispersed. Having learned about these properties of the instrument and the airflow it produces, it is important to investigate more about the stimulus. More specifically, its mode of stimulation.

As described in Section 2.6 of the Literature review, non-invasive gas-jet aesthesiometers, such as the Dolphin Aesthesiometer, use a pulse of air or gas directed at the ocular surface to produce a stimulus for the sensory nerves. However, it is unclear whether the sensory response is due to a tactile element of the stimulus caused by surface deformation of the cornea produced by the impact of the airflow, and/or by localised cooling caused by increased evaporation from the tear film over the area of the cornea that the airflow spreads (Murphy et al., 1996, Murphy et al., 1998; Murphy et al., 1999b).

In order to verify and/or measure the force component of the airflow of previous gas-jet aesthesiometers, several *in vivo* and *in vitro* methods have been used. Murphy et al. (1999b) instilled sodium fluorescein into the eye and applied a high pressure airflow from the Non-Contact Corneal Aesthesiometer (NCCA) to the corneal surface. The tear film was observed using the cobalt blue filter and the binocular viewing system of a slit-lamp biomicroscope. It was expected that at high intensities, the tear film would appear to be distorted. However, no such distortion was observed. Having previously verified the thermal component of the stimulus, the authors confirmed that any surface distortion component of the stimulus generated by the NCCA was small (Murphy et al., 1999b; Nosch, 2015). Similarly, Nosch (2015) used high-speed photography to determine if the corneal deformation occurred when a high intensity stimulus from the NCCA was applied perpendicularly to a true cornea 1 cm away. She directed a light source onto the center of the cornea, causing a light reflex, which would be distorted if the stimulus caused deformation. However, no distortion occurred, thus further confirming that the force component of the stimulus generated by the NCCA was indeed small (Nosch, 2015).

Lum (2014) measured the non-invasive force produced by the Belmonte Ocular Pain Meter (BOPM) gas-jet aesthesiometer using an analytical microbalance. The air-jet of the instrument was positioned 0.5 cm from the plate of the microbalance, and a continuous flow of gas of varying airflow rates was produced for 60 seconds. The entire air-jet and microbalance system was in a glass casing in order to reduce turbulent interferences, and the maximum force exerted onto the microbalance was measured. Using the same procedure and equipment, force measurements were performed using the

Non-Contact Corneal Aesthesiometer (NCCA). Two nozzle sizes and two test/working distances were used. The stimulus was applied to the microbalance for 9.9 seconds, and the stimulus intensity was varied. The results revealed that the force of the stimulus generated by both aesthesiometers was quadratically related to the airflow rate, and the force increased when no nozzle was used. Furthermore, decreasing the nozzle diameter resulted in higher forces being applied to the microbalance, and that increasing the test/working distance decreased the force applied, as energy from the gas-jet was lost, and hence the velocity of the airflow was reduced with increasing distance from its exit air-jet. The studies also concluded that the force exerted by the NCCA was smaller than that of the BOPM for similar airflow rates. Nosch (2015) performed a similar study with the BOPM using the same experimental set-up. However, the test/working distance between the air-jet and the plate of the microbalance was 0.4 cm, and the stimulus was applied to the plate for 20 seconds. She found a linear progression, whereby the force increased with increasing airflow rates.

The aim of this study was to determine if the stimulus generated by the Dolphin aesthesiometer had a force component, which may mean that the air pulse has the potential to stimulate the mechanically sensitive Aδ fibers. Furthermore, if force was determined to be a mode of stimulation, it was important to verify if the stimulus was produced with a consistent level of force. To measure the force, a microbalance was used. From the results of Chapter 6 it was anticipated that when the airflow stimulus encountered the sample plate of the microbalance, the airflow would be dispersed, but that the spread rate would be constant for each airflow rate. Since the force applied by the stimulus is proportional to the airflow rate, and hence the stimulus strength of the instrument, it follows that the force produced by the stimulus of the Dolphin aesthesiometer could be measured using a microbalance of high precision (Lum, 2014).

With respect to the stimulus parameters, such as test/working distance and stimulus duration, the literature has been inconsistent. This is partly due to the fact that there are different aesthesiometer designs. Murphy et al. used a test/working distance of 1 cm and stimulus duration of 1 second with the Non-Contact Corneal Aesthesiometer (NCCA) (Murphy, 1996; Murphy et al., 1999a; Nosch, et al., 2017). Based on this previous use, the exit air-jet was first positioned 1 cm away from the microbalance plate.

7.3 Methods

A retort stand was used to hold a selfie stick that had been modified to house the yellow micro-blower of the Dolphin aesthesiometer. The exit air-jet of the micro-blower was positioned vertically above and perpendicular to the plate of the microbalance (Mettler Toledo AB265-S/FACT) (precision: 0.0001 g) (Figures 7.1 and 7.2). The microbalance was calibrated before taking measurements using a range of standard weights from 1 mg to 100 g. The plate of the microbalance was enclosed within a glass box that came to reduce the effect of external room turbulences, which could have affected the measurements. However, the main part of the retort stand had to be placed outside the glass box and to the side of the scale, while the selfie stick holding the micro-blower extended inside the glass casing. Consequently, one side of the glass box had to remain partially open.

A series of air-puffs were then applied to the microbalance plate and the deflection in the weighing scale observed. A stimulus duration of 10 seconds was selected in order to provide enough time for the airflow to interact with the microbalance, and therefore provide a stable output. By using an Android Smartphone, the digital mass values on the scale were video recorded during the period of each stimulus presentation. Recording began approximately 5 seconds before the stimulus was released and lasted until the stimulus had stopped. Each stimulus strength, duration, and test/working distance combination was tested nine times to produce an average result. All masses registered by the microbalance were converted to force as explained below.

The airflow against the microbalance produced a consistent waveform of response. There was an initial rapid rise to a maximum force (peak force) followed by a recovery to a period of stability when the mass was relatively consistent (stability force plateau), and finally a recovery to baseline with the removal of the airflow (Figure 7.3).

To determine the maximum/peak force (PF), the maximum/peak mass exerted by the exit air-jet onto the microbalance was obtained from the video recordings by replaying the scale measurements. It was simply the highest mass registered by the digital output screen of the scale. The results were recorded in a pre-designed Microsoft Excel test matrix, converted to force using g (gravitational acceleration) = 9.8 ms^{-2}, and then the resulting peak forces were averaged for analysis. The peak force was used as a proxy for the impulse (the initial force applied to the scale when the airflow first makes contact with it) since there was no reliable temporal information to compute the impulse.

The average steady state force (SSF) was determined by first measuring the mass registered by the microbalance at three points during the stability plateau, which occurred after the peak mass. In order to have some form of standardization when selecting these three points, and given that the stimulus only lasted for 10 seconds, the mass was taken: 1 second after the peak mass where the steady state first began (point A), 5 seconds after the air puff started to have a measure of the steady state between the start and end of the stability plateau (point B), and the last mass registered on the scale before the digital output values start descending to zero, and hence when the steady state process ended (point C). However for cases where the stimulus duration was 5 seconds long, the mass measured for point B was measured 3 seconds after the air puff started) (Figure 7.3). The mass at each of the three points were converted to force and then averaged for analysis, so that the average steady state force for any particular stimulus strength, test/working distance, and duration combination was a result of the measurements at points A to C. Figure 7.3 illustrates the profile of the change in force during the time the airflow is applied to the microbalance. The steady state force is equivalent to the average force generated by the instrument.

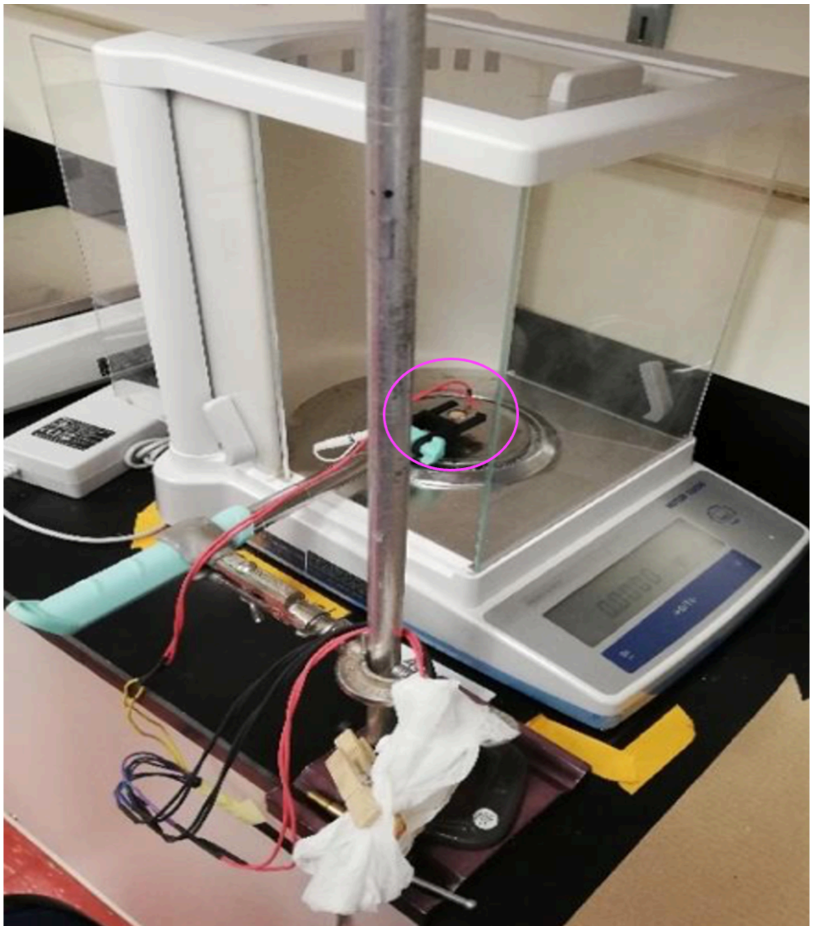

Figure 7.1: Equipment set-up showing the position of the retort stand and modified selfie stick with the micro-blower (pink circle) in relation to the microbalance and microbalance chamber.

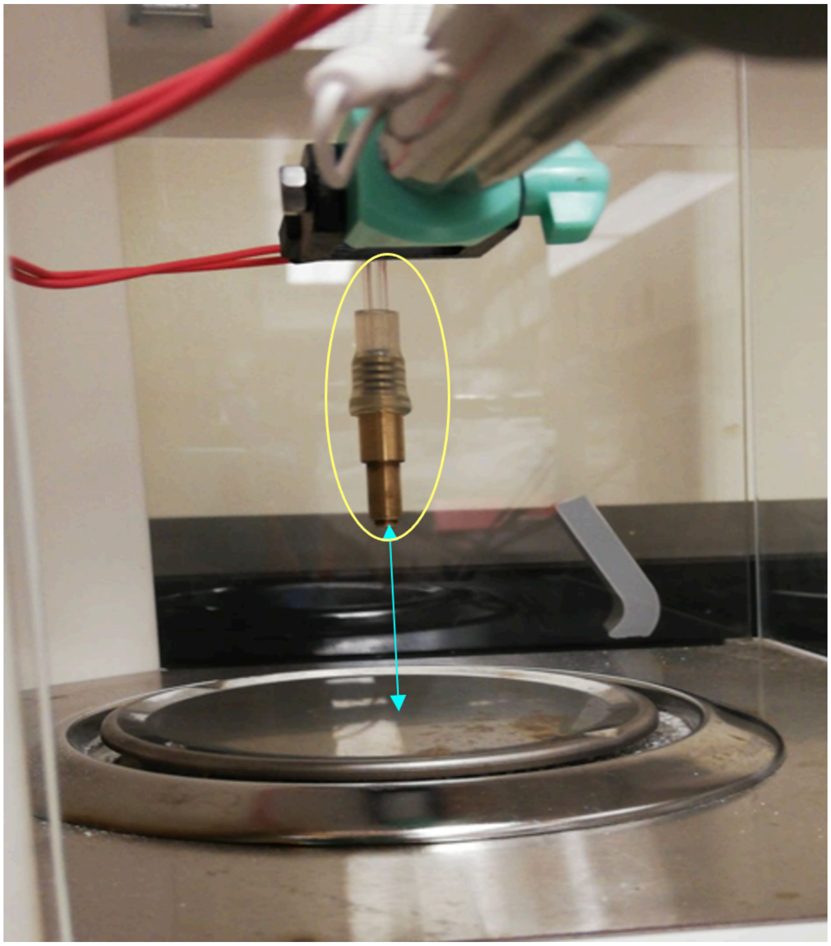

Figure 7.2: Equipment set-up showing a magnified view of the micro-blower with the brass nozzle attached to the exit air-jet (entire modified nozzle system in yellow circle) and directed towards the microbalance plate. The test/working distance (blue arrow) is the distance from the exit of the brass nozzle to the microbalance plate.

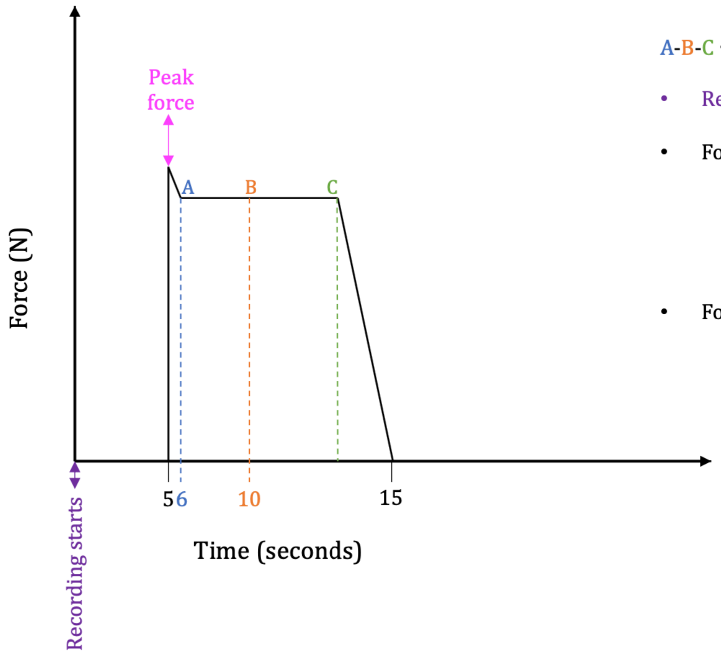

A-B-C → Steady state force

- Recording starts 5 seconds before the stimulus is released.
- For a stimulus duration of **10** seconds:
    - A = 1 second after peak force
    - B = 5 seconds after air puff started
    - C = Last force on the scale before the values start descending to zero.
- For a stimulus duration of **5** seconds:
    - A = 1 second after peak force
    - B = 3 seconds after air puff started
    - C = Last force on the scale before the values start descending to zero.

Figure 7.3: Illustration of the force profile showing the peak/maximum force and stability plateau used to determine the steady state force when a stimulus is applied for 10 seconds long. For the steady state force, the mass was taken at three points and converted to force using g (gravitational acceleration) = 9.8 ms^{-2}.

Point A was 1 second after the peak mass, point B was 5 seconds after the air puff started, and point C was the last mass on the scale before the values start descending to zero. When the stimulus duration was reduced from 10 seconds to 5 seconds, the mass measured at point B was 3 seconds after the air puff started.

It should also be noted that all of the connections between the apparatus were disconnected and reconnected at random intervals throughout the experiment in order to reduce systematic errors (errors that are repeatable from measurement to measurement).

7.4 Microbalance and single puffs

7.4.1 Purpose

To measure the force exerted by the air stimulus of the Dolphin aesthesiometer at various stimulus strengths, durations of air puff, and test/working distances using a digital microbalance.

7.4.2 Procedure

Part A: Micro-blower without plastic nozzle

1. The MLEO Dolphin management software was set to deliver a single air-puff of stimulus strength 250, 210, 140 or 70 units for a stimulus duration of 10 seconds, and test/working distance of 1 cm. The stimulus strengths were randomised in terms of the order of their delivery.
2. The test/working distance was then changed to 3 cm and 1.5 cm and step 1 repeated for each test/working distance, respectively.
3. The stimulus duration was then changed to 5 seconds and steps 1 and 2 were repeated.

Part B: Micro-blower with plastic nozzle

4. The entire experiment was then repeated using a nozzle system that was modified to offer more control of the stimulus as compared to the Tygon nozzle used in previous chapters. This modified system consisted of a brass nozzle (internal diameter: 0.05 cm) that was connected to a 1-inch long section of Tygon tubing (internal diameter 0.16 cm) using a 2.2 cm long silicone adapter. In turn, the Tygon tubing was connected to the micro-blower exit air-jet. For these experiments, the test/working distance refers to the distance from the brass nozzle exit to the microbalance plate.

7.4.3 Analyses

Data were tested for normality using the Shapiro-Wilk assumption test. A correlation analysis was performed on the normally distributed data, and subsequent linear regressions were executed. JASP version 0.13.1 (University of Amsterdam, Netherlands) was used for data analysis procedures. A probability value of 0.05 or less was considered to be statistically significant.

7.4.4 Results

Stimulus strength (units)	Duration (seconds)	Test/Working distance (cm)	Nozzle	Mean peak force (N)	Standard deviation	Mean steady state or stability force (N)	Standard deviation
70	10	3.0	0	7.34E-05	1.99E-06	7.09E-05	2.02E-06
140	10	3.0	0	4.31E-04	1.12E-05	4.08E-04	1.75E-05
210	10	3.0	0	8.43E-04	1.92E-05	7.95E-04	3.42E-05
250	10	3.0	0	9.49E-04	4.11E-05	9.17E-04	5.20E-05
70	10	1.5	0	6.30E-05	9.80E-07	6.00E-05	1.61E-06
140	10	1.5	0	3.56E-04	7.89E-06	3.28E-04	1.61E-05
210	10	1.5	0	6.80E-04	2.05E-05	6.29E-04	3.83E-05
250	10	1.5	0	7.76E-04	2.47E-05	7.20E-04	5.16E-05
70	10	1.0	0	5.96E-05	1.18E-06	5.71E-05	1.75E-06
140	10	1.0	0	3.29E-04	5.52E-06	3.05E-04	1.23E-05
210	10	1.0	0	5.41E-04	1.70E-05	5.07E-04	2.11E-05
250	10	1.0	0	6.15E-04	1.80E-05	5.90E-04	3.05E-05
70	5	3.0	0	7.30E-05	1.56E-06	7.13E-05	7.24E-05
140	5	3.0	0	4.42E-04	1.33E-05	4.11E-04	1.49E-05
210	5	3.0	0	8.52E-04	7.91E-06	8.08E-04	3.32E-05
250	5	3.0	0	9.54E-04	3.41E-05	9.39E-04	4.56E-05
70	5	1.5	0	6.42E-05	9.94E-07	6.05E-05	1.61E-06
140	5	1.5	0	3.56E-04	6.43E-06	3.33E-04	1.07E-05
210	5	1.5	0	6.92E-04	2.15E-05	6.75E-04	2.70E-05
250	5	1.5	0	7.83E-04	2.23E-05	6.12E-04	3.06E-04
70	5	1.0	0	6.07E-05	1.80E-06	6.07E-05	1.03E-06
140	5	1.0	0	3.32E-04	8.66E-06	3.08E-04	7.73E-06
210	5	1.0	0	5.62E-04	1.48E-05	5.25E-04	1.78E-05
250	5	1.0	0	6.33E-04	1.99E-05	6.09E-04	2.62E-05
70	10	3.0	1	2.00E-05	8.64E-07	1.84E-05	1.18E-06
140	10	3.0	1	1.50E-04	4.59E-06	1.39E-04	7.77E-06
210	10	3.0	1	3.20E-04	1.54E-05	3.09E-04	1.23E-05
250	10	3.0	1	3.87E-04	1.92E-05	3.77E-04	2.20E-05
70	10	1.5	1	1.86E-05	1.10E-06	1.83E-05	1.30E-06
140	10	1.5	1	1.40E-04	1.63E-06	1.27E-04	7.59E-06
210	10	1.5	1	3.01E-04	5.32E-06	2.80E-04	1.23E-05
250	10	1.5	1	3.53E-04	1.54E-05	3.18E-04	3.16E-05
70	10	1.0	1	2.07E-05	7.66E-07	1.92E-05	8.64E-07
140	10	1.0	1	1.39E-04	2.08E-06	1.27E-04	6.26E-06
210	10	1.0	1	2.92E-04	7.10E-06	2.67E-04	1.64E-05
250	10	1.0	1	3.33E-04	1.38E-05	3.24E-04	2.32E-05
70	5	3.0	1	2.28E-05	6.53E-07	2.18E-05	6.16E-07
140	5	3.0	1	1.57E-04	2.66E-06	1.53E-04	6.31E-06
210	5	3.0	1	3.40E-04	7.01E-06	3.29E-04	1.26E-05
250	5	3.0	1	3.90E-04	1.04E-05	3.69E-04	1.53E-05
70	5	1.5	1	1.95E-05	9.09E-07	1.84E-05	4.32E-07
140	5	1.5	1	1.48E-04	2.08E-06	1.41E-04	5.41E-06
210	5	1.5	1	3.11E-04	7.98E-06	3.04E-04	1.26E-05
250	5	1.5	1	3.55E-04	1.13E-05	3.56E-04	1.39E-05
70	5	1.0	1	2.08E-05	6.53E-07	2.03E-05	1.30E-06
140	5	1.0	1	1.46E-04	3.46E-06	1.36E-04	5.22E-06
210	5	1.0	1	3.07E-04	5.33E-06	2.88E-04	1.19E-05
250	5	1.0	1	3.48E-04	1.04E-05	3.46E-04	1.25E-05

Table 7.1: Mean peak force and steady state or stability force for different stimulus strengths, durations, and distances from the microbalance. Nozzle is coded as 0 = no nozzle attached and 1 = nozzle attached to the exit air-jet.

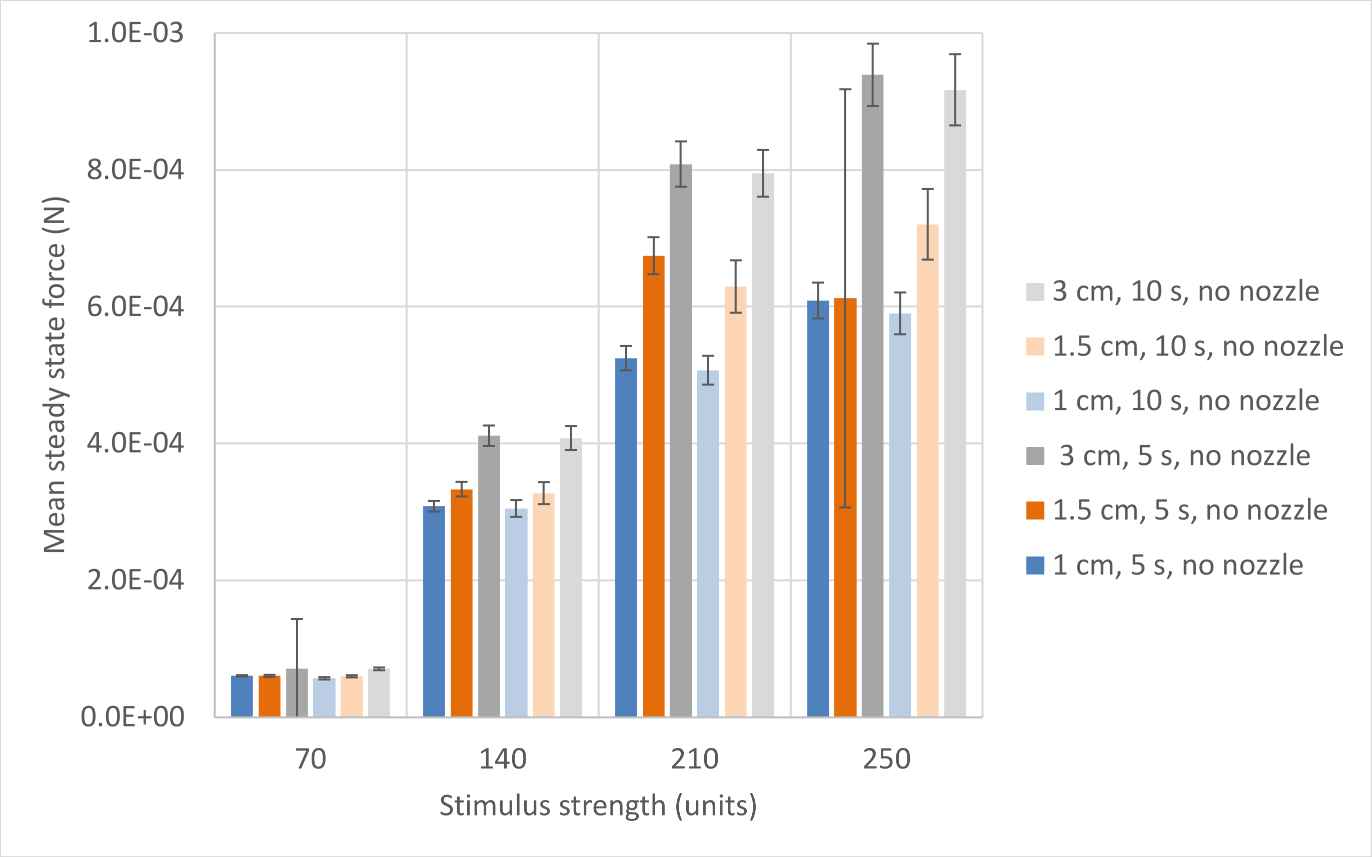

Figure 7.4: Graph of mean steady state force (N) versus stimulus strength (units) for different combinations of stimulus duration and test/working distance, when <u>no nozzle</u> was attached to micro-blower exit air-jet. Error bars denote ± 1 standard deviation.

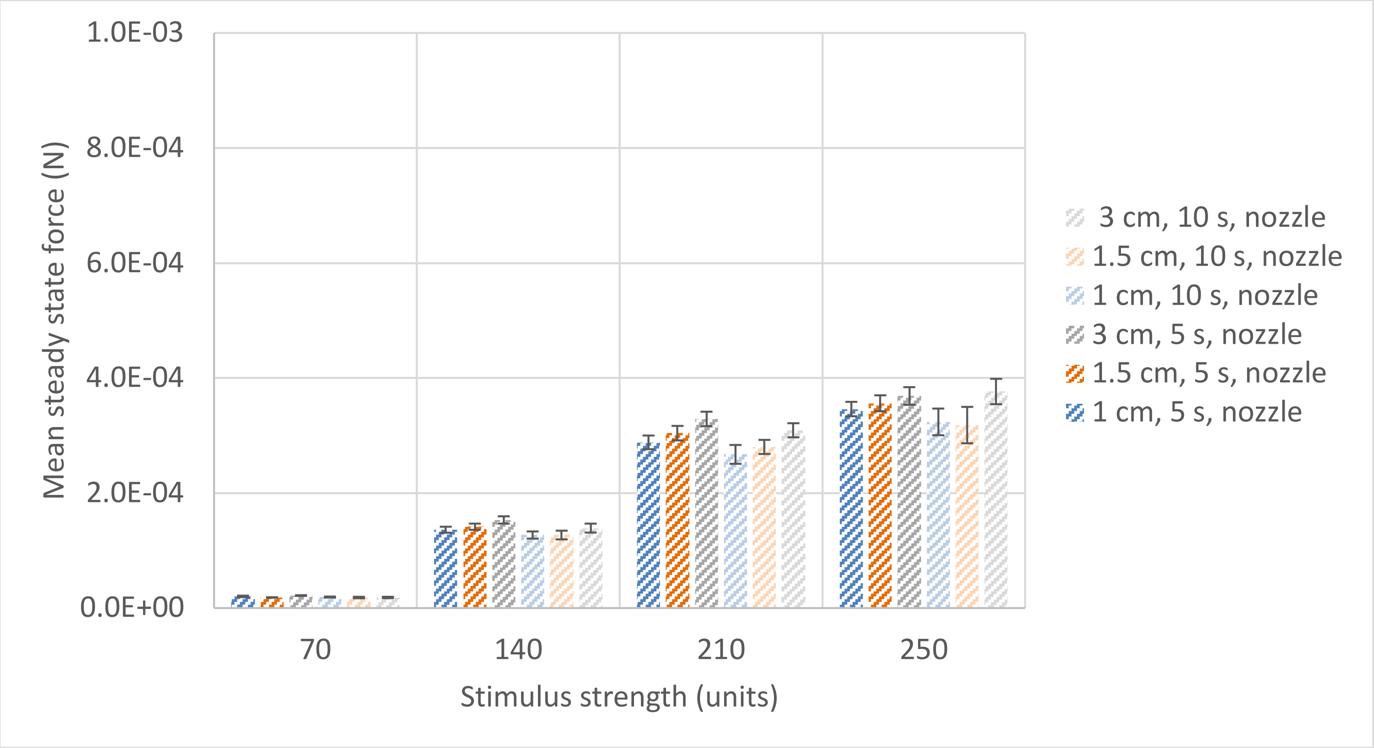

Figure 7.5: Graph of mean steady state force (N) versus stimulus strength (units) for different combinations of stimulus duration and test/working distance, with a brass nozzle attached to micro-blower exit air-jet. Error bars denote ± 1 standard deviation.

Figures 7.4 and 7.5 show that as the stimulus strength increased, the mean steady state force also increased. The duration of the puff had no effect on the steady state force since for any given distance, the steady state forces at 5 and 10 seconds are equivalent. It should be noted that for the no nozzle case when the test/working distance was 1.5 cm, the steady state forces differed when the duration of the puff was 5 and 10 seconds. The steady state forces were reduced (approximately halved) when a brass nozzle was attached to the micro-blower exit air-jet. The figures also show that as the test/working distance increased the mean steady state force increased.

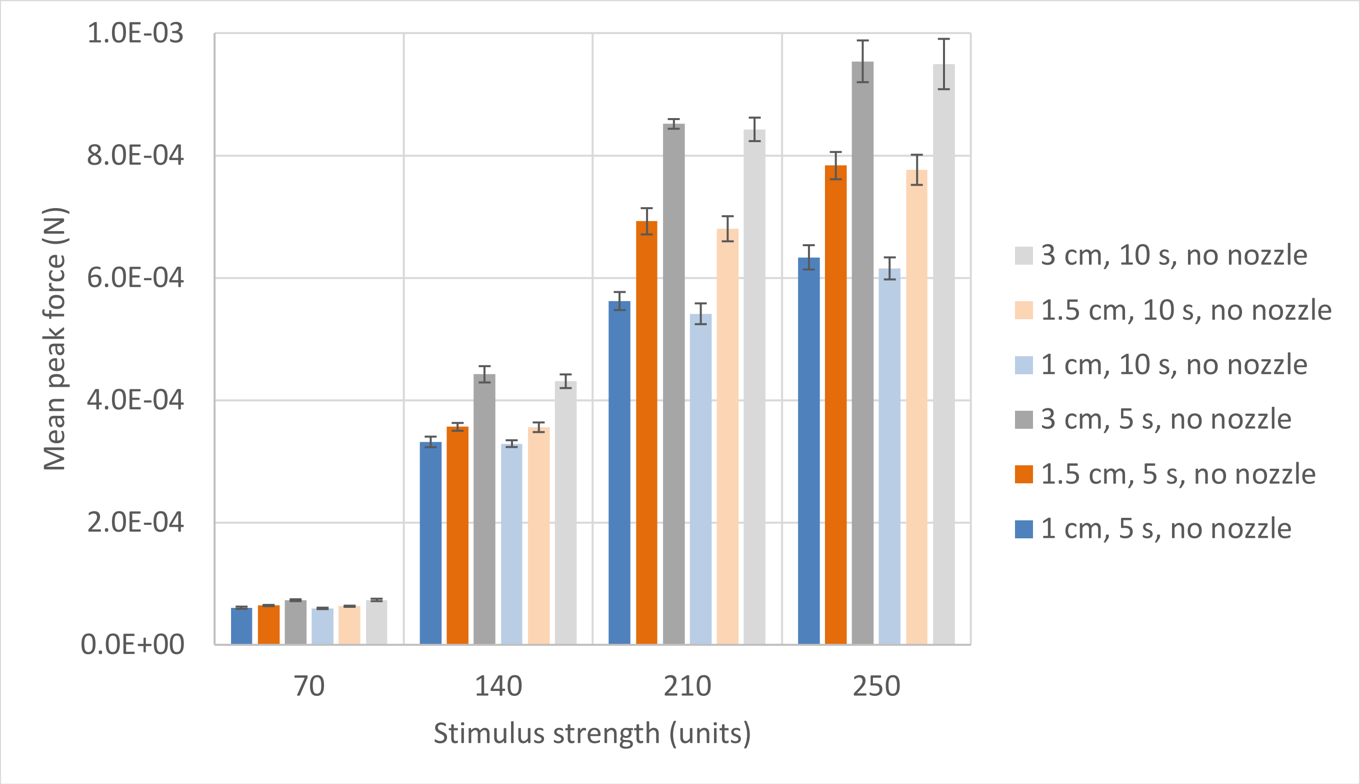

Figure 7.6: Graph of mean peak force (N) versus stimulus strength (units) for different combinations of test/working distance and stimulus duration, when no nozzle was attached to the micro-blower exit air-jet. Error bars denote ± 1 standard deviation.

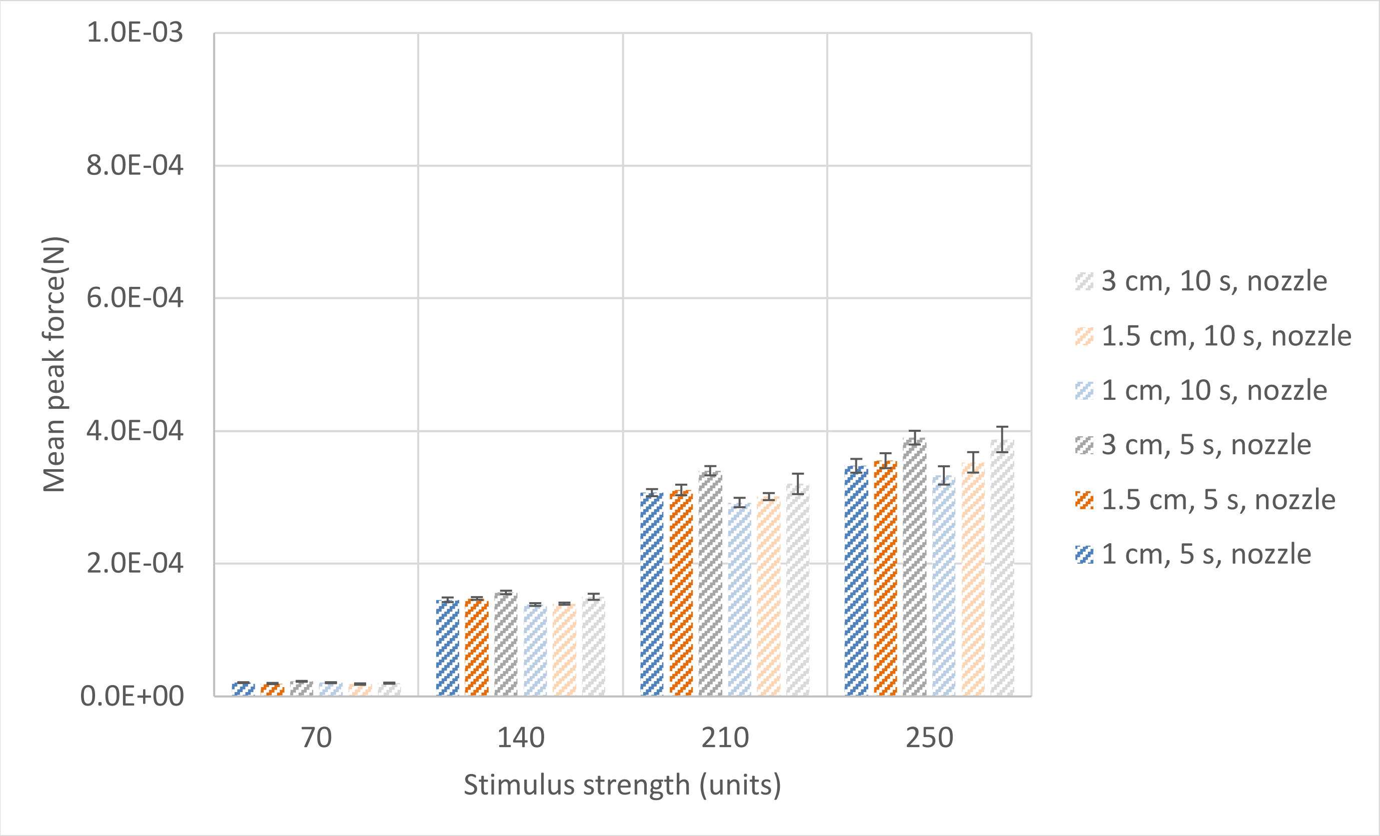

Figure 7.7: Graph of mean peak force (N) versus stimulus strength (units) for different combinations of test/working distance and stimulus duration, when a brass nozzle was attached to micro-blower exit air-jet. Error bars denote ± 1 standard deviation.

Figures 7.6 and 7.7 show that as the stimulus strength increased, the mean peak force also increased. Like the steady state force, duration had no effect on the peak force (for any given distance, the peak forces at 5 and 10 second lines are equivalent), and as the test/working distance increased the peak force also increased. In addition, the peak forces were reduced (approximately halved) when a brass nozzle was attached to the exit air-jet of the Dolphin aesthesiometer.

Variables	Pearson Correlation r	p-values
Stimulus strength and peak force*	0.776	< 0.001
Stimulus strength and steady state force*	0.777	< 0.001
Test/working distance and peak force*	0.157	0.001
Test/working distance and steady state force*	0.162	< 0.001
Duration and peak force	-0.014	0.775
Duration and steady state force	-0.027	0.574
Peak force and nozzle*	-0.502	< 0.001
Steady state force and nozzle*	-0.496	< 0.001
Peak force and steady state force*	0.997	< 0.001

Table 7.2: Results of correlation analysis performed using JASP version 0.13.1 (significant results in blue*).

Correlation and regression analyses were specifically selected to determine how the two types of forces (peak force and steady state force) varied with factors such as stimulus strength, test/working distance, duration, and the presence or absence of a nozzle attachment; the strength of any relationships that did exist; and to convey the relationship between predictor and outcome variables in the form of an equation. This will become important when calibrating the device in units of the mode of stimulation, which will be further discussed in Chapter 10 (overview and future works). In addition, when the results are coupled with that of other studies, the optimal test/working distance and duration for aesthesiometry can be determined.

A Pearson correlation on the data showed significant associations between each type of force (peak and steady state) and:

1. Stimulus strength ($R^2 = 0.460$, $p < 0.001$).
2. Test/working distance ($R^2 = 0.03$, $p = 0.001$ (peak force), $p < 0.001$ (steady state force).

Multiple linear regression (using the entry method) showed that stimulus strength, test/working distance, and the presence or absence of a nozzle could significantly predict:

1. Peak force (PF) (4, 427) = 780.157, $p < 0.001$ using the regression equation:

PF= $-1.08 \times 10^{-4} + 3.04 \times 10^{-6}$ (strength) + 4.95×10^{-5} (distance) - 2.70×10^{-4} (nozzle) - 1.41×10^{-6} (duration), where nozzle is coded as 0 = no nozzle attached and 1 = a nozzle attached to the exit air-jet.

2. Steady state force (SSF) (4, 427) = 757.016, $p < 0.001$ using the regression equation:

SSF = $-1.02 \times 10^{-4} + 2.92 \times 10^{-6}$ (strength) + 4.92×10^{-5} (distance) - 2.56×10^{-4} (nozzle) - 2.80×10^{-6} (duration), where nozzle is coded as 0 = no nozzle attached and 1 = a nozzle attached to the exit air-jet.

In particular, it should be noted that both peak force and steady state force were reduced when the nozzle was present.

7.5 Microbalance and repeated puffs

7.5.1 Purpose

To measure the force exerted by the air stimulus of the Dolphin aesthesiometer using a digital microbalance when both the number of air puffs and stimulus strength of the puffs are varied.

7.5.2 Procedure

<u>Part A: Micro-blower without plastic nozzle</u>

1. Using the same set-up of the equipment described in Section 7.3, the MLEO Dolphin management software was set to deliver two puffs of air using the multiple puffs option. The stimulus strength of both puffs of air was 140 units, and each puff lasted 1 second in duration. There was a 1 second delay between the two puffs of air, and a test/working distance of 1 cm was used.
2. The MLEO Dolphin management software was then set to deliver two puffs of air of different stimulus strengths. The stimulus strength of the first puff of air was 140 units, and of the second was 210 units. Each puff lasted 1 second in duration, and there was a 1 second delay between the two puffs. A test/working distance of 1 cm was used.

<u>Part B: Micro-blower with plastic nozzle</u>

3. The entire experiment was then repeated using a brass nozzle (internal diameter: 0.05 cm), which was connected to a 1-inch long section of Tygon tubing (internal diameter 0.16 cm) using a 2.2 cm long silicone adapter. In turn, the Tygon tubing was then connected to the micro-blower exit air-jet. The test/working distance now refers to the distance from the brass nozzle exit to the microbalance (Figure 7.2).

7.5.3 Results

Stimulus strength and puff	Nozzle	Mean Peak force (N)	Standard deviation
140 puff 1	0	3.27E-04	4.28E-06
140 puff 2	0	3.24E-04	2.81E-06
140 puff 1	1	1.51E-04	3.74E-06
140 puff 2	1	1.47E-04	1.40E-06
140 puff 1	0	3.30E-04	3.96E-06
210 puff 2	0	5.45E-04	5.94E-06
140 puff 1	1	1.48E-04	3.43E-06
210 puff 2	1	3.11E-04	2.50E-06

Table 7.3: Mean peak force versus stimulus strength for multiple puffs. Nozzle is coded as 0 = no nozzle attached and 1 = nozzle attached to the exit air-jet.

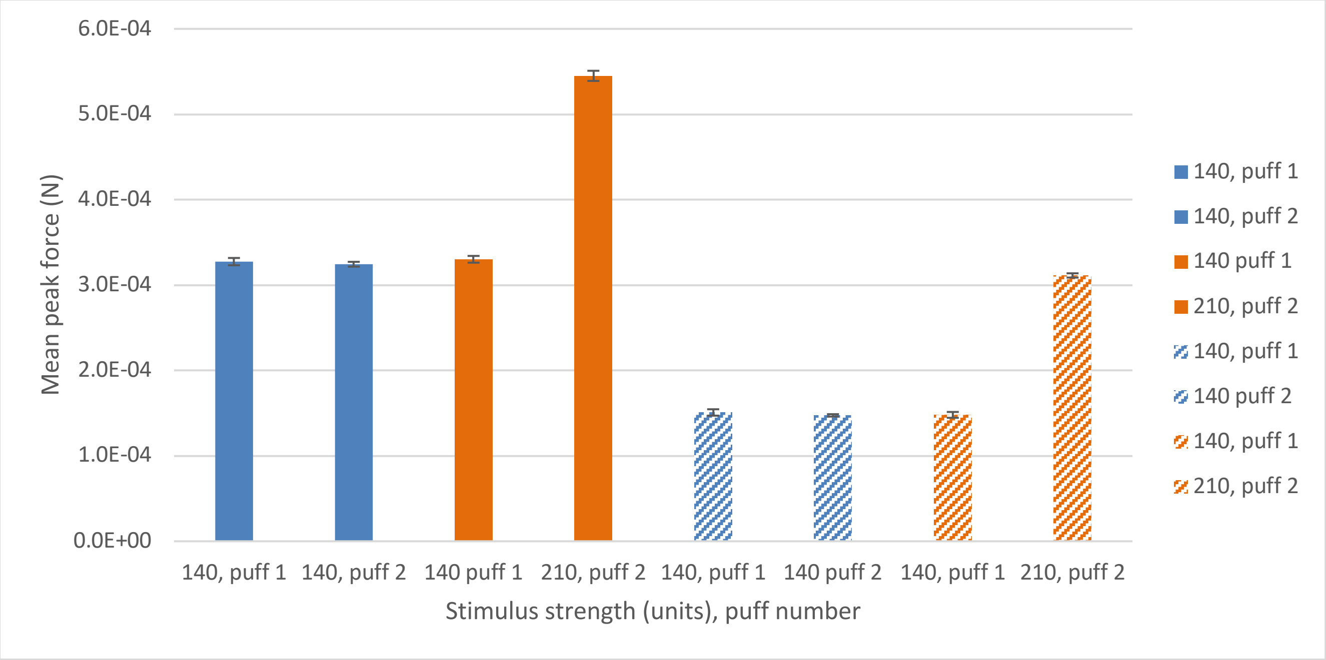

Figure 7.8: Graph of the mean peak force (N) for multiple puffs of different strengths (puff duration: 1 second, puff delay: 1 second) when <u>no nozzle</u> was attached to the micro-blower exit air-jet (solid colour) and when <u>a brass nozzle</u> was attached (striped pattern). Error bars denote ± 1 standard deviation.

One of the features of the novel aesthesiometer is that it can produce multiple stimuli. Figure 7.8 shows that the peak force generated by repeated puffs of the same stimulus strength were consistently similar. When the stimulus strength for puff 2 was increased, the peak force increased as expected. Also, as previously indicated for single puffs, when the nozzle was attached to the exit air-jet of the instrument all peak forces were reduced (almost halved).

7.6 Discussion

This study confirms that the stimulus of the Dolphin aesthesiometer, like other gas-jet aesthesiometers, can produce changes in the force it generates and therefore has a mechanical/force component.

The correlation and regression analyses showed that both the peak force and steady state force could be predicted by stimulus strength and test/working distance, and by the presence or absence of the brass nozzle. Stimulus strength had the greatest influence on both types of forces. The fact that duration had no effect on both types of forces is not only supported statistically, but also by the similar results obtained in Chapter 6, where the airflow stimulus dispersed when it encountered a surface.

The nozzle effectively narrowed the area in which the air could flow, and hence decreased the flow rate and the force of the air leaving the device. It would therefore be important to indicate whether the brass nozzle is used when recording and reporting stimulus strength and thresholds. In addition, the fact that the peak and steady state forces are relatively the same in Figures 7.5 and 7.7 when the stimulus strength was 70 units at durations 5 and 10 seconds may because at such low stimulus strengths, the forces are dampened by the nozzle, thereby making them even smaller. Consequently, under these conditions, the microbalance may have reached its limit of precision.

Overall the error bars in Figures 7.4 to 7.7 were relatively small, suggesting little variability and confirming the consistency of the hardware and, hence, the stimulus. However, more variability was noted at higher stimulus strengths and larger test/working distances. This was most evident when the strength was 250 units, test/working distance was 1.5 cm, and the duration of the puff was 5 seconds. This might be due to the fact that at higher stimulus strengths more dispersion occurs when the airflow stimulus meets a surface as seen in Chapter 6, and since the chamber could not be made air-tight, the dispersion could have further added to the turbulent air already in the chamber. However, it should be noted that even though the error bar is larger than the others, given the scale on the y-axis it is still considered to be small.

Previous aesthesiometry studies found that the average force decreased as the test/working distance increased, because the energy from the jet dissipated with increasing distance from the device (Lum 2014, Nosch, 2015). According to Figures 7.4 to 7.7, as the test/working distance increased, both the peak and steady state forces increased. Statistically, there was a weak association between the test/working distance and the two types of force. However, the steady state force should really be constant with distance as explained in detail in Section 5.2.1.

Typically, transient effects are different from steady state effects, so it would not be surprising if the peak force trends differed from those of the steady state force. However, given the strong correlation between peak force and steady state force, it is fairly safe to assume that, like the steady state force, the peak force should also be constant with increasing test/working distance given the width of the exit air-jet to that of the microbalance plate. It is difficult to explain the trend noted between the peak force and test/working distance in this experiment. However, the increase in the steady force in line with an increase in the test/working distance could be a consequence of the experimental set-up. More specifically, the initial puffs of air may have created a circulation of air within the chamber that continued throughout the experiment and potentially contributed to the readings registered by the microbalance. In addition, as previously mentioned, the chamber could not be made air-tight, so it is also possible that draughts of air could be invading the chamber.

When multiple puffs were generated by the Dolphin aesthesiometer there was little variability, as indicated by the small error bars in Figure 7.8. This further showed the consistency and repeatability of the hardware, and hence the stimulus produced by the instrument.

As previously reported, Murphy et al.(1999b) found that the surface deformation component of the air stimulus produced by the Non-Contact Corneal Aesethesiometer (NCCA) was very small compared to the distinct temperature change component of the stimulus. They concluded that the mechanical mode of the stimulus played a minor role in moderating the sensitive nerve fibers of the cornea (Murphy et al., 1999b). The studies conducted by Lum (2014) and Nosch (2015), which measured the force exerted by the air stimulus of aesthesiometers (Belmonte Ocular Pain Meter (BOPM), NCCA) used test/working distances that were less than 1 cm, and therefore could not be reliably compared to the findings of this study. However, the average force generated by the NCCA with a nozzle attachment (nozzle diameter: 0.125 cm) at a test/working distance of 1 cm ranged from 0 to 1.37×10^{-5} N. Figure 7.4 showed that at 1 cm when no nozzle was attached (exit jet-diameter: 0.086 cm) the average or steady state force ranged from 0 to 6.09×10^{-4} N, and Figure 7.5 showed that at 1 cm when a brass nozzle (nozzle diameter: 0.1 cm) was attached the average or steady state force ranged from 0 to 3.46×10^{-4} N. Larger forces are expected as the internal diameter of the nozzle is reduced because velocity increases as diameter decreases, and force is dependent on velocity. It is therefore no surprise that at a test/working distance of 1 cm, the forces are larger with the Dolphin aesthesiometer when compared to that of the NCCA. When compared to the gold standard aesthesiometer, namely the Cochet-Bonnet aesthesiometer (C-BA), it is expected that the pressure exerted by the Dolphin aesthesiometer would be smaller than that of the NCCA. The reason for this being that pressure is mathematically described as the force divided by the area, and the narrow diameter of the filament would therefore apply a larger pressure onto the cornea than the airflow stimulus, which is known to disperse as it leaves the exit air-jet. However, overall the forces measured are quite small. In fact, both the peak and steady state forces measured under various conditions in this experiment were small.

Typically thresholds varies from person to person, and with respect to the aesthesiometry literature, the units in which thresholds are reported are not standardized. For instance, the Cochet-Bonnet aesthesiometer which is known for delivering a mechanical stimulus measures threshold in $mgmm^{-2}$, whereas the NCCA, which has both mechanical and thermal mode of stimulus measures the mechanical threshold in millibars (Douthwaite & Kaye, 1980; Murphy et al., 1996). This makes it difficult to compare measurements across aesthesiometers, and this is especially the case given that factors such as test/working distances are not consistent. However, with respect to the forces measured with the Dolphin aesthesiometer it is quite possible that such small forces may go undetected by the human cornea. Therefore, one may be inclined to focus solely on temperature as a mode of stimulus for this novel aesthesiometer.

7.7 Conclusion

The results of the experiment confirm that the stimulus generated by the Dolphin aesthesiometer has a force component, which is repeatable. In addition, the brass nozzle provided further control of the stimulus. Further *in vitro* studies, which explore the thermal mode of stimulation can be performed.

CHAPTER 8: STIMULUS CHARACTERISTICS, THERMAL

8.1 Purpose and hypotheses

8.1.1 Purpose

To determine if the stimulus generated by the Dolphin aesthesiometer produces a thermal effect, and if so, is it produced in a repeatable form.

8.1.2 Hypotheses

1. The stimulus will have a thermal component.
2. The temperature change and the diameter of the model eye affected by the stimulus will both increase as the stimulus strength increases, and as the duration of the stimulus is prolonged.

8.2 Background

8.2.1 Temperature effect studies

Chapter 7 verified that the force produced by the air stimulus of the Dolphin aesthesiometer was repeatable and similar to that of other aesthesiometers. Force is therefore one mode of action of the stimulus. However, it is unclear as to whether or not there is a temperature change component. It is therefore important to determine if detectable temperature changes occur, since from an aesthesiometry perspective, it will determine if the temperature sensitive C fibers are aroused when a stimulus is applied to the cornea.

In order to measure temperature changes produced by previous aesthesiometers, a variety of *in vitro* and *in vivo* methods have been used. Murphy (1996) used a thermocouple covered with standard filter paper moistened with saline, which was meant to simulate the corneal surface covered by the tear film. As an air-pulse stimulus from the Non-Contact Corneal Aesthesiometer (NCCA) was applied to the system a consistent level of reduction in temperature was noted using a thermometer. The temperature decrease was at first small and limited to the area of application. However, as the air spread over the surface there was a sharp decrease in the thermocouple system, and the change in temperature eventually stabilized as the latent evaporation energy was removed. As airflow increased, the drop in surface temperature was also greater. When temperature change was examined within a human cornea using infrared thermal imaging methods, the reduction in temperature was even more pronounced as the stimulus pressure increased, and the temperature change was localized to only the cornea.

Nosch (2015) replicated the aforementioned *in vitro* (moistened thermocouple) and *in vivo* (human subjects and thermal infrared camera) studies using the Belmonte Ocular Pain Meter (OPM) air-jet aesthesiometer. The results revealed that more prominent temperature differences were produced on the moistened thermocouple and the human cornea as the applied airflow rate increased.

When these results were coupled with the results of other experiments that Murphy (1996) and Nosch each performed, namely studies that explored mechanical deformation of the cornea, they concluded that the surface distortion component of the stimulus was small, compared to the temperature change component for both air-gas aesthesiometers. Therefore, the stimulation was mainly thermal, and consequently moderated by the temperature sensitive C nerve fibers (Murphy, 1996; Murphy et al., 1999b; Nosch, 2015).

To determine if the stimulus generated by the Dolphin aesthesiometer produces a thermal effect, an experiment was designed that used a model eye and thermal infrared camera. The model eye was selected because it could be warmed up to ocular surface temperature (OST), and the thermal camera would allow real-time thermal imaging, which would facilitate temperature measurements with a high degree of accuracy. This experiment provides a means of determining the mode of stimulus of the Dolphin aesthesiometer.

8.3 Test instruments

8.3.1 Thermal infrared camera

Heat transfer is the movement of thermal energy and is due to spatial temperature difference. Heat is typically transferred to the surface of the body by conduction and convection, and it is radiated to the surrounding environment (Incropera et al., 2007; Purslow & Wolffsohn, 2005). Conduction is defined as heat transfer that occurs across a medium (a solid or a stationary fluid). Convection is the transference of heat between a moving fluid and a surface when they are both at different temperatures, whereas radiation is the net transference of heat between two surfaces at different temperatures (Incropera et al., 2007).

Thermography is a non-invasive imaging procedure, which allows the recording of real-time thermal patterns using an infrared camera. The 2-D thermogram gives the spatial distribution of temperature, rather than a single temperature value. Current infrared thermography systems are composed of a camera with detachable optics and an infrared detector that absorbs the radiation from a defined field of view. The detector converts the infrared radiation into an electrical voltage for data processing. Camera operation is controlled by a computer, which also collates the data output (Purslow & Wolffsohn, 2005).

The anterior portion of the eye has a characteristic thermal profile in which the central area is coolest. Ocular surface temperature (OST) is defined as the temperature of the central region overlying the cornea and limbal areas. Studies have reported normal OST to range between 32.9 to 36°C (Purslow & Wolffsohn, 2005). OST is measured using a thermal camera, which can be done manually, or by either semi-automated or automated methods. With respect to manual measures, the researcher determines the OST by selecting discrete single points, or by drawing circles or squares onto the captured image. This allows the minimum, maximum, and the average OST of the selected areas to be determined (Tan et al., 2009; Zare Bidaki, et al., 2017).

The Teledyne FLIR A655sc infrared camera (FLIR Systems Inc., Portland, USA) is capable of producing clear, detailed, and highly accurate thermal images of 640 x 480 pixels. It is compact enough that it can be mounted easily to a slit lamp. The standard temperature range is -40°C to 150°C, 100°C to 650°C, spectral range is 7.5 to 14.0 µm and the full window frame rate is 50 Hz. The camera can detect temperature differences as small as 50 mK, and provides up to 50 frames per second at full frame resolution. Readings are accurate to ± 2°C. The device can be focused automatically or manually, and is operated using the Teledyne FLIR ResearchIR Version 4.0 software. The software allows viewing, recording, and advanced processing of the thermal data obtained (FLIR Systems, Inc., 2014; FLIR Systems, Inc., 2018).

Thermography has been successfully used in a wide variety of fields to qualitatively and visually document temperature changes. With respect to the eye, it has been applied in areas such as contact lens wear, corneal sensitivity, dry eye, and refractive surgery. Infrared thermography is renowned for its ability to detect physiological and pathological changes in the eye that are either unreachable or obscured by traditional instruments used to examine the anatomy of the eye (Murphy et al., 1999a; Purslow & Wolffsohn, 2005; Tan et al., 2009).

8.3.2 MLEO model eye

The MLEO model eye is composed of a 20 mm LED dome light, a Type K thermocouple, and a 15 mm diameter mini-scleral lens (Jupiter, Essilor, France) with a base curve of 7.70 mm. The thermocouple is positioned on top of the LED dome, and between the LED dome and the scleral lens, with the scleral lens glued into positioned on top of the LED dome. The LED dome light is fixed onto a circuit board (Figure 8.1 (top)), and connected through the circuit board to a power source (Figure 8.1 (bottom)). The entire structure is spray painted matt black in order to simulate a black body source (Figure 8.2). It is important to note that the surface of the model is dry. The mean baseline surface temperature at the center of the model eye has been measured to be 32.7 ± 0.6°C (Wong, 2017). Once the power supply (8 V) is turned on, the temperature of the model eye quickly increases to 32°C during the first 20 minutes (Wong, 2017; S. Wong, personal communication, July 12, 2018). However, the model eye should be heated for at least 45 minutes to ensure temperature stability within the LED light (Wong, 2017). This model eye or similar versions have been used to assess ocular thermography and contact lens wear (Nishimura, 2014; Purslow, 2005; Wong, 2017).

As air is blown onto the scleral lens surface of the model eye it produces a localized cooling where the moving air touches the surface. Two types of heat transfer methods occur to produce this effect. Convection cooling is the primary mechanism of heat transfer, and it results from the influence of the movement of the airflow (Figure 8.3). The rate of change in the surface temperature of the model eye depends on the difference between the surface temperature and the ambient temperature, as given by Newton's law of cooling (Gockenbach & Schmidtke, 2009; Incropera et al., 2007). The second mode of heat transfer is conduction, and it is driven by the temperature gradient within the model eye that is established by the cooling. This temperature gradient will drive the heat from the warmer parts to the cooled parts of the model eye. Essentially, heat energy moves into the model eye through conduction, and moves out of it through the convection created by an air-jet. For the purpose of this thesis, the main mechanism of heat transference is convection since this is controlled by the airflow rate/strength of the stimulus applied to the model eye (Incropera et al., 2007).

As the stimulus strength is increased, the airflow rate also increases, and hence convective cooling increases. Moreover, convective cooling spreads to the periphery of the model as the duration of the airflow continues (Figure 8.3). As a result, a greater temperature change will occur centrally, and a larger region/diameter of the model eye will be affected. When the stimulus is applied for a longer period of time, more air is added to the system, more convective cooling occurs, which extends to the periphery leading to greater temperature changes and wider diameters. If the stimulus is applied for a sufficiently long period of time, it is possible to achieve a new steady state temperature distribution. The exact length of time required to achieve this steady state temperature distribution depends on factors such as the amount of applied cooling and the thermal mass of the model eye (which goes beyond the scope of this thesis), but essentially, at some point, when the stimulus duration is increased, there will be no change in the temperature or the diameter of the model being affected, and the temperature and diameters will remain fixed. It is important to note that the shorter duration bursts used in this experiment are not sufficiently long for the system to reach equilibrium (steady state), so it is expected that duration will have an impact on the temperature changes and the diameter of the model eye affected by the airflow rate (Incropera et al., 2007; S. Peterson, personal communication, July 8, 2021).

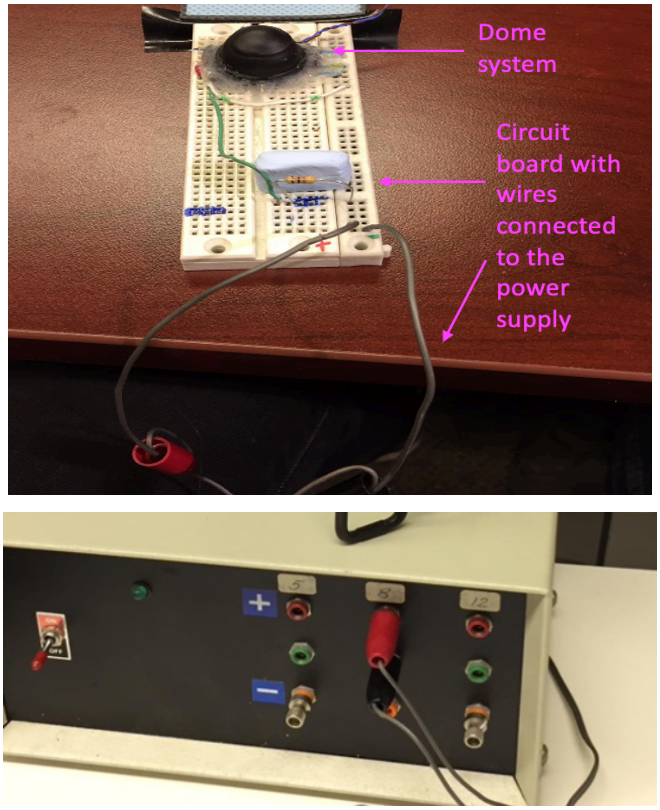

Figure 8.1: Photograph of the MLEO model eye system (top) and its power supply (bottom). (Photo courtesy of Stephanie Wong).

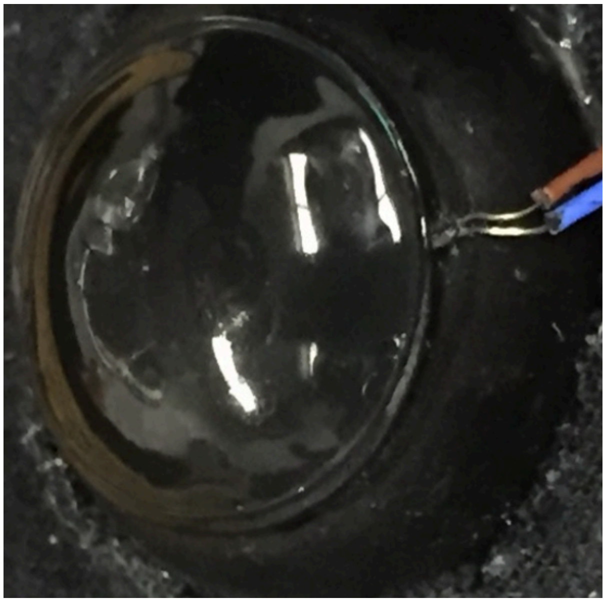

Figure 8.2: Magnified view of the MLEO model eye with the scleral lens over the dome and thermocouple before the model eye is spray painted matte black. (Photo courtesy of Stephanie Wong).

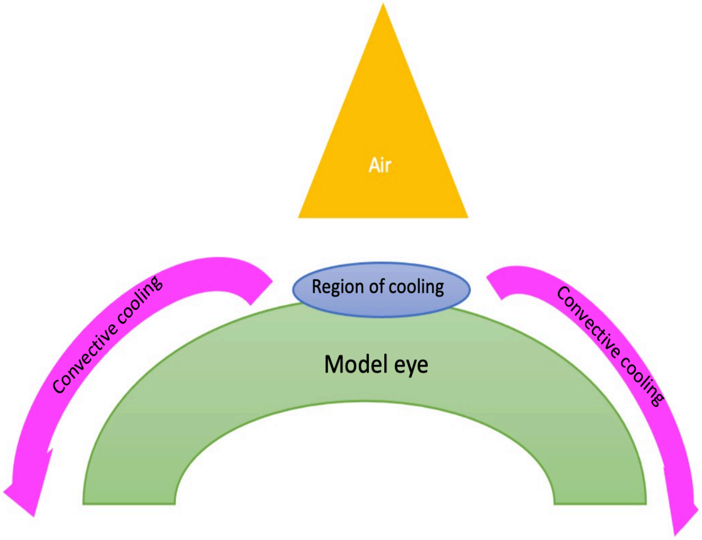

Figure 8.3: Side view illustration showing the effects of the airflow stimulus (yellow) generated by the Dolphin aesthesiometer on the surface of MLEO model eye (green). Localized cooling occurs centrally, as represented by the blue circle, and convective cooling (pink arrows) extends from the center to the periphery of the model.

8.4 Methods

8.4.1 General set-up

The MLEO model eye was firmly held within the head/chin rest frame of a slit-lamp using a specially made mounting system. The model eye was switched on approximately 45 minutes prior to the start of the experiment in order to allow it to heat up to ocular surface temperature (OST) (32°C), and therefore simulate the human cornea. The temperature of the model eye was monitored using the thermocouple incorporated into the model eye, which was attached to a data logger managed by PicoLog 6 software for Windows (Pico Technology, St Neots, UK). The PicoLog software gave an output of the temperature reading by the thermocouple.

The thermal camera was focused using the edge of the scleral lens on the model eye. This edge produced a sufficiently different change in thermal output between the lens and underlying LED dome.

Two brass nozzles (length: 3.5 cm, internal diameter: 0.05 cm), were connected to a 1-inch long section of Tygon tubing (internal diameter 0.16 cm) using a 2.2 cm long a silicone adapter. The Tygon tubing was then connected to the exit air-jet of either the green or blue micro-blowers (Murata^{TM} Manufacturing Co., Kyoto, Japan) (Figures 8.4 and 8.5).

Each micro-blower and nozzle combination was then positioned so that the nozzle was in line with the target zone of the MLEO model eye. The distance between the MLEO model eye and each nozzle (known as the test/working distance) was measured to be 1 cm using a pupillary distance ruler. The test distance was selected based on prior aesthesiometry literature (Lum, 2014; Murphy, 1996, Murphy et al., 1996).

Both the MLEO model eye and the nozzle/micro-blowers were mounted on a slit-lamp table modified to house the thermal camera (Teledyne FLIR A655sc infrared camera (FLIR Systems Inc., Portland, USA)) (Figures 8.4 and 8.5). The Teledyne FLIR A655sc infrared camera recorded infrared video thermography at 24 Hz during the time at which the stimulus was released onto the MLEO model eye. Imaging began 5 seconds before the stimulus was released.

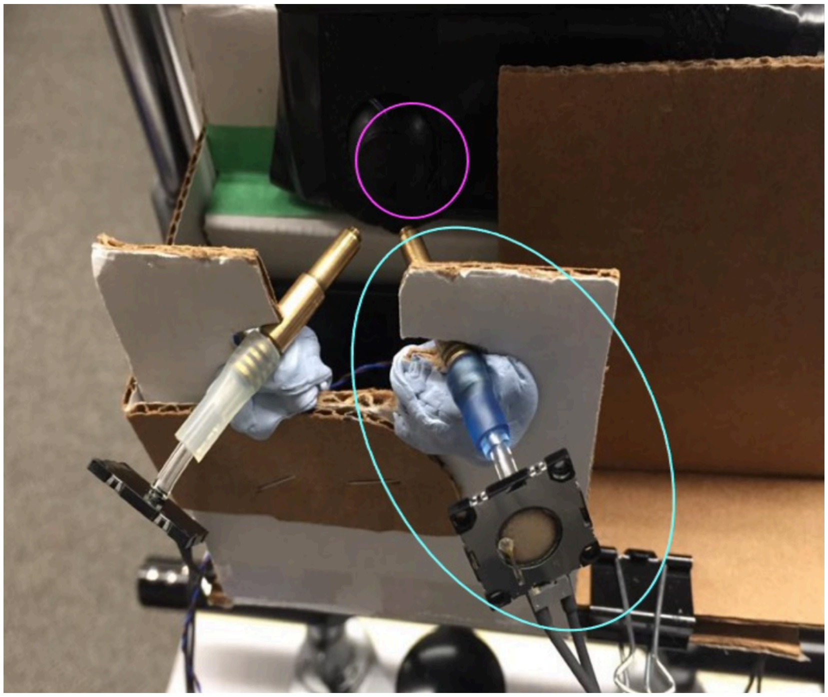

Figure 8.4: Mounting and positioning of the two micro-blowers and their brass nozzles (blue ellipse), showing their relative position to the MLEO model eye (pink circle).

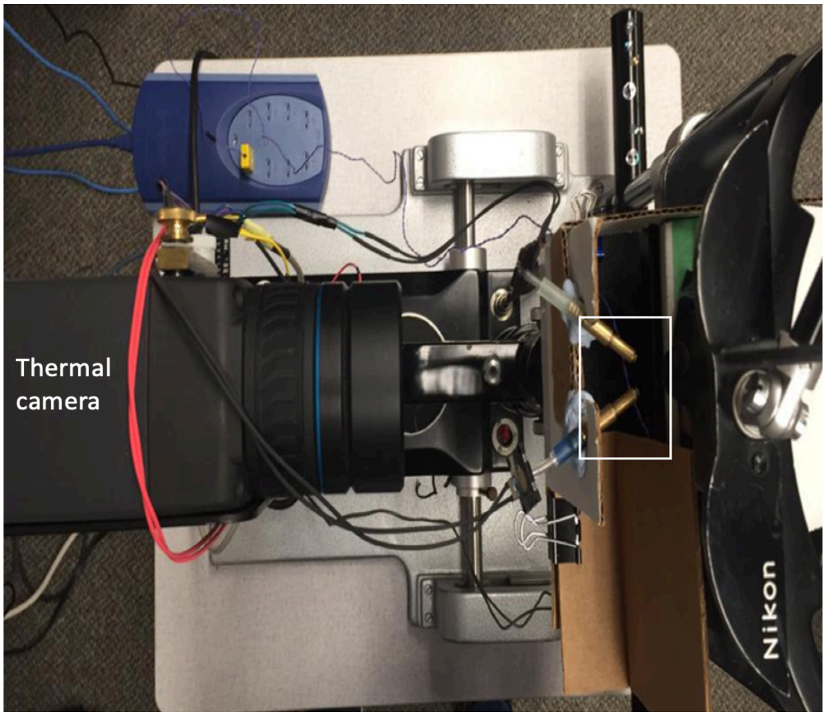

Figure 8.5: Aerial view of the set-up of the experimental set-up showing the thermal camera to the left, and the micro-blowers and brass nozzles (white box).

The proprietary software of the thermal camera (Teledyne FLIR ResearchIR Max Version 4.30.1.70) was used for temperature data collection. Output from the thermal camera was recorded for subsequent analysis. Temperature change was expected to occur on the surface of the model eye with stimulus presentation. To gather temperature data from this area of temperature change, a circle was drawn over the area/region of the model eye that the airflow was expected to make contact with throughout the duration of the stimulus presentation (Figure 8.6). Care was taken when drawing the circle to ensure that the majority of the expected model eye surface that would be affected by the stimulus was covered, but that hot zones around the edge of the model eye were not included. The maximum and minimum temperatures within the sampling circle could be reported using the software for any time point during the stimulus presentation. A second sampling method was also used for data collection within the area of interest on the model eye. For this, a straight line was drawn to intersect the middle of the area of expected temperature change. Care was taken to ensure the line intersected with the locus of minimum temperature within the sample circle, and that the line extended beyond the affected area of the model eye. The temperature for each sampling pixel along the line could then be outputted in table or graphical format (Figure 8.7).

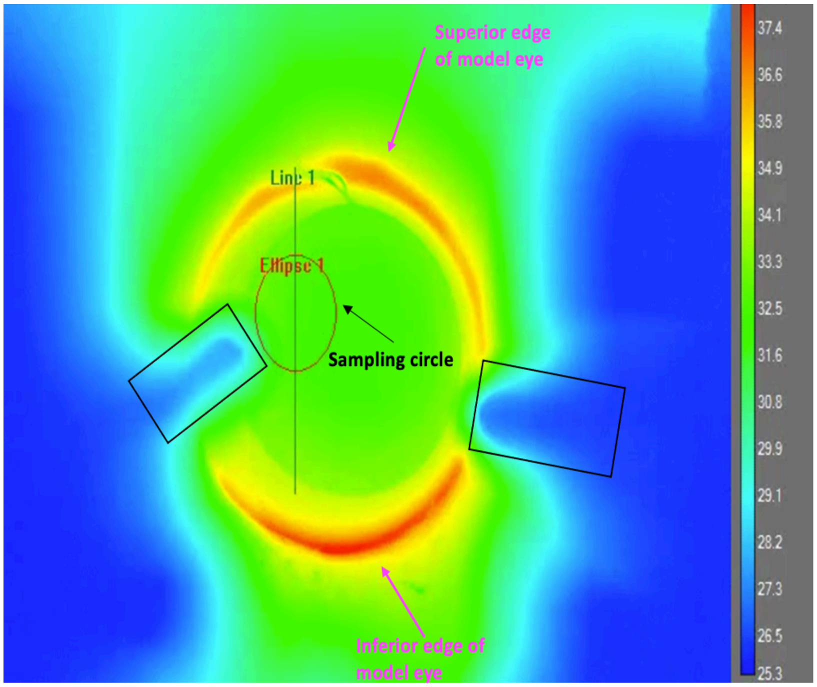

Figure 8.6: Sample thermal image of the MLEO model eye captured by the Teledyne FLIR A655sc infrared camera and displayed here using the Teledyne FLIR proprietary software.

The colour scale on the right-hand side represents warmer to cooler temperatures from top to bottom: red colours indicate hotter areas and blue colours represent cooler areas. The hot ring around the edge of the model eye is produced by the circuit board. The circular central green zone of even temperature is produced by the scleral lens on top of the LED dome. The sample circle is shown as the red circle (Ellipse 1), and the sample line is in blue (Line 1). The out-of-focus nozzles attached to the micro-blowers are marked by the black rectangles.

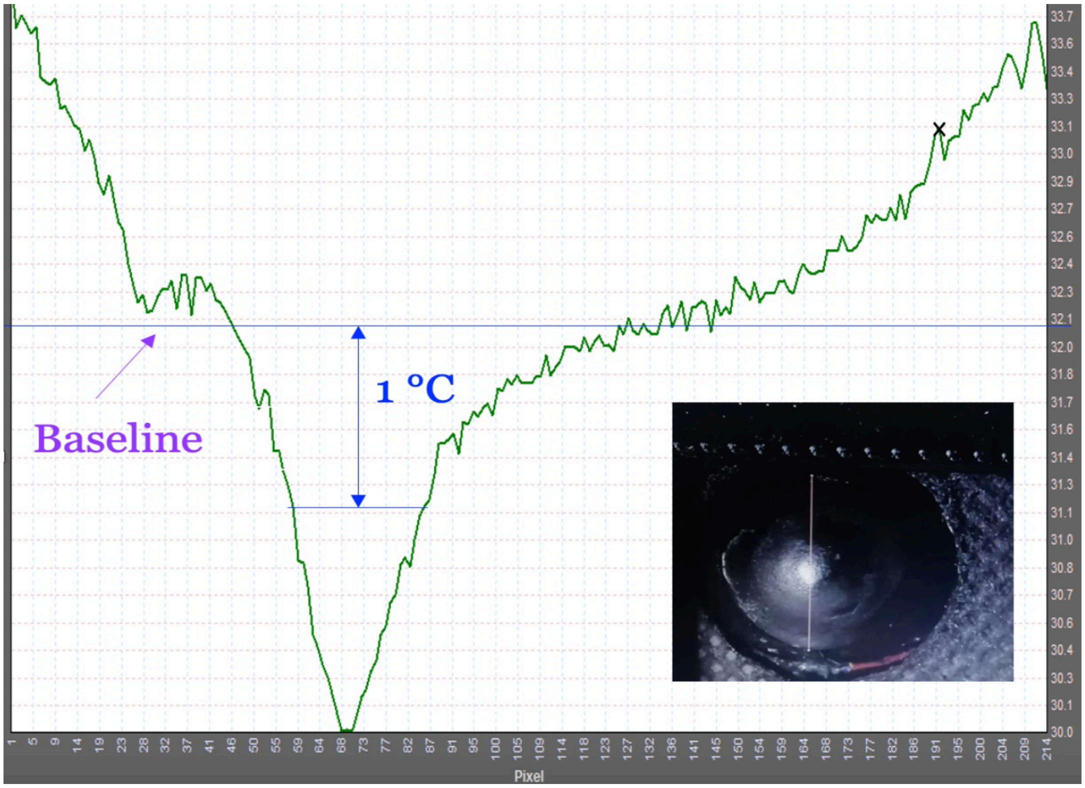

Figure 8.7: Thermal profile plot (V-profile) generated by the Teledyne FLIR ResearchIR Max for the frame with the minimum temperature (temperature on the y-axis and pixel numbers on the x-axis).

The pixel numbers represent the sampling pixel along the line of interest, and are therefore spatial in nature. The baseline temperature before the stimulus was applied (32°C) is depicted by the longest blue line on the plot. The shorter blue line represents the 1°C temperature change from baseline temperature. The picture in the bottom right-hand corner shows the diameter of the scleral lens on the MLEO model eye being verified using Image J 1.52k (National Institutes of Health, USA, Java 1.8.0_172 (64-bit)).

Using the recorded video from the camera, the presented frame from the video sequence could be altered using the video tracking control bar and the maximum and minimum temperatures within the sample circle and along the sample line could be noted for any time point in the video sequence.

8.4.2 Single stimulus presentations

Whilst the apparatus was arranged in such a way that two micro-blowers could be used, it is important to note that for the purpose of this study only one of the micro-blowers was used, and only one single stimulus was applied. This was the simplest stimulus presentation format. The first step was to identify the pre-stimulus baseline temperature within the sample circle. To complete this step, the video tracking control bar was used to adjust the time point to find the video frame and time at which the minimum temperature within the sampling circle was produced by the stimulus. The minimum temperature and the time point were noted. The pixel location of the minimum temperature on the sample line was also identified and marked. The video sequence was then rewound by 40 time stamped frames to get to a time point prior to the stimulus presentation. The temperature at the marked location on the sample line was then noted and recorded as the baseline temperature for this stimulus presentation. Based on knowledge of the baseline temperature and the minimum temperature, the maximum temperature change produced by the stimulus could be calculated.

The video sequence was then returned to time point for the minimum temperature. Attention was given to the sample line profile to observe the characteristic V-shaped profile that describes the temperature profile across the sample line. A cursor can be moved along this line to identify the specific temperature at each pixel location along the profile. Using the baseline temperature as a reference, the two pixel locations along the profile (to the left and to the right of the minimum temperature location) at which a temperature difference of 1°C from the baseline temperature was first noted were recorded. This gave a representation of the spread and depth of the temperature change produced by the stimulus. The diameter of the scleral lens on the model eye was previously measured using Image J 1.52k (National Institutes of Health, USA, Java 1.8.0_172 (64-bit)), and by ensuring the length of the sample line matched this diameter, the relative diameter of each pixel could be calculated. From this ratio, the diameter of the zone with a 1°C temperature change relative to the baseline was calculated. A 1°C temperature change was specifically selected because during the pilot studies the effects of all the stimulus and duration combinations were very apparent. The results were recorded in a pre-designed test matrix using Microsoft Excel for further analysis.

In order to reduce systematic errors, that is, errors that are repeatable from measurement to measurement, the connections between all the apparatus were disconnected and reconnected at random intervals throughout the experiment. To ensure consistency/reproducibility when taking measurements, the same investigators operated the aesthesiometer, thermal camera, and the MLEO model eye. The investigators underwent extensive and comprehensive training to ensure that they were each capable of using the instrument they were assigned to in a reproducible manner. This study was completed with the help of Stephanie Wong, from the School of Optometry and Vision Science, University of Waterloo, who monitored the temperature of the model before stimulus application using the PicoLog 6 software, and operated the Teledyne FLIR A655sc infrared camera, and by Dr. Paul J. Murphy, from the School of Optometry and Vision Science, University of Waterloo, who assisted with gathering the data from the proprietary software. Assistance with data gathering became necessary since the main researcher would become very ill when exposed to lycopodium powder (which was used to conduct the experiments in Chapters 5 & 6), and unfortunately, despite efforts to remove all residue of the powder, there was still powder residing in the instrument and computer used to conduct these *in vitro* studies.

8.5 Procedure

1. Once the temperature of the MLEO model eye had reached 32°C, the MLEO Dolphin management software was used to select one of the micro-blowers and have it deliver an airflow pulse of stimulus strength of 210 units for a duration of 1.0 second onto the surface of the model eye.

2. Infrared imaging of the temperature effect was recorded using the Teledyne FLIR A655sc infrared camera. It should be noted that the MLEO model eye took 10-15 minutes for its temperature to returned to 32°C after each stimulus presentation.
3. Stimulus strengths of 140 units and 70 units were also tested and steps 1 and 2 were repeated. The stimulus strengths were randomized in terms of the order of their delivery.
4. The stimulus duration was then changed to 1.5 and 0.5 seconds and steps 1-3 were repeated.
5. Five stimulus presentations were made for each stimulus strength and stimulus duration combination.

8.6 Analyses

Data were tested for normality using the Shapiro-Wilk assumption test. A correlation analysis was performed on the normally distributed data, and subsequent linear regressions were executed. These analyses were selected for the same reasons outlined in Section 7.4.4. In addition, the data were also analyzed using repeated measures ANOVA (rm-ANOVA). A rm-ANOVA was conducted to allow multiple comparisons. Tukey HSD tests were used for post-hoc analysis. JASP version 0.13.1 (University of Amsterdam, Netherlands) and Jamovi 1.6.23.0 (Sydney, Australia) were used for data analysis procedures. A probability value of 0.05 or less was considered to be statistically significant.

8.7 Results

Stimulus strength (units)	Duration (seconds)	Mean maximum temperature change from baseline (°C)	Standard deviation	Mean diameter of zone with a 1°C temperature change relative to baseline (mm)	Standard deviation
70	0.5	-2.22	0.11	5.16	0.76
140	0.5	-3.44	0.17	7.51	0.49
210	0.5	-3.02	0.08	7.83	0.26
70	1.0	-2.74	0.17	5.46	0.74
140	1.0	-4.08	0.11	8.00	0.27
210	1.0	-3.64	0.31	8.22	0.45
70	1.5	-3.06	0.11	6.23	0.63
140	1.5	-4.44	0.15	8.48	0.29
210	1.5	-4.12	0.15	8.34	0.22

Table 8.1: Mean model eye surface temperature change from baseline and diameter of cooling zone with a 1°C temperature change relative to the baseline for the different stimulus strength and pulse duration combinations for a single stimulus presentation.

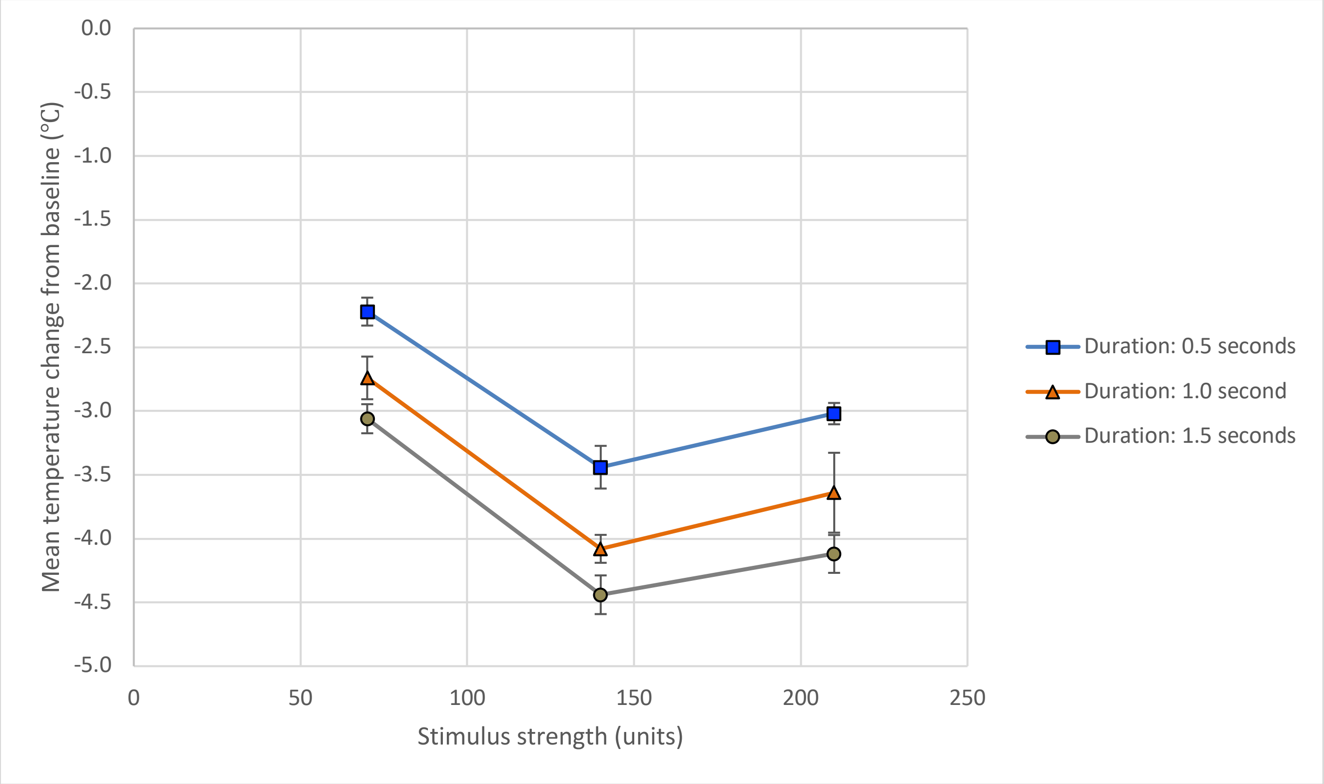

Figure 8.8: Mean maximum model eye surface temperature change (°C) from baseline versus stimulus strength for each duration setting. Error bars denote ± 1 standard deviation.

Table 8.1 and Figure 8.8 show that when the stimulus strength was 70 units, the temperature change from baseline increased as the duration of the stimulus increased. As the stimulus strength doubled to 140 units, the temperature change became more pronounced. However, whilst the effects of duration were maintained, this trend was not seen for the 210 unit stimulus strength. Relative to the 140 unit strength, the magnitude of the temperature change decreased.

There was a significant effect of stimulus strength on mean temperature change from baseline (rm-ANOVA, F (2, 8) = 130.79, $p < 0.001$, $\omega^2 = 0.929$). Post-hoc testing revealed the mean temperature change from baseline increased significantly in going from 70 to 140 units, indicating that more cooling had occurred, and decreased significantly in going from 140 to 210 units indicating an unexpected increase in temperature (Table 8.2).

Stimulus strengths compared	Temperature change when the strength is **70 units** - Temperature change when the strength is **140 units***	Temperature change when the strength is **70 units** - Temperature change when the strength is **210 units***	Temperature change when the strength is **140 units** - Temperature change when the strength is **210 units***
Absolute mean difference in temperature change (°C)	0.593	0.980	0.387
p-value	$p = 0.003$	$p < 0.001$	$p = 0.005$

Table 8.2: Post-hoc comparisons (using Tukey correction) of absolute mean difference in temperature change for different stimulus strengths (significant results in blue*).

There was also a significant effect of duration on mean temperature change from baseline (rm-ANOVA, $F(2, 8) = 206.86$, $p < 0.001$, $\omega^2 = 0.957$). Post-hoc testing revealed the mean temperature change from baseline increased significantly as duration increased (Table 8.3).

Durations compared	Temperature change when the duration is **0.5 seconds** – Temperature change when the duration is **1.0 seconds***	Temperature change when the duration is **0.5 seconds** – Temperature change when the duration is **1.5 seconds***	Temperature change when the duration is **1.0 seconds** – Temperature change when the duration is **1.5 seconds***
Absolute mean difference in temperature change (°C)	1.313	0.920	0.393
p-value	$p < 0.001$	$p < 0.001$	$p = 0.006$

Table 8.3: Post-hoc comparisons (using Tukey correction) of absolute mean difference in temperature change for different durations (significant results in blue*).

There was no significant effect of an interaction between stimulus strength and duration on the mean temperature change from baseline (rm-ANOVA, F (4, 16) = 1.418, p = 0.273, ω^2= 0.044).

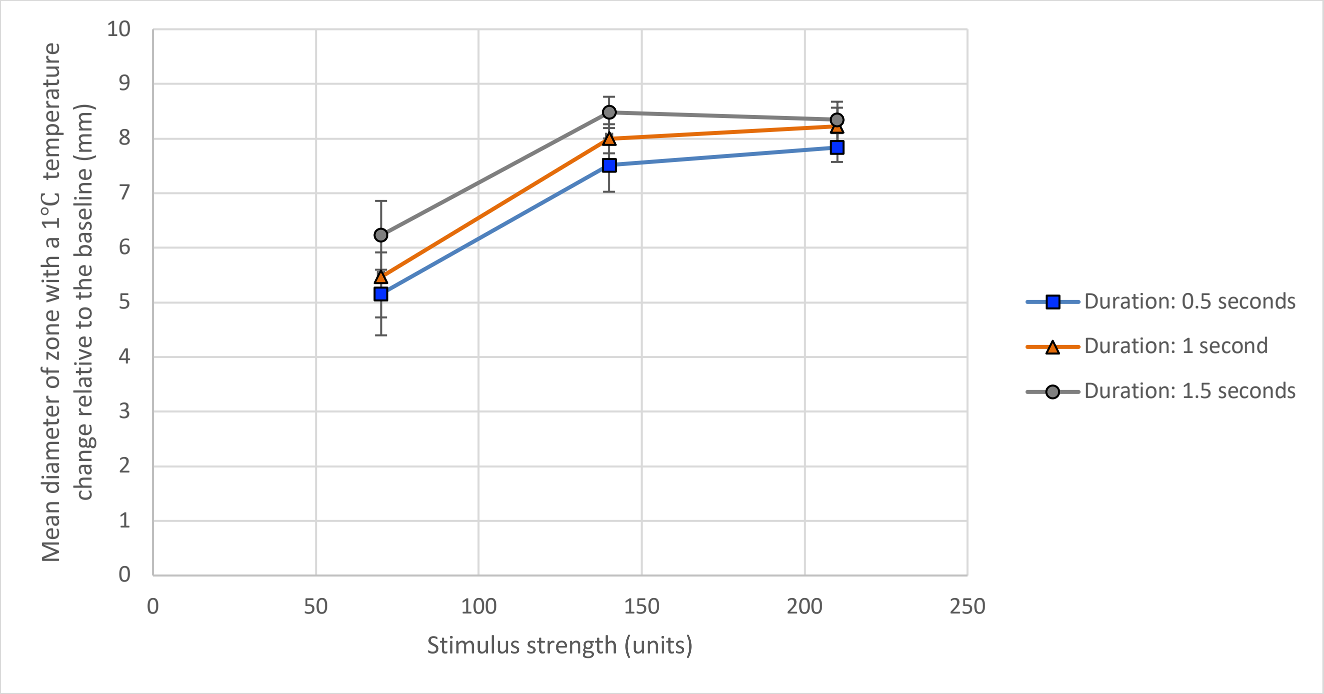

Figure 8.9: Mean diameter of cooling zone with a 1°C temperature change relative to baseline (mm) for each stimulus strength for each duration setting. Error bars denote ± 1 standard deviation.

Table 8.1 and Figure 8.9 show that when the stimulus strength was 70 units, the diameter of the zone with a 1°C temperature change increased as the duration of the stimulus increased. As the stimulus strength doubled to 140 units, the diameter noted was even more prominent. However, whilst the effects of duration were maintained, this trend was not seen for the 210 unit stimulus strength. Instead, relative to the 140 unit strength, the diameter of the zone with a 1 °C temperature change exhibited a plateauing effect.

There was a significant effect of strength on mean diameter of zone with a 1°C temperature change (rm-ANOVA, F (2, 8) = 6.18, p = 0.024, ω^2= 0.483). However, post-hoc testing revealed no statistical difference in the diameters between the three levels of strength (Table 8.4).

Stimulus strengths compared	Diameter of zone with a 1°C when the strength is **70 units** – Diameter of zone with a 1°C when the strength is **140 units**	Diameter of zone with a 1°C when the strength is **70 units** – Diameter of zone with a 1°C when the strength is **210 units**	Diameter of zone with a 1°C when the strength is **140 units** – Diameter of zone with a 1°C when the strength is **210 units**
Absolute mean difference in diameter of zone with a 1°C temperature change (mm)	0.395	0.849	0.453
p-value	p = 0.433	p = 0.072	p = 0.071

Table 8.4: Post-hoc comparisons (using Tukey correction) of absolute mean difference in diameter of cooling zone with a 1°C temperature change for different stimulus strengths (significant results in blue*).

There was also a significant effect of duration on mean diameter of the zone with a 1°C temperature change (rm-ANOVA, F (2, 8) = 235.01, p < 0.001, ω^2= 0.971). Post-hoc testing revealed the mean diameter of the zone with a 1°C temperature change was significantly higher when the durations were 1.0 and 1.5 seconds than when the duration was 0.5 seconds (Table 8.5).

Durations compared	Diameter of zone with a 1°C when the duration is **0.5 seconds** – Diameter of zone with a 1°C when the duration is **1.0 second***	Diameter of zone with a 1°C when the duration is **0.5 seconds** – Diameter of zone with a 1°C when the duration is **1.5 second***	Diameter of zone with a 1°C when the duration is **1.0 second** – Diameter of zone with a 1°C when the duration is **1.5 seconds**
Absolute mean difference in diameter of zone with a 1°C temperature change (mm)	2.379	2.519	0.139
p-value	$p < 0.001$	$p < 0.001$	$p = 0.157$

Table 8.5: Post-hoc comparisons (using Tukey correction) of absolute mean difference in diameter of cooling zone with a 1°C temperature change for different durations (significant results in blue*).

There was no significant effect of an interaction between stimulus strength and duration on the diameter of the zone with a 1°C temperature change (rm-ANOVA, F (4, 16) = 0.168 $p = 0.623$, $\omega^2 = 0$).

Variables	**Pearson Correlation r**	**p-values**
Stimulus strength and temperature change from baseline*	-0.537	< 0.001
Stimulus strength and diameter of the zone with a 1°C temperature change*	0.796	< 0.001
Duration and temperature change from baseline*	-0.572	< 0.001
Duration and diameter of the zone with a 1°C temperature change	0.268	0.075

Table 8.6: Results of correlation analysis performed using JASP version 0.13.1 (significant results in blue*).

A Pearson correlation showed a significant moderate positive association between stimulus strength and diameter of zone with a 1°C temperature change ($R^2 = 0.634$, $p < 0.001$). A significant moderate negative association was found between stimulus strength and temperature change from baseline ($R^2 = 0.288$, $p < 0.001$), as well as duration and temperature change from baseline ($R^2 = 0.327$, $p < 0.001$).

Multiple linear regression (using the entry method) showed that stimulus strength and duration could significantly predict:

1. Temperature change from baseline, F (2, 42) = 33.658, $p < 0.001$ using the regression equation:

   Temperature change from baseline = - 1.158 - 0.007 (strength) - 0.980 (duration)

2. Diameter of the zone with a 1°C temperature change, F (2, 42) = 50.219, $p < 0.001$ using the regression equation:

   Diameter of the zone with a 1°C temperature change = + 3.881 + 0.018 (strength) + 0.849 (duration)

8.8 Discussion

The study confirms that stimulus of the Dolphin aesthesiometer, like other gas-jet aesthesiometers, can produce thermal changes and therefore has a thermal component.

Figure 8.8 shows that when the stimulus strength is 70 units, as duration increases, the temperature change from baseline also increases. This can be attributed to the fact that as air is applied to the model eye for a longer period of time, more air is added to the system thereby causing more convective cooling, which leads to an increase in the temperature change. As the stimulus strength is increased from 70 to 140 units (effectively doubled), a bigger effect is noted. A larger temperature change is produced because the airflow rate, and hence the amount of convective cooling, increased. Up to this point, as the stimulus strength increased, the temperature change also increased. However, when the stimulus strength is increased from 140 to 210 units, whilst the effect of duration previously mentioned is maintained, the effect of a further increase in stimulus strength is different. Instead, the temperature change does not increase as expected. These trends are supported by the results of the repeated measures ANOVAs.

When the stimulus strength is increased from 140 to 210 units there is a decrease in temperature change (Figure 8.8). It is difficult to explain this trend. However, it is possible that an airflow of 140 units is able to remove nearly all of the available heat from the model eye. Increasing the airflow further therefore produces little or no further effect. The model eye/airflow interaction has reached the maximum capacity for heat exchange, and hence its limit for responding to temperature effects.

Another way to look at the effects of the stimulus on the model eye is to use the thermal profile plots (V-profile), such as the one shown in Figure 8.7. This allows us to determine the effects of the stimulus on the surface of the model, namely the spread of the temperature change produced by the stimulus, and this effect is represented by the diameter of the zone with a 1°C temperature change from baseline. Figure 8.9 shows that when the stimulus strength is 70 units and duration increases, the diameter of the 1°C temperature change zone increases. As previously explained, when air is applied to the model eye for a longer period of time, more air is added to the system thereby causing more convective cooling, which spreads out to the periphery, resulting in wider diameter measures. As the stimulus strength is increased from 70 to 140 units, a bigger effect is noted, and a wider diameter is produced because the airflow rate and hence the amount of convective cooling increased, and extended to the periphery. Like temperature change, up to this point as the stimulus strength increased, the diameter of the model being affected increased. When the stimulus strength is increased from 140 to 210 units, whilst the effect of duration previously mentioned is maintained, the effect of a further increase in stimulus strength is different. More specifically, the diameter of the zone with a 1°C temperature change appears to plateau. The trends seen with duration are supported by the results of the repeated measures ANOVAs. However, with respect to the main effect of stimulus strength on the diameter, but the lack of significant difference between the three levels of strength, it should be noted that the magnitudes of the mean differences are small (<1 mm) and variable as seen in Table 8.4. This would therefore explain why the p-values in the post-hoc tests were all more than 0.05. Furthermore, additional post-hoc tests such as Holm, Scheffe, and Bonferroni were performed, and they all produced similar results. Another explanation for the lack of significance detected by the post-hoc test is that there is a loss of power in going from a test that assesses the global effect (overall F statistics) to one with three comparisons.

With respect to the observed plateauing effect seen with the diameter of the 1°C temperature change zone, as the stimulus strength is increased from 140 to 210 units, there are two possible explanations. The first is a fluids explanation and the other is related to the design of the experiment.

Chapter 6 showed that when the airflow generated by the Dolphin aesthesiometer encounters a surface it disperses. It is possible that at such high stimulus strengths, and hence airflow rates, the dispersion is so great that the airflow can no longer remain attached to the curved surface of the model eye as it did before, thus causing the plateauing effect observed. This fluid or jet projection phenomenon cannot be confirmed without performing additional complementary experiments.

The plateauing effect may also be attributed to the design of the experiment. As previously mentioned, when the airflow comes into contact with the model eye, localized cooling is produced. As the stimulus strength increases, more convective cooling occurs, which spreads to the periphery of the model eye leading to larger diameters of the model eye being affected. The pink horizontal lines in Figure 8.10 represent the diameters of the flat planes one would see when looking at the model from the perspective of the stimulus air-jet. The orange vertical lines represent the difference in diameter as the stimulus strength increases. It is evident that as the strength increases, the differences in the diameter are not only small, but relatively the same. This would explain the plateauing effect noted in Figure 8.9. Figure 8.10 also shows that the area of the curved surface of the model eye being affected/cooled is what is changing on a larger scale. When the stimulus strength is 70 units, the area being affected is represented by the green stripes, and when the strength is doubled, the area being affected is much larger as seen by the purple stripes. It is difficult to determine if the measurements in this experiment are being sampled from the blue box seen in Figure 8.10, or further out to the edges, thus leading to larger surface areas being affected relative to such small differences in diameter as the stimulus strength is increased. Therefore, diameter may not be the best proxy for determining the region truly being affected/cooled as the ability of the thermal camera to detect such changes gets worse and worse as one moves to edge of the model because the relationship of the area of this curved structure (known as a spherical cap) is not linear with diameter (S. Peterson, personal communication, July 8, 2021).

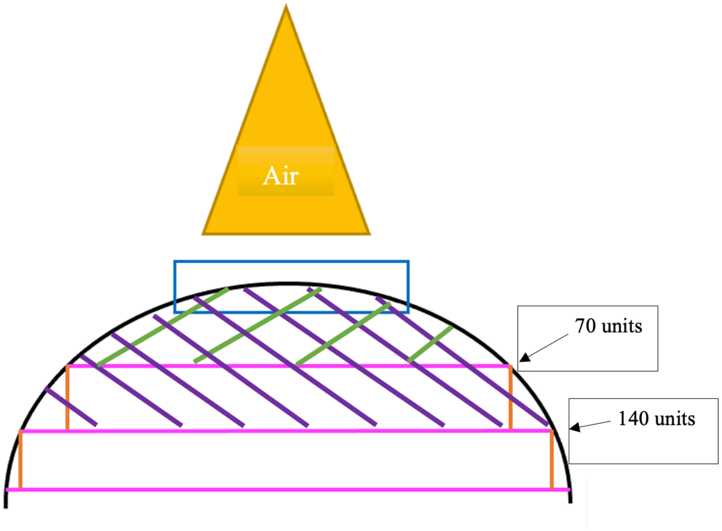

Figure 8.10: Side view illustration showing the effects of the airflow stimulus (yellow) generated by the Dolphin aesthesiometer on the MLEO model eye (black).

The pink horizontal lines represent the diameters of the zone with a 1°C temperature change relative to the baseline as stimulus strength increases from 70 to 140 units. These pink lines are the flat plane one would see when looking at the model eye from the perspective of the exit air-jet of the aesthesiometer. The orange vertical lines depict the difference in the diameter as the stimulus strength increases. When the stimulus strength is 70 units, the area of the curved surface of the model eye being affected is given by the green stripes, whereas the purple stripes show the area being affected when the strength is increased to 140 units.

From an aesthesiometry perspective, if the thresholds for corneal sensitivity are measured using the diameter as a metric, it could mean that the ability to detect a difference would get worse because the difference is already small. Instead, the depth or volume of the model eye being affected might be a better measure of threshold and hence sensitivity. Furthermore, when the anatomy of the corneal nerve supply is factored in (the wide and extensive receptive field overlap, as well as the presence of the different nerves in the various layers of the cornea), using the volume affected instead of the diameter might be a more appropriate way to the explain the neural responses that result from stimulating the human cornea.

The correlation analyses showed that the mean temperature change from baseline was associated with both the stimulus strength and the duration, whereas the mean diameter of the 1°C temperature change zone was only strongly associated with the strength of the stimulus. The regression analyses showed that the temperature change from baseline and the diameter of the 1°C temperature change zone could both be predicted by the duration and stimulus strength. The fact that duration had an effect on both parameters, as seen in Figures 8.8 and 8.9, as well as the regression analyses, confirms that the temperature distribution of the model eye was not at a steady state and did not achieve equilibrium.

The study shows that at higher stimulus strengths, the precision is lower. These results are in keeping with the findings of previous studies, such as the airflow dispersion on a surface experiment in Chapter 6, which showed that at higher airflow rates more lycopodium powder was displaced. It is also evident that the temperature change from baseline and the diameter of the zone with a 1°C temperature change for each duration and stimulus strength combinations were relatively consistent with very little variability as given by the small error bars in Figures 8.8 and 8.9.

The results confirmed that there is a thermal component to the stimulus generated by the Dolphin aesthesiometer. In addition, Chapter 7, also showed that there is a mechanical component, although the forces generated were small (ranged from 0 to 3.46×10^{-4} N). It is quite possible, that like the NCCA, temperature change may play the primary mode in nerve stimulation, given the small forces measured (Murphy, 1996; Murphy et al., 1999b). As mentioned in Chapter 7, there is a lack of standardization among the various gas-jet aesthesiometers. Despite the different units, Murphy et al. (1999b) found that when the NCCA was positioned 1 cm away from the human cornea, and the stimulus strength was varied, participants detected temperature changes which ranged from -0.32 to -1.72°C (Murphy et al., 1999b). Therefore, given that at the same test distance the Dolphin aesthesiometer produced temperature changes from baseline that ranged from -2.74 to -4.08°C, it is conceivable to think that the temperature changes brought about by the Dolphin aesthesiometer would be detected by the human cornea. However, *in vivo* studies would need to be conducted in order to obtain conclusive evidence about the role each component plays in measuring corneal sensitivity and the detectability of the stimulus.

As previously mentioned, the MLEO model eye is composed of an LED dome with a thermocouple glued to it. The entire system is covered by a scleral lens, and painted matted black in order to produce a black body source. The model eye therefore represents a large receptive field when in actuality the nerves of the cornea are arranged in such a way that there is overlapping of the receptive fields, which magnifies their response to stimuli, and hence sensitivity. In addition, the surface of the model is dry, and it is heated to OST, whereas the actual eye has a tear film, which has layers that play an active role in reducing evaporation. Therefore, it is not possible to directly compare the results of this experiment to that of the corneal surface as the temperature differences obtained cannot indicate a change in the OST during stimulus application (Murphy, 1996; Murphy et al., 1999b; Nosch, 2015).

In order to learn more about the thermal component of the stimulus, several further studies should be performed. Firstly, it would be helpful to determine the volume of the V in the thermal profile plots as it would provide more information about the overall effects of the stimulus strength. Secondly, current *in vitro* eye models are considered to be very elementary as they do not facilitate complex ocular physiological attributes such as natural tear flow, the blinking reflex, or the basic vertical orientation of the eye (Phan et al., 2016; Phan et al., 2019). Using a model eye that can be heated to OST, and can simulate physiological factors of the blink, such as tear flow, tear volume, and blink rate would also allow the exploration of the evaporative effects as another form of heat loss. One such model is the Ocublink (Ocublink, Inc., Centre for Ocular Research & Education, School of Optometry and Vision Science, University of Waterloo). In addition, *in vivo* studies, which measure changes in OST when a stimulus is applied, should also be performed to explore the effects of the stimulus on the ocular surface and its impact on sensitivity measurements (Nosch, 2015). It would also be beneficial to test the stimulus on human subjects, and measure the detection threshold for temperature/cooling, and the discomfort threshold for pain. Moreover, a focus group study whereby a suprathreshold is applied and the participant is either given an attribute to specify the stimulus, or is asked to describe it in their own words could also be done to further characterize the sensation. However, given that our device has a unique multiple jet feature, and can therefore deliver multiple stimuli, it may be prudent to first explore its potential to study the neurophysiological concept of summation at the *in vitro* level with the simple MLEO model eye before using more advanced ocular models and performing *in vivo* studies.

8.9 Conclusion

The results of the experiment confirm that the stimulus generated by the Dolphin aesthesiometer has a thermal mode of stimulation, and the temperature effects are repeatable. Having studied the stimulus characteristics of the instrument, further experiments, which employ the unique multiple air-jet property of the device and facilitate testing temporal and spatial stimuli on an in vitro model eye can be conducted.

CHAPTER 9: *IN VITRO* INVESTIGATION OF TEMPORAL AND SPATIAL SUMMATION USING A MODEL EYE

9.1 Purpose and hypotheses

9.1.1 Purpose

To determine the effects of (i) time delay and (ii) spatial separation on the surface temperature of a model eye produced by the airflow stimulus, when two stimuli of the same strength, generated by the Dolphin aesthesiometer, are applied to a model eye.

9.1.2 Hypotheses

1. The amount of temperature change produced and the diameter of the area on the model eye surface affected by the stimuli will increase as the time delay between two stimulus presentations, at the same test location, decreases.
2. The amount of temperature change produced and the diameter of the area on the model eye surface affected by the stimuli will increase as the cooling zone separation distance decreases.

9.2 Background

Previous studies reported in this thesis have verified that the airflow exiting the air-jet is coherent, the rate of airflow spread is constant, and a nozzle assists in controlling the degree of dispersion of the airflow over a surface. Furthermore, the mode of stimulation of the air stimulus of the Dolphin aesthesiometer has both force and thermal components. Having studied the stimulus airflow characteristics of the Dolphin aesthesiometer, the next step was to assess the ability of its unique multiple exit air-jet capability to produce temporal and spatial manipulations of the stimuli on the *in vitro* model eye surface.

Research has shown that the free nerve endings in the sub-epithelial layer of the cornea exhibit large receptive field overlap (Belmonte et al., 2011, Shaheen et al., 2014). In addition, studies have shown that more than one type of corneal receptor may be activated by a particular mode of stimulation during aesthesiometry (Murphy, 1996; Murphy et al., 1999a; Nosch et al., 2015). This raises the question of whether there is neural summation of stimuli for the ocular surface. Summation of light-induced photoreceptor activity occurs in the eye at the retinal level, and summation of external stimuli also occurs in the skin, which, like the cornea, is a touch-based tissue. However, to date, no studies have assessed temporal and spatial summation (the adding-up of sensory information over time and space, respectively) in the cornea. The lack of studies regarding summation in the cornea may be due to current non-contact gas-jet aesthesiometers only being capable of presenting a single stimulus (repeated single stimuli are possible but not with the short time-delays required), and so cannot be easily used to investigate summation in the cornea.

The Dolphin aesthesiometer is a novel device, which consists of several micro-blowers and, hence, multiple exit air-jets. It was developed to overcome many of the drawbacks of current aesthesiometers and allow researchers to study temporal and spatial summation in the cornea. Whilst *in vivo* human studies are considered to be the absolute standard for testing the performance of a new instrument, *in vitro* studies are useful for early testing and development. Moreover, these types of studies can be beneficial in isolating the effects of certain variables, thereby making the new device ready for human trials (Phan et al., 2019).

To determine the effect of timing differences and spatial separation on surface temperature of the model eye, from the application of two air-jet stimuli of the same strength, two experiments were designed. Both experiments used the same model eye and thermal camera described in Chapter 8. These experiments are proof of concept studies; that is, the aim was to determine whether or not the Dolphin aesthesiometer can be used to study summation *in vivo*.

9.3 Test instruments

The test instruments used for this study, namely the Teledyne FLIR A655sc infrared camera (FLIR Systems Inc., Portland, USA) and the MLEO model eye, are described in Section 8.3.

9.4 Methods

9.4.1 General set-up

A detailed description of the arrangement of the apparatus and the general method used for this study can be found in Section 8.4.1.

9.4.2 Multiple stimulus presentations

For multiple stimulus presentations, the data collection method described in Section 8.4.2 was repeated, with some modifications. For repeated stimulus presentations at the same location separated by time (Figure 9.1), the data collection method for the second stimulus repeated that used for the first stimulus. To do so, the video sequence was moved to find the next time frame within the second stimulus presentation containing the next minimum temperature. This time point and minimum temperature were recorded. The baseline temperature before the first presentation was again used to determine temperature change. The time difference between the two minimum temperature frames was also noted. Lastly, the profile analysis was completed for the second sample line to describe the stimulus spread and depth (Figure 9.2).

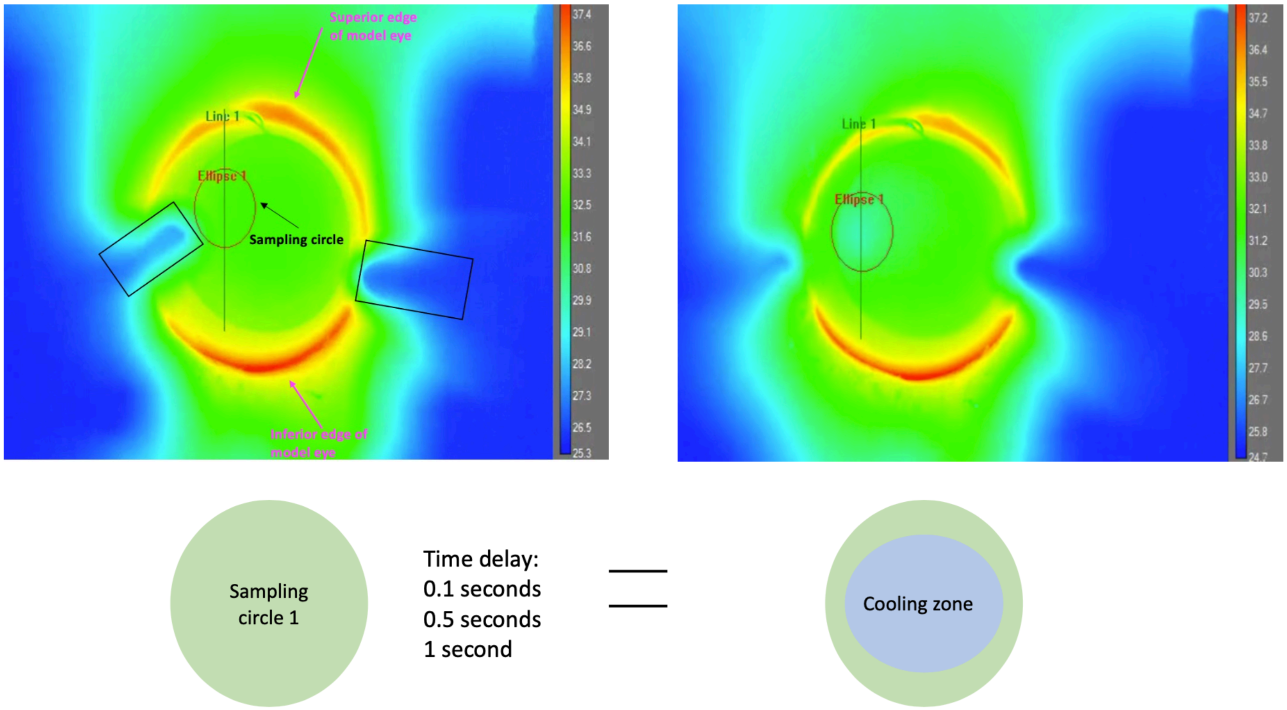

Figure 9.1: Thermal images of the model eye before (left) and after (right) the presentation of two time-separated stimuli applied to the same location of the central region of the MLEO model eye.

The colour scale on the right-hand side represents warmer to cooler temperatures from top to bottom: red colours indicate hotter areas and blue colours represent cooler areas. The sampling circle is marked by Ellipse 1, and the cross-sectional sampling line by Line 1. The lower graphic illustrates the area of cooling produced within the sampling area. Since the stimuli are temporally separated, the cooling zone is always found within the sampling circle, although the size of the zone may vary with time delay (larger zone with shorter time delays).

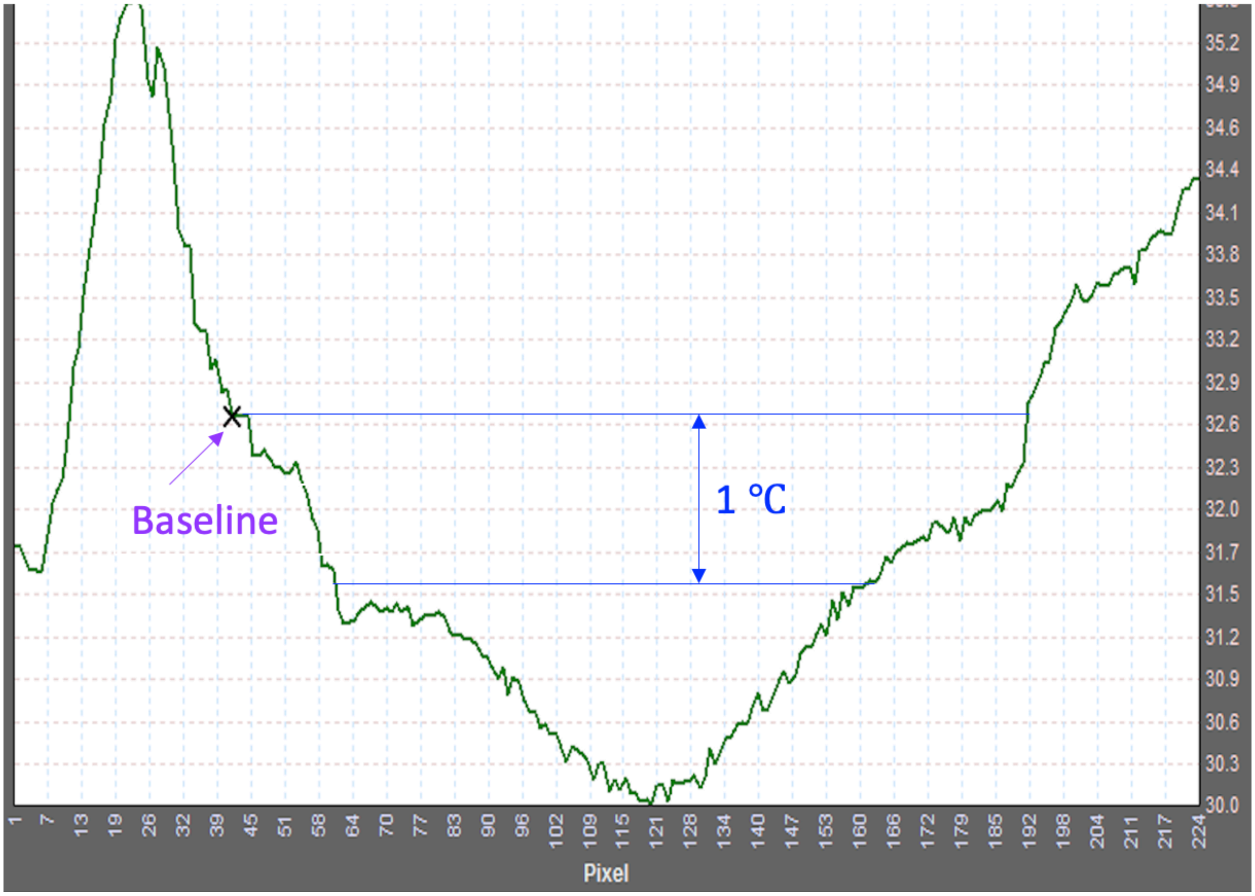

Figure 9.2: Thermal profile plot (V-profile) generated by the Teledyne FLIR ResearchIR Max software for the video frame with the minimum temperature detected in the sampling circle (temperature on the y-axis and pixel numbers on the x-axis).

The baseline temperature before the stimulus was applied (32.6 °C) is depicted by the upper horizontal line on the plot. The lower horizontal line represents the 1°C temperature change from baseline temperature. In comparison to Figure 8.7 this V-shape profile is wider due to the additive effect of two consecutively stimuli delivered with a short stimulus delay between them (Experiment 1).

For the simultaneous presentation of two stimuli at two separate locations on the model eye, a second set of sample circle and sample line analysis tools were drawn onto the video display using the

Teledyne FLIR proprietary software. This second set of sampling tools were aligned in the same way as the first set (Figures 9.3 to 9.5).

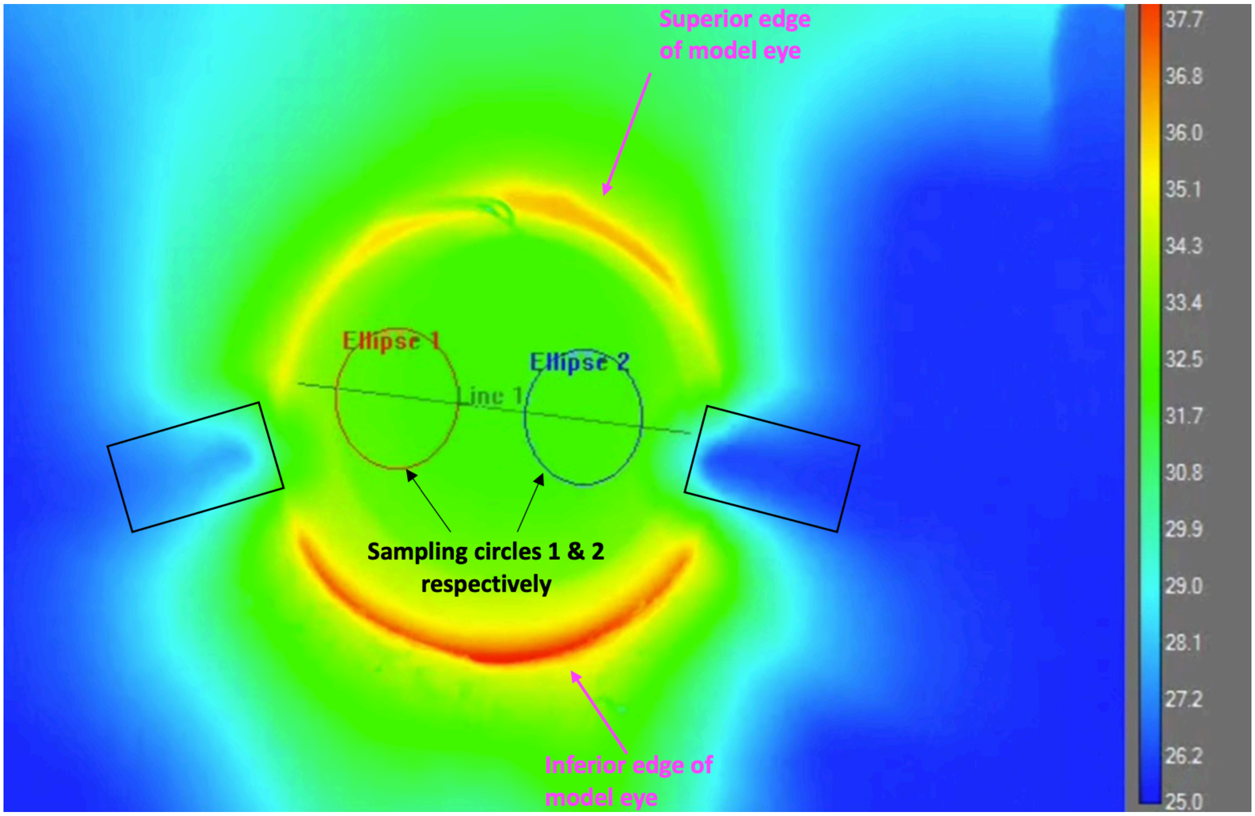

Figure 9.3: Sample thermal image of the MLEO model eye captured by the Teledyne FLIR A655sc infrared camera and displayed here using the Teledyne FLIR proprietary software.

The colour scale on the right-hand side represents warmer to cooler temperatures from top to bottom: red colours indicate hotter areas and blue colours represent cooler areas. The hot ring around the edge of the model eye is produced by the circuit board on which the model eye is mounted. The circular central green zone of even temperature is produced by the scleral lens on top of the LED dome. The sample circles are shown as the red circle (Ellipse 1) and dark blue circle (Ellipse 2), and the sample line is in grey (Line 1). The out-of-focus nozzles attached to the micro-blowers are marked by the black rectangles.

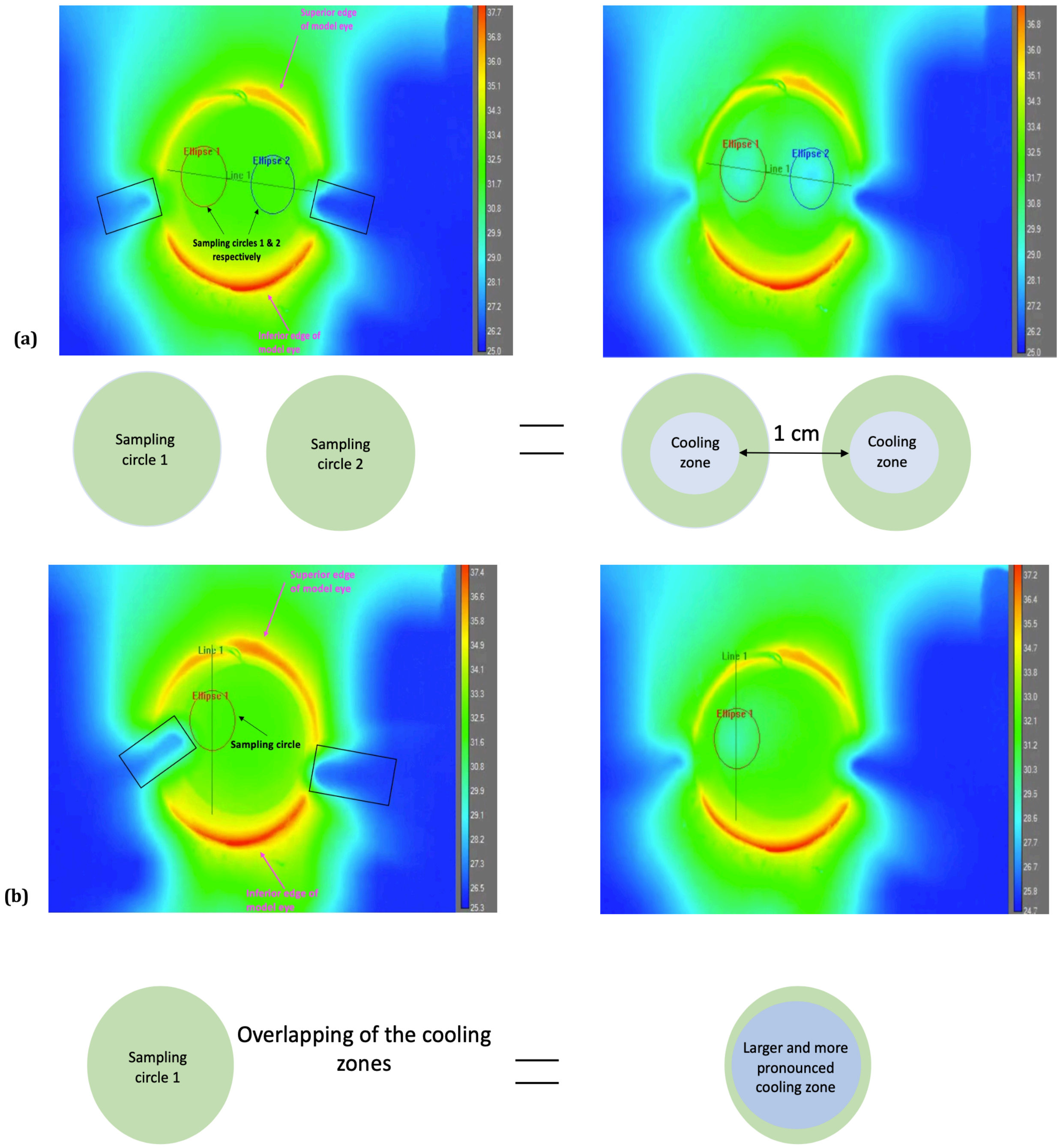

Figure 9.4: Illustration depicting sampling circle(s) before and after two stimuli are applied to separate locations within the central region of the MLEO model eye for different stimulus strength settings with the cooling zone separation of: (a) c.1 cm and (b) 0 cm.

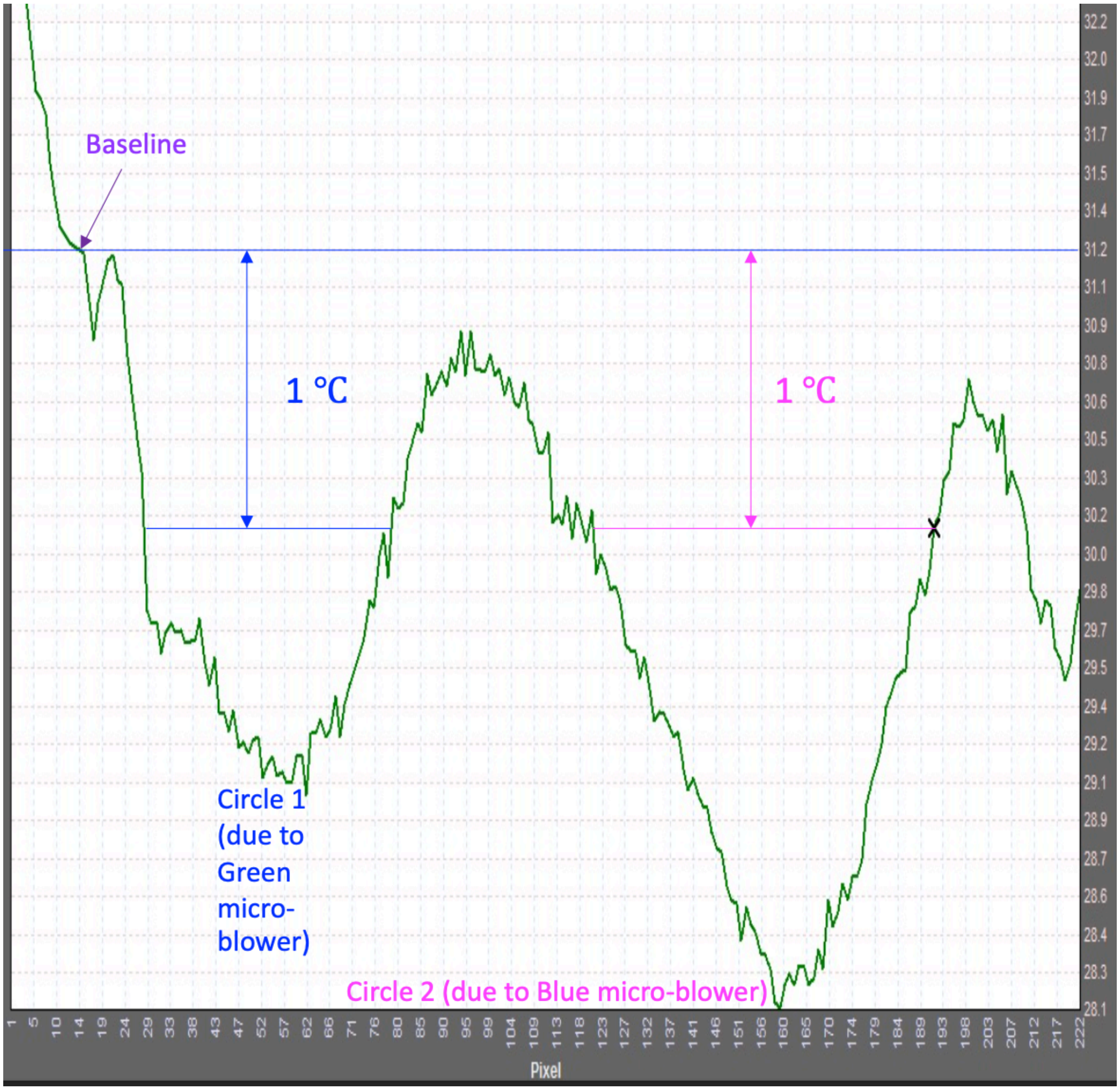

Figure 9.5: Thermal profile plot (W-profile) generated by the Teledyne FLIR ResearchIR Max software for the video frame with the minimum temperature detected in the sampling circle (temperature on the y-axis and pixel numbers on the x-axis).

The W-shape profile is due to the separation of the two stimuli presented simultaneously. The baseline temperature before the stimulus was applied (31.2°C) is depicted by the upper horizontal line on the plot. The lower horizontal lines represent the 1°C temperature change from baseline temperature for the green micro-blower (left), and the blue micro-blower (right). When the two simultaneous stimuli overlap on the model eye surface, only one circle is formed.

In such a case, the thermal profile plot will look like that of Figure 9.2 and only a single V-profile will be formed.

To ensure consistency/reproducibility when taking measurements, the investigators underwent training to ensure that they were each capable of using the instrument they were assigned to in, and each investigator operated the same equipment as in Chapter 8. This study was completed with the help of Stephanie Wong, from the School of Optometry and Vision Science, University of Waterloo, who monitored the temperature of the model before stimulus application using the PicoLog 6 software, and operated the Teledyne FLIR A655sc infrared camera, and by Dr. Paul J. Murphy, from the School of Optometry and Vision Science, University of Waterloo, who assisted with gathering the data from the proprietary software.

9.5 Experiment 1: Effect of time delay when multiple stimuli are generated by a single micro-blower

9.5.1 Purpose

To determine the effect of time delay on the surface temperature of the model eye when two stimuli of the same strength, generated by the Dolphin aesthesiometer, are presented with a known time delay between each stimulus, to the same central location of the model eye.

9.5.2 Procedure

1. Once the temperature of the MLEO model eye had reached 32°C, the MLEO Dolphin management software was set to deliver a sequence of two stimuli of stimulus strength 210 units and duration of 0.5 seconds onto the surface of the model eye. The time delay between

each stimulus puff was 0.1 seconds. The exit air-jet was positioned 1 cm away from the surface of the model eye.

2. Infrared imaging of the temperature effect was recorded using the Teledyne FLIR A655sc infrared camera.
3. Stimulus strengths of 140 units and 70 units were also tested, and steps 1 and 2 were repeated. The stimulus strengths were randomized in terms of the order of their delivery.
4. The stimulus delay was then changed to 1.0 and 0.5 seconds and steps 1-3 were repeated.
5. Five stimulus presentations were made for each stimulus strength and stimulus delay combination.

9.5.3 Analyses

The data was first tested for normality using the Shapiro-Wilk assumption test. However, the small sample size made it difficult to test all the assumptions, such as sphericity. Some assumptions of normality were violated and outliers were present in the temperature data set. The outliers could not be removed as the data set was small and statistical power would be lost. However, for the large majority of data sets, normality was present and parametric testing was performed. (Statistical research has shown the “F statistic is immune to non-normality” (Sawilowsky. 2006, p. 208)). A repeated measures ANOVA (rm-ANOVA) was performed, followed by Tukey HSD tests for post-hoc analysis. JASP version 0.13.1 (University of Amsterdam, Netherlands) and Jamovi 1.6.23.0 (Sydney, Australia) were used for data analysis procedures. A probability value of 0.05 or less was considered to be statistically significant.

9.5.4 Results

Stimulus strength (units)	Single pulse duration (s)	Test distance (cm)	Stimulus delay (s)	Pre-stimulus baseline temperature (°C)	SD	Mean maximum temperature change of Puff 1 from pre-stimulus baseline (°C)	SD	Inter-stimulus baseline (°C)	SD	Mean maximum temperature change of Puff 2 from pre-stimulus baseline (°C)	SD	Mean maximum temperature change of Puff 2 from inter-stimulus baseline (°C)	SD	Mean diameter of zone with a 1°C temperature change after Puff 1 (pre-stimulus baseline temperature to 1°C) (mm)	SD	Mean diameter of zone with a 1°C temperature change after Puff 2 (from pre-stimulus baseline temperature to 1°C) (mm)	SD
70	0.5	1	0.1	32.70	0.12	-2.14	0.11	33.22	0.08	-2.66	0.09	-0.8	0.07	2.02	0.21	2.93	0.21
140	0.5	1	0.1	32.52	0.16	-2.34	0.11	32.54	0.18	-2.98	0.08	-0.98	0.08	4.00	0.45	6.24	0.40
210	0.5	1	0.1	32.62	0.13	-2.44	0.13	32.40	0.16	-3.08	0.08	-0.98	0.08	4.96	0.57	7.07	0.17
70	0.5	1	0.5	32.54	0.05	-2.14	0.11	33.02	0.08	-2.48	0.08	-1.44	0.05	2.01	0.24	2.77	0.13
140	0.5	1	0.5	32.38	0.25	-2.38	0.13	32.34	0.23	-2.92	0.08	-1.7	0.00	4.27	0.15	6.32	0.23
210	0.5	1	0.5	32.56	0.09	-2.50	0.10	32.26	0.24	-2.94	0.11	-1.54	0.05	5.22	0.68	7.02	0.27
70	0.5	1	1	32.80	0.31	-2.14	0.05	33.32	0.37	-2.44	0.05	-1.68	0.04	2.33	0.12	2.69	0.17
140	0.5	1	1	32.64	0.63	-2.44	0.05	32.60	0.64	-2.84	0.13	-1.84	0.05	4.41	0.19	5.99	0.57
210	0.5	1	1	32.74	0.23	-2.36	0.11	32.64	0.40	-2.72	0.11	-1.76	0.05	4.54	0.69	6.05	0.63

Table 9.1: Mean model eye surface temperature change from pre-stimulus baseline (Puffs 1 and 2), inter-stimulus baseline (Puff 2), and diameter of cooling zone with a 1°C temperature change, for Puffs 1 and 2 at different stimulus strength and stimulus delay combinations.

Stimulus strength (units)	Single pulse duration (s)	Test distance (cm)	Stimulus delay (s)	Mean video time stamp of Pre-stimulus baseline	SD	Mean video time stamp for maximum temperature change for Puff 1	SD	Mean video time stamp of Inter-stimulus baseline	SD	Mean video time stamp for maximum temperature change for Puff 2	SD	Mean video time stamp difference between Pre-stimulus baseline and Puff 1	SD	Mean video time stamp difference between Inter-stimulus baseline and Puff 1	SD	Mean video time stamp difference between Inter-stimulus baseline and Puff 2	SD
70	0.5	1	0.1	118.00	42.80	158.00	42.80	160.80	43.42	168.60	44.04	40.00	0.00	2.80	0.84	7.80	0.84
140	0.5	1	0.1	124.20	56.34	164.20	56.34	166.20	56.62	175.20	59.29	40.00	0.00	2.00	0.71	9.00	2.92
210	0.5	1	0.1	218.80	57.68	255.80	51.78	258.00	52.16	267.60	53.97	37.00	6.71	2.20	0.45	9.60	2.88
70	0.5	1	0.5	140.20	33.98	180.20	33.98	190.60	33.58	200.40	33.00	40.00	0.00	10.40	1.82	9.80	1.79
140	0.5	1	0.5	114.80	85.96	154.80	85.96	163.00	87.21	171.80	88.54	40.00	0.00	8.20	1.64	8.80	1.64
210	0.5	1	0.5	147.40	58.83	187.40	58.83	196.60	59.71	206.60	59.71	40.00	0.00	9.20	1.30	10.00	0.00
70	0.5	1	1	159.80	60.38	199.80	60.38	220.60	62.02	230.40	72.71	40.00	0.00	20.80	3.27	9.80	2.17
140	0.5	1	1	117.00	38.16	157.00	38.16	175.20	39.44	185.00	39.66	40.00	0.00	18.20	5.45	9.80	1.92
210	0.5	1	1	162.20	47.77	202.20	47.77	219.40	48.75	230.20	48.85	40.00	0.00	17.20	1.92	10.80	2.17

Table 9.2: Mean video time stamps of Pre-stimulus baseline, Puff 1, Inter-stimulus baseline, and Puff 2; and the time stamp differences between Pre-stimulus baseline and Puff 1, Puff 1 and Inter-stimulus baseline, and Inter-stimulus baseline and Puff 2 at different stimulus strength and time delay combinations.

9.5.4.1 Time delay

Table 9.2 confirms that the pre-stimulus baseline temperature of the surface of the MLEO model eye was always taken 40 frames before the release of the stimulus (with one exception), as shown in the orange column. It also shows that there were detectable time gaps in minimum surface temperature produced by each stimulus (purple columns). Moreover, these columns show that for each stimulus delay, the gaps between the two stimuli were relatively consistent between the three levels of stimulus strength.

9.5.4.2 Temperature change

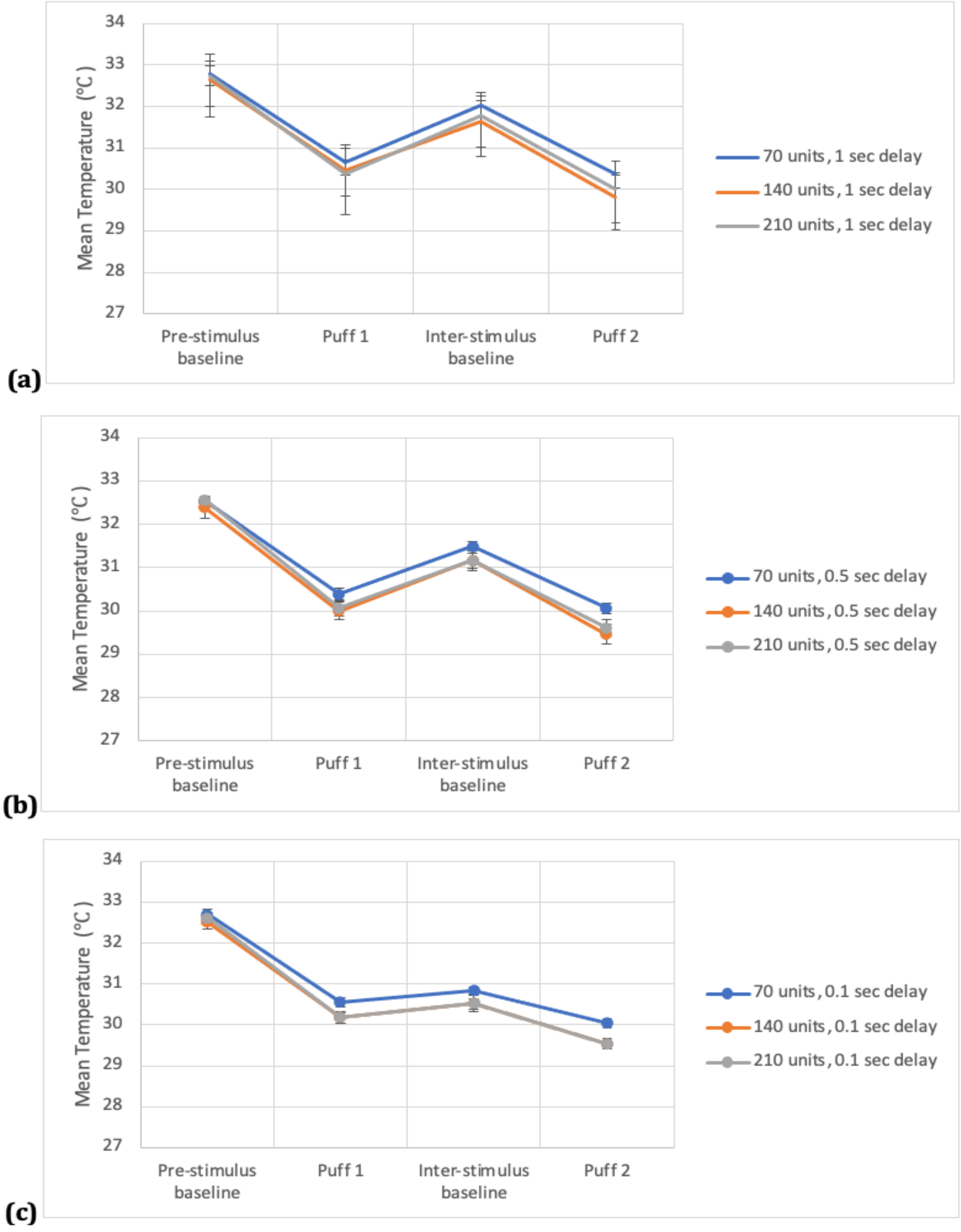

Figure 9.6: Mean surface temperature at the Pre-stimulus baseline, after Puff 1, at the Inter-stimulus baseline, and after Puff 2, when the time delay is (a) 1 s, (b) 0.5 s and (c) 0.1 s, for different stimulus strength settings. Error bars denote ± 1 standard deviation.

Figure 9.6 shows that a drop in surface temperature of the model eye was produced after the first stimulus is released (Puff 1). On cessation of the stimulus airflow, there was a partial recovery in the surface temperature to an inter-stimulus peak, which was called the Inter-stimulus baseline. This was followed by a second temperature drop after the release of the second stimulus (Puff 2).

The temperature change after Puff 1 was highest when the stimulus strength was 140 units and lowest when the strength was 70 units. For a stimulus strength of 210 units, the surface temperature change after Puff 1 was similar to the 140 units stimulus strength (Figure 9.7).

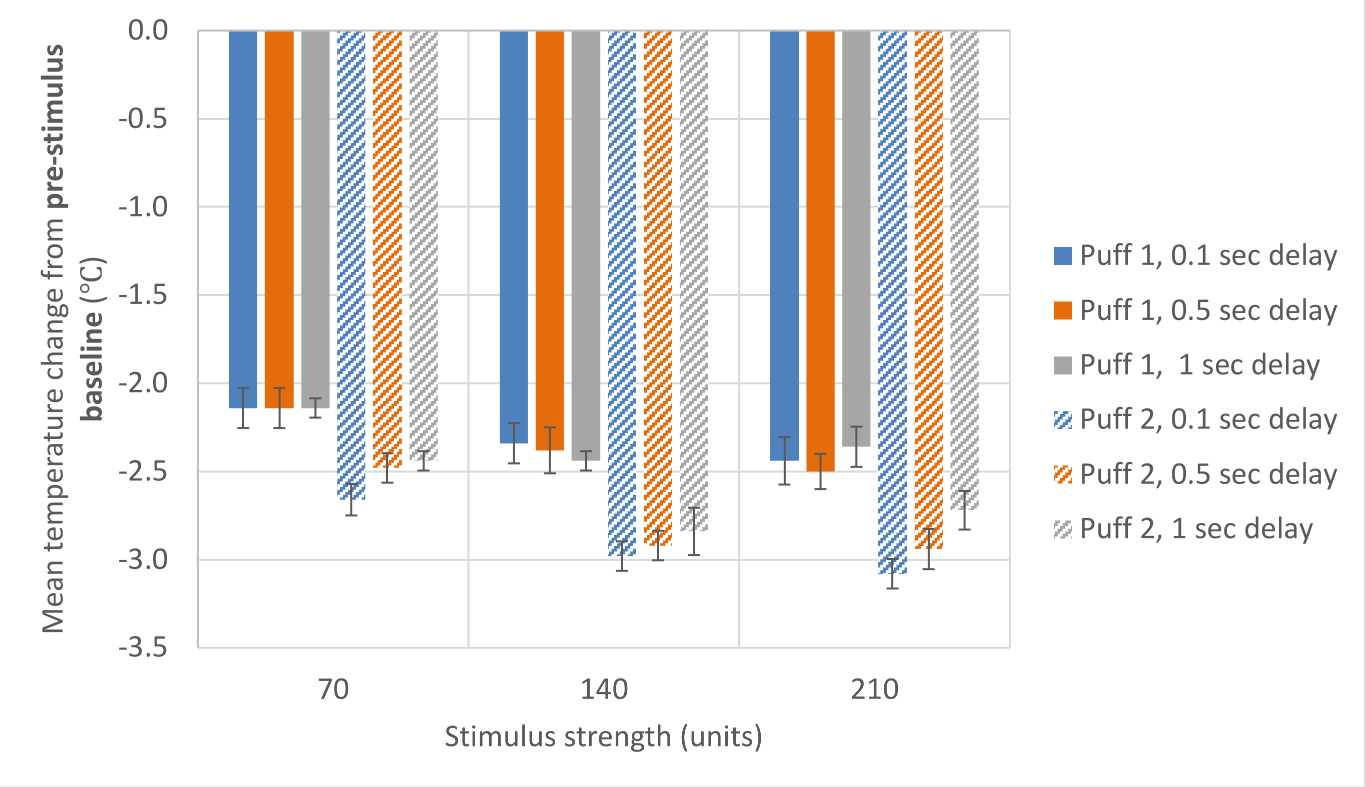

Figure 9.7: Mean maximum temperature change from the pre-stimulus baseline versus stimulus strength for each puff, for different stimulus delay settings (solid colours: Puff 1; patterned colours: Puff 2). Error bars denote ± 1 standard deviation.

Figure 9.7 also shows the cumulative effect of presenting the two stimuli with a short separating time delay. When temperature change was measured relative to the pre-stimulus baseline, there was a greater overall effect after the second puff than was possible with only the first puff. The same plateauing pattern in temperature change effect from 140 to 210 units was observed.

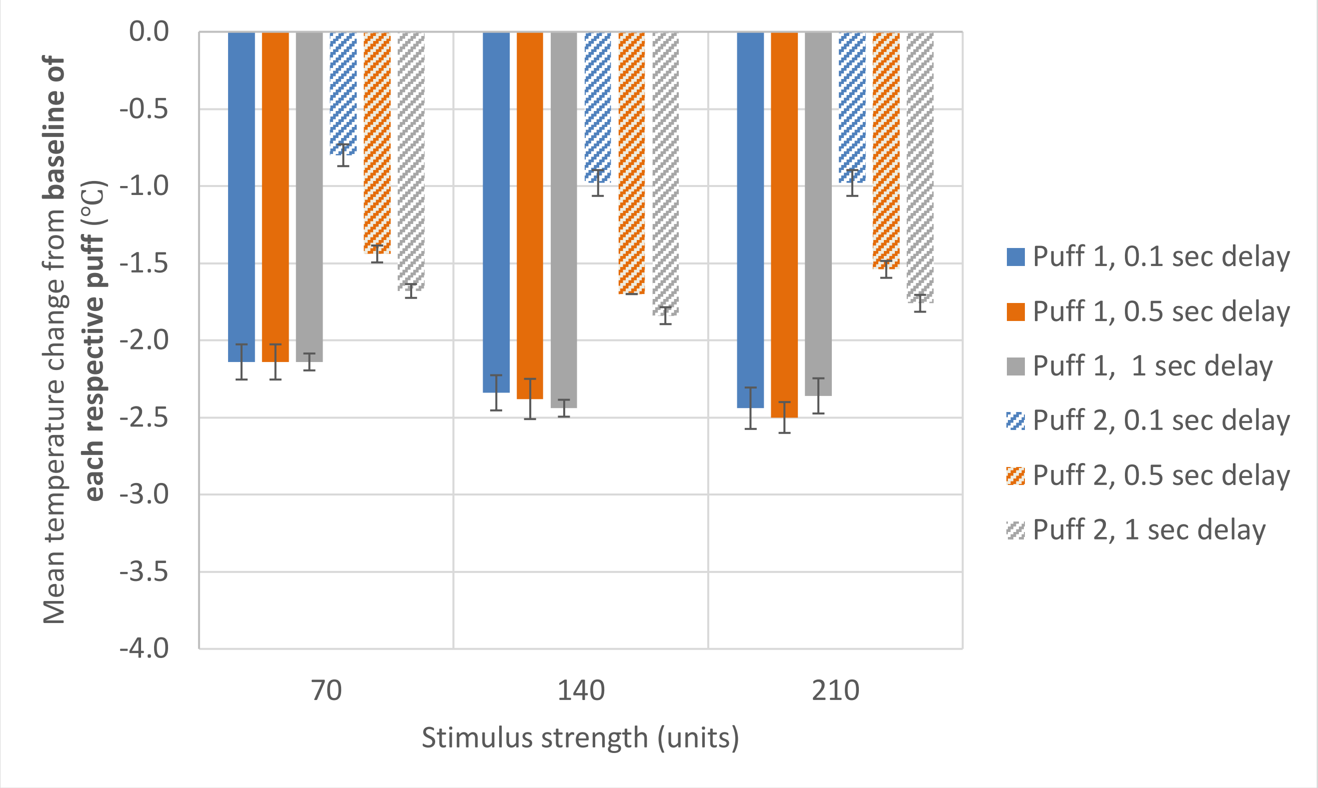

Figure 9.8: Mean maximum temperature change from <u>baselines of each respective puff</u> (Puff 1: pre-stimulus; Puff 2: inter-stimulus) versus stimulus strength for the different stimulus delay settings (solid colours: Puff 1; patterned colours: Puff 2). Error bars denote ± 1 standard deviation.

Figure 9.8 describes the maximum surface temperature change produced by each stimulus relative to its respective baseline (Puff 1: pre-stimulus baseline; Puff 2: inter-stimulus baseline). The temperature change effect of Puff 2 was less than that of Puff 1 for all test conditions, although with a longer inter-stimulus delay, there was a larger relative effect after the second stimulus was observed.

This effect was due to the partial recovery of surface temperature that was only possible between stimuli, as noted earlier. For a shorter time delay (0.1 seconds), compared to a longer time delay (1 second), less recovery was possible and thus, for Puff 2 after a shorter time delay, there was less capacity in the model eye for a temperature change to occur.

There was a significant effect between the time points of temperature measurement (Pre-stimulus baseline, Puff 1, Inter-stimulus baseline, and Puff 2) (rm-ANOVA, F (3, 12) = 7.648 x 10^3, $p < 0.001$, $\omega^2 = 0.980$). Post-hoc testing (Tukey correction) revealed significant differences between the temperatures at all temperature measurement timepoints (Table 9.3).

Temperature measurement time points compared		Absolute mean difference in temperature (°C)	p-value
Pre-stimulus baseline*	Puff 1*	2.320	< 0.001
Pre-stimulus baseline*	Inter-stimulus baseline*	1.371	< 0.001
Pre-stimulus baseline*	Puff 2*	2.784	< 0.001
Puff 1*	Inter-stimulus baseline*	0.949	< 0.001
Puff 1*	Puff 2*	0.464	< 0.001
Inter-stimulus baseline*	Puff 2*	1.413	< 0.001

Table 9.3: Post-hoc comparisons (Tukey correction) of absolute mean difference in temperature (°C) between each temperature measurement time point (significant results are in blue*).

The stimulus strength results for each time duration were combined for analysis of stimulus strength. There was a significant effect of stimulus strength (rm-ANOVA, F (2, 8) = 18.528, $p < 0.001$, $\omega^2 = 0.448$). Post-hoc testing revealed a significant difference between the temperatures at stimulus strengths 70 and 140 units, and 70 and 210 units, but not between 140 and 210 units (Table 9.4).

Stimulus strengths compared		Absolute mean difference in temperature (°C)	p-value
70 units*	140 units*	0.372	0.005
70 units*	210 units*	0.277	< 0.001
140 units	210 units	0.095	0.314

Table 9.4: Post-hoc comparison (Tukey correction) of absolute mean difference in temperature (°C) between each stimulus strengths (significant results are in blue*).

The time delay results for each stimulus strength were combined for analysis of time delay. A significant effect of time delay was found (rm-ANOVA, F (2, 8) = 6.624, p = 0.020, ω^2= 0.382). but post-hoc testing found no significant differences in the temperature change produced between the three time delay periods (Table 9.5).

Time delays compared		Absolute mean difference in temperature (°C)	p-value
1 second	0.5 seconds	0.347	0.167
1 second	0.1 seconds	0.442	0.066
0.5 seconds	0.1 seconds	0.095	0.574

Table 9.5: Post-hoc comparison (Tukey correction) of absolute mean difference in temperature (°C) for each time delay period (significant results are in blue*).

There was a significant interaction between the temperature measurement time point and the stimulus strength on the resulting temperature of the MLEO model eye (rm-ANOVA, F (6, 24) = 58.327, p < 0.001, ω^2= 0.166). Post-hoc testing revealed a significant difference between the temperatures at:

- Pre-stimulus baseline and Puff 1 for all stimulus strengths (t-value range: 24.558 to 171.582; all p-values (with Tukey correction) < 0.001);

- Pre-stimulus baseline and Puff 2 for all stimulus strengths (t-value range: 31.919 to 129.996; all p-values (with Tukey correction) < 0.001);
- Inter-stimulus baseline and Puff 2 for all stimulus strengths (t-value range: 14.749 to 196.000; p-value range (with Tukey correction): < 0.001 to 0.002);
- Puffs 1 and 2 when the stimulus strengths are identical (t-value range: 22.749 to 36.000; all p-values (with Tukey correction) < 0.001).
- Puff 1 at strengths 70 and 210 units (t-value: 10.000; p (with Tukey correction) $= 0.007$);
- Puff 2 at strengths 70 and 140 units (t-value: 10.375; p (with Tukey correction) $= 0.006$) as well as 70 and 210 unit (t-value: 13.202; $p = 0.002$).

There was a significant interaction between the temperature measurement time point and the time delay on the resulting temperature of the MLEO model eye (rm-ANOVA, $F(6, 24) = 263.425$, $p < 0.001$, $\omega^2 = 0.606$). Post-hoc testing revealed a significant difference between the temperatures at:

- Pre-stimulus baseline and Puff 1 for all levels of time (t-value range: 15.644 to 85.426; p-value range (with Tukey correction): < 0.001 to 0.002);
- Pre-stimulus baseline and Puff 2 for all levels of time (t-value range: 16.853 to 109.000; all p-values (with Tukey correction) < 0.001);
- Inter-stimulus baseline and Puff 2 for all levels of time (t-value range: 4.160 to 246.000; all p-values (with Tukey correction) < 0.001 to 0.015);
- Puffs 1 and 2 when the stimulus strengths are identical (t-value range: 20.788 to 66.000; all p-values (with Tukey correction) < 0.001).

9.5.4.3 Cooling zone diameter

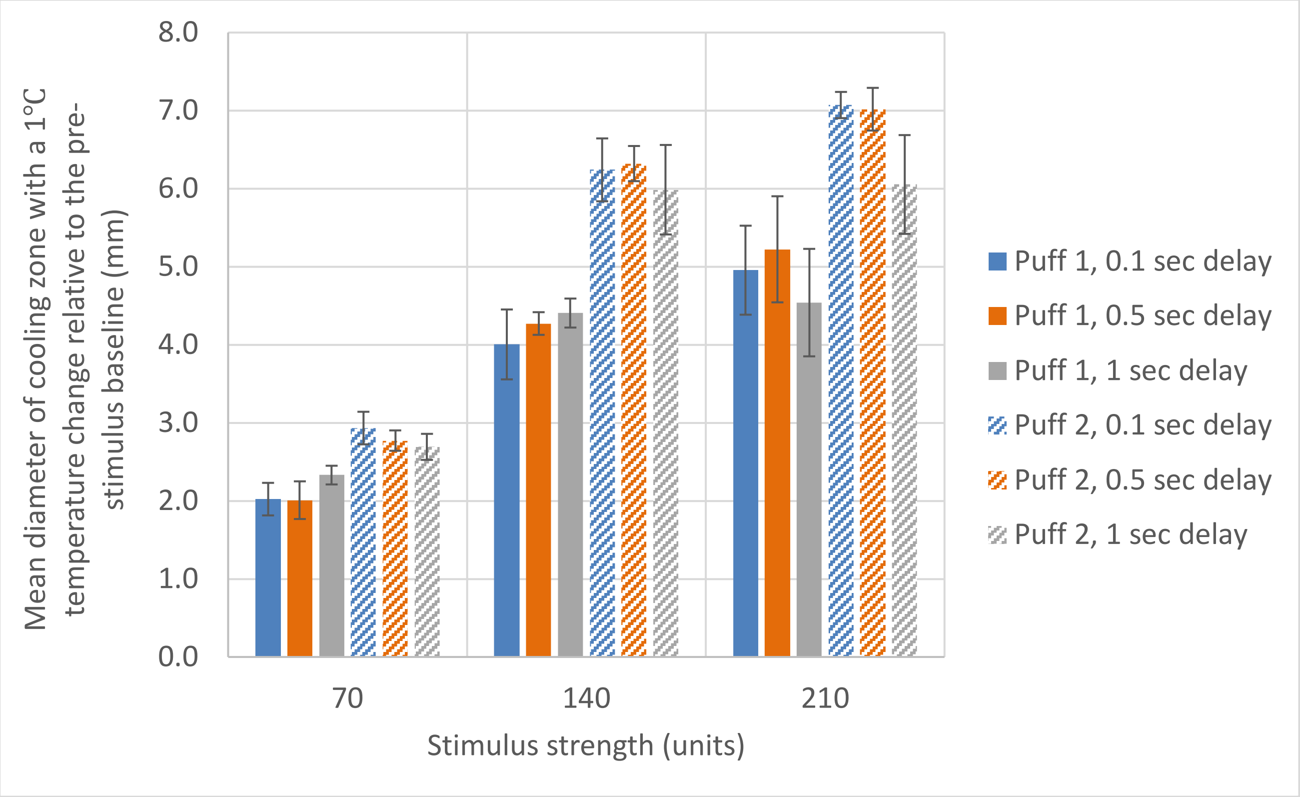

Figure 9.9: Mean diameter of cooling zone with a 1°C temperature change versus stimulus strength for the two puffs at different stimulus delay settings (solid colours: Puff 1; patterned colours: Puff 2). Error bars denote ± 1 standard deviation.

Figure 9.9 describes the spread of the stimulus over the model eye surface by reporting on the diameter of the cooling zone produced with a minimum 1°C change from the pre-stimulus baseline. As the strength of the stimulus (Puff 1) increases, the diameter measured also increases. Like the temperature change parameter, there was a cumulative effect from the two stimuli, which produced an overall larger diameter after the second stimulus (Puff 2). The same plateauing effect between 140 and 210 units was also observed.

There was a significant effect on the diameter of the minimum 1°C temperature change cooling zone between Puff 1 and Puff 2: absolute mean difference: 1.48°C, standard error: 0.064 (rm-ANOVA, F (1, 4) = 528.573, $p < 0.001$, $\omega^2 = 0.918$).

There was a significant effect from stimulus strength (rm-ANOVA based on Huynh-Feldt correction, F (3.560, 14.240) = 387.950, $p < 0.001$, $\omega^2 = 0.968$). Post-hoc testing revealed significant differences in the diameter of cooling zone between all stimulus strengths (Table 9.6).

Stimulus strengths compared		Absolute mean difference in cooling zone diameter with a minimum 1°C temperature change (mm)	p-value
70 units*	140 units*	2.747	< 0.001
70 units*	210 units*	3.350	< 0.001
140 units*	210 units*	0.603	0.021

Table 9.6: Post-hoc comparison (Tukey correction) of absolute mean difference in diameter of cooling zone with a minimum 1°C temperature change (mm) between each stimulus strength (significant results are in blue*).

There was no significant effect of time delay between stimuli on the cooling zone diameter with a 1°C temperature change (rm-ANOVA based on Huynh-Feldt correction, F (1.116, 4.462) = 3.492, p = 0.127, $\omega^2 = 0.131$).

There was a significant interaction between the cooling zone diameter with a minimum 1°C temperature change for each puff and stimulus strength (rm-ANOVA based on Huynh-Feldt correction, F (1.762, 14,420) = 42.991, $p < 0.001$, $\omega^2 = 0.600$). Post-hoc testing revealed significant difference for the cooling zone diameters for both puffs and all stimulus strength interactions (t-value range: -6.55 to -55.04; p-values range (with Tukey correction) < 0.001 to 0.016) **except:**

- Diameter of Puff 1 cooling zone when stimulus strengths were 140 and 210 units (Absolute mean difference: 0.677°C, standard error: 0.177, p (with Tukey correction) = 0.098).

- Diameter of Puff 2 cooling zone when stimulus strengths were 140 and 210 units (Absolute mean difference: 0.530·C, standard error: 0.144, p (with Tukey correction) = 0.111).

9.6 Experiment 2: Effect of spatial separation when multiple stimuli are simultaneously generated by two micro-blowers

9.6.1 Purpose

To determine the effect of spatial separation on surface temperature of a model eye when two stimuli of the same strength, generated by the Dolphin aesthesiometer, are simultaneously applied to the same surface location on a model eye.

9.6.2 Procedure

1. The green and blue micro-blowers were selected and each positioned in a such a way that the respective exit air-jets were focused on the central region of the MLEO model eye, but with the cooling zone of each exit air-jet separated by a distance of c. 1 cm on the model eye surface. Both exit air-jets were positioned 1 cm away from the model eye surface. Once the temperature of the model eye had reached 32°C, the MLEO Dolphin management software was set for each micro-blower to simultaneously deliver a stimulus of strength of 210 units for a duration of 1.0 second onto the surface of the model eye.
2. Infrared imaging of the temperature effect was recorded using the Teledyne FLIR A655sc infrared camera.
3. Stimulus strengths of 140 units and 70 units were also tested and steps 1 and 2 were repeated. The stimulus strengths were randomized in terms of the order of their delivery.

4. The micro-blower cooling zone separation was then changed to 0 cm so that the stimuli now over-lapped and steps 1-3 were repeated.
5. Five stimulus presentations were made for each stimulus strength and micro-blower separation combination.

9.6.3 Analyses

Data were tested for normality using the Shapiro-Wilk assumption test. Data were analyzed using parametric tests. More specifically, repeated measures ANOVA (rm-ANOVA) were conducted followed by Tukey HSD tests for post-hoc analysis. JASP version 0.13.1 (University of Amsterdam, Netherlands) and Jamovi 1.6.23.0 (Sydney, Australia) were used for data analysis procedures. A probability value of 0.05 or less was considered to be statistically significant.

9.6.4 Results

9.6.4.1 Separated stimuli

Stimulus strength of Green micro-blower (units)	**Stimulus strength of Blue micro-blower (units)**	**Pulse duration (s)**	**Test distance (cm)**	**Separation between the zones of cooling on the actual surface of the model eye (cm)**	**Mean maximum temperature change from baseline (Circle 1) (°C)**	**SD**	**Mean maximum temperature change from baseline (Circle 2) (°C)**	**SD**	**Mean diameter of zone with a 1°C temperature change (from baseline) (Circle 1) (mm)**	**SD**	**Mean diameter of zone with a 1°C temperature change (from baseline) (Circle 2) (mm)**	**SD**	**Average of Sum of diameters of Circles 1 and 2**	**SD**
70	70	1	1	1	-2.10	0.22	-1.88	0.24	1.65	0.31	2.08	0.54	3.72	0.81
140	140	1	1	1	-2.60	0.27	-3.38	0.13	3.38	0.10	4.51	0.17	7.89	0.13
210	210	1	1	1	-2.42	0.04	-3.00	0.10	3.66	0.08	5.13	0.15	8.79	0.11
70	70	1	1	0	-2.54	0.11			4.21	0.34				
140	140	1	1	0	-3.18	0.11			8.05	0.49				
210	210	1	1	0	-2.96	0.05			7.71	0.32				

Table 9.7: Mean maximum temperature change from the pre-stimulus baseline within the cooling zone, and diameter of the 1°C temperature change from baseline cooling zone (0 cm separation) or zones (1 cm separation), for the two different cooling zone separations.

9.6.4.1.1 Temperature change

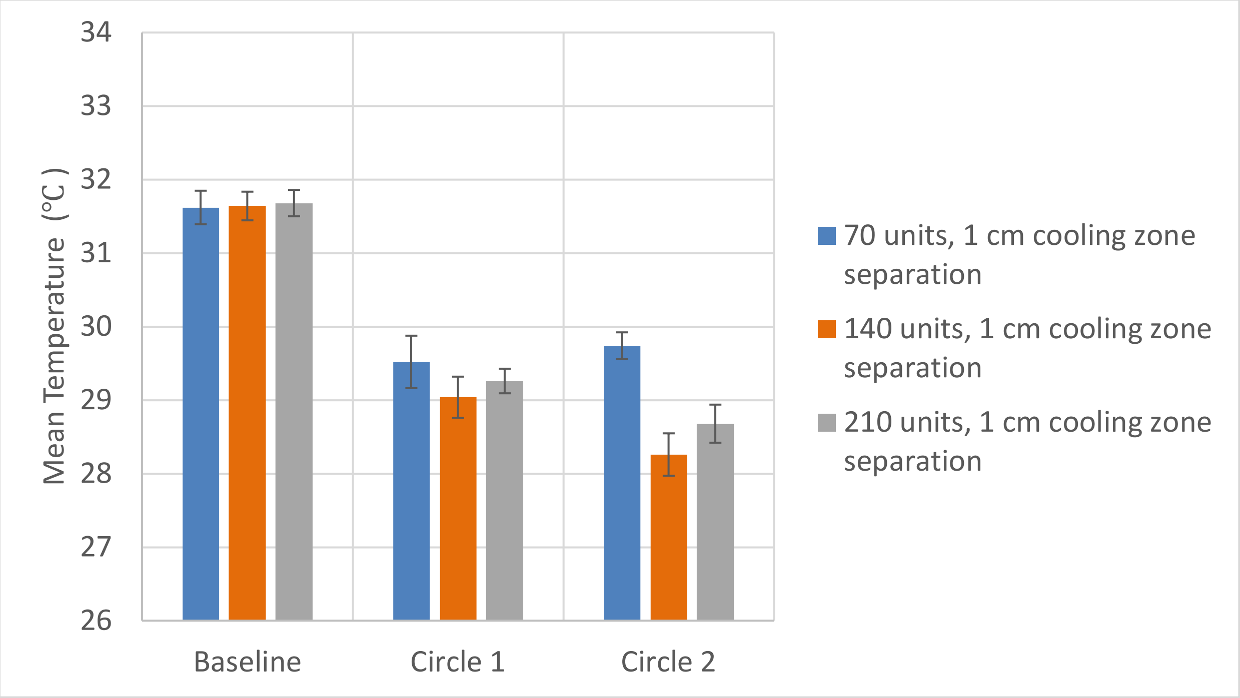

Figure 9.10: Mean temperature (°C) at the pre-stimulus baseline, and mean minimum temperature within Circles 1 and 2 for a <u>cooling zone separation of c. 1 cm</u> for different stimulus strength settings. Error bars denote ± 1 standard deviation.

Figure 9.10 shows that both stimulus air-jets were able to produce a cooling temperature change on the surface of the model eye. A greater temperature change was produced by the 140 units airflow.

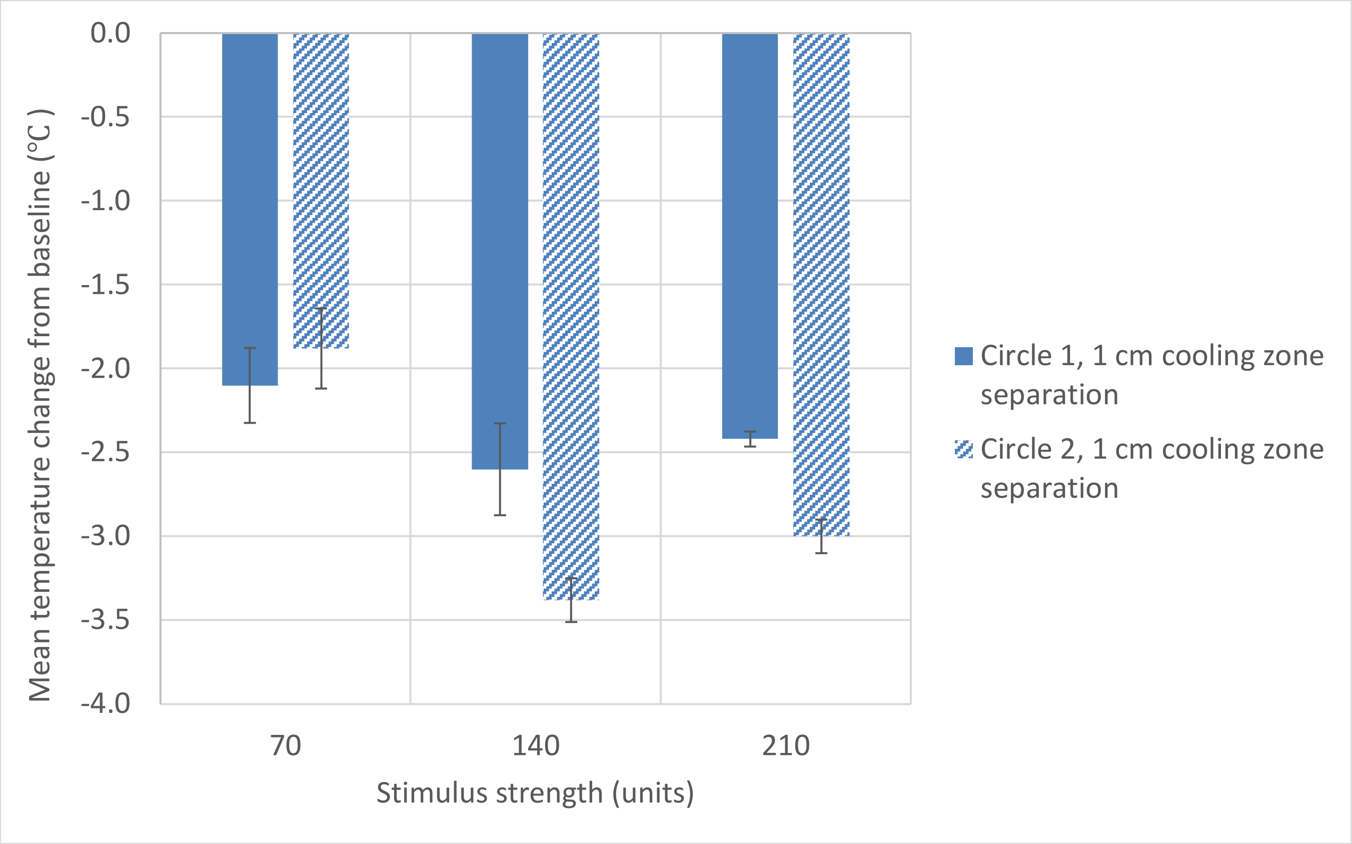

Figure 9.11: Mean maximum temperature change (°C) from the pre-stimulus baseline within Circles 1 and 2 versus stimulus strength (units) for a cooling zone separation of c. 1 cm. Error bars denote ± 1 standard deviation.

Figure 9.11 shows the mean maximum temperature change within each circle for each air-jet. A similar pattern as that observed in Chapter 8, and for Experiment 1, was again noted. As stimulus strength increases from 70 to 140 units, there is an increase in the temperature change for both air-jets. However, as the strength is further increased from 140 to 210 units, the temperature change decreases.

A difference in effect is also seen between the two micro-blowers used in this experiment. The temperature change is similar when the stimulus strength is 70 units, but at higher stimulus strengths, the blue micro-blower (Circle 2) produces a larger effect than the green micro-blower (Circle 1). This may reflect the output differences between the micro-blowers observed in Figure 4.3.

There was a significant effect of stimulus strength on the mean temperature change (rm-ANOVA, F (2, 8) = 56.745, $p < 0.001$, $\omega^2 = 0.877$). However, post-hoc testing revealed some variation in the significance of the effects for each micro-blower, especially when the difference reported was small (Table 9.8). This may be due to the small sample size and larger variation

Stimulus strengths compared		Circle/Micro-blower compared	Absolute mean difference in temperature change (°C)	p-value
70 units	140 units	Circle 1/Green micro-blower	0.320	0.107
70 units*	210 units*	Circle 1/Green micro-blower	1.280	0.003
140 units*	210 units*	Circle 1/Green micro-blower	0.960	< 0.001
70 units*	140 units*	Circle 2/Blue micro-blower	0.720	0.015
70 units	210 units	Circle 2/Blue micro-blower	0.400	0.227
140 units*	210 units*	Circle 2/Blue micro-blower	1.120	0.010

Table 9.8: Post-hoc comparison subset (using Tukey correction) of absolute mean difference in maximum temperature change (°C) for different stimulus strengths and the two micro-blowers (significant results are in blue*).

There was a significant effect of micro-blower type on the mean temperature change (mean difference: 0.140°C) (rm-ANOVA, F (1, 4) = 11.455, $p = 0.028$, $\omega^2 = 0.741$).

There was a significant interaction between the stimulus strength and micro-blower on the mean temperature change (rm-ANOVA, F (2, 8) = 52.854, $p < 0.001$, $\omega^2 = 0.930$). When the temperature change was compared between micro-blowers with the same stimulus strength, post-hoc testing revealed significant differences in the cooling effects produced (Table 9.9).

Stimulus strengths and circle/micro-blower interactions compared		Absolute mean difference in temperature change (°C)	p-value
70 units, Circle 1*	70 units, Circle 2*	0.500	0.017
140 units, Circle 1*	140 units, Circle 2*	0.540	0.025
210 units, Circle 1*	210 units, Circle 2*	0.380	0.001

Table 9.9: Post-hoc comparison sub-set (Tukey correction) of absolute mean difference in temperature change (°C) for different stimulus strength and micro-blower interactions (significant results are in blue*).

9.6.4.1.2 Cooling zone diameter

Figure 9.12 shows that as the stimulus strength increases, the cooling zone diameter also increases. The diameter of the cooling zone produced by the blue micro-blower (Circle 2) is consistently larger than that produced by the green micro-blower (Circle 1).

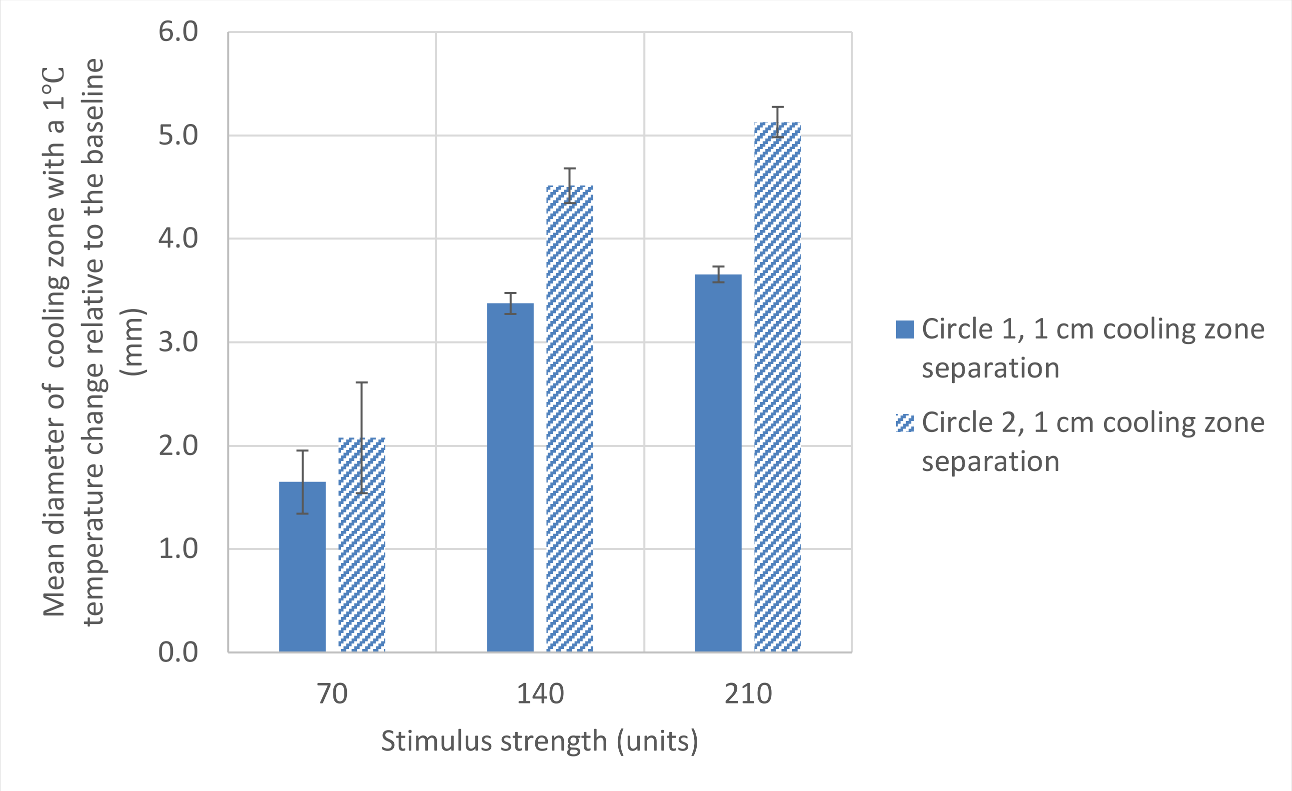

Figure 9.12: Mean diameter of cooling zone (mm) with a 1°C temperature change from baseline for <u>Circles 1 (blue micro-blower)</u> and <u>2 (green micro-blower)</u> versus stimulus strength (units), when the <u>cooling zone separation on the model eye is c. 1 cm</u>. Error bars denote ± 1 standard deviation.

There was a significant effect of stimulus strength on the mean diameter of the cooling zone produced with a 1°C temperature change from baseline (rm-ANOVA, $F(2, 8) = 355.069$, $p < 0.001$,

ω^2= 0.964). Post-hoc testing revealed the mean diameter was significantly different between all levels of stimulus strength for each micro-blower (Table 9.10).

Stimulus strengths compared		Circle/Micro-blower	Absolute mean difference in cooling zone diameter with 1°C temperature change (mm)	p-value
70 units*	140 units*	Circle 1/Green micro-blower	2.010	< 0.001
70 units*	210 units*	Circle 1/Green micro-blower	2.868	< 0.001
140 units*	210 units*	Circle 1/Green micro-blower	0.858	0.002
70 units*	140 units*	Circle 2/Blue micro-blower	1.300	0.043
70 units*	210 units*	Circle 2/Blue micro-blower	1.756	< 0.001
140 units*	210 units*	Circle 2/Blue micro-blower	3.056	0.002

Table 9.10: Post-hoc comparison subset (using Tukey correction) of absolute mean difference in diameter of cooling zone (mm) with a 1°C temperature change for different stimulus strengths and the two micro-blowers (significant results are in blue*).

There was a significant effect of micro-blower type on the mean diameter of cooling zone with a 1°C temperature change from baseline (rm-ANOVA, F (1, 4) = 38.794, p = 0.003, ω^2= 0.380). Post-hoc testing revealed the mean diameter was significantly different between the green and blue micro-blowers (Table 9.11).

Circle/Micro-blower compared	Absolute mean difference in cooling zone diameter with 1°C temperature change (mm)	p-value
Circle 1/Green micro-blower **-** **Circle 2/Blue micro-blower***	0.256	p = 0.003

Table 9.11: Post-hoc comparison (using Tukey correction) of absolute mean difference in cooling zone diameter (mm) with 1°C temperature change between the two micro-blowers (significant results in blue*).

There was a significant interaction between the stimulus strength and micro-blower on the mean cooling zone diameter with (rm-ANOVA, $F(2, 8) = 70.208$, $p < 0.001$, $\omega^2 = 0.890$). When the diameters were compared between micro-blowers with the same stimulus strength, post-hoc testing revealed a significant difference between the size of the regions of the model eye affected by the stimulus for all levels of strength (Table 9.12).

Stimulus strengths and circle/micro-blower interactions compared		Absolute mean difference in cooling zone diameter with 1°C temperature change (mm)	p-value
70 units, Circle 1*	70 units, Circle 2*	1.730	0.001
140 units, Circle 1*	140 units, Circle 2*	1.580	0.015
210 units, Circle 1*	210 units, Circle 2*	0.618	0.028

Table 9.12: Post-hoc comparison subset (using Tukey correction) of absolute mean difference in diameter of cooling zone (mm) with a 1°C temperature change for different stimulus strength and circles/micro-blowers interactions (significant results in blue*).

9.6.4.2 Overlapping stimuli

9.6.4.2.1 Temperature change

Figure 9.13 shows that the combined effect of the overlapping stimuli produced when the two exit air-jets are positioned to aim at the same location on the surface of the model eye. Since the cooling zones were overlapping, only one sampling circle was needed.

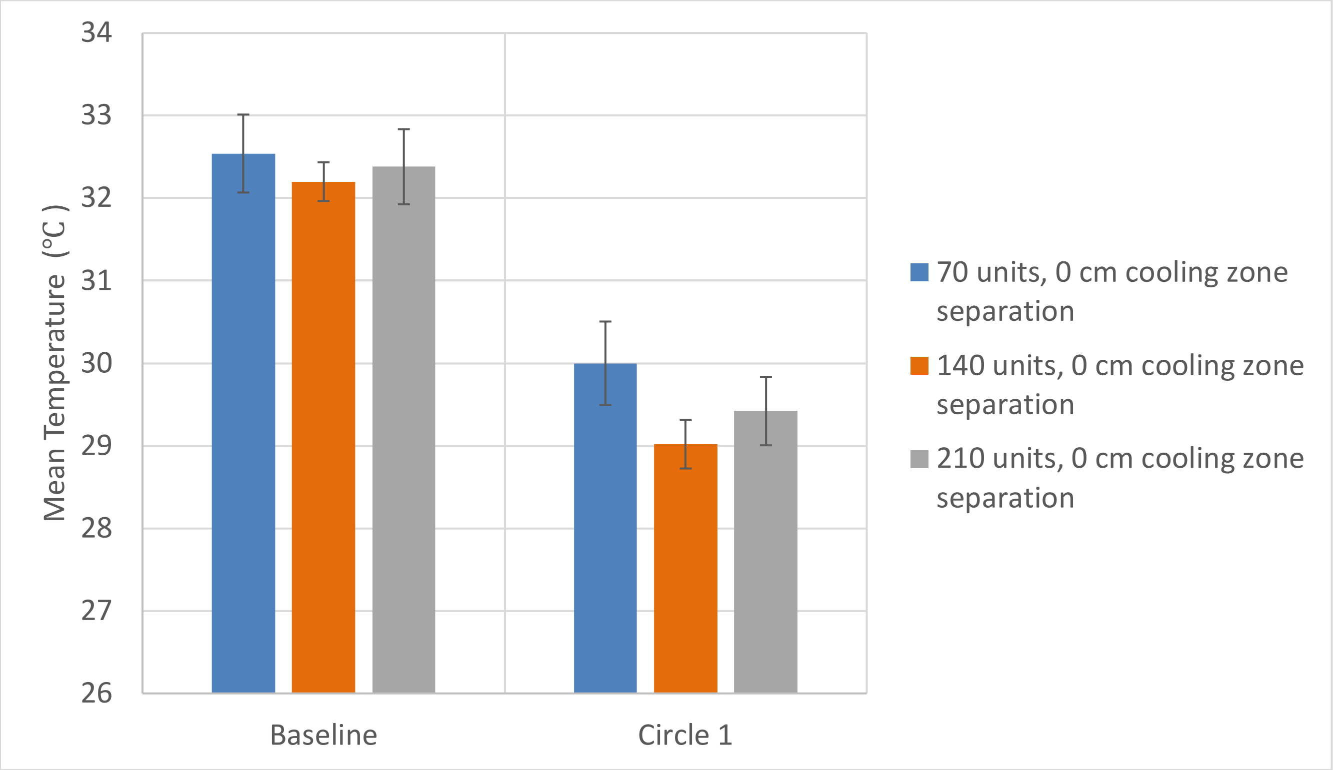

Figure 9.13: Mean temperature (°C) at baseline and mean minimum temperature within Circle 1 after both stimuli presentations, when the <u>cooling zones produced by the two micro-blower exit air-jets are overlapping</u>, for different stimulus strengths. Error bars denote ± 1 standard deviation.

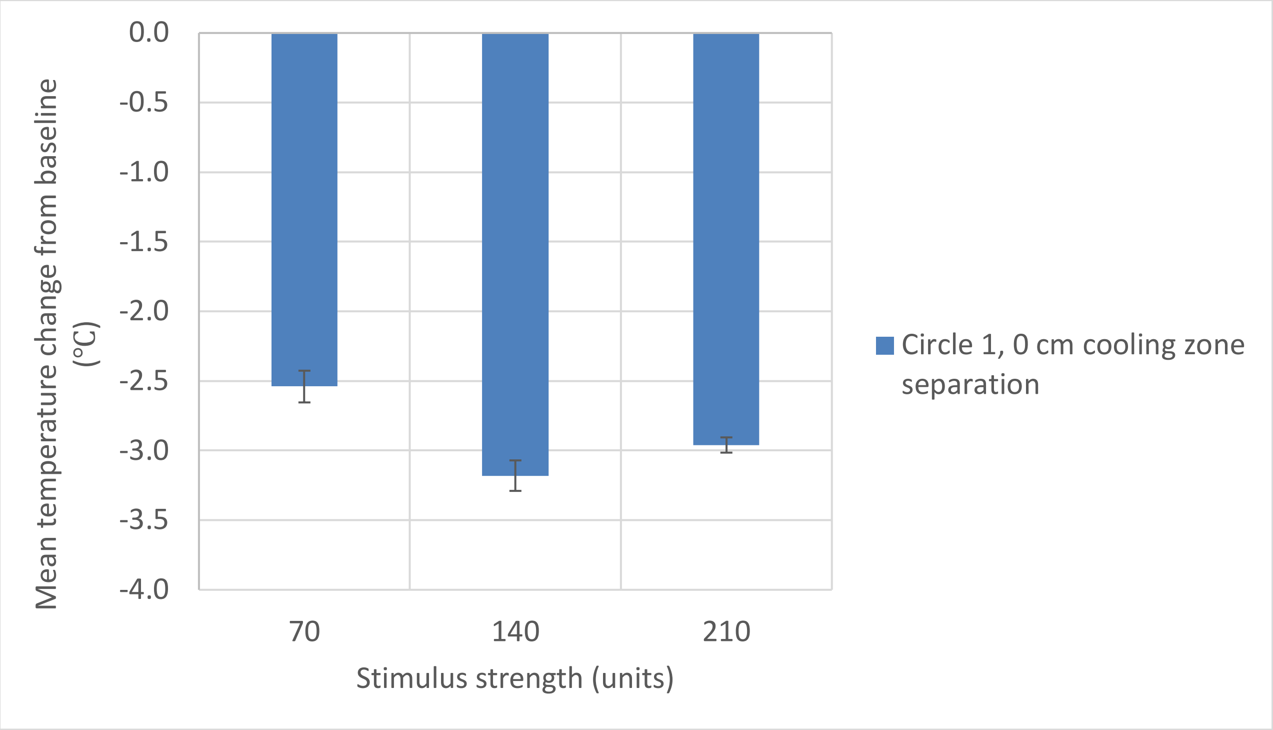

Figure 9.14: Mean maximum temperature change from baseline (°C) within Circle 1, when the <u>cooling zones produced by the two micro-blower exit air-jets are overlapping</u>, for different stimulus strengths (units). Error bars denote ± 1 standard deviation.

Figure 9.14 repeats the same trends noted in Figures 9.10 and 9.11. There was a significant effect of stimulus strength on the mean temperature change (rm-ANOVA, F (2, 8) = 47.343, $p < 0.001$, $\omega^2 = 0.881$). Moreover, post-hoc testing revealed a significant difference in the mean temperature changes between all levels of stimulus strength (Table 9.13).

Stimulus strengths compared		Absolute mean difference in temperature change (°C)	p-value
70 units*	140 units*	0.640	0.002
70 units*	210 units*	0.420	0.010
140 units*	210 units*	0.220	0.042

Table 9.13: Post-hoc comparisons (using Tukey correction) of absolute mean difference in temperature change (°C) for different stimulus strength (significant results are in blue*).

9.6.4.2.2 Cooling zone diameter

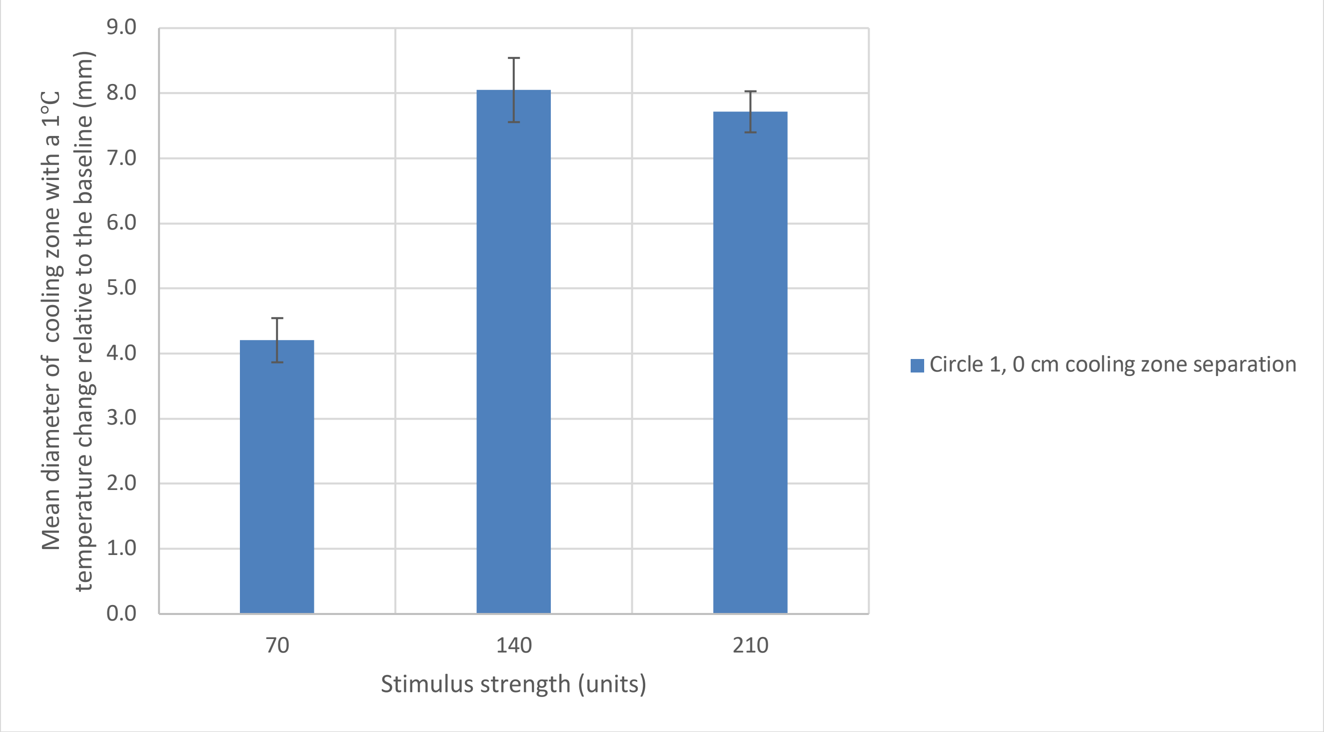

Figure 9.15: Mean diameter of cooling zone (mm) with a 1°C temperature change from baseline within Circle 1, when <u>the cooling zones produced by the two exit micro-blower air-jets are overlapping</u>, for different stimulus strengths (units). Error bars denote ± 1 standard deviation.

Figure 9.15 shows the combined effect of overlapping stimuli on the diameter of the cooling zone. Like the temperature change parameter, there is a cumulative effect from the two stimuli that produces a larger diameter as the strength of the stimulus increases from 70 to 140 units, and a plateauing effect observed between 140 and 210 units.

There was a significant effect for stimulus strength on the mean diameter of the cooling zone (rm-ANOVA, F (2, 8) = 115.514, $p < 0.001$, $\omega^2 = 0.952$). Post-hoc testing revealed the mean diameter was similar for stimulus strengths 140 and 210 units, and different for stimulus strength 70 units and both 140 and 210 units (Table 9.14).

Stimulus strengths compared		Absolute mean difference in diameter of 1°C temperature change zone (mm)	p-value
70 units*	140 units*	3.846	< 0.001
70 units*	210 units*	3.508	< 0.001
140 units	210 units	0.338	0.626

Table 9.14: Post-hoc comparisons (using Tukey correction) of absolute mean difference in diameter of cooling zone (mm) with a 1°C temperature change for the different stimulus strengths (significant results in blue*), when the cooling zones are overlapping.

9.6.4.3 Comparison of cooling zone diameters depending on stimulus separation

A comparison can be made of the single cooling zone diameter produced by the overlapping stimuli with the combined diameters of the two separate cooling zones produced by the separated stimuli. Figure 9.16 shows that the diameters are similar for a stimulus strength of 140 units, but are larger for the overlapping stimuli at a stimulus strength of 70 units and larger for the separated stimuli at 210 units.

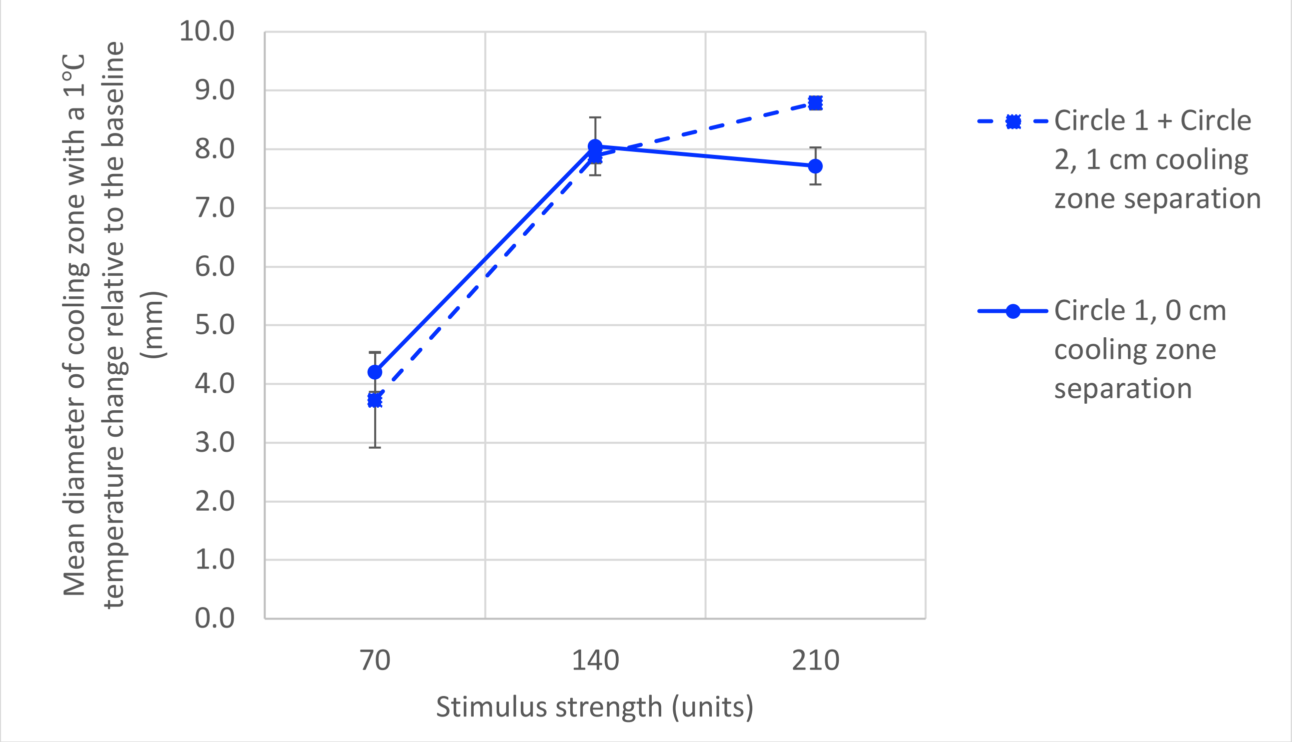

Figure 9.16: Mean diameter of cooling zone (mm) with a 1°C temperature change from baseline (mm) for the overlapping cooling zone (solid line) compared to the sum of the diameters for the separated cooling zones (broken line) for different stimulus strengths (units). Error bars denote ± 1 standard deviation.

There was a significant effect of stimulus strength on the diameter (rm-ANOVA, F (2, 8) = 276.014, $p < 0.001$, ω^2= 0.956).

There was no effect of cooling zone separation on the 1°C zone diameter (rm-ANOVA, F (1, 4) = 1.588, $p = 0.276$, ω^2= 0.064). However, there was a significant interaction between the strength and cooling zone separation on the diameter (rm-ANOVA, F (2, 8) = 164.903, $p < 0.001$, ω^2= 0.957). Post-hoc testing revealed that the diameter of the overlapping zone of cooling was larger than the cumulative diameters of the separated stimuli at smaller stimulus strengths. When the strength was 140 units, the diameters for the overlapping and separate cooling zones were equivalent, but as the stimulus strength increased to 210 units, the diameter for the 0 cm separation was smaller (Table 9.15).

Stimulus strengths and cooling zone separation interactions compared		Absolute mean difference in diameter of zone with a 1 °C temperature change (mm)	p-value
70 units, 0 cm*	70 units, 1 cm*	3.846	0.001
140 units, 0 cm *	140 units, 1 cm*	3.988	0.006
210 units, 0 cm*	210 units, 1 cm*	0.902	< 0.001

Table 9.15: Post-hoc comparison subset (using Tukey correction) of absolute mean difference in diameter of cooling zone with a 1°C temperature change for the different stimulus strength and cooling zone separation interactions (significant results in blue*).

9.7 Discussion

9.7.1 Temporal stimulus separation

Experiment 1 investigated the ability of the aesthesiometer to provide stimuli with a temporal delay between stimuli. The study found that a single micro-blower could be used to produce:

1. The delivery of two time-separated stimuli at the same location on the surface of the model eye;
2. A localised cooling at that location by each stimulus independently;
3. An increased cumulative temperature change on the surface of the model eye after the second stimulus;
4. A measurable time delay between the maximum temperature cooling produced by each stimulus.

Figure 9.6 showed that a decrease in surface temperature in the model eye was produced upon the release of each stimuli (Puff 1 and Puff 2, respectively). The mechanism for this temperature decrease is convective cooling, as discussed in Chapter 8.

Each puff independently produces a temperature change, as determined by measuring from the respective pre-stimulus and inter-stimulus baselines. However, a greater overall temperature change was noted after Puff 2 due to the cumulative effect from Puff 1 on the temperature change produced after Puff 2 (Figure 9.7). The effect of Puff 1 on the temperature change after Puff 2 can be noted in the inter-stimulus baseline between stimulus presentations. The inter-stimulus baseline temperature is lower than the pre-stimulus baseline temperature since there is insufficient time for the surface temperature of the model eye to recover back to the pre-stimulus level (~32°C). It is therefore no surprise that the effective temperature change after Puff 2 is greater than that after Puff 1, because the surface of the model eye is already affected by Puff 1, thus giving Puff 2 a head-start in producing a larger overall temperature change for the model eye surface. These trends are supported by the results of the repeated measures ANOVAs.

The limited inter-stimulus recovery also has an impact on the size of temperature change produced by the second puff (Figure 9.8). Generally, Puff 2 produces a smaller level of temperature change in comparison to Puff 1. This effect is emphasized by the effect of the inter-stimulus time delay. A shorter time delay permits less recovery in the model eye surface temperature, and so the temperature change produced after a 0.1 second time delay is less for all stimulus strengths than that produced after a 1 second time delay. This effect reveals an underlying limitation of the model eye as a method for simulating the stimulus: the model eye is unable to rapidly recover its baseline temperature in the same way that an eye can.

Figure 9.7, which focuses on the temperature change that occurs relative to the pre-stimulus baseline temperature, shows that as the stimulus strength increases from 70 to 140 units, the temperature change after the release of Puff 1 increases. The increase in temperature change can be attributed to an increase in airflow rate, and hence an increase in the amount of convective cooling, which results in a drop in temperature. However, as the stimulus strength is increased from 140 to 210 units the temperature change appears to plateau. A similar effect after Puff 2 is observed in Figure 9.6. These effects are supported by the results of the repeated measures ANOVAs. This plateauing effect is more evident as the time delay between the two stimuli decreases. This reveals a second limitation with the model eye: there is a limit to the amount of temperature change that can be produced by the airflow stimulus over the model eye surface. It appears that this limit occurs as we move towards the higher flow rate (210 units).

As in Chapter 8, another way to look at the time delay effects of the stimulus on the model eye is to use the thermal profile plots (V-profile) (Figure 9.2). This allows us to determine the spread of the airflow over the model eye, as revealed by the temperature change produced by the stimulus. Figure 9.9 reveals that, as the strength of the first stimulus increases, the diameter of cooling zone also increases. With a larger stimulus intensity, the airflow increases and spreads over the surface of the model eye producing convective cooling over a wider area. The same plateauing effect observed in temperature change when increasing stimulus strength from 140 to 210 units was also seen in diameter change. In combination with the temperature change results, this reveals a further limitation of the model eye: there is a limit to the amount of temperature change that can be produced by the airflow stimulus over the model eye surface.

It is possible that, at high airflow rates, the airflow can no longer remain attached to the surface of model eye as much as it did before, thus causing less interaction between the airflow stimulus and the model eye, and therefore less convective cooling. This fluid or jet projection phenomenon cannot be confirmed without performing additional complementary tests/experiments.

Statistically, there was no effect of time delay on the diameters. However, there were interactions between the time delay and the diameters of Puff 1 and Puff 2, and the results of the interactions support the graphical findings reported.

Overall, Experiment 1 allowed the effect of time delay to be determined when two stimuli of the same strength are produced by the Dolphin aesthesiometer and applied to a model eye. The small error bars in in Figures 9.6 to 9.9 also speak to the relative consistency of the instrument.

9.7.2 Spatial stimulus separation

Experiment 2 investigated the ability of the aesthesiometer to simultaneously provide two stimuli, each capable of producing a temperature change on the surface of the model eye. The study found that a combination of two micro-blowers could produce:

1. The delivery of two spatially separated stimuli on the surface of the model eye;
2. A localised cooling at that location by each stimulus independently;
3. An increased cumulative temperature change on the surface of the model eye where the two stimuli overlap;
4. A measurable area of reduced inter-stimulus temperature change between the maximum temperature cooling produced by each stimulus.

Figure 9.10 shows that the Dolphin aesthesiometer can deliver two simultaneous stimuli to the model eye, and that each is capable of producing a localized area of temperature change on the surface of the eye. A similar pattern of temperature change and cooling zone diameter with increasing airflow is observed with both areas of cooling, as was noted in Chapter 8 and Experiment 1.

A difference in temperature change produced and cooling zone diameter was also noted between the two micro-blowers. These trends are supported by the results of the repeated measures ANOVAs. This may be due to inherent differences between the two micro-blowers, as identified in Chapter 4, but may also be due to variation in how the airflow from each air-jet impacts the surface of the model eye. Although an effort was made to have similar positioning angles for both exit air-jets, this was not controlled, nor was there precision in ensuring that each airflow impacted the surface of the eye at the same incident angle. Any differences in these angles could have produced the variations noted.

When the cooling zone separation is reduced, the stimulus from each exit air-jet can be made to overlap to produce a single zone of cooling (Figures 9.13 to 9.15), within which a cumulatively greater temperature change and cooling zone diameter is produced than for each stimulus individually.

One reason for performing this experiment was to see if the aesthesiometer could be used to study spatial summation in the cornea. To do so, the question was asked whether two stimuli of the same strength, delivered at the same location or at two separate locations, could produce the same cumulative change in temperature or cooling diameter. To do so, the results from the separated stimuli were added and compared to that of the overlapping stimuli. Figure 9.16 shows that at a stimulus strength of 70 units, the cooling zone diameter was larger for overlapping stimuli; that the diameters were very similar for both overlapping and cumulative separated stimuli at 140 units, and that at 210 units, the diameter for the overlapping stimuli decreased relative to the cumulative separated stimuli. These trends are supported by the results of the repeated measures ANOVAs.

These differences in performance may be due to the limitations in the model eye noted earlier. At low flow rates, smaller temperature change effects are produced by each individual stimulus, ensuring that the temperature change limits of the model eye are not reached. Thus, two simultaneous stimuli at 70 units at the same location can combine to produce a cumulatively larger effect (similar to that seen in Experiment 1), in comparison to the two separated stimuli which must individually produce a temperature change. When the stimulus strength increases to 140 units, the cumulative effect from the overlapping stimuli reaches the capacity for change in the model eye, and instead the separated stimuli can individually produce a stronger effect. When the 210 units strength stimuli are delivered, the effect of the airflow from the overlapping stimuli exceeds the thermal capacity of the model eye, whereas the separated stimuli are each able to produce a larger effect.

As previously mentioned, the Dolphin aesthesiometer was based on the design of the Non-Contact Corneal Aesthesiometer (NCCA). According to the aesthesiometry literature, when the NCCA was positioned 1 cm away from the human eye, subjects were able to detect temperature changes of-0.32 to -1.72°C (Murphy et al., 1999b). Given that, at the same test distance, the Dolphin aesthesiometer produced temperature changes of -0.8 to -3.08°C (Experiment 1), and -1.88 to -3.18°C (Experiment 2), it is highly plausible that these temperature changes would be detected by the human cornea. However, *in vivo* studies would need to be conducted to be sure of this.

Overall, Experiment 2 showed that this novel instrument is capable of delivering two simultaneous stimuli to the MLEO model eye. However, factors such as the angle at which the exit air-jets are positioned and the actual separation between the stimuli on the surface of the model should be carefully considered in instrument set-up. Whilst both factors would provide more experimental control, the latter is important to ensure that the central region of the model is stimulated. This will become extremely crucial for *in vivo* studies, since the sensitivity is considered to be greater in the central region of the cornea compared to the periphery because of the anatomical distribution of the never fibers in the ocular structure (Millodot, 1984). In addition, since the normative corneal diameter of the adult human is 11 mm (horizontally) and 12 mm (vertically) (Mashige, 2013), accurate alignment of the stimulus on the cornea is important. In comparison, for the MLEO model eye, the diameter of the scleral lens is 15 mm, and its LED dome light below the lens is 20 mm (Wong, 2017). This means that when the two separate cooling zones were formed (cooling zone separation of c. 1 cm), the stimuli were not exactly in the central region of the model eye. Therefore, pilot *in vivo* studies should be performed to improve alignment of the air-jets to ensure that only the central corneal innervation is sampled.

Whilst the novel instrument offers the conditions to potentially study both temporal and spatial summation in the future, further studies with increased sample size and additional parameter measurements (such as a wider range of time delays, angle of separation between the air-jets and actual separation between stimuli on the surface being stimulated) should be performed. These studies can be done *in vitro* or *in vivo*. If performed *in vitro* it is recommended that the Ocublink (Ocublink, Inc., Centre for Ocular Research & Education, School of Optometry and Vision Science, University of Waterloo), which can be heated to OST and simulate physiological factors of blinking, such as tear flow, be used as it would provide a better model of what would happen on the eye (Phan et al., 2016; Phan et al., 2019). However, it is important to be mindful that models are not substitutes for the real eye, and summation is a neurophysiological concept, which ultimately must be studied *in vivo*.

9.8 Conclusion

This study confirms that the Dolphin aesthesiometer can deliver multiple stimuli either simultaneously or with time delay between them. With some complementary studies and calibration, these conditions make it a potential aesthesiometer to pursue summation studies *in vivo*.

CHAPTER 10: SUMMARY, CONCLUSIONS AND FUTURE DIRECTIONS

10.1 General summary

This thesis reports on the development and use of a novel air-based aesthesiometer, known as the Dolphin Aesthesiometer. The instrument was designed around a collection of micro-blowers (Murata^{TM} Manufacturing Co., Japan) under software management, which provides refined control of airflow rate and duration. It is the first aesthesiometer of its kind capable of delivering multiple stimuli that are either separated by a time delay or spatial separation, or both. Another unique design quality is the fact that it is the first portable and lightweight gas-jet aesthesiometer. These properties offer benefits not seen in other gas-jet aesthesiometers.

The studies described were conducted to: verify the accuracy and consistency of the customized software used to control the micro-blowers, which form the main hardware of the aesthesiometer (Chapter 4); and to characterize the stimulus generated by the instrument, whilst also relating it to current round air-jet theory (Chapters 5 to 8).

The software control system was validated and the accuracy of the duration setting was verified. In terms of the stimulus characteristics, the stimulus airflow is coherent for a wider range of distances, which extend beyond that of typical test distances used in aesthesiometry. Moreover, this is especially the case when a nozzle is applied, as it adds to the unidirectionality of the airflow. Being able to position the exit air-jet of the aesthesiometer at further distances might help to promote subject compliance.

In keeping with round air-jet theory, the spread rate is the same with or without a nozzle, and is independent of strength, which further speaks to the coherent nature of the airflow. In addition, it could also mean that once certain factors are controlled, there is a higher probability that the same region of the cornea would be stimulated with repeated trials. Another important characteristic of the stimulus is that the amount of airflow dispersion when it encounters a surface or boundary is dependent on the strength of the stimulus.

The multiple air-jet feature of the aesthesiometer was exploited when performing *in vitro* studies using a model eye (Chapter 9). This allowed an assessment of whether the instrument has the potential to be used in future *in vivo* studies on neural signal summation at the corneal level, which would allow a better understanding of how the corneal nerves work at the neuroscience level.

The studies in Chapters 7 and 8 showed that the mode of stimulus has two components: force and temperature change (thermal). Given that the force applied was small and that the temperature changes produced are most like be detected by a human cornea, it is most likely that the chief mode of stimulation is thermal. However, *in vivo* testing would be required to be certain.

The instrument can generate stimuli separated by time and space. Furthermore, as the time delay between two stimuli, or the separation distance between the stimulus application target points are decreased, there is cumulative effect of the stimuli, which was manifested as a more pronounced temperature change and wider areas being stimulated.

The consistency and the repeatability of the stimulus was verified in all the experiments, and this was extended to cases in which multiple puffs were generated. The studies also highlighted the need for a nozzle in order to have more control of the dispersion, and to be sure that only the cornea is stimulated. The modified nozzle system, which consisted of a brass nozzle attached to the Tygon tubing using a silicone adapter, offered the rigid structure needed.

Therefore, the four chief objectives of this thesis were successful met:

1. To develop an aesthesiometer capable of delivering air-based stimuli that produce a cooling stimulus to the corneal nerves;
2. To investigate and describe the mode of stimulation produced by the new aesthesiometer;

3. To investigate that the new aesthesiometer is capable of delivering multiple stimuli of the same or different intensity simultaneously to the ocular surface;
4. To investigate that the new aesthesiometer is capable of delivering repeat stimuli of the same or differing intensities in a controlled time separated sequence to the ocular surface.

10.2 Optimal test distance and stimulus duration for the Dolphin Aesthesiometer

There is a lack of standardization among the various non-contact gas aesthesiometers due to the mode of simulation, and to variations in stimulus duration and distance from the ocular surface, which makes it difficult to compare corneal threshold measurements across instruments. According to the literature, when the Non-Contact Corneal Aesthesiometer (NCCA) presents a stimulus, it lasts for 0.9 seconds and its probe was positioned 1 cm from the eye (Murphy 1996; Murphy et al., 1996; Murphy et al. 1998). The Noncontact pneumatic esthesiometer, which was based on the NCCA, was also positioned 1 cm from the ocular surface, but had an air pulse duration of 0.6 seconds (Vega et al., 1999). With the Belmonte Gas Aesthesiometer, the distance between the probe and cornea was 0.5 cm and the stimulus duration ranged from 1 to 4 seconds (Stapleton et al., 2004; Nosch 2015; Nosch et al., 2017).

In terms of the optimal stimulus duration for the Dolphin aesthesiometer, the studies reported in this thesis provide a series of conclusions. Chapter 4 showed that the stimulus management software produced a consistent output ensuring that a reliable stimulus duration could be delivered. Chapters 5 and 6 found that the dispersion of the stimulus and the force generated by the instrument varied with airflow rate, but were consistent for each airflow rate and not affected by changes in the stimulus duration. However, when looking at the thermal effects of the stimulus in Chapter 8, the temperature change produced for each airflow rate was found to significantly increase as the duration increased. This illustrates the thermal mode of stimulation of the airflow on the model eye surface. These results indicate that any stimulus duration could be used. However, from an aesthesiometry perspective, a duration of 1 second might be best since a duration of 1.5 seconds or greater may cause drying of the human tear film with repeated applications, and durations as small as 0.5 seconds may be too fast for human participants to detect (Murphy, 1996).

With respect to the optimal test distance, Chapter 5 found that airflow coherence was maintained for distances up to 5 cm from the air-jet exit when no nozzle was applied, and 9 cm when the Tygon nozzle was attached. Whilst the test distance had no effect on the dispersion of the stimulus in Chapter 6, there was a weak association between the test distance and the peak and steady state forces measured in Chapter 7. The test/working distances used in Chapter 7 were 1.0, 1.5, and 3.0 cm. Based on these results, a test/working distance of 1 cm was selected and used for Chapters 8 and 9. Distances less than 1 cm were not chosen in order to prevent the airflow from being influenced by any turbulence that might be created by the backflow of the air from the surface. In addition, since the nozzle system was modified after Chapter 6, and therefore the exact point of transitioning from coherent to turbulent flow was not known for the modified system, it was thought best not to use the 1.5 and 3 cm distances in an effort to avoid any chance of being too close to the point where the airflow transitions into turbulent flow.

In terms of future aesthesiometer studies a test distance of 1 cm, and stimulus duration of 1 second can be used. However, it may be best to run a pilot study on human subjects to ensure that these parameters are ideal for *in vivo* experiments (Murphy, 1996).

10.3 Strengths and Limitations

The studies have shown the need for calibration between each micro-blower, and this was particularly evident by the discrepancies in output voltage and temperature change produced by each micro-blower. Calibration could help to eradicate the disparity among the micro-blowers, and may even ensure that a wide range of stimulus strengths could be used with increased precision.

One other significant factor that affected many of the *in vitro* studies was the limitation of the MLEO model eye to simulate the thermal heat transfer aspect of the human eye. Whilst the model eye could be heated to ocular surface temperature (OST), the results of the thermal experiments indicated that the model may have reached it maximum capacity for heat exchange at some of the higher stimulus strengths used. Furthermore, it was not truly representative of the ideal model as it had a dry surface, and therefore could not simulate the tear film and the evaporative effects that would have occurred in human subjects. Despite this, the thermal component of the stimulus could still be described, and it was shown that the aesthesiometer could provide the conditions needed to investigate summation in the cornea.

The Dolphin aesthesiometer is the first portable and lightweight gas-jet aesthesiometer capable of delivering multiple stimuli separated by a time delay or spatial separation. These characteristics are not seen in current gas-jet aesthesiometers.

10.4 Future work

10.4.1 Calibrating the Dolphin aesthesiometer

As previously mentioned, the results of Chapter 4 to 9 highlighted the need for instrument calibration. Calibration can be done by generating a graph of the predictor variable or, in the case of this thesis, the stimulus strength versus the outcome variable. However, the regression equations obtained in thesis can also be used to calibrate the instrument. Table 10.1 below summarizes the multiple linear regression equations obtained throughout this thesis.

Chapter/ Experiment	Significant predictors	Multiple linear regression equation
Chapter 6 (Airflow dispersion on a surface)	• Stimulus strength • Presence or absence of a nozzle	Powder displacement diameter (PDD) = + 0.567 + 0.004 (strength) - 0.164(distance) - 0.339(nozzle) + 0.108 (duration), where nozzle is coded as 0 = no nozzle attached and 1 = a nozzle attached to the exit air-jet.
Chapter 6 (Airflow dispersion on a surface)	• Stimulus strength • Presence or absence of a nozzle • Micro-blower type	Powder displacement diameter (PDD) = + 0.941 + 0.004 (strength) - 0.862(nozzle) + 0.106(micro-blower type) where nozzle was coded as 0 = no nozzle attached and 1 = a nozzle attached to the exit air-jet; and the micro-blowers were coded as 0 = yellow, 1 = purple, and -1 = green.
Chapter 7 (Verification of stimulus force component)	• Stimulus strength • Presence or absence of a nozzle • Test/working distance	Peak force (PF)= $-1.08 \times 10^{-4} + 3.04 \times 10^{-6}$ (strength) + 4.95×10^{-5} (distance) - 2.70×10^{-4} (nozzle) - 1.41×10^{-6} (duration), where nozzle is coded as 0 = no nozzle attached and 1 = a nozzle attached to the exit air-jet. Steady state force (SSF) = $-1.02 \times 10^{-4} + 2.92 \times 10^{-6}$ (strength) + 4.92×10^{-5} (distance) - 2.56×10^{-4} (nozzle) - 2.80×10^{-6} (duration), where nozzle is coded as 0 = no nozzle attached and 1 = a nozzle attached to the exit air-jet.
Chapter 8 (Verification of stimulus thermal component)	• Stimulus strength • Stimulus duration	Temperature change from baseline = - 1.158 - 0.007 (strength) - 0.980 (duration) Diameter of the zone with a 1°C temperature change = + 3.881 + 0.018 (strength) + 0.849 (duration)

Table 10.1: Summary of the multiple linear regression equations obtained throughout this thesis.

Two equations were generated for Chapter 6. The first equation involved using a single micro-blower, whereas the second equation incorporated the various micro-blower types. Despite being the only experiment to provide an equation that includes all three micro-blower types, calibrating the instrument based on that regression equation is not appropriate. This is because the equation is based on the dispersion of lycopodium powder on a flat surface, which does not exactly represent what would happen in the actual eye given the presence of the tear film and curved structure of the cornea. Furthermore, from a psychophysical perspective, a subject would not be able to describe tear film spreading, whereas they could describe cooling and mechanical or touch effects on their tear film.

Two equations were also obtained in Chapter 8, with one representing the temperature change from baseline and the other representing another way to look at thermal effects, more specifically the diameter of the zone with a 1°C temperature change. These equations are also not the best for calibration purposes because, whilst they are based on the convection and spread of the airflow, they do not include evaporative effects that one would see on the actual eye. Furthermore the equation was obtained using an *in vitro* model eye which represents a large receptive field, whereas with the actual cornea there is overlapping of receptive fields that causes magnification of the nerve responses. Therefore, the results of this Chapter, and hence the regression equations produced, do not translate to the temperature differences one would see on the actual corneal surface. Instead, in order to calibrate in terms of temperature, it would be best to have a model that would allow the exploration of evaporative effects.

Force is the best choice for calibrating the instrument because it is most emblematic of the mechanical effects one would see on the cornea. Furthermore, of the two types of forces measured in Chapter 7, namely the peak force (PF) and steady state force (SSF), the peak force would be most appropriate as it serves as a proxy for the impulse, that is, the initial force that is applied to the eye when the stimulus first comes into contact with it. However, given that the forces produce by the instrument were small, before calibrating the instrument in terms of mechanical effects, it would be prudent to first perform pilot studies to roughly determine if such forces are even detectable by human subjects. In addition, a graph of the force versus temperature could also be plotted to see quantitively how they compare, and this can be used to inform the calibration.

10.4.2 *In vivo* studies

Having a thorough understanding of the stimulus characteristics of the Dolphin Aesthesiometer, the next step, after calibration, would be to test the stimulus *in vivo* to determine the repeatability of corneal threshold measurement. This would give more information about the mode of stimulation from a psychophysical perspective. Furthermore, it would help to determine the optimal stimulus duration and test distance for threshold measurements. The threshold should also be compared to the gold standard for measuring corneal sensitivity (CS), namely the Cochet-Bonnet Aesthesiometer (C-BA) as well as its predecessor, the Non-Contact Corneal Aesthesiometer (NCCA), in order to validate it. Summation studies using human subjects would also provide insight into how the corneal nerves process sensory information.

There is currently no data with respect to the representation of corneal sensation in the primary somatosensory cortex. Research focused on induced pain stimulation in the cornea using a bright light to produce photophobia in a subject with a rigid contact lens corneal abrasion has suggested that there is cortical representation for the corneal sensory nerves in the primary somatosensory cortex (Moulton et al., 2012). Given the compact nature of the Dolphin Aesthesiometer, it may be suitable for stimulating the cornea with a supra-threshold stimulus while a subject is in an fMRI, which may permit a determination those areas of the primary somatosensory cortex responsible for cornea sensitivity. However, it is important to note that the metal conductors in the micro-blowers would need to be replaced by non-metal conductors.

Typically, corneal sensitivity is described using a detection threshold, that is, the difference between no sensation and the presence of a sensation. However, “nothing in the world really occurs only at detection threshold levels” (Rao & Simpson, 2014, p. 1098). Having an instrument that can supply multiple stimuli would allow discrimination thresholds (the difference in the size of the sensation of two stimuli) to be studied, and this would facilitate an understanding of how the ocular surface sensory system performs. From a clinical perspective, with ocular discomfort treatments, the sensory changes that occur as the symptoms resolve usually involve some sort of discrimination judgement, and by understating discrimination one can perhaps quantify effects of these therapeutics (Rao & Simpson, 2014). The multiple exit air-jet property of the Dolphin aesthesiometer can be used to explore two point discrimination in the cornea. If successful, it could also be used to determine the effectiveness of lubricants used to treat dry eye symptoms. In addition, it may even create another way to grade dry eye severity.

10.5 Conclusion

Current non-contact aesthesiometers possess several drawbacks in their design and inconsistency of neural stimulation (Belmonte et al., 1999; Belmonte et al., 2017; Murphy et al., 1999; Nosch et al., 2017). Such shortcomings and a lack of standardization in their use has led to the limited use of corneal sensitivity measurement in the clinical situation. In contrast, this novel air-based aesthesiometer offer benefits unseen in other gas-jet aesthesiometers by delivering a finely controlled stimulus of known modes of stimulation with accurate duration settings, and it also provides new opportunities for corneal neuroscience investigations by being able to generate multiple stimuli separated by a time delay or spatial separation. These properties will not only facilitate future corneal studies, but they could lead to more standardization and potentially the use of corneal aesthesiometry clinically, which would ultimately promote a better understanding of the physiological and neural function of the cornea (Nosch, 2015).

LETTERS OF COPYRIGHT PERMISSION

Permission regarding Figure 2.1

This is a License Agreement between Melanie Mungalsingh ("User") and Copyright Clearance Center, Inc. ("CCC") on behalf of the Rightsholder identified in the order details below. The license consists of the order details, the CCC Terms and Conditions below, and any Rightsholder Terms and Conditions which are included below.

All payments must be made in full to CCC in accordance with the CCC Terms and Conditions below.

Order Date

06-Oct-2021

Order License ID

1152635-1

ISSN

0022-3077

Type of Use

Republish in a thesis/dissertation

Publisher

AMERICAN PHYSIOLOGICAL SOCIETY [ETC.]

Portion

Chart/graph/table/figure

Licensed Content

Publication Title

Journal of neurophysiology

Article Title

Free nerve ending terminal morphology is fiber type specific for A delta and C fibers innervating rabbit corneal epithelium.

Author/Editor

AMERICAN PHYSIOLOGICAL SOCIETY (1887-)

Date

01/01/1938

Language

English

Country

United States of America

Rightsholder

American Physiological Society

Publication Type

Journal

Start Page

1779

End Page

1783

Issue

5

Volume

69

Request Details

Portion Type

Chart/graph/table/figure

Number of charts / graphs / tables / figures requested

1

Format (select all that apply)

Print, Electronic

Who will republish the content?

Academic institution

Duration of Use

Life of current and all future editions

Lifetime Unit Quantity

Up to 499

Rights Requested

Main product

Distribution

Canada

Translation

Original language of publication

Copies for the disabled?

No

Minor editing privileges?

No

Incidental promotional use?

No

Currency

CAD

New Work Details

Title

PhD Thesis (Title not finalized)

Instructor name

Melanie Mungalsingh

Institution name

University of Waterloo

Expected presentation date

2021-10-08

Additional Details

Order reference number

N/A

The requesting person / organization to appear on the license

Melanie Mungalsingh

Reuse Content Details

Title, description or numeric reference of the portion(s)

Figure 1

Editor of portion(s)

MacIver, M B; Tanelian, D L

Volume of serial or monograph

69

Page or page range of portion

1779-1783

Title of the article/chapter the portion is from

Free nerve ending terminal morphology is fiber type specific for A delta and C fibers innervating rabbit corneal epithelium.

Author of portion(s)

MacIver, M B; Tanelian, D L

Issue, if republishing an article from a serial

5

Publication date of portion

1993-05-01

Rightsholder Terms and Conditions

1) Attribution: You must publish in your new or derivative work a citation to the original source of the material(s) being licensed herein, including publication name, author(s), volume, yr, and page number prominently displayed in the article or in the figure/image legend. 2) For requests for reuse of three or more images, please contact APS directly at cvillemez@the-aps.org. 3) Please use article pricing. No per page pricing.

CCC Terms and Conditions

1. Description of Service; Defined Terms. This Republication License enables the User to obtain licenses for republication of one or more copyrighted works as described in detail on the relevant Order Confirmation (the "Work(s)"). Copyright Clearance Center, Inc. ("CCC") grants licenses through the Service on behalf of the rightsholder identified on the Order Confirmation (the "Rightsholder"). "Republication", as used herein, generally means the inclusion of a Work, in whole or in part, in a new work or works, also as described on the Order Confirmation. "User", as used herein, means the person or entity making such republication.

2. The terms set forth in the relevant Order Confirmation, and any terms set by the Rightsholder with respect to a particular Work, govern the terms of use of Works in connection with the Service. By using the Service, the person transacting for a republication license on behalf of the User represents and warrants that he/she/it (a) has been duly authorized by the User to accept, and hereby does accept, all such terms and conditions on behalf of User, and (b) shall inform User of all such terms and conditions. In the event such person is a "freelancer" or other third party independent of User and CCC, such party shall be deemed jointly a "User" for purposes of these terms and conditions. In any event, User shall be deemed to have accepted and agreed to all such terms and conditions if User republishes the Work in any fashion.
3. Scope of License; Limitations and Obligations.
    1. All Works and all rights therein, including copyright rights, remain the sole and exclusive property of the Rightsholder. The license created by the exchange of an Order Confirmation (and/or any invoice) and payment by User of the full amount set forth on that document includes only those rights expressly set forth in the Order Confirmation and in these terms and conditions, and conveys no other rights in the Work(s) to User. All rights not expressly granted are hereby reserved.
    2. General Payment Terms: You may pay by credit card or through an account with us payable at the end of the month. If you and we agree that you may establish a standing account with CCC, then the following terms apply: Remit Payment to: Copyright Clearance Center, 29118 Network Place, Chicago, IL 60673-1291. Payments Due: Invoices are payable upon their delivery to you (or upon our notice to you that they are available to you for downloading). After 30 days, outstanding amounts will be subject to a service charge of 1-1/2% per month or, if less, the maximum rate allowed by applicable law. Unless otherwise specifically set forth in the Order Confirmation or in a separate written agreement signed by CCC, invoices are due and payable on "net 30" terms. While User may exercise the rights licensed immediately upon issuance of the Order Confirmation, the license is automatically revoked and is null and void, as if it had never been issued, if complete payment for the license is not received on a timely basis either from User directly or through a payment agent, such as a credit card company.
    3. Unless otherwise provided in the Order Confirmation, any grant of rights to User (i) is "one-time" (including the editions and product family specified in the license), (ii) is non-exclusive and non-transferable and (iii) is subject to any and all limitations and restrictions (such as, but not limited to, limitations on duration of use or circulation) included in the Order Confirmation or invoice and/or in these terms and conditions. Upon completion of the licensed use, User shall either secure a new permission for further use of the Work(s) or immediately cease any new use of the Work(s) and shall render inaccessible (such as by deleting or by removing or severing links or other

    locators) any further copies of the Work (except for copies printed on paper in accordance with this license and still in User's stock at the end of such period).
    4. In the event that the material for which a republication license is sought includes third party materials (such as photographs, illustrations, graphs, inserts and similar materials) which are identified in such material as having been used by permission, User is responsible for identifying, and seeking separate licenses (under this Service or otherwise) for, any of such third party materials; without a separate license, such third party materials may not be used.
    5. Use of proper copyright notice for a Work is required as a condition of any license granted under the Service. Unless otherwise provided in the Order Confirmation, a proper copyright notice will read substantially as follows: "Republished with permission of [Rightsholder's name], from [Work's title, author, volume, edition number and year of copyright]; permission conveyed through Copyright Clearance Center, Inc. " Such notice must be provided in a reasonably legible font size and must be placed either immediately adjacent to the Work as used (for example, as part of a by-line or footnote but not as a separate electronic link) or in the place where substantially all other credits or notices for the new work containing the republished Work are located. Failure to include the required notice results in loss to the Rightsholder and CCC, and the User shall be liable to pay liquidated damages for each such failure equal to twice the use fee specified in the Order Confirmation, in addition to the use fee itself and any other fees and charges specified.
    6. User may only make alterations to the Work if and as expressly set forth in the Order Confirmation. No Work may be used in any way that is defamatory, violates the rights of third parties (including such third parties' rights of copyright, privacy, publicity, or other tangible or intangible property), or is otherwise illegal, sexually explicit or obscene. In addition, User may not conjoin a Work with any other material that may result in damage to the reputation of the Rightsholder. User agrees to inform CCC if it becomes aware of any infringement of any rights in a Work and to cooperate with any reasonable request of CCC or the Rightsholder in connection therewith.
4. Indemnity. User hereby indemnifies and agrees to defend the Rightsholder and CCC, and their respective employees and directors, against all claims, liability, damages, costs and expenses, including legal fees and expenses, arising out of any use of a Work beyond the scope of the rights granted herein, or any use of a Work which has been altered in any unauthorized way by User, including claims of defamation or infringement of rights of copyright, publicity, privacy or other tangible or intangible property.
5. Limitation of Liability. UNDER NO CIRCUMSTANCES WILL CCC OR THE RIGHTSHOLDER BE LIABLE FOR ANY DIRECT, INDIRECT, CONSEQUENTIAL OR INCIDENTAL DAMAGES (INCLUDING WITHOUT LIMITATION DAMAGES FOR LOSS OF BUSINESS PROFITS OR INFORMATION, OR FOR BUSINESS INTERRUPTION) ARISING OUT OF THE

USE OR INABILITY TO USE A WORK, EVEN IF ONE OF THEM HAS BEEN ADVISED OF THE POSSIBILITY OF SUCH DAMAGES. In any event, the total liability of the Rightsholder and CCC (including their respective employees and directors) shall not exceed the total amount actually paid by User for this license. User assumes full liability for the actions and omissions of its principals, employees, agents, affiliates, successors and assigns.

6. Limited Warranties. THE WORK(S) AND RIGHT(S) ARE PROVIDED "AS IS". CCC HAS THE RIGHT TO GRANT TO USER THE RIGHTS GRANTED IN THE ORDER CONFIRMATION DOCUMENT. CCC AND THE RIGHTSHOLDER DISCLAIM ALL OTHER WARRANTIES RELATING TO THE WORK(S) AND RIGHT(S), EITHER EXPRESS OR IMPLIED, INCLUDING WITHOUT LIMITATION IMPLIED WARRANTIES OF MERCHANTABILITY OR FITNESS FOR A PARTICULAR PURPOSE. ADDITIONAL RIGHTS MAY BE REQUIRED TO USE ILLUSTRATIONS, GRAPHS, PHOTOGRAPHS, ABSTRACTS, INSERTS OR OTHER PORTIONS OF THE WORK (AS OPPOSED TO THE ENTIRE WORK) IN A MANNER CONTEMPLATED BY USER; USER UNDERSTANDS AND AGREES THAT NEITHER CCC NOR THE RIGHTSHOLDER MAY HAVE SUCH ADDITIONAL RIGHTS TO GRANT.
7. Effect of Breach. Any failure by User to pay any amount when due, or any use by User of a Work beyond the scope of the license set forth in the Order Confirmation and/or these terms and conditions, shall be a material breach of the license created by the Order Confirmation and these terms and conditions. Any breach not cured within 30 days of written notice thereof shall result in immediate termination of such license without further notice. Any unauthorized (but licensable) use of a Work that is terminated immediately upon notice thereof may be liquidated by payment of the Rightsholder's ordinary license price therefor; any unauthorized (and unlicensable) use that is not terminated immediately for any reason (including, for example, because materials containing the Work cannot reasonably be recalled) will be subject to all remedies available at law or in equity, but in no event to a payment of less than three times the Rightsholder's ordinary license price for the most closely analogous licensable use plus Rightsholder's and/or CCC's costs and expenses incurred in collecting such payment.
8. Miscellaneous.
    1. User acknowledges that CCC may, from time to time, make changes or additions to the Service or to these terms and conditions, and CCC reserves the right to send notice to the User by electronic mail or otherwise for the purposes of notifying User of such changes or additions; provided that any such changes or additions shall not apply to permissions already secured and paid for.
    2. Use of User-related information collected through the Service is governed by CCC's privacy policy, available online here:https://marketplace.copyright.com/rs-ui-web/mp/privacy-policy
    3. The licensing transaction described in the Order Confirmation is personal to User. Therefore, User may not assign or transfer to any other person (whether

a natural person or an organization of any kind) the license created by the Order Confirmation and these terms and conditions or any rights granted hereunder; provided, however, that User may assign such license in its entirety on written notice to CCC in the event of a transfer of all or substantially all of User's rights in the new material which includes the Work(s) licensed under this Service.

4. No amendment or waiver of any terms is binding unless set forth in writing and signed by the parties. The Rightsholder and CCC hereby object to any terms contained in any writing prepared by the User or its principals, employees, agents or affiliates and purporting to govern or otherwise relate to the licensing transaction described in the Order Confirmation, which terms are in any way inconsistent with any terms set forth in the Order Confirmation and/or in these terms and conditions or CCC's standard operating procedures, whether such writing is prepared prior to, simultaneously with or subsequent to the Order Confirmation, and whether such writing appears on a copy of the Order Confirmation or in a separate instrument.
5. The licensing transaction described in the Order Confirmation document shall be governed by and construed under the law of the State of New York, USA, without regard to the principles thereof of conflicts of law. Any case, controversy, suit, action, or proceeding arising out of, in connection with, or related to such licensing transaction shall be brought, at CCC's sole discretion, in any federal or state court located in the County of New York, State of New York, USA, or in any federal or state court whose geographical jurisdiction covers the location of the Rightsholder set forth in the Order Confirmation. The parties expressly submit to the personal jurisdiction and venue of each such federal or state court.If you have any comments or questions about the Service or Copyright Clearance Center, please contact us at 978-750-8400 or send an e-mail to support@copyright.com.

v 1.1

Permission regarding Figures 3.1 to 3.4

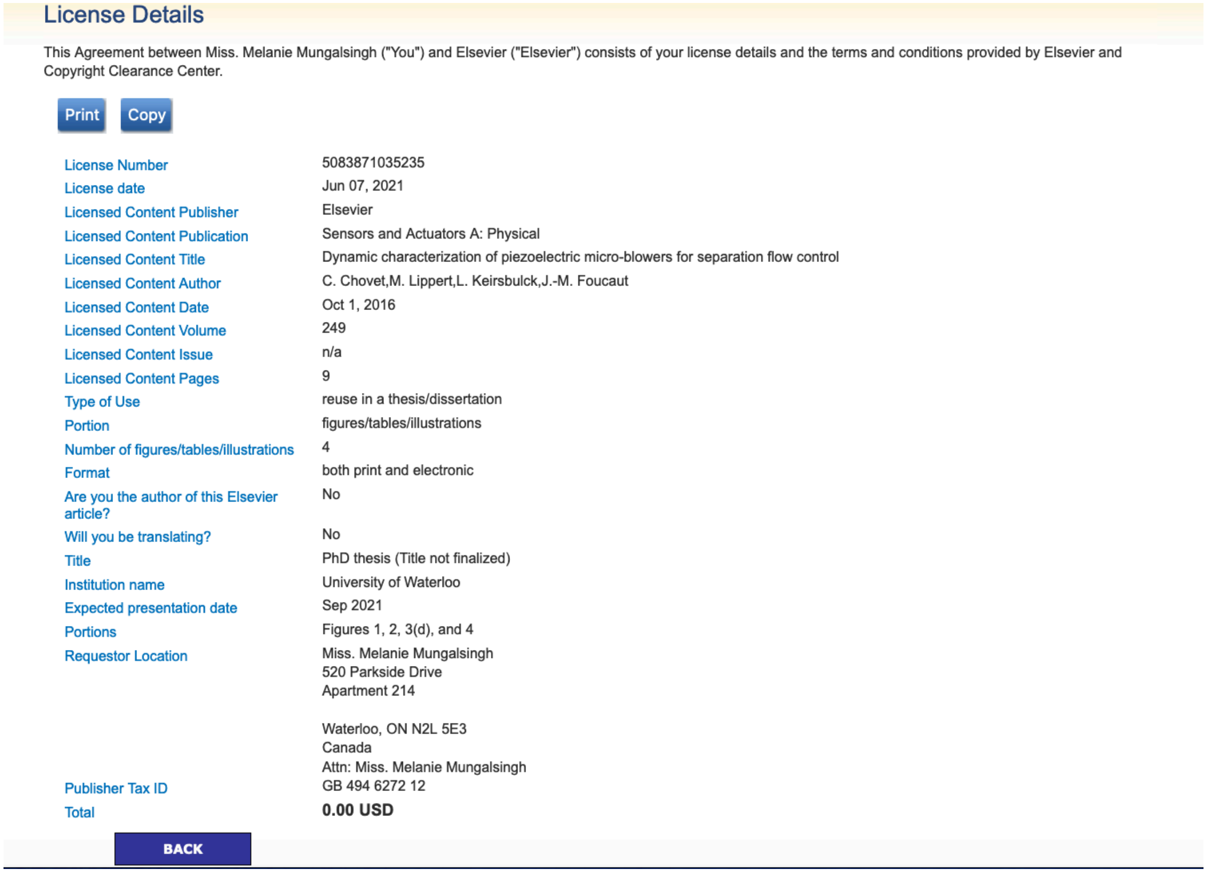

License Details

This Agreement between Miss. Melanie Mungalsingh ("You") and Elsevier ("Elsevier") consists of your license details and the terms and conditions provided by Elsevier and Copyright Clearance Center.

License Number	5083871035235
License date	Jun 07, 2021
Licensed Content Publisher	Elsevier
Licensed Content Publication	Sensors and Actuators A: Physical
Licensed Content Title	Dynamic characterization of piezoelectric micro-blowers for separation flow control
Licensed Content Author	C. Chovet,M. Lippert,L. Keirsbulck,J.-M. Foucaut
Licensed Content Date	Oct 1, 2016
Licensed Content Volume	249
Licensed Content Issue	n/a
Licensed Content Pages	9
Type of Use	reuse in a thesis/dissertation
Portion	figures/tables/illustrations
Number of figures/tables/illustrations	4
Format	both print and electronic
Are you the author of this Elsevier article?	No
Will you be translating?	No
Title	PhD thesis (Title not finalized)
Institution name	University of Waterloo
Expected presentation date	Sep 2021
Portions	Figures 1, 2, 3(d), and 4
Requestor Location	Miss. Melanie Mungalsingh 520 Parkside Drive Apartment 214 Waterloo, ON N2L 5E3 Canada Attn: Miss. Melanie Mungalsingh
Publisher Tax ID	GB 494 6272 12
Total	**0.00 USD**

ELSEVIER LICENSE

TERMS AND CONDITIONS

Sep 14, 2021

This Agreement between Miss. Melanie Mungalsingh ("You") and Elsevier ("Elsevier") consists of your license details and the terms and conditions provided by Elsevier and Copyright Clearance Center.

License Number	5083871035235
License date	Jun 07, 2021
Licensed Content Publisher	Elsevier

Licensed Content Publication	Sensors and Actuators A: Physical
Licensed Content Title	Dynamic characterization of piezoelectric micro-blowers for separation flow control
Licensed Content Author	C. Chovet,M. Lippert,L. Keirsbulck,J.-M. Foucaut
Licensed Content Date	Oct 1, 2016
Licensed Content Volume	249
Licensed Content Issue	n/a
Licensed Content Pages	9
Start Page	122
End Page	130
Type of Use	reuse in a thesis/dissertation
Portion	figures/tables/illustrations
Number of figures/tables/illustrations	4
Format	both print and electronic
Are you the author of this Elsevier article?	No
Will you be translating?	No
Title	PhD thesis (Title not finalized)
Institution name	University of Waterloo
Expected presentation date	Sep 2021
Portions	Figures 1, 2, 3(d), and 4
Requestor Location	Miss. Melanie Mungalsingh 520 Parkside Drive Apartment 214 Waterloo, ON N2L 5E3 Canada

	Attn: Miss. Melanie Mungalsingh
Publisher Tax ID	GB 494 6272 12
Total	0.00 USD

Terms and Conditions

INTRODUCTION

1. The publisher for this copyrighted material is Elsevier. By clicking "accept" in connection with completing this licensing transaction, you agree that the following terms and conditions apply to this transaction (along with the Billing and Payment terms and conditions established by Copyright Clearance Center, Inc. ("CCC"), at the time that you opened your Rightslink account and that are available at any time at http://myaccount.copyright.com).

GENERAL TERMS

2. Elsevier hereby grants you permission to reproduce the aforementioned material subject to the terms and conditions indicated.

3. Acknowledgement: If any part of the material to be used (for example, figures) has appeared in our publication with credit or acknowledgement to another source, permission must also be sought from that source. If such permission is not obtained then that material may not be included in your publication/copies. Suitable acknowledgement to the source must be made, either as a footnote or in a reference list at the end of your publication, as follows:

"Reprinted from Publication title, Vol /edition number, Author(s), Title of article / title of chapter, Pages No., Copyright (Year), with permission from Elsevier [OR APPLICABLE SOCIETY COPYRIGHT OWNER]." Also Lancet special credit - "Reprinted from The Lancet, Vol. number, Author(s), Title of article, Pages No., Copyright (Year), with permission from Elsevier."

4. Reproduction of this material is confined to the purpose and/or media for which permission is hereby given.

5. Altering/Modifying Material: Not Permitted. However figures and illustrations may be

altered/adapted minimally to serve your work. Any other abbreviations, additions, deletions and/or any other alterations shall be made only with prior written authorization of Elsevier Ltd. (Please contact Elsevier's permissions helpdesk here). No modifications can be made to any Lancet figures/tables and they must be reproduced in full.

6. If the permission fee for the requested use of our material is waived in this instance, please be advised that your future requests for Elsevier materials may attract a fee.

7. Reservation of Rights: Publisher reserves all rights not specifically granted in the combination of (i) the license details provided by you and accepted in the course of this licensing transaction, (ii) these terms and conditions and (iii) CCC's Billing and Payment terms and conditions.

8. License Contingent Upon Payment: While you may exercise the rights licensed immediately upon issuance of the license at the end of the licensing process for the transaction, provided that you have disclosed complete and accurate details of your proposed use, no license is finally effective unless and until full payment is received from you (either by publisher or by CCC) as provided in CCC's Billing and Payment terms and conditions. If full payment is not received on a timely basis, then any license preliminarily granted shall be deemed automatically revoked and shall be void as if never granted. Further, in the event that you breach any of these terms and conditions or any of CCC's Billing and Payment terms and conditions, the license is automatically revoked and shall be void as if never granted. Use of materials as described in a revoked license, as well as any use of the materials beyond the scope of an unrevoked license, may constitute copyright infringement and publisher reserves the right to take any and all action to protect its copyright in the materials.

9. Warranties: Publisher makes no representations or warranties with respect to the licensed material.

10. Indemnity: You hereby indemnify and agree to hold harmless publisher and CCC, and their respective officers, directors, employees and agents, from and against any and all claims arising out of your use of the licensed material other than as specifically authorized pursuant to this license.

11. No Transfer of License: This license is personal to you and may not be sublicensed, assigned, or transferred by you to any other person without publisher's written permission.

12. No Amendment Except in Writing: This license may not be amended except in a writing signed by both parties (or, in the case of publisher, by CCC on publisher's behalf).

13. Objection to Contrary Terms: Publisher hereby objects to any terms contained in any purchase order, acknowledgment, check endorsement or other writing prepared by you, which terms are inconsistent with these terms and conditions or CCC's Billing and Payment terms and conditions. These terms and conditions, together with CCC's Billing and Payment terms and conditions (which are incorporated herein), comprise the entire agreement between you and publisher (and CCC) concerning this licensing transaction. In the event of any conflict between your obligations established by these terms and conditions and those established by CCC's Billing and Payment terms and conditions, these terms and conditions shall control.

14. Revocation: Elsevier or Copyright Clearance Center may deny the permissions described in this License at their sole discretion, for any reason or no reason, with a full refund payable to you. Notice of such denial will be made using the contact information provided by you. Failure to receive such notice will not alter or invalidate the denial. In no event will Elsevier or Copyright Clearance Center be responsible or liable for any costs, expenses or damage incurred by you as a result of a denial of your permission request, other than a refund of the amount(s) paid by you to Elsevier and/or Copyright Clearance Center for denied permissions.

LIMITED LICENSE

The following terms and conditions apply only to specific license types:

15. **Translation**: This permission is granted for non-exclusive world **English** rights only unless your license was granted for translation rights. If you licensed translation rights you may only translate this content into the languages you requested. A professional translator must perform all translations and reproduce the content word for word preserving the integrity of the article.

16. **Posting licensed content on any Website**: The following terms and conditions apply as

follows: Licensing material from an Elsevier journal: All content posted to the web site must maintain the copyright information line on the bottom of each image; A hyper-text must be included to the Homepage of the journal from which you are licensing at http://www.sciencedirect.com/science/journal/xxxxx or the Elsevier homepage for books at http://www.elsevier.com; Central Storage: This license does not include permission for a scanned version of the material to be stored in a central repository such as that provided by Heron/XanEdu.

Licensing material from an Elsevier book: A hyper-text link must be included to the Elsevier homepage at http://www.elsevier.com . All content posted to the web site must maintain the copyright information line on the bottom of each image.

Posting licensed content on Electronic reserve: In addition to the above the following clauses are applicable: The web site must be password-protected and made available only to bona fide students registered on a relevant course. This permission is granted for 1 year only. You may obtain a new license for future website posting.

17. **For journal authors:** the following clauses are applicable in addition to the above:

Preprints:

A preprint is an author's own write-up of research results and analysis, it has not been peer-reviewed, nor has it had any other value added to it by a publisher (such as formatting, copyright, technical enhancement etc.).

Authors can share their preprints anywhere at any time. Preprints should not be added to or enhanced in any way in order to appear more like, or to substitute for, the final versions of articles however authors can update their preprints on arXiv or RePEc with their Accepted Author Manuscript (see below).

If accepted for publication, we encourage authors to link from the preprint to their formal publication via its DOI. Millions of researchers have access to the formal publications on ScienceDirect, and so links will help users to find, access, cite and use the best available version.

Please note that Cell Press, The Lancet and some society-owned have different preprint policies. Information on these policies is available on the journal homepage.

Accepted Author Manuscripts: An accepted author manuscript is the manuscript of an article that has been accepted for publication and which typically includes author-incorporated changes suggested during submission, peer review and editor-author communications.

Authors can share their accepted author manuscript:

- immediately
    - via their non-commercial person homepage or blog
    - by updating a preprint in arXiv or RePEc with the accepted manuscript
    - via their research institute or institutional repository for internal institutional uses or as part of an invitation-only research collaboration work-group
    - directly by providing copies to their students or to research collaborators for their personal use
    - for private scholarly sharing as part of an invitation-only work group on commercial sites with which Elsevier has an agreement
- After the embargo period
    - via non-commercial hosting platforms such as their institutional repository
    - via commercial sites with which Elsevier has an agreement

In all cases accepted manuscripts should:

- link to the formal publication via its DOI
- bear a CC-BY-NC-ND license - this is easy to do
- if aggregated with other manuscripts, for example in a repository or other site, be shared in alignment with our hosting policy not be added to or enhanced in any way to appear more like, or to substitute for, the published journal article.

Published journal article (JPA): A published journal article (PJA) is the definitive final record of published research that appears or will appear in the journal and embodies all value-adding publishing activities including peer review co-ordination, copy-editing, formatting, (if relevant) pagination and online enrichment.

Policies for sharing publishing journal articles differ for subscription and gold open access articles:

Subscription Articles: If you are an author, please share a link to your article rather than the full-text. Millions of researchers have access to the formal publications on ScienceDirect, and so links will help your users to find, access, cite, and use the best available version.

Theses and dissertations which contain embedded PJAs as part of the formal submission can be posted publicly by the awarding institution with DOI links back to the formal publications on ScienceDirect.

If you are affiliated with a library that subscribes to ScienceDirect you have additional private sharing rights for others' research accessed under that agreement. This includes use for classroom teaching and internal training at the institution (including use in course packs and courseware programs), and inclusion of the article for grant funding purposes.

Gold Open Access Articles: May be shared according to the author-selected end-user license and should contain a CrossMark logo, the end user license, and a DOI link to the formal publication on ScienceDirect.

Please refer to Elsevier's posting policy for further information.

18. **For book authors** the following clauses are applicable in addition to the above: Authors are permitted to place a brief summary of their work online only. You are not allowed to download and post the published electronic version of your chapter, nor may you scan the printed edition to create an electronic version. **Posting to a repository:** Authors are permitted to post a summary of their chapter only in their institution's repository.

19. **Thesis/Dissertation**: If your license is for use in a thesis/dissertation your thesis may be submitted to your institution in either print or electronic form. Should your thesis be published commercially, please reapply for permission. These requirements include permission for the Library and Archives of Canada to supply single copies, on demand, of the complete thesis and include permission for Proquest/UMI to supply single copies, on demand, of the complete thesis. Should your thesis be published commercially, please reapply for permission. Theses and dissertations which contain embedded PJAs as part of the formal submission can be posted publicly by the awarding institution with DOI links back to the formal publications on ScienceDirect.

Elsevier Open Access Terms and Conditions

You can publish open access with Elsevier in hundreds of open access journals or in nearly 2000 established subscription journals that support open access publishing. Permitted third party re-use of these open access articles is defined by the author's choice of Creative Commons user license. See our open access license policy for more information.

Terms & Conditions applicable to all Open Access articles published with Elsevier:

Any reuse of the article must not represent the author as endorsing the adaptation of the article nor should the article be modified in such a way as to damage the author's honour or reputation. If any changes have been made, such changes must be clearly indicated.

The author(s) must be appropriately credited and we ask that you include the end user license and a DOI link to the formal publication on ScienceDirect.

If any part of the material to be used (for example, figures) has appeared in our publication with credit or acknowledgement to another source it is the responsibility of the user to ensure their reuse complies with the terms and conditions determined by the rights holder.

Additional Terms & Conditions applicable to each Creative Commons user license:

CC BY: The CC-BY license allows users to copy, to create extracts, abstracts and new works from the Article, to alter and revise the Article and to make commercial use of the Article (including reuse and/or resale of the Article by commercial entities), provided the user gives appropriate credit (with a link to the formal publication through the relevant DOI), provides a link to the license, indicates if changes were made and the licensor is not represented as endorsing the use made of the work. The full details of the license are available at http://creativecommons.org/licenses/by/4.0.

CC BY NC SA: The CC BY-NC-SA license allows users to copy, to create extracts, abstracts and new works from the Article, to alter and revise the Article, provided this is not done for commercial purposes, and that the user gives appropriate credit (with a link to the formal publication through the relevant DOI), provides a link to the license, indicates if changes were made and the licensor is not represented as endorsing the use made of the work. Further, any new works must be made available on the same conditions. The full details of the license are available at http://creativecommons.org/licenses/by-nc-sa/4.0.

CC BY NC ND: The CC BY-NC-ND license allows users to copy and distribute the Article, provided this is not done for commercial purposes and further does not permit distribution of the Article if it is changed or edited in any way, and provided the user gives appropriate credit (with a link to the formal publication through the relevant DOI), provides a link to the license, and that the licensor is not represented as endorsing the use made of the work. The full details of the license are available at http://creativecommons.org/licenses/by-nc-nd/4.0. Any commercial reuse of Open Access articles published with a CC BY NC SA or CC BY NC ND license requires permission from Elsevier and will be subject to a fee.

Commercial reuse includes:

- Associating advertising with the full text of the Article
- Charging fees for document delivery or access
- Article aggregation
- Systematic distribution via e-mail lists or share buttons

Posting or linking by commercial companies for use by customers of those companies.

20. **Other Conditions**:

v1.10

Questions? customercare@copyright.com or +1-855-239-3415 (toll free in the US) or +1-978-646-2777.

Permission regarding Figure 5.1

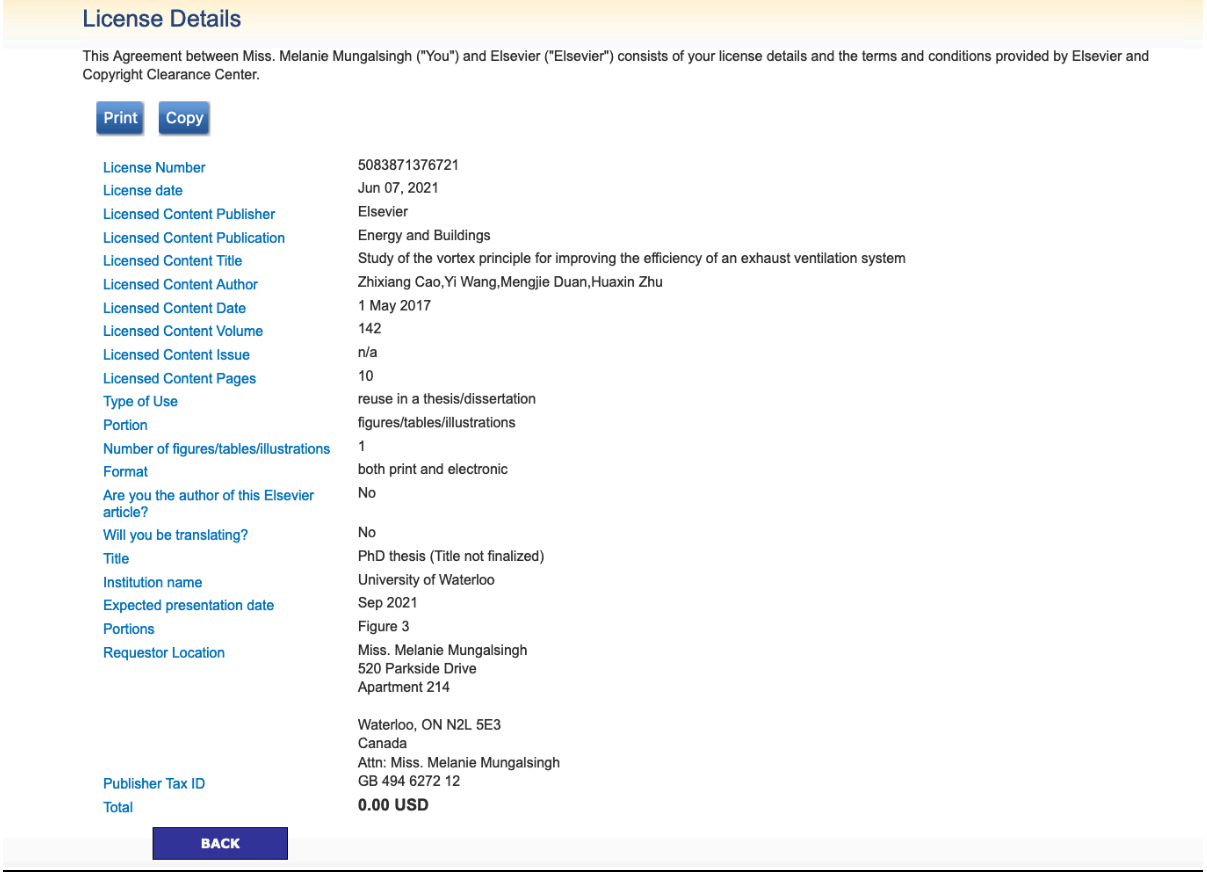

License Details

This Agreement between Miss. Melanie Mungalsingh ("You") and Elsevier ("Elsevier") consists of your license details and the terms and conditions provided by Elsevier and Copyright Clearance Center.

License Number	5083871376721
License date	Jun 07, 2021
Licensed Content Publisher	Elsevier
Licensed Content Publication	Energy and Buildings
Licensed Content Title	Study of the vortex principle for improving the efficiency of an exhaust ventilation system
Licensed Content Author	Zhixiang Cao,Yi Wang,Mengjie Duan,Huaxin Zhu
Licensed Content Date	1 May 2017
Licensed Content Volume	142
Licensed Content Issue	n/a
Licensed Content Pages	10
Type of Use	reuse in a thesis/dissertation
Portion	figures/tables/illustrations
Number of figures/tables/illustrations	1
Format	both print and electronic
Are you the author of this Elsevier article?	No
Will you be translating?	No
Title	PhD thesis (Title not finalized)
Institution name	University of Waterloo
Expected presentation date	Sep 2021
Portions	Figure 3
Requestor Location	Miss. Melanie Mungalsingh 520 Parkside Drive Apartment 214 Waterloo, ON N2L 5E3 Canada Attn: Miss. Melanie Mungalsingh
Publisher Tax ID	GB 494 6272 12
Total	**0.00 USD**

ELSEVIER LICENSE

TERMS AND CONDITIONS

Sep 14, 2021

This Agreement between Miss. Melanie Mungalsingh ("You") and Elsevier ("Elsevier") consists of your license details and the terms and conditions provided by Elsevier and Copyright Clearance Center.

License Number	5083871376721

License date	Jun 07, 2021
Licensed Content Publisher	Elsevier
Licensed Content Publication	Energy and Buildings
Licensed Content Title	Study of the vortex principle for improving the efficiency of an exhaust ventilation system
Licensed Content Author	Zhixiang Cao,Yi Wang,Mengjie Duan,Huaxin Zhu
Licensed Content Date	1 May 2017
Licensed Content Volume	142
Licensed Content Issue	n/a
Licensed Content Pages	10
Start Page	39
End Page	48
Type of Use	reuse in a thesis/dissertation
Portion	figures/tables/illustrations
Number of figures/tables/illustrations	1
Format	both print and electronic
Are you the author of this Elsevier article?	No
Will you be translating?	No
Title	PhD thesis (Title not finalized)
Institution name	University of Waterloo
Expected presentation date	Sep 2021
Portions	Figure 3
Requestor Location	Miss. Melanie Mungalsingh 520 Parkside Drive Apartment 214

	Waterloo, ON N2L 5E3 Canada Attn: Miss. Melanie Mungalsingh
Publisher Tax ID	GB 494 6272 12
Total	0.00 USD
Terms and Conditions	

INTRODUCTION

1. The publisher for this copyrighted material is Elsevier. By clicking "accept" in connection with completing this licensing transaction, you agree that the following terms and conditions apply to this transaction (along with the Billing and Payment terms and conditions established by Copyright Clearance Center, Inc. ("CCC"), at the time that you opened your Rightslink account and that are available at any time at http://myaccount.copyright.com).

GENERAL TERMS

2. Elsevier hereby grants you permission to reproduce the aforementioned material subject to the terms and conditions indicated.

3. Acknowledgement: If any part of the material to be used (for example, figures) has appeared in our publication with credit or acknowledgement to another source, permission must also be sought from that source. If such permission is not obtained then that material may not be included in your publication/copies. Suitable acknowledgement to the source must be made, either as a footnote or in a reference list at the end of your publication, as follows:

"Reprinted from Publication title, Vol /edition number, Author(s), Title of article / title of chapter, Pages No., Copyright (Year), with permission from Elsevier [OR APPLICABLE SOCIETY COPYRIGHT OWNER]." Also Lancet special credit - "Reprinted from The Lancet, Vol. number, Author(s), Title of article, Pages No., Copyright (Year), with permission from Elsevier."

4. Reproduction of this material is confined to the purpose and/or media for which permission is

hereby given.

5. Altering/Modifying Material: Not Permitted. However figures and illustrations may be altered/adapted minimally to serve your work. Any other abbreviations, additions, deletions and/or any other alterations shall be made only with prior written authorization of Elsevier Ltd. (Please contact Elsevier's permissions helpdesk here). No modifications can be made to any Lancet figures/tables and they must be reproduced in full.

6. If the permission fee for the requested use of our material is waived in this instance, please be advised that your future requests for Elsevier materials may attract a fee.

7. Reservation of Rights: Publisher reserves all rights not specifically granted in the combination of (i) the license details provided by you and accepted in the course of this licensing transaction, (ii) these terms and conditions and (iii) CCC's Billing and Payment terms and conditions.

8. License Contingent Upon Payment: While you may exercise the rights licensed immediately upon issuance of the license at the end of the licensing process for the transaction, provided that you have disclosed complete and accurate details of your proposed use, no license is finally effective unless and until full payment is received from you (either by publisher or by CCC) as provided in CCC's Billing and Payment terms and conditions. If full payment is not received on a timely basis, then any license preliminarily granted shall be deemed automatically revoked and shall be void as if never granted. Further, in the event that you breach any of these terms and conditions or any of CCC's Billing and Payment terms and conditions, the license is automatically revoked and shall be void as if never granted. Use of materials as described in a revoked license, as well as any use of the materials beyond the scope of an unrevoked license, may constitute copyright infringement and publisher reserves the right to take any and all action to protect its copyright in the materials.

9. Warranties: Publisher makes no representations or warranties with respect to the licensed material.

10. Indemnity: You hereby indemnify and agree to hold harmless publisher and CCC, and their respective officers, directors, employees and agents, from and against any and all claims arising

out of your use of the licensed material other than as specifically authorized pursuant to this license.

11. No Transfer of License: This license is personal to you and may not be sublicensed, assigned, or transferred by you to any other person without publisher's written permission.

12. No Amendment Except in Writing: This license may not be amended except in a writing signed by both parties (or, in the case of publisher, by CCC on publisher's behalf).

13. Objection to Contrary Terms: Publisher hereby objects to any terms contained in any purchase order, acknowledgment, check endorsement or other writing prepared by you, which terms are inconsistent with these terms and conditions or CCC's Billing and Payment terms and conditions. These terms and conditions, together with CCC's Billing and Payment terms and conditions (which are incorporated herein), comprise the entire agreement between you and publisher (and CCC) concerning this licensing transaction. In the event of any conflict between your obligations established by these terms and conditions and those established by CCC's Billing and Payment terms and conditions, these terms and conditions shall control.

14. Revocation: Elsevier or Copyright Clearance Center may deny the permissions described in this License at their sole discretion, for any reason or no reason, with a full refund payable to you. Notice of such denial will be made using the contact information provided by you. Failure to receive such notice will not alter or invalidate the denial. In no event will Elsevier or Copyright Clearance Center be responsible or liable for any costs, expenses or damage incurred by you as a result of a denial of your permission request, other than a refund of the amount(s) paid by you to Elsevier and/or Copyright Clearance Center for denied permissions.

LIMITED LICENSE

The following terms and conditions apply only to specific license types:

15. **Translation**: This permission is granted for non-exclusive world **English** rights only unless your license was granted for translation rights. If you licensed translation rights you may only translate this content into the languages you requested. A professional translator must perform all

translations and reproduce the content word for word preserving the integrity of the article.

16. **Posting licensed content on any Website**: The following terms and conditions apply as follows: Licensing material from an Elsevier journal: All content posted to the web site must maintain the copyright information line on the bottom of each image; A hyper-text must be included to the Homepage of the journal from which you are licensing at http://www.sciencedirect.com/science/journal/xxxxx or the Elsevier homepage for books at http://www.elsevier.com; Central Storage: This license does not include permission for a scanned version of the material to be stored in a central repository such as that provided by Heron/XanEdu.

Licensing material from an Elsevier book: A hyper-text link must be included to the Elsevier homepage at http://www.elsevier.com . All content posted to the web site must maintain the copyright information line on the bottom of each image.

Posting licensed content on Electronic reserve: In addition to the above the following clauses are applicable: The web site must be password-protected and made available only to bona fide students registered on a relevant course. This permission is granted for 1 year only. You may obtain a new license for future website posting.

17. **For journal authors:** the following clauses are applicable in addition to the above:

Preprints:

A preprint is an author's own write-up of research results and analysis, it has not been peer-reviewed, nor has it had any other value added to it by a publisher (such as formatting, copyright, technical enhancement etc.).

Authors can share their preprints anywhere at any time. Preprints should not be added to or enhanced in any way in order to appear more like, or to substitute for, the final versions of articles however authors can update their preprints on arXiv or RePEc with their Accepted Author Manuscript (see below).

If accepted for publication, we encourage authors to link from the preprint to their formal publication via its DOI. Millions of researchers have access to the formal publications on ScienceDirect, and so links will help users to find, access, cite and use the best available version. Please note that Cell Press, The Lancet and some society-owned have different preprint policies. Information on these policies is available on the journal homepage.

Accepted Author Manuscripts: An accepted author manuscript is the manuscript of an article that has been accepted for publication and which typically includes author-incorporated changes suggested during submission, peer review and editor-author communications.

Authors can share their accepted author manuscript:

- immediately
    - via their non-commercial person homepage or blog
    - by updating a preprint in arXiv or RePEc with the accepted manuscript
    - via their research institute or institutional repository for internal institutional uses or as part of an invitation-only research collaboration work-group
    - directly by providing copies to their students or to research collaborators for their personal use
    - for private scholarly sharing as part of an invitation-only work group on commercial sites with which Elsevier has an agreement
- After the embargo period
    - via non-commercial hosting platforms such as their institutional repository
    - via commercial sites with which Elsevier has an agreement

In all cases accepted manuscripts should:

- link to the formal publication via its DOI
- bear a CC-BY-NC-ND license - this is easy to do
- if aggregated with other manuscripts, for example in a repository or other site, be shared in alignment with our hosting policy not be added to or enhanced in any way to appear more like, or to substitute for, the published journal article.

Published journal article (JPA): A published journal article (PJA) is the definitive final record of published research that appears or will appear in the journal and embodies all value-adding publishing activities including peer review co-ordination, copy-editing, formatting, (if relevant) pagination and online enrichment.

Policies for sharing publishing journal articles differ for subscription and gold open access articles:

Subscription Articles: If you are an author, please share a link to your article rather than the full-text. Millions of researchers have access to the formal publications on ScienceDirect, and so links will help your users to find, access, cite, and use the best available version.

Theses and dissertations which contain embedded PJAs as part of the formal submission can be posted publicly by the awarding institution with DOI links back to the formal publications on ScienceDirect.

If you are affiliated with a library that subscribes to ScienceDirect you have additional private sharing rights for others' research accessed under that agreement. This includes use for classroom teaching and internal training at the institution (including use in course packs and courseware programs), and inclusion of the article for grant funding purposes.

Gold Open Access Articles: May be shared according to the author-selected end-user license and should contain a CrossMark logo, the end user license, and a DOI link to the formal publication on ScienceDirect.

Please refer to Elsevier's posting policy for further information.

18. **For book authors** the following clauses are applicable in addition to the above: Authors are permitted to place a brief summary of their work online only. You are not allowed to download and post the published electronic version of your chapter, nor may you scan the printed edition to create an electronic version. **Posting to a repository:** Authors are permitted to post a summary of their chapter only in their institution's repository.

19. **Thesis/Dissertation**: If your license is for use in a thesis/dissertation your thesis may be submitted to your institution in either print or electronic form. Should your thesis be published commercially, please reapply for permission. These requirements include permission for the Library and Archives of Canada to supply single copies, on demand, of the complete thesis and include permission for Proquest/UMI to supply single copies, on demand, of the complete thesis. Should your thesis be published commercially, please reapply for permission. Theses and dissertations which contain embedded PJAs as part of the formal submission can be posted publicly by the awarding institution with DOI links back to the formal publications on

ScienceDirect.

Elsevier Open Access Terms and Conditions

You can publish open access with Elsevier in hundreds of open access journals or in nearly 2000 established subscription journals that support open access publishing. Permitted third party re-use of these open access articles is defined by the author's choice of Creative Commons user license. See our open access license policy for more information.

Terms & Conditions applicable to all Open Access articles published with Elsevier:

Any reuse of the article must not represent the author as endorsing the adaptation of the article nor should the article be modified in such a way as to damage the author's honour or reputation. If any changes have been made, such changes must be clearly indicated.

The author(s) must be appropriately credited and we ask that you include the end user license and a DOI link to the formal publication on ScienceDirect.

If any part of the material to be used (for example, figures) has appeared in our publication with credit or acknowledgement to another source it is the responsibility of the user to ensure their reuse complies with the terms and conditions determined by the rights holder.

Additional Terms & Conditions applicable to each Creative Commons user license:

CC BY: The CC-BY license allows users to copy, to create extracts, abstracts and new works from the Article, to alter and revise the Article and to make commercial use of the Article (including reuse and/or resale of the Article by commercial entities), provided the user gives appropriate credit (with a link to the formal publication through the relevant DOI), provides a link to the license, indicates if changes were made and the licensor is not represented as endorsing the use made of the work. The full details of the license are available at http://creativecommons.org/licenses/by/4.0.

CC BY NC SA: The CC BY-NC-SA license allows users to copy, to create extracts, abstracts and new works from the Article, to alter and revise the Article, provided this is not done for commercial purposes, and that the user gives appropriate credit (with a link to the formal publication through the relevant DOI), provides a link to the license, indicates if changes were made and the licensor is not represented as endorsing the use made of the work. Further, any new works must be made available on the same conditions. The full details of the license are available at http://creativecommons.org/licenses/by-nc-sa/4.0.

CC BY NC ND: The CC BY-NC-ND license allows users to copy and distribute the Article, provided this is not done for commercial purposes and further does not permit distribution of the Article if it is changed or edited in any way, and provided the user gives appropriate credit (with a link to the formal publication through the relevant DOI), provides a link to the license, and that the licensor is not represented as endorsing the use made of the work. The full details of the license are available at http://creativecommons.org/licenses/by-nc-nd/4.0. Any commercial reuse of Open Access articles published with a CC BY NC SA or CC BY NC ND license requires permission from Elsevier and will be subject to a fee.

Commercial reuse includes:

- Associating advertising with the full text of the Article
- Charging fees for document delivery or access
- Article aggregation
- Systematic distribution via e-mail lists or share buttons

Posting or linking by commercial companies for use by customers of those companies.

20. **Other Conditions**: v1.10

Questions? customercare@copyright.com or +1-855-239-3415 (toll free in the US) or +1-978-646-2777.

BIBLIOGRAPHY

Accornero, N., Berardelli, A., Bini, G., Cruccu, G., & Manfredi, M. (1980). Corneal reflex elicited by electrical stimulation of the human cornea. *Neurology*, *30*(7), 782-785.

Acosta, M. C., Alfaro, M. L., Borrás, F., Belmonte, C., & Gallar, J. (2006). Influence of age, gender, and iris colour on mechanical and chemical sensitivity of the cornea and conjunctiva. *Experimental Eye Research, 83*(4), 932-938.

Acosta, M. C., Belmonte, C., & Gallar, J. (2001a). Sensory experiences in humans and single unit activity in cats evoked by polymodal stimulation of the cornea. *Journal of Physiology, 534*(2), 511-525.

Acosta, M. C., Berenguer-Ruiz, L., García-Gálvez, A., Perea-Tortosa, D., Gallar J., & Belmonte, C. (2005). Changes in mechanical, chemical, and thermal sensitivity of the cornea after topical application of nonsteroidal anti-inflammatory drugs. *Investigative Ophthalmology & Visual Science, 46*(1), 282-286.

Acosta, M. C., Tan, M. E., Belmonte, C., & Gallar, J. (2001b). Sensations evoked by selective mechanical, chemical, and thermal stimulation of the conjunctiva and cornea. *Investigative Ophthalmology & Visual Science, 42*(9), 2063-2067.

Belmonte, C., Acosta, M. C., & Gallar, J. (2004). Neural basis of sensation in intact and injured corneas. *Experimental Eye Research, 78*(3), 513-525.

Belmonte, C., Acosta, M. C., Schmelz, M., & Gallar, J. (1999). Measurement of corneal sensitivity to mechanical and chemical stimulation with a CO_2 esthesiometer. *Investigative Ophthalmology & Visual Science, 40*(2), 513-519.

Belmonte, C., Gallar, J., Pozo, M. A., & Rebello, I. (1991). Excitation by irritant chemical substances of sensory afferent units in the cat's cornea. *Journal of Physiology, 437*, 709-725.

Belmonte, C., & Giraldez, F. (1981). Responses of cat corneal sensory receptors to mechanical and thermal stimulation. *Journal of Physiology, 321*, 355-368.

Belmonte, C., Nicholas, J. J., Cox, S. M., Brock, J. A., Begley, C. G., Bereiter, D. A.,…& Wolffsohn, J. S. (2017). TFOS DEWS II pain and sensation report. *Ocular Surface, 15*(2017), 404-437.

Belmonte, C., Tervo, T. T., & Gallar, J. (2011). Sensory innervation of the eye. In L. A. Levin, A. F. E. Nilsson, J. V. Hoeve, & S. M. Wu (Eds.), *Adler's Physiology of the Eye* (pp. 363- 384). Philadelphia, USA: Elsevier Inc.

Bessou, P. & Perl, E. R. (1969). Response of cutaneous sensory units with unmyelinated fibres to noxious stimuli. *Journal of Neurophysiology, 32*(6), 1025-1043.

Beuerman, R. W., & Rozsa, A. J. (1985). Threshold and signal detection measures of the effect of soft contact lenses on corneal sensitivity. *Current Eye Research, 4*, 742-744.

Blattenberger. (2020). *Square wave voltages: Vpk, vpk-pk, vavg, vrms.* Internet Version. Retrieved on Thursday 20th February, 2020 from: https://www.rfcafe.com/references/electrical/square-wave-voltage-conversion.htm

Boberg-Ans, J. (1952). *On the corneal sensitivity with special reference to clinical methods of examination.* Ph.D. Thesis. University of Copenhagen.

Boberg-Ans, J. (1995). Experience in clinical examination of corneal sensitivity: Corneal sensitivity and the naso-lacrimal reflex after retrobulbar anaesthesia. *British Journal of Ophthalmology, 39*(12), 705-726.

Bonnet, R., & Millodot, M. (1966). Corneal aesthesiometry: its measurement in the dark. *American Journal of Optometry and archives of American Academy of Optometry, 43*(4), 238-243.

Brilliant.org. (2021). *Affine transformation.* Internet Version. Retrieved on Tuesday 16th February, 2021 from: https://brilliant.org/wiki/affine-transformations/

Cao, Z., Wang, Y., Mengjie, D., & Zhu, H. (2017). Study of the vortex principle for moving the efficiency of an exhaust ventilation system. *Energy and Buildings, 142*(2017), 39-48.

Çengel, Y. A., & Cimbala, J. M. (2006). *Fluid mechanics: Fundamental and applications* (pp. 172). McGraw-Hill.

Chen, S., Huang, J., Wen, D., Chen, W., Huang, D., & Wang, Q. (2012). Measurement of central corneal thickness by high-resolution Scheimpflug imaging, Fourier domain optical coherence tomography, and ultrasound pachymetry. *Acta Ophthalmologica, 90*(5), 449-455.

Chovet, C., Lippert, M., & Foucaut, J. M. (2016). Dynamic characterization of piezoelectric micro-blowers for separation flow control. *Sensors and Actuators A, 249*(2016), 122-130.

Cochet P, & Bonnet R. (1960). L'esthÈsie cornÈenne. *La Clin Ophthalmolgia, 4*, 3-27.

Corliss, D. A., & Norton, T. T. (2002). Principles of psychophysical measurements. In T. T. Norton, D. A. Corliss, & J. E. Bailey, *The psychophysical measurement of visual function* (pp. 5-14, 15-18, 32-34). New York, USA: Butterworth-Heinemann.

Douthwaite, W. A., & Kaye, N. A. (1980). Is corneal sensitivity related to corneal thickness? *The Ophthalmic Optician, 20*, 735-758.

Feng, Y., & Simpson, T. (2004). Characteristics of human corneal psychophysical channels. *Investigative Ophthalmology & Visual Science, 45*(9), 3005-3010.

FLIR Systems, Inc. (2014). *FLIR A655sc*. Internet Version. Retrieved on Thursday 14th June, 2018 from https://www.flirmedia.com/MMC/THG/Brochures/RND_011/RND_011_US.pdf

FLIR Systems, Inc. (2018). *FLIR A655sc: High-resolution science grade LWIR camera*. Internet Version. Retrieved on Thursday 14th June, 2018 from http://www.flir.ru/science/display/?id=46802

FLIR Systems. (2019). *Extech EX520:11 Function heavy duty true RMS industrial multimeter.* Internet Version. Retrieved on Friday 5th April, 2019 from:
http://www.extech.com/display/?id=14835

Gallar, J., Pozo, M. A., Tuckett, R. P., & Belmonte, C. (1993). Response of sensory units with unmyelinated fibres to mechanical, thermal, and chemical stimulation of the cat's cornea. *Journal of Physiology, 468*, 609-622.

García-Pérez, M. A. (2001). Yes-no staircases with fixed step sizes: Psychometric properties and optimal setup. *Optometry and Vision Science, 78*(1), 56-64. *Experimental Eye Research, 92*(5), 408-413.

Gescheider, G. A. (1997). *Psychophysics: The fundamentals (3rd ed.)* (pp. 55-64, 105-145, 371,392-407). London: Lawrence Erlbaum Associates, Publishers.

Giraldez, F., Geijo, E., & Belmonte, C. (1979). Response characteristics of corneal sensory fibres to mechanical and thermal stimulation. *Brain Research, 177*(3), 571-576.

Goldstein, E. B. (1989). *Sensation and perception (3rd ed.)* (pp. 527-529). Pacific Grove, California: Brooks/Cole Publishing Company.

Gockenbach, M., & Schmidtke, K. (2009). Newton's law of heating and the heat equation. *Involve, 2*(4), 419-437.

Golebiowski, B., Papas, E. B., & Stapleton, F. (2005). Corneal mechanical sensitivity measurement using a staircase technique. *Ophthalmic & Physiological Optics, 25*(3), 246-253.

Golebiowski, B., Papas, E. B., & Stapleton, F. (2011). Assessing the sensory function of the ocular surface: Implications of use of a non-contact air-jet aesthesiometer versus the Cochet-Bonnet aesthesiometer. *Experimental Eye Research, 92*(5), 408-413.

Golebiowski, B., Papas, E. B., & Stapleton, F. (2012). Corneal and conjunctival sensory function: The impact on ocular surface sensitivity of change from low to high oxygen transmissibility contact lenses. *Investigative Ophthalmology & Visual Science, 53*(3), 1177-1181.

Good Will Instrument CO., Ltd. (2004). *Digital storage oscilloscope, GDS-800 series, operation manual.* Internet Version. Retrieved on Wednesday 19th February, 2020 from: http://www.electroninvest.com/shop/items/instek/GDS-800-user_manual.pdf

Holmes, R., Victora, M., Wang, R. F., & Kwiat, P. G. (2017). Measuring temporal summation in visual detection with a single-photon source. *Vision Research, 140*(2017), 33-43.

Incropera, F. P., Dewitt, D. P., Bergman, T. L., & Lavine, A. S. (2007). *Fundamentals of heat and mass transfer* (6th ed.) (pp. 1-41). John Wiley & Sons.

Illinois Institute of Technology. (2019). *Experiment 2: Instrumentation and oscilloscope introduction.* Internet Version. Retrieved on Wednesday 19th February, 2020 from: https://www.iit.edu/sites/default/files/2019-11/13f_lab_02_instrumentation.pdf

Kalra, A. (2017). Decoding the Bland-Altman plot: Basic review. *Journal of the practice of Cardiovascular Sciences, 3*(1), 36-48.

Khuu, S. K., & Kalloniatis, M. (2015). Spatial summation across the central visual field: Implications for visual field testing. *Journal of Vision, 15*(1), 1-15.

Lawrenson, J. G., & Ruskell, G. L. (1993). Investigation of limbal touch sensitivity by using a Cochet-Bonnet aesthesiometer. *British Journal of Ophthalmology & Visual Science, 77*, 339-343.

Lowther, G. E., & Hill, R. M. (1968). Sensitivity threshold of the lower lid margin in the course of adaptation to contact lenses. *American Journal of Optometry and Archives of American Academy of Optometry, 1*, 587-594.

Lum, E. (2014). *The impact of overnight orthokeratology on sub-basal nerve plexus morphology and corneal sensitivity.* Ph.D. Thesis. The University of New South Wales.

Lum, E., Corbett, M. C., & Murphy, P. J. (2019). Corneal sensitivity after ocular surgery. *Eye and Contact Lens.*

Lum, E., & Murphy, P. J. (2018). Effects of ambient humidity on the Cochet-Bonnet aesthesiometer. *Eye, 32*, 1644-1651.

MacIver, M. B., & Tanelian, D. L. (1993a). Free nerve ending terminal morphology is fibre type specific for A delta and C fibres innervating rabbit corneal epithelium. *Journal of Neuroscience, 69*(5), 1779-1783.

MacIver, M. B., & Tanelian, D. L. (1993b). Structural and functional specialization of A delta and C fibre free nerve endings innervating rabbit corneal epithelium. *Journal of Neuroscience, 13*(10), 4511-4524.

Mashige, K. P. (2013). A review of corneal diameter, curvature and thickness values and influencing factors. *The South African Optometrist, 72*(4), 185-194.

Mihelcic, M., Päällysaho, J., Raudasoja, M., Honkanen, V., Seppä, V., Salkola, M., & Schollmayer, P. (2021). A novel rebound technology-based method for measuring corneal sensitivity. [Abstract]. *Investigative Ophthalmology & Visual Science, 62*(8), 787.

Millodot, M. (1984). A review of research on the sensitivity of the cornea. *Ophthalmic & Physiological Optics, 4*(4), 305-318.

Millodot, M., & O'Leary, D. J. (1981). Corneal fragility and its relationship to sensitivity. *Acta Ophthalmologica, 59*(6), 820-826.

Misra, S., Ahn, H. N., Craig, J. P., Pradhan, M., Patel, D. V., & McGhee, C. N. J. (2013). Effect panretinal photocoagulation on corneal sensation and corneal subbasal nerve plexus in diabetes mellitus. *Investigative Ophthalmology & Vision Science, 54*(7), 4485-4490.

Moulton, E. A., Becerra, L., Rosenthal, P., & Borsook, D. (2012). An approach to localizing corneal pain representation in human primary somatosensory cortex. *PLoS ONE, 7*(9), e44643.

Müller, L., Marfurt, C. F., Kruse, F., & Tervo, T. M. T. (2003). Corneal nerves: structure, contents, and function. *Experimental Eye Research, 76*(5), 521-524.

Murphy, P. J. (1996). *An examination of human corneal sensitivity by non-invasive methods.* Ph.D. Thesis. Glasgow Caledonian University.

Murphy, P. J., Corbett, M. C., David, P. S., Verma, S., Patel, S., & Marshall, J. (1999a). Loss and recovery of corneal sensitivity following photorefractive keratectomy for myopia. *Journal of Refractive Surgery, 15*(1), 38-45.

Murphy, P. J., Lawrenson, J. G., Patel, S., & Marshall, J. (1998). Reliability of the non-contact corneal aesthesiometer and its comparison with the Cochet-Bonnet aesthesiometer. *Ophthalmic & Physiological Optics, 18*(6), 532-538.

Murphy, P. J., Morgan, P. B., Patel, S., & Marshall, J. (1999b). Corneal surface temperature change as a mode of stimulation of the non-contact corneal aesthesiometer. *Cornea, 18*(3), 333-342.

Murphy, P. J., Patel, S., Kong, N., Ryder, R. E. J., & Marshall, J. (2004). Noninvasive assessment of corneal sensitivity in young and elderly diabetic and nondiabetic subjects. *Investigative Ophthalmology & Visual Science, 45*(6), 1737-1742.

Murphy, P. J., Patel, S., & Marshall, J. (1996). A new non-contact corneal aesthesiometer (NCCA). *Ophthalmic & Physiological Optics, 16*(2), 101-107.

Murphy, P. J., Patel, S., & Marshall, J. (2001). The effect of long-term, daily contact lens wear on corneal sensitivity. *Cornea, 20*(3), 264-269.

Nishimura, S. (2014). The investigation of the thermal effect of contact lens wear. Master of Philosophy Thesis. Cardiff University.

Norn, M. (1973). Conjunctival sensitivity in normal eyes. *Acta Ophthalmologica, 51*, 58-66.

Nosch, D. S. (2015). *Influence of stimulus characteristics and ocular surface conditions on non-invasive corneal sensitivity measurements*. Ph.D. Thesis. Cardiff University.

Nosch, D. S., Pult, H., Albon, J., Purslow, C., & Murphy, P. J. (2017). Does air gas aesthestiometry generate a true mechanical stimulus for corneal sensitivity measurement? *Clinical and Experimental Optometry, 101*(2), 193-199.

Phan, C-M, Walther, H., Gao, H., Rossy, J., Subbaraman, L. N., & Jones, L. (2016). Development of an *in vitro* ocular platform to test contact lenses. *Journal of Visualised Experiments,* (110), 1-7.

Phan, C-M, Walther, H., Qiao, H., Shinde, R., & Jones, L. (2019). Development of an eye model with a physiological blink mechanism. *Translational Vision Science and Technology, 8*(5):1, 1-12.

Pritchard, N., Edwards, K., Vagenas, D., Russell, A. W., Malik, R. A., & Efron, N. (2012). Corneal sensitivity is related to established measures of diabetic peripheral neuropathy. *Clinical and Experimental Optometry, 95*(3), 355-361.

Purslow, C., & Wolffsohn, J. S. (2005). Ocular surface temperature: A review. *Eye & Contact Lens, 31*(3), 117-123.

Rao, S. B. S. , & Simpson, T. L. (2014). Measurement of difference thresholds on the ocular surface. *Investigative Ophthalmology and Vision Science, 55*(2) 1095-1100.

Riordan-Eva, P., & Cunningham, E. T. (Eds.). (2011). *Vaughan & Asbury's General Ophthalmology* (18th ed.) (pp. 8-11). Lange Medical Books, New York, USA.

Sawilowsky, S. S. (2007). Effect Sizes, Simulating Interaction Versus Main Effects, and a Modified ANOVA Table. In S. S. Sawilowsky (Ed.), *Real data Analysis* (pp. 191-212). Information Age Publishing, North Carolina, USA.

Schwartz. D. E. (1974). Corneal sensitivity in diabetics. *Archives of Ophthalmology, 91*(3), 174-178.

Shaheen, B. S., Bakir, M., & Sandeep, J. (2014). Corneal nerves in health and disease. *Survey of Ophthalmology, 59*(3), 263-285.

Stapleton, F., Tan, M. E., Papas, E. B., Ehrmann, K., Golebiowski, B., Vega, J., & Holden, B. A. (2004). Corneal and conjunctival sensitivity to air stimuli. *British Journal of Ophthalmology, 88*(12), 1547-1551.

Swets, J. A. (1961). Is there a sensory threshold? *American Association for the Advancement of Science, 134* (3473), 168-177.

Tan, J., & Ng, E. Y. K., Rajendra Acharya, U., & Chee, C. (2009). Infrared thermography on ocular surface temperature: A review. *Infrared Physics & Technology, 52*(4), 97-108.

Tanelian, D. L., & Beuerman, R. (1984). Responses of rabbit corneal nociceptors to mechanical and thermal stimulation. *Experimental Neurology, 84*(1), 165-178.

Téson, M., Calonge, M., Fernádez, I., Stern, M. E., & González-García, M. J. (2012). Characterization by Belmonte's gas esthesiometer of mechanical, chemical, and thermal corneal sensitivity thresholds in a normal population. *Investigative Ophthalmology & Visual Science, 53*(6), 3154-3160.

Treutwein, B. (1995). Adaptive psychophysical procedures. *Vision Research, 35*(17), 2503-2522.

Vega, J., Simpson, T., & Fonn, D. (1999). A noncontact pneumatic esthesiometer for measurement of ocular sensitivity: A preliminary report. *Cornea, 18*(6), 675-681.

Weisstein, E. W. (2021). *Affine transformation.* Internet Version. Retrieved on Tuesday 16th February, 2021 from: https://mathworld.wolfram.com/AffineTransformation.html

White, F. M. (2006). *Viscous fluid flow* (3rd ed.) (pp. 297-299). McGraw-Hill.

Wong, S. (2017). *Examination of contact lenses using evaporimetry and infrared thermography*. Accelerated Ph.D. Thesis Proposal. University of Waterloo.

Zare Bidaki, E., Lum, E., Jones, L., & Murphy, P.J. (2017). *Ocular surface temperature measurement using infra-red thermography* [Canadian Optometry Schools Research Conference (COSRC) Poster Presentation]. University of Waterloo, Waterloo, Canada.